Redox-Dependent Transformations in Molecular Self-Assembly of Ferrocenyl Surfactants

By

Timothy J. Smith

A dissertation submitted in partial fulfillment of

the requirements for the degree of

Doctor of Philosophy

(Chemical Engineering)

at the

UNIVERSITY OF WISCONSIN-MADISON

2017

Date of final oral examination: 12/14/2017

The dissertation is approved by the following members of the Final Oral Committee:

Nicholas L. Abbott, Professor, Chemical and Biological Engineering
Reid C. Van Lehn, Assistant Professor, Chemical and Biological Engineering
George W. Huber, Professor, Chemical and Biological Engineering
Thatcher W. Root, Professor, Chemical and Biological Engineering
Padma Gopalan, Professor, Materials Science Engineering

Redox-Dependent Transformations in Molecular Self-Assembly of Ferrocenyl Surfactants

Timothy J. Smith

Under the supervision of Professor Nicholas L. Abbott
at the University of Wisconsin-Madison

Abstract

This thesis explores the effects of redox-triggered changes in the molecular architecture of ferrocenyl surfactants on their self-assembly in aqueous solution. Specifically, we investigated the redox-dependent behavior of 11-ferrocenyltrimethylammonium bromide (FTMA) in the design of surfaces at which the interfacial assemblies formed by FTMA allow for charge transfer in one direction while blocking it in the reverse (i.e. current rectification). First, we showed that aqueous solutions of FTMA exhibit current rectification during cyclic voltammograms performed at gold electrodes that are functionalized with a hydrophobic monolayer. Analysis of the scan rate dependence of the measured current during cyclic voltammograms revealed the current rectification we observe results from the inability of oxidized FTMA in bulk solution to access the electrode. We concluded that reduced FTMA forms a layer on the electrode surface that oxidized FTMA is unable to displace or mix with, leading to current rectification. Further support for this conclusion was found by investigating mixing of reduced and oxidized FTMA in bulk solution via measurement of the surface tension of aqueous solutions containing mixtures of reduced and oxidized FTMA. We concluded that the change in molecular architecture of FTMA when it is oxidized leads to demixing of oxidized FTMA from micellar assemblies of either reduced FTMA or dodecyltrimethylammonium bromide (DTAB) in bulk solution and at hydrophobic surfaces. We also used these redox-triggered changes in FTMA assembly to induce

triggered phases transformations in lyotropic liquid crystalline dispersions through the incorporation of FTMA into phytantriol assemblies. Next we show that the electrode surface chemistry plays an important role in templating interfacial FTMA self-assembly that leads to current rectification. Last, we demonstrate, through proof of concept experiments that the self-assembly of FTMA can be used to generate power in a dye-sensitized solar cell. We found that cells using FTMA generated 17.5 ± 0.2 μW of power under illumination, whereas cells using the otherwise comparable non-self-assembling redox mediator (2-methyl-1-ferrocenylmethyl) trimethylammonium iodide (MFMT) produced only 3 ± 2 μW. Overall, the work presented in this thesis demonstrates that the reversible self-assembly of FTMA can be exploited to influence interfacial charge transfer processes in potentially useful ways.

This thesis is dedicated *ad majorem Dei gloriam*.

Acknowledgments

A Ph.D. is a long and arduous journey that I could not have made without the help of a great many people. First, I would like to thank my parents, Philip G. and Mary P. Smith and many family members for instilling within me the virtues needed to pursue a Ph. D, and for their constant support and encouragement throughout my life. I especially thank my mom for her efforts to push me outside the bounds of my comfort zone to actualize my potential in so many aspects of life. I also particularly thank my dad for his constant example of remaining collected in the face of difficulties. I would like to thank my brother Mark P. Smith and my sister Meghan P. Smith for their indispensable contributions to my formation as an adult. I thank my grandparents Victor and Elizabeth Smith for their sharp wit and tireless courage in the face of many hardships, and for teaching me so much about the world. I would like to thank, in loving memory, my grandmother Virginia Bodner for her extraordinary love for her family, community, and history. Inspired by her example, no matter where my career may take me, I will never forget where I came from. I could ask for a more loving family or one that provided for me a better example.

Second, I thank my advisor, Professor Nicholas L. Abbott for his unceasing assistance throughout my graduate school career. He has been a great help in all of my professional endeavors, from research to writing to coursework to developing my career path. Even here, in an elite department at an elite university, I can recognize that Nick stands out as an extraordinary researcher through his unceasing curiosity, creativity, and unwillingness to settle for incomplete answers. I would like to thank Professors Reid C. Van Lehn, George W. Huber, Thatcher W. Root, and Padma Gopalan for serving on my thesis committee. I greatly appreciate their willingness to sacrifice time and energy for my benefit. I would like to thank Professor Ben J.

Boyd at Monash University with whom I collaborated on the work presented in chapter 6 of this thesis. I thank him and his group for the warm reception I received when traveling to Melbourne, Australia to work with them. I would also like to thank all of the past and present members of the Abbott group for their comradery and assistance, particularly Travis Nelson, Hongseung Yeon, Dan Abras, Emre Bukusoglu, Peter Mushenheim, Maggie Herron, Hector Fuster, Robert Gottlieb, Reza Abbasi, Chenxuan Wang, Michael Tsuei, Marco Bedolla, Karthik Nayani, William Wang, Young-Ki Kim, Mohit Goel, C. Derek Ma, Rishabh Jain, Abhijit Dan, Rebecca Carlton, Chulsoon Park, Huaizhe Yu, Yu Yang, Xin Wang, Nanqi Bao, and Dan Miller. I also acknowledge the help of Ritvind Suketana, Hunter Carlson, and Sonia Chandrasekharan for their contribution as undergraduate researchers, and Ben Gillian-Daniel, who worked with me for a summer as a high school student. I would like to thank Professor Daniel J. Lacks, my research and academic advisor at Case Western Reserve University, for his help in my initial days as a researcher and for his guidance in my decision to pursue a Ph.D.

Third, I would like to thank my friends here in Madison for their encouragement and support throughout my years in graduate school. Life during graduate school is often described as survived rather than enjoyed, but I never really felt that way about my time here. This is a testament to the incredible friends I made in graduate school. Specifically, I would like to thank my classmates Matt Long, Josh Duncan, Mrunmayi Kumbhalkar, Zach Brentzel, Ryan Clark, Tyler Perlenfein, and Insoo Ro for their help throughout many long hours of coursework and research discussion. In addition, I would like to thank numerous other members of our department for their comradery; in particular Chris Mehrer, Eric McCurry, Joe Chada, Douglas Allan, and Jackie Rand. I would like to thank all of my many friends with whom I have enjoyed running with over the years, especially Hector Fuster, Chris Mehrer, J.T. McCrone, and my

friends in the University of Wisconsin Running Club: Stephen, Matthias, Joe Mueller, Zane McInturff, Josh Bendorf, Nicholas Scharping, Jered Sweeney-Demezas, Nash Weiss, Nathan Koch, Clint Carney, Taishi Ikeda, Freddie Mildenhall, and others. Running has provided me with considerable help at handling the stresses of graduate school, and of life. Lastly, I would like to thank my friends at St. Paul's University Catholic Center for help and prayers to keep me grounded and focused throughout my Ph.D. Specifically, I thank Josh Sauppe, Chris Mehrer, Michael Tinio, Quinn Bongers, J.T McCrone, Geoffrey Ludvik, Tom Dobbins, Andrew Conley, Konrad Paczuski, John O'Brien, Jack Bredemann, Andrew Higgins, and many others. Without the friendship and help of so many people, I do not think I could have finished this journey.

Table of Contents

List of Figures and Tables

Chapter 1 : Introduction and Overview

1.1 Introduction

The use of surfactants is ubiquitous in numerous scientific fields, from textiles to detergents to oil recovery due to their influence on bulk and interfacial properties. One class of surfactant that has attracted significant attention in recent years is responsive surfactants, which allow for reversible control over the surfactant-based properties of aqueous systems.[1-3] Responsive surfactant systems have been designed that react to triggers ranging from photoillumination[4-6] to pH[7] to redox state.[2,3,8-11] The project presented in this thesis is an investigation of the use of changes in the self-assembly of ferrocenyl surfactants with changes in redox state to control (i) interfacial charge transfer and (ii) the phase state of lyotropic liquid crystalline (LC) dispersions. Chapters 2-5 of this thesis focus on the use of the self-assembly of ferrocenyl surfactants in aqueous solutions at electrode surfaces to control charge transfer across those interfaces. Chapter 6 focuses on the incorporation of redox surfactants into lyotropic LC dispersions in order to trigger changes in their phase state and the release of encapsulated solutes.

The work described in this thesis was performed, primarily, using the ferrocenyl surfactant 11-ferrocenyltrimethylammonium bromide (FTMA). FTMA (see Figure 1.1), contains a ferrocene moiety and a trimethylammonium group at opposite ends of an 11-member alkyl chain. Oxidation of FTMA leads to a transformation of ferrocene (initially in FTMA's reduced state), which can generally be considered hydrophobic, into the ferrocenium ion (in FTMA's oxidized state). Previous studies have shown that this transformation leads to changes in surface activity [11-14] and bulk aggregation[9,15-16] In this thesis, we explore the ability of redox-driven changes in the interfacial self-assembly of FTMA at solid electrode surfaces to control charge

transfer. Specifically, we exploit demixing of reduce and oxidized FTMA within interfacial assemblies on an electrode in order to rectify current. Underlying the demixing between reduced and oxidized FTMA in interfacial assemblies is a change in molecular architecture from a conventional surfactant to a bolaform surfactant upon oxidation. We further explore the effects of changes in molecular architecture between reduced and oxidized FTMA by incorporating FTMA into lyotropic LC dispersions and investigating triggered phase changes via manipulation of the redox state of FTMA.

The section below presents an excerpt from a review chapter on responsive surfactants that provides an overview of previous investigations of ferrocenyl surfactants. The subsequent section provides additional background and motivation for the use of ferrocenyl surfactants in the design of rectifying interfaces and lyotropic LC dispersions. This chapter is concluded by a summary of the work presented in each subsequent chapter of this thesis.

1.2 Background and Motivation

1.2.1 Background on Ferrocenyl Surfactants‡

While the earliest redox-active surfactant systems used viologen derivatives as a redox group within the surfactant molecules [8,17-19], most of the more recent work performed with redox-active surfactants has been based on surfactants containing the ferrocene moiety. In contrast to viologens, ferrocenyl surfactants are largely insensitive to oxygen. Ferrocenyl surfactants were first synthesized by Saji and coworkers[9,10] in 1985 and have been the subject of extensive research since that time.[2] Although ferrocenyl surfactants with varied molecular architectures have been synthesized, this chapter focuses on amphiphiles with the structures shown in Figure 1.1: FTMA, bis(11-ferrocenylundecyl) dimethylammonium bromide (BFDMA),

11-ferrocenylundecylammonium bromide (11-FAB), and sodium (11-ferrocenylundecyl) sulfonate (SFS).

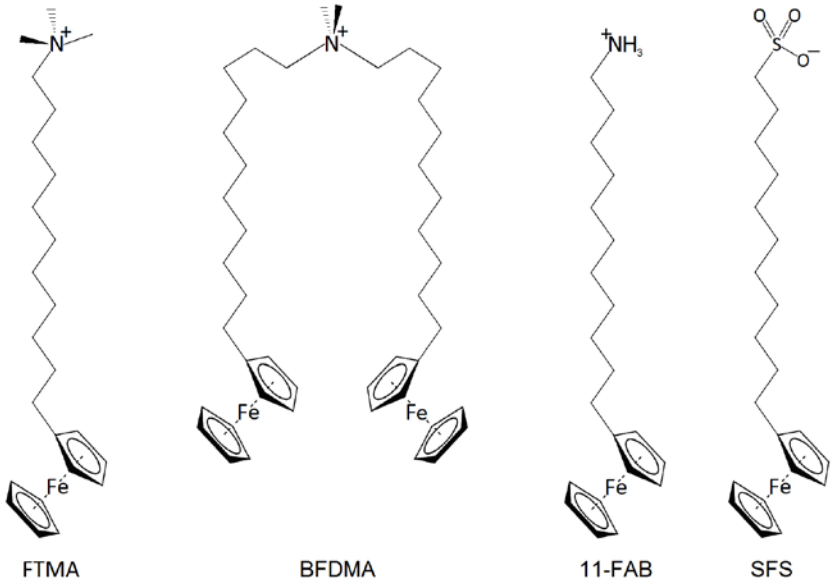

Figure 1.1 Molecular structures of ferrocenyl surfactants
Molecular structures of ferrocenyl surfactants addressed in this chapter: 11-ferrocenylundecyl trimethylammonium bromide (FTMA), bis(11-ferrocenylundecyl) dimethylammonium bromide (BFDMA), 11-ferrocenylundecylammonium bromide (11-FAB), and sodium (11-ferrocenylundecyl) sulfonate (SFS) (counter ions not shown).

1.2.1.1 Reversible Changes in Interfacial Properties

Redox-active surfactants have been used extensively to drive reversible changes in interfacial adsorption and associated properties such as surface tension. The effect of a change in oxidation state of ferrocene on interfacial properties depends strongly on the architecture of the surfactant that hosts the ferrocene. To illustrate this point, here we contrast studies of the changes in surface tension resulting from the oxidation and reduction of two redox-active surfactants that have been studied extensively: FTMA[9,11,12,20] and SFS.[21] FTMA (see Figure 1.1) has the architecture of a conventional cationic surfactant with a +1 charge in its reduced state

and, upon oxidation to a +2 state, it transforms to a cationic bolaform surfactant-like structure. Gallardo *et al.*[11,12] measured the surface tensions of aqueous solutions of FTMA in

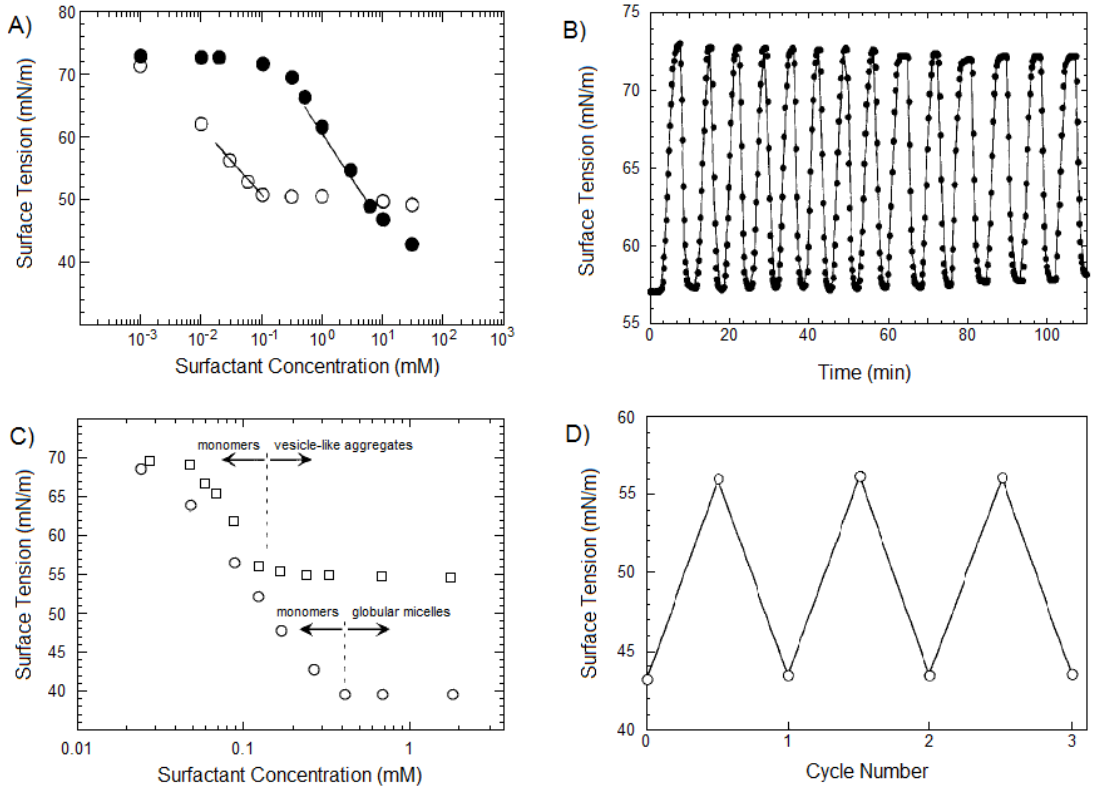

Figure 1.2 Surface tension of ferrocenyl surfactants
(A) Equilibrium surface tensions of aqueous solutions (0.1 M Li_2SO_4, pH 2, 25°C) of reduced FTMA (○) and oxidized FTMA (●). (B) Dynamic surface tension of an aqueous solution of 0.3 mM reduced/oxidized FTMA (0.1 M Li_2SO_4, pH 2, 20°C) measured during the repeated cycling of the surfactant between oxidation states. (C) Equilibrium surface tensions of aqueous solutions of reduced SFS (○) and oxidized SFS (□) (10 mM Li_2SO_4, pH 5, 37°C). (D) Dynamic surface tensions of an aqueous solution of 0.6 mM oxidized and reduced SFS (10 mM Li_2SO_4, pH 5, 37°C) measured during the repeated cycling of the surfactant between oxidation states. In (B) and (D), the high values of surface tension correspond to a solution of oxidized surfactant, and the low values correspond to a solution of reduced surfactant. **(A)** and **(B)** reproduced from Ref. 12 with permission and **(C)** and **(D)** reproduced from Ref. 21 with permission.

100 mM Li_2SO_4 as a function of FTMA concentration. The plots of surface tension vs concentration measured for reduced FTMA (see Figure 1.2A) are seemingly typical of a

conventional cationic surfactant: the surface tension decreases until a critical micelle concentration (CMC) (~0.1 mM for reduced FTMA) is reached, above which the surface tension maintains a value of 49 mN/m. Oxidized FTMA also causes a decrease in the surface tension of water but a higher concentration is necessary to see a significant effect. Oxidized FTMA, however, does not exhibit a break in the surface tension vs concentration plot up to concentrations of at least 30 mM. At concentrations below 1 mM FTMA, oxidation of FTMA thus leads to an increase in surface tension of up to 23 mN/m (see Figure 1.1). At higher concentrations (above 10 mM), in contrast, oxidation of FTMA leads to a decrease in surface tension of the aqueous solution.

To provide insight into the above observations, the excess surface concentrations of FTMA, Γ_s, (and area per molecule) were calculated from measured changes in surface tension, γ, with concentration, C_s, using the Gibbs adsorption isotherm:

$$\Gamma_s = -\frac{1}{kT}\frac{d\gamma}{d[\ln C_s]} \qquad (1)$$

where k is the Boltzmann constant and T is the temperature. Evaluation of the surface excess led to the proposal that both oxidized and reduced forms of FTMA exist in a looped configuration at the air/water interface. Specifically, for reduced FTMA, the limiting area per molecule at the interface was 85 ± 5 $Å^2$/molecule, a value that is substantially larger than for conventional cationic surfactants (dodecyltrimethylammonium bromide, DTAB, for example, has a limiting area per molecule of 63 ± 2 $Å^2$/molecule).[11] The large value of the limiting area per molecule for reduced FTMA supports the interpretation of the looped configuration and also gives rise to the interesting conclusion that the dominant mechanism by which reduced FTMA lowers surfactant tension is not via electrostatics (as is the case with conventional ionic surfactants) but instead via

an entropic term associated with constraints on the configuration of the molecules at the interface. The existence of the looped configuration also underlies the higher surface tension plateau (49 mN/m) measured with reduced FTMA than with DTAB (40 mN/m)[22,23] as elucidated by a molecular-thermodynamic model of FTMA.[20] Interestingly, because oxidized FTMA does not form micelles in bulk solution (see below for additional discussion), the limiting area per molecule of oxidized FTMA at the surface of the aqueous solution was 75 ± 5 $Å^2$/molecule. This small value of the area per molecule (as compared to reduced FTMA), when combined with the +2 charge, explains the relatively lower surface tensions generated by oxidized FTMA as compared to reduced FTMA at high bulk concentrations.

Whereas the results above apply to the cationic ferrocenyl surfactant FTMA, an anionic ferrocenyl surfactant, SFS, has also been shown to permit redox-induced, reversible changes in surface tension.[21] SFS is similar to FTMA except that the trimethylammonium group is replaced by a sulfonate group. This change in the head group charge, however, leads to significantly different response of SFS to oxidation of the ferrocene as compared to FTMA. First, inspection of Fig 1.2C reveals that oxidation of SFS results in a decrease in the CAC of the SFS in solution (recall that the CMC of FTMA increased with its oxidation). As discussed below, the morphologies of the assemblies formed by SFS are also strikingly different from FTMA. Second, at concentrations below which either oxidized or reduced SFS self-assembles in bulk solution, we observe that both states of FTMA lower the surface tension. Oxidized FTMA at these concentrations did not measurably lower surface tension. In contrast to FTMA, however, oxidation of reduced SFS (within a monolayer formed at the surface of the solution) leads to a decrease in both the electrostatic free energy of the monolayer (as the resulting zwitterionic species does not have a net charge) and the hydrophobicity of SFS that drives formation of the

monolayer. These two effects appear to largely counterbalance, with the net result being only a small change in surface tension upon oxidation of SFS at low concentrations. Below we discuss differences in the bulk solution behaviors of FTMA and SFS that underlie observations reported above.

1.2.1.2 Reversible Changes in Bulk Solution Properties

Underlying the changes in interfacial properties described in the previous section are, of course, changes in bulk solution self-assembly that are triggered by the redox reactions. As inferred from the surface tension vs. concentration plots, for concentrations from 0.1 mM to 10 mM, FTMA forms aggregates in its reduced state but not in its oxidized state. By using dynamic light scattering measurements[21] (see Table 1.1) and small angle neutron scattering (SANS), it has been shown that reduced FTMA forms globular micelles with a hydrodynamic diameter, D_h, of 6 ± 2 nm, similar to what is typically observed for a conventional ionic surfactant. Reduced SFS behaves similarly to reduced FTMA, forming globular micelles with D_h = 6 ± 2 nm. Interestingly, however, oxidized SFS has the architecture of a zwitterionic bolaform and forms vesicle-like aggregates with D_h = 70 ± 8 nm. This behavior is consistent with that seen for many conventional zwitterionic surfactants.[24] We note also that the critical aggregation concentration (CAC) of oxidized SFS is lower than that of reduced SFS (in contrast to the effects of oxidation of ferrocene on the CAC of FTMA).

The bulk solution properties of 11-FAB, which differs from FTMA by having an ammonium moiety rather than trimethylammonium as its headgroup, have also been characterized.[7] The smaller headgroup of reduced 11-FAB leads to the formation of vesicles in aqueous solutions (at low pH) rather than micelles. Upon oxidation, similar to FTMA, the

reduced 11-FAB aggregates disassemble into oxidized 11-FAB monomers. However, 11-FAB is also responsive to pH changes. Under basic conditions, for example, reduced 11-FAB will precipitate out of solution, thus providing a convenient means to recover 11-FAB from solution.

surfactant	D_h (nm)	concentration (mM)
$Fc(CH_2)_{11}SO_3^-$	6 ± 2	>0.4
$Fc^+(CH_2)_{11}SO_3^-$	70 ± 8	>0.15
$Fc(CH_2)_{11}N^+(CH_3)_3$	6 ± 2	>0.1
$Fc^+ (CH_2)_{11}N^+(CH_3)_3$	does not aggregate	<10

Table 1.1.1 Hydrodyanmic diameters of assemblies formed by ferrocenyl surfactants
Hydrodynamic diameters, D_h, of assemblies formed by ferrocenyl surfactants (0.6 mM) within aqueous solutions of 10 mM Li_2SO_4 for the SO_3^--based surfactants and 100 mM Li_2SO_4 for the $N^+(CH_3)_3$-based surfactants, all at 37°C. Table reproduced from Ref. 21 with permission.

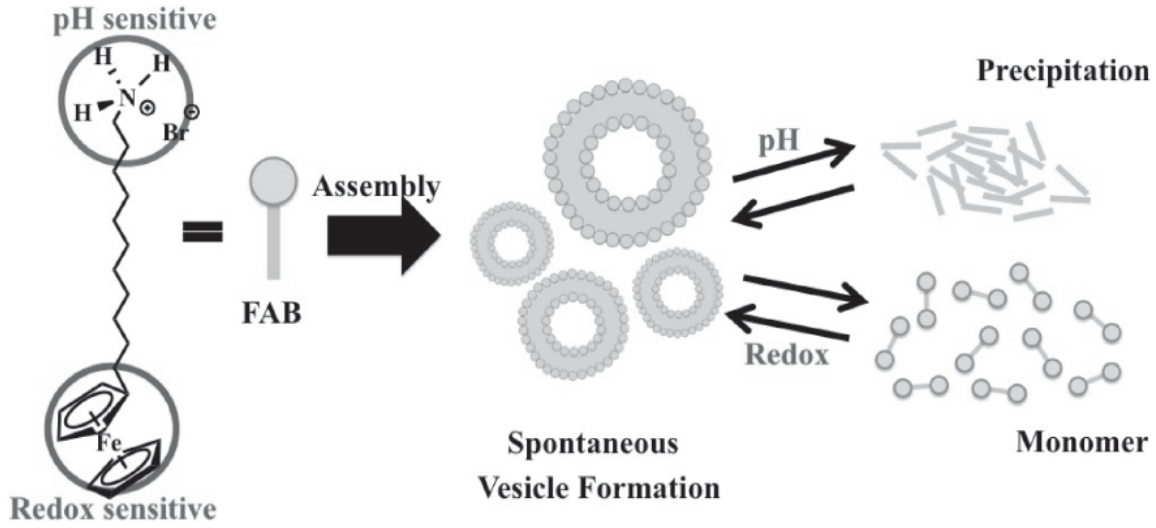

Figure 1.3 Triggered changes in the assembly of 11-FAB
Possible mechanism leading to the formation and disruption of vesicles by pH variation and redox chemistry. Pure 11-FAB spontaneously forms vesicles in aqueous solutions. Disappearance of charge associated with the ammonium headgroup with increasing pH leads to disruption of vesicles and formation of precipitates in water. Vesicles reform by decreasing pH again. Reduced 11-FAB also forms vesicles in electrolyte solutions. Vesicles are disassembled by electrochemical oxidation, and oxidized 11-FAB behaves as a bola surfactant. Subsequently, chemical reduction of oxidized 11-FAB brings about reformation of vesicles. Figure reproduced from Ref. 7 with permission.

In addition to the formation of globular micelles or vesicles, redox-active surfactants have also been used to form worm-like micelles and thus provide control over bulk solution properties such as viscosity. For example, Abe and coworkers[25] found that reduced FTMA forms giant worm-like micelles with sodium salicylate. Solutions containing these worm-like micelles exhibit viscoelastic behavior and high zero-shear viscosities (around 15 Pa·s). Upon oxidation of the ferrocene, the worm-like micelles break into ellipsoidal micelles, thus generating a Newtonian fluid with a viscosity of 2.5×10^{-3} Pa·s, which is around $1/6000^{th}$ the zero-shear-rate viscosity of the solution containing reduced FTMA (and salicylate).

FTMA has also been used to tune the interactions between surfactants and polymers such as ethyl(hydroxyethyl) cellulose (EHEC).[15] Reduced FTMA, for example, was found to promote the aggregation of ethyl(hydroxyethyl) cellulose (EHEC) at low FTMA concentrations and disperse aggregates at high FTMA concentrations. In contrast, oxidized FTMA did not strongly associate with EHEC and thus had very little effect on the state of aggregation of the EHEC. The use of redox-active surfactants to tune the interactions and state of dispersion of polymers in solution has also been extended to a range of biopolymers including DNA.[16] DNA adopts a coiled configuration in aqueous solution in the absence of surfactant. The addition of 2-5 μM of reduced FTMA, however, was measured to generate coexisting populations of coils and compact globules of DNA. Upon further addition of reduced FTMA to a concentration of 30 μM, all of the coils were transformed to compact globules. In contrast, oxidized FTMA had no measurable effect on the DNA conformation at concentrations up to 75 μM, allowing for reversible control of DNA conformations via manipulation of the redox state of FTMA.

Several past studies have also reported on complexes (lipoplexes) formed by DNA and the double-tailed ferrocenyl surfactant BFDMA.[26] These studies were motivated by the widespread use of double-tailed cationic surfactants for the packaging and delivery of DNA to cells. BFDMA was measured to form lipoplexes with DNA in both redox states. These lipoplexes vary in both size and zeta potential as a function of BFDMA concentration (see Figure 1.4). As the concentration of reduced BFDMA increased, the hydrodynamic sizes of the lipoplexes passed through a maximum. Over this same range of concentrations, the zeta potentials of the complexes increased from -40 mV to +40 mV. Interestingly, for oxidized BFDMA, however, the lipoplex size passed through a minimum as a function of increasing BFDMA concentration and the zeta potential was measured to be negative across all BFDMA concentrations. These measurements led to the conclusion that redox state-dependent changes in the transfection efficiency of BFDMA lipoplexes (see the next section) likely reflect the dependence of the zeta potential of BFDMA-DNA complexes on the oxidation state of BFDMA.

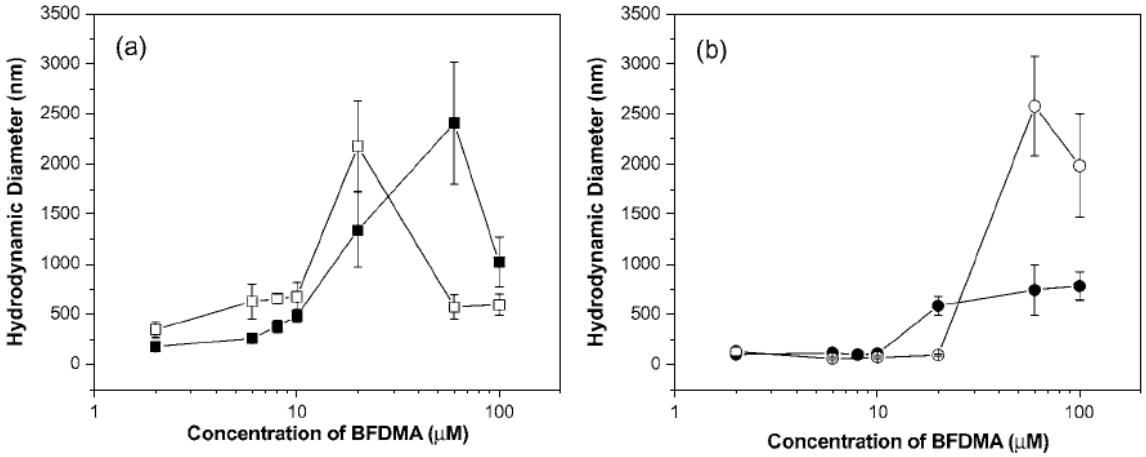

Figure 1.4 Hydrodynamic diameter of complexes formed by BFDMA
Hydrodynamic diameters of complexes formed from reduced and oxidized BFDMA as a function of concentration of BFDMA, as calculated from dynamic light scattering measurements. **(A)** Lipoplexes formed by reduced BFDMA and DNA in 1 mM Li_2SO_4 (□) and OptiMEM (■). **(B)** Complexes formed by oxidized BFDMA and DNA in 1 mM Li_2SO_4 (○) and OptiMEM(●). Figure reproduced from Ref. 26 with permission.

1.2.1.3 Control of Biomolecule-Surfactant Assemblies

As noted above, DNA forms complexes (called lipoplexes) with many double-tailed cationic surfactants, and the resulting complexes are able to be transported across cell membranes leading to "transfection" of cells. The capability to control the transport of DNA across cell membranes has the potential to be useful in a range of contexts such as gene therapy and, more broadly, biotechnology.[27,28] As discussed in the previous section, BFDMA forms lipoplexes with DNA in both redox states. Recently, however, it was reported that reduced BFDMA forms complexes with plasmids that encode for enhanced green fluorescent protein (EGFP) and are transported into cells (COS-7 cell line), resulting in expression of the EGFP. In contrast, the complexes formed between the plasmids and oxidized BFDMA do not result in the delivery of the plasmids to the cells.[29] This difference in behavior between the two redox states allows the DNA to be transfected upon delivery of a trigger that reduces oxidized BFDMA.

Examples of chemical reducing agents that have been used as a trigger include glutathione[30] and ascorbic acid.[31,32] One such demonstration is shown in Figure 1.5, in which lipoplexes of oxidized BFDMA and DNA (encoding for EGFP) are dispersed in culture media in which cells are growing. Ascorbic acid is added locally to the culture media (via a hollow cylinder). The BFDMA-containing lipoplexes exposed to ascorbic acid are reduced and the associated DNA is able to enter the cells. Fluorescence is detected only in the regions to which the ascorbic acid was delivered, demonstrating that transfection is limited to cells in the activated area.

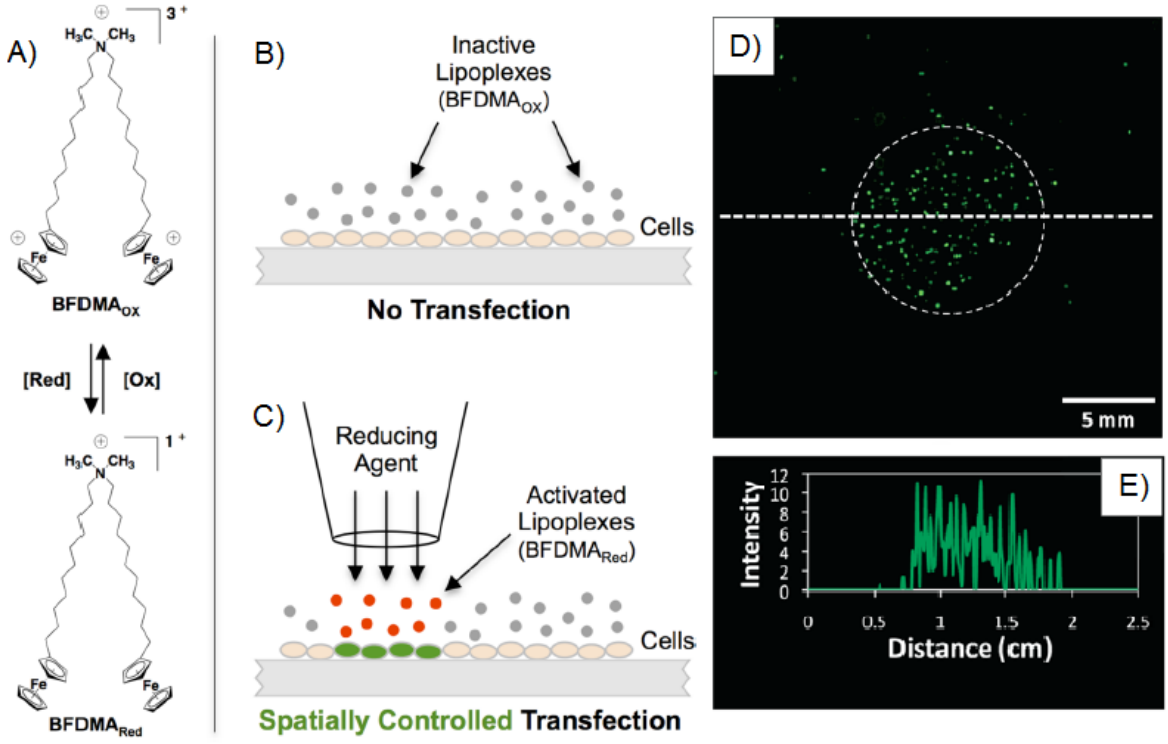

Figure 1.5 Controlled transfection via BFDMA lipoplexes
(A) Structure of BFDMA; **(B−C)** Schematic illustration demonstrating core principles: **(B)** Lipoplexes of oxidized BFDMA (gray) are inactive and can be distributed uniformly over cells without promoting transfection, **(C)** Controlled administration of soluble or solid-phase reducing agents results in localized activation of lipoplexes (red) and spatially controlled transfection (green); adjacent cells are unaffected. **(D)** Composite of fluorescence micrographs showing the area of a cell culture well containing inactive lipoplexes of oxidized BFDMA and a hollow cylinder (dotted circle) used to localize delivery of ascorbic acid. The lipoplexes within the cylinder are activated upon reduction and transfer plasmid DNA encoding enhanced green fluorescent protein (EGFP). **(E)** Line intensity profile of EGFP fluorescence measured along the dotted line shown in (D). Figure reproduced from Ref. 32 with permission.

1.2.1.4 Spatial Control of Surfactant-Based Properties

As illustrated by the example above, localized delivery of reducing agents to solutions containing redox-active surfactants can be used to generate spatially localized changes in surfactant-based properties. This concept has also been extended to create controlled gradients in bulk and interfacial properties. Here we summarize, in particular , two types of spatial

gradients that have been explored in redox-active surfactant systems: surface tension-driven (Marangoni) flows and spatial gradients in the concentrations of micelles in bulk solution.

Marangoni flows are generated by stresses associated with gradients in surface or interfacial tension. As discussed in section 1.2.1.1, oxidation and reduction of redox-active surfactants can generate significant changes in surface tensions of aqueous solutions. These changes in surface tension can be exploited to generate surface tension gradients and thus drive interfacial flows. Gallardo *et al.*[13] demonstrated (see Figure 1.6) that Marangoni flows can be generated using FTMA in a fluidic network comprising of two intersecting channels. Electrodes were placed at the ends of each of the channels. Liquid crystal droplets were used to visualize the interfacial flows. At each electrode, FTMA was either reduced or oxidized, thus leading to gradients in the concentrations of these species across the interface and thus to surface tension gradient-driven flows. In contrast to Marangoni flows driven by conventional surfactants, we emphasize that steady-state gradients in surface concentrations can be generated by redox-active surfactants (based reversible changes in oxidation state) and that the magnitudes of the gradients can also be controlled by manipulation of the potentials applied to the electrodes. We comment also that the flows in Figure 1.6 are not electrokinetic in nature, but arise from gradients in surfactant concentration and thus surface tension.

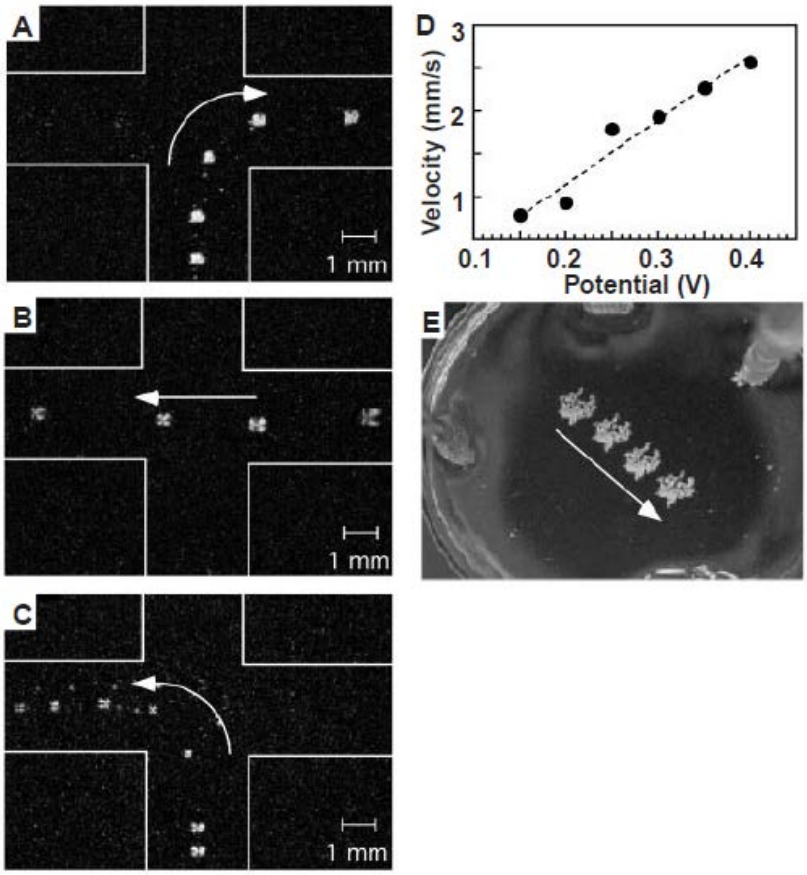

Figure 1.6 Microfluidic transport of LC droplets using Marangoni flows
(A-C) Time-lapse images (4-6 frames obtained at ~0.5 Hz) of the pumping of liquid crystal (LC) droplets across the surface of an aqueous solution of 0.3 mM FTMA (0.01 M Li_2SO_4) contained within a simple fluidic network formed by four glass microscope slides affixed to a larger glass plate. Platinum (Pt) electrodes protrude through the surface of the solution at the ends of the left, right, and lower channels (widths 4 mm). The end of the top channel contains a saturated calomel reference electrode and Pt counterelectrode. **(A)** Droplet of LC dispensed into the bottom channel of the intersection is pumped into the right channel by application of a potential of -0.3 V to the bottom Pt electrode and +0.3 V to the right Pt electrode. **(B)** The droplet of LC in the right channel of the intersection is pumped into the left channel by application of a potential of -0.3 V to the right Pt electrode and +0.3 V to the left Pt electrode. **(C)** A droplet of LC dispensed into the bottom channel of the intersection is pumped into the left channel by application of a potential of -0.3 V to the bottom Pt electrode and +0.3 V to the left Pt electrode. **(D)** The velocity of fluid motion measured in a straight channel (width 4 mm) as a function of applied potential. The x axis indicates the magnitude of the anodic and cathodic potentials. **(E)** Time-lapse image (four frames obtained at 0.3 Hz) of sulfur microparticles supported on an unconfined surface of a solution of oxidized FTMA. Application of -0.3 V to two Pt electrodes placed at the top and left sides of the image caused the sulfur microparticles to be pumped in the direction indicated by the arrow. The horizontal dimension of the image is ~40 mm. Figure reproduced from Ref. 13 with permission.

on

Redox-active surfactants have also been used to generate gradients in the concentration of micelles in bulk solution. Here we illustrate the opportunity associated with such gradients in bulk solution[33,34] by describing recent studies that have used microfluidic channels with opposing side-walls that are each lined with an electrode. Application of reducing and oxidizing potentials to the opposing electrodes leads to the rapid generation of steady-state gradients in reduced and oxidized FTMA concentrations across the channel. Since reduced FTMA forms micelles whereas oxidized FTMA does not (see above), a spatial gradient in the concentration of micelles across the channel is also generated. Because sparingly water soluble and amphiphilic solutes interact with the micelles within the microfluidic channel, the gradients in micelle concentration can be used to selectively partition solutes across the channel via their interaction with the micelles, thus offering the basis of a continuous separations process (the outlet stream is fractionated by splitting the flow into a series of small channels that sample the lateral concentration profile across the microfluidic system) (see Figure 1.7).

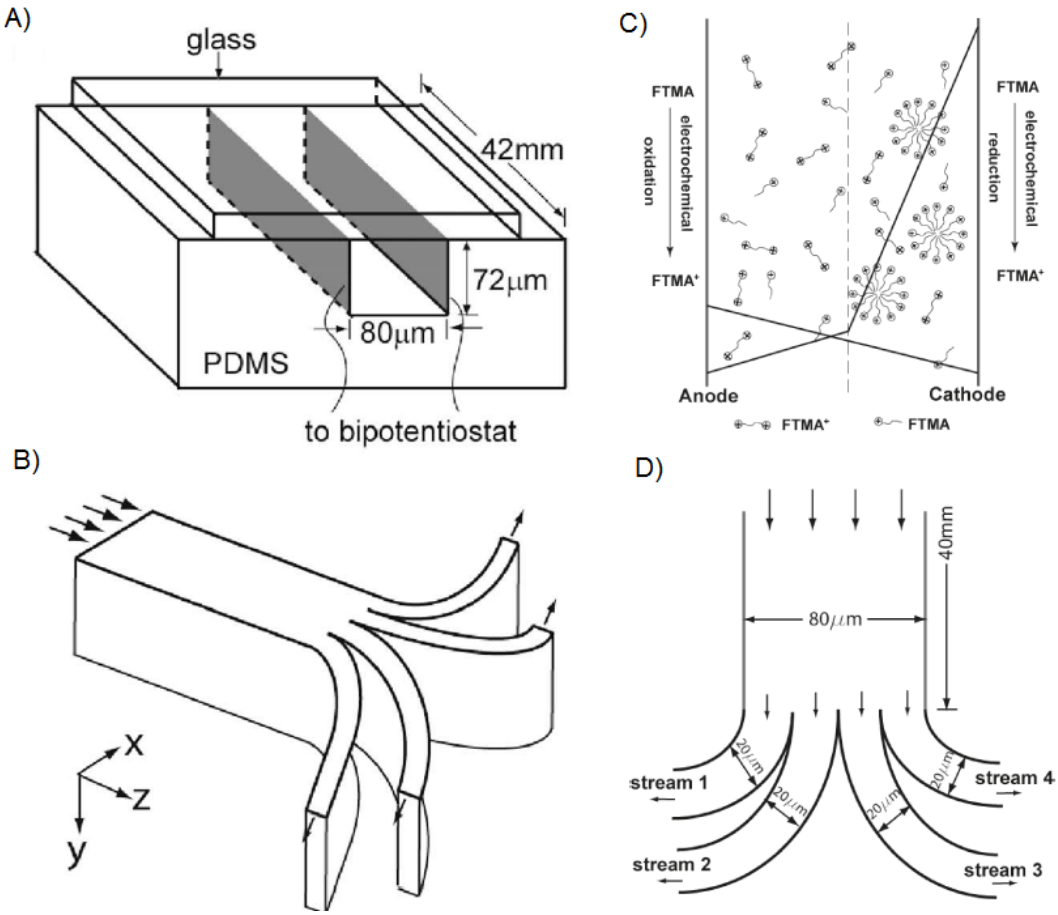

Figure 1.7 Electrochemical separation via concentration gradients in microfluidics
(A) Expanded view of a microfluidic channel with two independent electrodes lining the vertical walls of the channel. **(B)** Schematic illustration of the microfluidic channel used to electrochemically generate and measure lateral gradients in the concentration of redox-active surfactant. **(C)** Schematic illustration of electrochemically generated gradient in concentration of FTMA across the microfluidic channel. **(D)** Schematic illustration of top view of the outlet of the microfluidic channel. (A) and (B) reproduced from Ref. 33 with permission and (C) and (D) reproduced from Ref. 34 with permission.

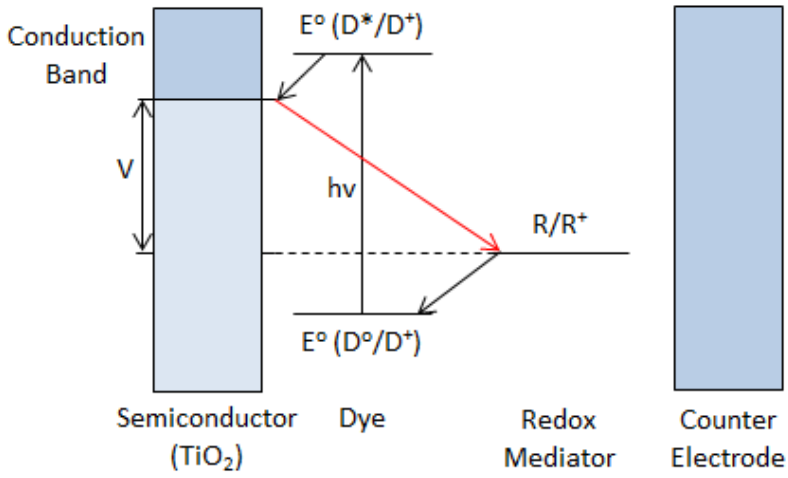

Figure 1.8 Schematic of energy levels in a DSC
Schematic diagram of different processes occurring in a DSC. The reaction shown in red is the unwanted recombination reaction.

1.2.2 Importance of Design of Solid/Liquid Rectifying Interfaces

The first system in which we investigated the use of the self-assembly of redox surfactants is in the design of surfaces that pass electrical current in one direction while blocking it in the reverse (i.e. current rectification). A common challenge to the design of efficient of efficient photoelectrochemical devices, such as dye-sensitized solar cells[35-46] or solar water splitters,[47-50] is the engineering of interfaces that charge can rectify current between a solid electrode and a redox mediator in solution. The process by which a dye-sensitized solar cell (see Figure 1.8) generates power makes use of a dye adsorbed to a semiconductor network that enters an excited state and releases an electron upon illumination. The intended path of the electron is to travel through the semiconductor network to an electrode; meanwhile electrons are replenished to the dye by adsorption of electrons from a redox mediator in solution. In order to maximize the effectiveness of these devices, they must be able to readily transfer electrons from solution to the semiconductor network and the dye, but not from the network to the solution (i.e. recombination reactions). The most common strategy for blocking recombination reactions

involves the use of the redox mediator iodide/triiodide, which prevents recombination reactions by harnessing its slow reaction kinetics for the reduction reaction on a semiconductor surface. However, iodide/triiodide has a non-optimal redox potential and is very corrosive, which limits the selection of materials that can be used in a rectifying device. In this thesis, we investigated the use of self-assembly of ferrocenyl surfactants as a means to rectify current. Our aim was to design systems in which recombination reactions can be blocked while allowing for dye replenishment.

1.2.2 Lyotropic Liquid Crystalline Phase Transformations

In addition to the elicitation of current rectification, we also sought to harness redox-dependent changes in self-assemblies formed by ferrocenyl surfactants to trigger transformations in the phase state of lyotropic liquid crystalline (LLC) dispersions. Past studies have shown that LLCs form a number of phase states including lamellar, inverse bicontinuous cubic (with multiple geometries), inverse hexagonal, and inverse discontinuous micellar cubic.[51,52] Solutes (such as drugs) can be encapsulated in aqueous dispersions of LLC aggregates and the diffusion (i.e. release) of solutes into the continuous phase depends greatly on the phase state of the aggregates.[53] These encapsulated solutes can be released by phase changes[54-59] occurring upon the application of external stimuli, such as changes in temperature,[60] pH,[61,62] or activation by electromagnetic radiation.[63] The phase state of LLC dispersions is sensitive to the presence of co-surfactants such as didodecyldimethylammonium bromide (DDAB)[20] or DTAB.[21] From these past studies, we hypothesized that the incorporation of linear cationic ferrocenyl surfactants, such as FTMA, into phytantriol aggregates would also lead to changes in packing geometry, and thus phase changes. Furthermore, we hypothesized that the phase state formed by LLC aggregates

containing FTMA would also differ by the redox state of FTMA, thus allowing for redox-triggered control over the LLC phase state.

1.2 Thesis Overview

This thesis focuses on five research topics which make use of the amphiphile FTMA. Chapters 2, 4, and 5 describe studies performed to explore the use of a self-assembling redox mediator to control interfacial charge transfer. In Chapter 2, we explore using FTMA to rectify current at a hydrophobized gold electrode. In chapter 4, we relax the constraint of a hydrophobized by exploring the self-assembly and charge transfer exhibited by FTMA at electrodes functionalized with charged monolayers. In chapter 5, we fabricate dye-sensitized solar cells that use the interfacial self-assembly of FTMA to generate power. Chapters 3 and 6 focus on the self-assembly of, and aggregates formed by FTMA in each redox state. In chapter 3, we investigate the effects of molecular architecture on the demixing of the reduced and oxidized states of FTMA in aggregates in bulk solution and at interfaces. In chapter 6, we incorporate FTMA in each redox state into lyotropic liquid crystalline dispersions and use changes in redox state to trigger phase transformations. A summary of each chapter is given below.

Chapter 2 reports on the influence of reversible self-assembly of amphiphilic redox-mediators on interfacial charge transfer at chemically functionalized electrodes. Specifically, we employed FTMA as a model self-assembling redox mediator and alkanethiol-modified gold films as hydrophobic electrodes. By performing cyclic voltammetry (CV, 10 mV/s) in aqueous solutions containing FTMA above its critical micellar concentration (CMC), we measured anodic (I_a) and cathodic (I_c) peak current densities of 18 ± 3 μA/cm^2 and 1.1 ± 0.1 μA/cm^2, respectively, revealing substantial current rectification (I_a/I_c= 17) at the hydrophobic electrodes. In contrast, hydroxymethyl ferrocene (a non-self-assembling redox mediator) at hydrophobic electrodes and

FTMA at bare gold electrodes yielded relatively low levels of rectification (I_a/I_c= 1.7 and 2.3, respectively). Scan-rate dependent measurements revealed I_a of FTMA to arise largely from diffusion of FTMA from bulk solution to the hydrophobic electrode whereas I_c was dominated by adsorbed FTMA, leading to the proposal that current rectification observed with FTMA is mediated by interfacial assemblies of reduced FTMA that block access of oxidized FTMA to the hydrophobic electrode. Support for this proposal was obtained by using atomic force microscopy and quartz crystal microbalance measurements to confirm the existence of interfacial assemblies of reduced FTMA (1.56 ± 0.2 molecules/nm^2). Additional characterization of a mixed surfactant system containing FTMA and dodecyltrimethylammonium bromide (DTAB) revealed that interfacial assemblies of DTAB also block access of oxidized FTMA to hydrophobic electrodes; this system exhibited I_a/I_c>80. These results suggest that current rectification occurs in this system because oxidized FTMA does not mix with interfacial assemblies of reduced FTMA or DTAB formed at hydrophobic electrodes. More broadly, these results show that self-assembling redox mediators, when combined with chemically functionalized electrodes, offer the basis of new principles for controlling charge transfer at electrode/solution interfaces.

Chapter 3 focuses on the hypothesis that redox-triggered changes in the architectures of surfactants permit control of mixing of surfactants within assemblies. Specifically, we describe surface tension, light scattering, atomic force microscopy, and quartz crystal microbalance measurements that characterize the redox-dependent behaviors of cationic surfactants with a ferrocene group located either at the surfactant terminus (FTMA) or head (N,N-dimethylferrocenylmethyldecyl ammonium bromide; DMFA). In bulk solution, we find that reduced and oxidized FTMA do not mix within micellar assemblies but that reduced and oxidized DMFA do form mixed micelles. Because oxidized FTMA has the architecture of a

bolaform surfactant whereas oxidized DMFA has a conventional surfactant architecture with a divalent head group, these results suggest that redox-triggered changes in molecular architecture permit control of the extent of mixing of surfactants in micellar assemblies in bulk solution. This conclusion receives further support from measurements performed with mixtures of DTAB and FTMA, with FTMA in either reduced or oxidized states, and was found to extend to hemimicellar assemblies formed at hydrophobic solid surfaces but not to mixed monolayers formed at the surface of water. The latter is attributed to differences in the conformations of surfactants within monolayers and micellar assemblies. Overall, these results provide insight into the design of surfactant assemblies within which mixing can be controlled reversibly using redox processes.

Chapter 4 explores the role played by the surface charge of electrodes in the electrochemical behavior of solid/liquid interfaces designed to allow electrons to readily cross in one direction while blocking them in the reverse direction (i.e. current rectification) for the design of efficient photoelectrochemical devices. The strategy outlined in Chapter 2 for rectifying current passed by a solid electrode in solution is to use an amphiphilic redox-active species that self-assembles on a hydrophobic surface in a manner that is dependent on oxidation state. Motivated by the prediction that self-assembly of the redox-mediator, and thus current rectification, will depend on the surface properties of the electrode, herein we report on the influence of the surface chemistry of model electrodes on interfacial charge transfer processes that are controlled by self-assembly of an amphiphilic redox mediator. Specifically we used FTMA as a self-assembling redox mediator in aqueous solutions that contacted gold electrodes functionalized with monolayers formed from either 1-dodecanethiol (DT; nonpolar electrode), 11-mercaptoundecansulfonate (MUS; negatively-charged electrode), or N,N,N-trimethyl-(11-

mercaptoundecyl)ammonium (TMUA; positively-charge electrode). By comparing the magnitude of the anodic (I_a) and cathodic (I_c) peak current passed during cyclic voltammetry (CV), we found that self-assembly of FTMA on gold electrodes functionalized with MUS or TMUS does not lead to the same extent of current rectification measured at hydrophobic electrodes ($I_a/I_c = 3.4 \pm 1.2$ and $I_a/I_c = 1.4 \pm 0.1$ vs. $I_a/I_c = 8 \pm 2$, respectively). Insights obtained from quartz crystal microbalance and atomic force microscopy hint that, similar to the behavior of FTMA at hydrophobic electrodes, adsorbed micellar assemblies of reduced FTMA form at negatively-charged electrodes that block access of oxidized FTMA in solution to electrode, but more reduced FTMA is needed to form the blocking layer than the amount of oxidized FTMA that adsorbs, requiring the recruitment of oxidized FTMA from bulk solution, thus leading to the loss of rectification. Significantly, however, we also reveal that addition of DTAB, which remains on the electrode surface throughout a CV, to aqueous solutions of FTMA in contact with anionic SAMs leads to current rectification ($I_a/I_c > 80$). Overall, these results provide insight into the design of self-assembling redox mediators for potential use at charged electrodes, a class of electrodes (e.g., titania) that are relevant to a wide range of energy harvesting devices.

Chapter 5 reports proof-of-concept experiments to explore how the self-assembly of a redox mediator at the surface of a working electrode can be used to reduce recombination reactions within a dye-sensitized solar cell. Specifically, we compare and contrast the behavior of dye-sensitized solar cells containing aqueous solutions (0.1 M Li_2SO_4, pH 5) of the self-assembling redox mediator 11-ferrocenylundecyltrimethylammonium bromide (FTMA) with cells containing the redox mediator (2-methyl-1-ferrocenylmethyl) trimethylammonium iodide (MFMT), which we establish not to self-assemble by performing surface tension measurements. We fabricated dye-sensitized solar cells using titania working electrodes onto which was

adsorbed cis-bis(isothiocyanato) bis(2,2'-bipyridyl-4,4'-dicarboxylato) ruthenium(II) (N3) dye. The electrodes were made hydrophobic with a dodecylphosphonate monolayer and contacted with an aqueous solution containing 20.9 mM of either redox mediator. From cyclic voltammetry and dark current measurements, we estimate the redox potential of FTMA to be 0.23 ± 0.02 V vs. Ag/AgCl and the redox potential of MFMT to be 0.37 ± 0.02 V vs. Ag/AgCl. Because the redox potential of MFMT is more positive, a greater voltage difference can be applied between the working and counter electrodes before the onset of water reduction. Measurement of photocurrent from the solar cells under illumination revealed that cells with FTMA generated 17.5 ± 0.2 μW of power whereas cells using MFMT produced only 3 ± 2 μW, despite MFMT having a more optimal redox potential for the cells used. In addition, we found that FTMA-based cells fabricated without a hydrophobic monolayer do not generate significant power. Our results support the hypothesis that reduced FTMA forms adsorbed hemimicelles on the hydrophobized surface of titania that expel oxidized FTMA, thus lowering charge recombination. The demixing between reduced and oxidized FTMA in micellar assemblies is due to reduced FTMA behaving as a classical surfactant whereas oxidized FTMA has the molecular architecture of a bolaform. Overall, these results provide the first proof of concept experiments that self-assembly of a redox mediator can lower charge recombination in a dye-sensitized solar cell. More broadly, our results highlight the potential utility of self-assembling redox mediators, in general, to control interfacial charge transfer processes.

Chapter 6 describes a study of redox-triggered changes in the phase state of lyotropic liquid crystalline (LC) dispersions. Specifically, we investigated the incorporation of FTMA into phytantriol-based lyotropic LC dispersions in aqueous solution. We explored three aspects of the behavior of the lyotropic LC dispersions containing phytantriol and FTMA: (i) the influence of

addition of FTMA (in each of its two redox states) on the phase behavior of the phytantriol-based LCs, (ii) in situ changes in the phase behavior of lyotropic LC dispersions containing reduced FTMA that were triggered by addition of the chemical oxidizing agent $Fe_2(SO_4)_3$, and (iii) the release of an encapsulated solute upon the addition of $Fe_2(SO_4)_3$ as a trigger. By using small angle x-ray scattering (SAXS), we found that mixtures containing ≥ 10% reduced FTMA (by weight of surfactant with the remainder being phytantriol) dispersed in excess water exhibited lamellar phases ("liposomes") at 25 °C. In contrast, our SAXS measurements revealed that mixtures containing 10% oxidized FTMA exhibited inverse bicontinuous cubic phases ("cubosomes"). Additional support for our conclusions regarding the nanostructure of these dispersions was obtained through cryogenic transmission electron microscopy. Finally, we demonstrated that a dispersion containing reduced FTMA and phytantriol initially forming liposomes could be transformed into cubosomes by the oxidation of FTMA via addition of $Fe_2(SO_4)_3$. We demonstrated also that this redox-surfactant triggered phase transformation could be used to release the water-soluble solute calcein blue that was loaded initially into reduced FTMA-containing liposomes. The results of this study suggested that the incorporation of redox surfactants could be a potentially useful means to trigger the release of active agents from loaded liposomes.

Chapter 7 summarizes the work presented in this thesis and describes possible directions of future investigation.

1.3 References

‡ Portions of this section have been previously published as: T.J. Smith, N.L. Abbott, In *Self-Assembly: From Surfactants to Nanoparticle*; Ch. 3 Self-Assembly of Responsive Surfactants, Wiley: New York, NY (In press).

1. J. Eastoe, A. Vesperinas, *Soft Matter* **2005**, *1*, 338–347

2. X. Liu, N. L. Abbott, *J. Colloid Interface Sci.* **2009**, *339*, 1–18.

3. P. Brown, C. P. Butts, J. Eastoe, *Soft Matter* **2013**, *9*, 2365–2374

4. J. Y. Shin, N. L. Abbott, *Langmuir* **1999**, *15*, 4404-4410.

5. Y. Lu, T. Zhou, Q. Fan, J. Dong, X. Li, *J. Colloid Interface Sci.* **2013**, *412*, 107–111.

6. E. Chevallier, A. Mamane, H. A. Stone, C. Tribet, F. Lequeux, C. Monteux, *Soft Matter* **2011**, *7*, 7866–7874.

7. S. Hata, H. Takahashi, Y. Takahashi, Y. Kondo, *J. Oleo. Sci.* **2014**, *63*, 239–248.

8. E. Baumgartner, J. Fuhrhop, *Angew. Chem. lnl. Ed. Engl.* **1980**, *19*, 550–551.

9. T. Saji, K. Hoshino, S. Aoyagui, *J. Chem. Soc., Chem. Commun.* **1985**, *13*, 865–866**.**

10. T. Saji, K. Hoshino, M. Goto, *J. Am. Chem. Soc.* **1991**, *113* (2), 450–456.

11. B. S. Gallardo, K. L. Metcalfe, N. L. Abbott, *Langmuir* **1996**, *12* (17), 4116–4124.

12. B. S. Gallardo, M. J. Hwa, N. L. Abbott, *Langmuir* **1995**, *11*, 4209–4212.

13. B. S. Gallardo, V. K. Gupta, F. D. Eagerton, L. I. Jong, V. S. Craig, R. R. Shah, N. L. Abbott, *Science* **1999**, *283*, 57–60.

14. N. Aydogan, N. L. Abbott, *Langmuir* **2001**, *17*, 5703–5706.

15. M. E. Hays, N. L. Abbott, *Langmuir* **2005**, *21*, 12007–12015.

16. M. E. Hays, C. M. Jewell, D. M. Lynn, N. L. Abbott, *Langmuir* **2007**, *23*, 5609–5614.

17. P. Brugger, M. Grätzel, *J. Am. Chem. Soc.* **1980**, *102*, 2461–2463.

18. M. Grätzel, *Farad. Discuss.* **1980**, *70*, 359–374.

19. K. Hoshino, T. Saji, T. *Chem. Lett.* **1987**, *7*, 1439–1442.

20. N. Aydogan, B. S. Gallardo, N. L. Abbott, *Langmuir* **1999**, *15*, 722–730.

21. N. Aydogan, N. L. Abbott, *Langmuir* **2001**, *17*, 5703–5706.

22. A. A. Ansari, M. Kamil, Kabir-ud-Din *J. Dispersion Sci. Technol.* **2013**, *34*, 722–730.

23. E. J. Acosta, A. Mesbah, T. Tsui, *J. Surfactants Deterg.* **2006**, *9*, 367–376.

24. E. W. Kaler, K. L. Herrington, A. K. Murthy, J. A. N. Zasasdzinski, *J. Phys. Chem.* **1992**, *96*, 6698–6707.

25. K. Tsuchiya, Y. Orihara, Y. Kondo, N. Yoshino, T. Ohkubo, H. Sakai, M. Abe, *J. Am. Chem. Soc.* **2004**, *126*, 12282–12283.

26. Hays, M. E.; Jewell, C. M.; Kondo, Y. Lynn, D. M.; Abbott, N. L. *Biophys. J.* **2007**, *93*, 4414–4424.

27. L. Naldini, U. Blömer, P. Gallay, D. Ory, R. Mulligan, F. H. Gage, I. M. Verma, D. Trono, D. *Science* **1996**, *272*, 263–267.

28. J. H. Felgner, R. Kumar, C. N. Sridhar, C. J. Wheeler, Y. J. Tsai, R. Border, P. Ramsey, M. Martin, P. L. Felgner, *J. Biol. Chem.* **1994**, *269*, 2550–2561.

29. N. L. Abbott, C. M. Jewell, M. E. Hays, Y. Kondo, D. M. Lynn, *J. Am. Chem. Soc.* **2005**, *127*, 11576–11577.

30. C. M. Jewell, M. E. Hays, Y. Kondo, N. L. Abbott, D. M. Lynn, *Bioconjugate Chem.* **2008**, *19*, 2120–2128.

31. B. S. Aytar, J. P. E. Muller, S. Golan, S. Hata, H. Takahashi, Y. Kondo, Y. Talmon, N L. Abbott, D. M. Lynn, *J. Controlled Release* **2012**, *157*, 249–259.

32. B. S. Aytar, J. P. E. Muller, Y. Kondo, N. L. Abbott, D. M. Lynn, *ACS Appl. Mater. Interfaces* **2013**, *5*, 8283−8288.

33. X. Liu, N. L. Abbott, *Anal. Chem.* **2009**, *81*, 772–781.

34. X. Liu, N. L. Abbott, N. L. *Anal. Chem.* **2011**, *83*, 3033–3041.

35. T. Stergiopoulos, P. Falaras, *Adv. Energy Mater.* **2012**, *2* (6), 616-627.

36. A. Hagfeldt, G. Boschloo, L. Sun, L. Kloo, H. Petterson, *Chem. Rev.* **2010**, *110* (11), 6595-6663.

37. B. P. Jelle, C. Breivik, H. D. Rokenes, *Sol. Energ. Mat. Sol. Cells* **2012**, *100*, 69-96.

38. G. Boschloo, A. Hagfeldt, *Acc. of Chem. Res.* **2009**, *42* (11), 1819-1826.

39. D. Song, M.-S. Kang, Y.-G. Lee, W. Cho, J. H. Lee, T. Son, K. J. Lee, S. Nagarajan, P. Sudhagar, J.-H. Yum, Y. S. Kang, *Phys. Chem. Chem. Phys.* **2012**, *14* (2), 469-472.

40. S. M. Feldt, E. A. Gibson, E. Gabrielsson, L. Sun, G. Boschloo, A. Hagfeldt, *J. Am. Chem. Soc.* **2010**, *132* (46), 16714-16724.

41. Y. Liu, J. R. Jennings, Y. Huang, Q. Wang, S. M. Zakeeruddin, M. Grätzel, *J. Phys. Chem. C* **2011**. *115* (38), 18847-18855.

42. B. A. Gregg, F. Pichot, S. Ferrere, C. L. Fields, *J. Phys. Chem. B* **2001**, *105* (7), 1422-1429.

43. Z. Zhang, P. Chen, T. N. Murakami, S. M. Zakeeruddin, M. Grätzel, *Adv. Funct. Mater.* **2008**, *18* (2), 341-346.

44. E. Palomares, J. N. Clifford, S. A. Haque, T. Lutz, J. R. Durrant, *J. Am. Chem. Soc.* **2003**, *125* (2), 475-482.

45. M. Wang, N. Chamberland, L. Breau, J.-E. Moser, R. Humphrey-Baker, B. Marsan, S. M. Zakeeruddin, M. Grätzel, M. *Nat. Chem.* **2010**, *2* (5), 385-389.

46. H. Tian, X. Jiang, Z. Yu, L. Kloo, A. Hagfeldt, L. Sun, *Angew. Chem. Int. Ed.* **2010**, *49* (40), 7328-7331.

47. A. Kudo, T. Miseki, *Chem. Soc. Rev.* **2009**, *38*, 253–278.

48. F. E. Osterloh, *Chem. Mater.* **2008**, *20*, 35–54.

49. W. J. Youngblood, S.-Y. A. Lee, K. Maeda, T. E. Mallouk, *Acc. Chem. Res.* **2009**, *42* (12), 1966-1973.

50. L. J. Minggu, W. R. W. Daud, M. B. Kassim, *Int. J. Hydrogen Energy* **2010**, *35*, 5233–5244.

51. K. Larsson, *J. Phys. Chem.* **1989**, *93* (21), 7304–7314.

52. G. J. T. Tiddy, *Phys. Rep.* **1980**, *57* (1), 1-46.

53. W.-K. Fong, T. Hanley, B. J. Boyd, *J. Control Release* **2009**, *135* (3), 218-226.

54. S. Phan, W.-K. Fong, N. Kirby, T. Hanley, B. J. Boyd, *Int. J. Pharm.* **2011**, *421*, 176–182.

55. R. Negrini, R. Mezzenga, *Langmuir* **2012**, 28, 16455−16462.

56. X. Mulet, B. J. Boyd, C. J. Drummond, *J. Colloid Interface Sci.* **2013**, *393*, 1–20.

57. S. Akbar, A. Anwar, A. Ayish, J. M. Elliott, A. M. Squires, *Eur. J. Pharm. Sci.* **2017**, *101*, 31–42.

58. C. Y. Guo, J. Wang, F. L. Cao, R.J. Lee, G. X. Zhai, *Drug Discov. Today* **2010**, *15* (23–24), 1032–1040.

59. A. Zabara, R. Mezzenga, *J. Control. Release* **2014**, *188*, 31–43.

60. Y.-D. Dong, A.W. Dong, I. Larson, M. Rappolt, H. Amenitsch, T. Hanley, B. J. Boyd, *Langmuir* **2008**, *24* (13), 6998-7003.

61. G. Milkereit, M. Morr, J. Thiem, V. Vill, *Chem. Phys. Lipids* **2004**, *127* (1), 47–63.

62. R. Negrini, R. Mezzenga, *Langmuir*, **2011**, *27* (9), 5296–5303.

63. K. J. Tangso, W.-K. Fong, T. Darwish, N. Kirby, B. J. Boyd, T. L. Hanley, *J. Phys. Chem. B* **2013**, *117* (35), 10203−10210.

Chapter 2 : Influence of Self-Assembling Redox Mediators on Charge Transfer at Hydrophobic Electrodes‡

2.1 Introduction

A common challenge that influences the efficiency of energy harvesting devices (e.g., dye sensitized solar cells[1-9] and solar water splitters,[10-12]) is the design of interfaces that pass charge in one direction while blocking its passage in the reverse direction. This asymmetry in charge-transfer permits light-induced, charge-separated states to recombine through an external circuit, thus performing useful work (rather than recombining across the interface). Many past studies have addressed this issue by using iodide (I^-)-triiodide (I_3^-), a redox mediator that is known to block recombination reactions.[38,39] The mechanism by which I^-/I_3^- minimizes recombination is complex (an adsorbed radical anion intermediate or a two-electron pathway slows the recombination), and a major disadvantage of the system is the corrosive nature of the redox pair. Alternative approaches include the use of cobalt derivatives with bulky ligands (steric hindrance retards back reactions),[40,41] organic mediators with two-electron reaction steps,[43-46] or barrier layers.[42,43] In this paper, for reasons detailed below, we report an investigation of an alternative approach to manipulation of interfacial charge transfer that is based on the concept of a self-assembling redox-mediator. We emphasize that the system described in this paper is a model system that was designed to test a principle – it is not intended as a technological system.

We use the term self-assembling redox mediator to refer to a mediator that cooperatively self-associates in solution or at interfaces in a manner that is dependent on oxidation state. In the

context of aqueous solvents used in the current study, the self-assembling redox mediator is amphiphilic in nature; it self-assembles into micelles in one oxidation state and remains singly dispersed in the other oxidation state. Our broad proposal that self-assembly of amphiphilic redox-mediators can be used to influence interfacial electron transfer processes is based on consideration of various possible mechanisms (see Discussion for additional detail) through which we hypothesized self-assembly and charge transfer might be coupled. Whereas it is straightforward to envisage physical scenarios in which one redox state of an amphiphilic mediator is adsorbed to an electrode whereas the other is not (thus impacting interfacial charge transfer), the amphiphilic redox mediator used in the study reported in this paper was found to generate interfacial assemblies on hydrophobic electrodes in both oxidation states. We found, however, that in mixed systems, interfacial assemblies formed by one oxidation state of the amphiphilic mediator restricted access of the other oxidation state of the mediator to the hydrophobic electrode. We provide evidence that this situation arises from the immiscibility of the two redox states of the amphiphilic mediator within interfacial assemblies. As detailed below, this selective blocking of the hydrophobic electrode by interfacial surfactant assemblies leads to substantial asymmetry in the forward and reverse rates of charge transfer.

The experiments reported in this paper are based on 11-ferrocenylundecyl-trimethylammonium bromide (FTMA), an amphiphilic redox-mediator that comprises a ferrocene group tethered to a quaternary ammonium head group via an aliphatic chain of 11 methylene units (Fig. 1).[13] The self-assembly of reduced FTMA (with a net charge of +1) in bulk aqueous solution has been studied by us[14-18] and others,[13,19-21] and it is known to form globular (approximately spherical) micelles at a critical micelle concentration of 0.1 mM in 100 mM Li_2SO_4 at 25 °C. Upon oxidation, a ferrocenium cation is formed, and FTMA transforms to

a bolaform surfactant-type architecture with a net charge of +2 that prevents self-association up to concentrations of at least 30 mM.[14-17] This change in self-assembly of FTMA with oxidation state is consistent with prior studies of bolaform surfactants (surfactants with two head-groups separated by a non-polar domain), which typically exhibit higher critical micelle concentrations and form smaller micelles than their conventional counterparts (with one head group and same length of tail).[22- 29] In this paper, we combine the use of electrochemical techniques, atomic force microscopy (AFM) and quartz crystal microbalance (QCM) measurements to investigate how redox-induced changes in the self-assembly of FTMA at hydrophobic electrodes can give rise to rectification of Faradaic currents.

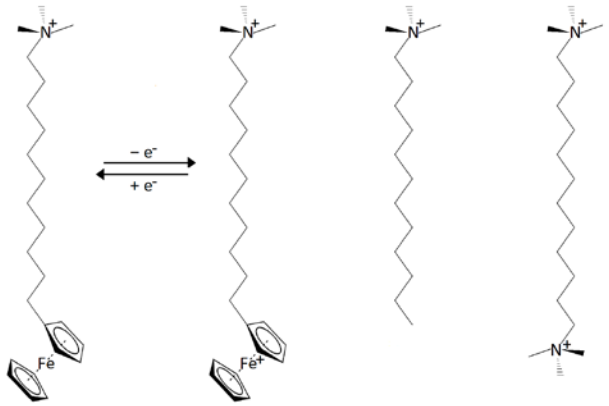

Figure 2.1 Molecular structures of FTMA, DTAB, and DBTAB
Molecular structures of reduced and oxidized 11-ferrocenylundecyltrimethylammonium (FTMA), dodecyltrimethylammonium bromide (DTAB), and dodecyl-1,12-bis(trimethylammonium bromide) (DBTAB) (bromide anions not shown).

We end this Introduction by noting that past studies have demonstrated that the self-assembly of surfactants at interfaces is dependent not only on the molecular architecture of the surfactants (as mentioned above) but also the physical properties of the interfaces.[30-32] For example, past studies using AFM have revealed that dodecyltrimethylammonium bromide (DTAB) forms cylindrical micelles on hydrophilic mica surfaces[30,31] and hemicylindrical

micelles on hydrophobic highly-oriented pyrolytic graphite (HOPG) surfaces.[32] Herein we report the use of alkanethiol-functionalized gold electrodes as model hydrophobic electrodes at which to explore the effects of surfactant self-assembly on interfacial charge transfer. We note that several past studies have reported cyclic voltammograms of FTMA at untreated electrodes.[13-15,33-36] We emphasize that these studies have not observed the effects of interfacial self-assembly on charge transfer that are described in this paper based on experiments performed with chemically functionalized (hydrophobic) electrodes.

2.2 Experimental section

2.2.1 Materials

FTMA was purchased from Dojindo Molecular Technologies (Rockville, MD) and used as received. Lithium sulfate monohydrate, DTAB, hydroxymethyl ferrocene (HMeFc), 1-dodecanethiol, 1-octanethiol and 1-hexadecanethiol were obtained from Sigma-Aldrich (St. Louis, MO). All aqueous solutions were prepared using deionized water (resistivity of 18.2 MΩ) purified by a Synergy Ultrapure Water System (Millipore, Darmstadt, Germany). Highly-oriented pyrolytic graphite sheets (HOPG), mica and AFM tips (MSCT model) were purchased from Bruker Nano Company (Santa Barbara, CA).

2.2.2 Experimental methods

2.2.2.1 Surfactant solutions

Solutions of reduced FTMA were prepared in aqueous 100 mM Li_2SO_4, adjusted to pH 5 by addition of sulfuric acid. Reduced FTMA solutions were degassed by bubbling a gaseous stream of nitrogen for approximately an hour prior to use. To prepare solutions of oxidized FTMA, solutions of reduced FTMA were oxidized by bulk electrolysis (and confirmed to be

oxidized by using UV-vis spectrophotometry), as detailed previously.[14] Aqueous solutions of HMeFc were prepared by dissolving 0.2 mM HMeFc in aqueous 100 mM Li_2SO_4 (adjusted to pH 5) by stirring overnight.

2.2.2.2 Hydrophobic electrodes

Gold electrodes were prepared by evaporating films of gold (thickness of 100 nm deposited at a rate of 1 nm/s) onto silicon wafers (with a 10 nm-thick titanium adhesion layer deposited at a rate of 0.2 nm/s) using an e-beam evaporator. The silicon wafers were used as provided by the manufacturer. AFM images of the deposited gold films can be found in the Supporting Information. The gold films were subsequently immersed overnight in 1 mM alkanethiol in anhydrous ethanol. The functionalized gold electrodes were rinsed in ethanol to remove excess thiols and dried under a stream of nitrogen prior to use. The formation of an alkanethiol monolayer on the surface of the gold film was confirmed by ellipsometry. For a dodecanethiol monolayer, the ellipsometric thickness was measured to be 17.1 ± 0.4 Å, consistent with literature values of 16.9 Å.[37]

2.2.2.3 Cyclic voltammetry

Cyclic voltammetry was performed using a Pine Instruments (Grove City, PA) AFCBP1 bipotentiostat. The electrochemical cell was arranged in a standard three-electrode configuration using an alkanethiol-functionalized gold film (working electrode), a platinum wire mesh (counter electrode), and a Ag/AgCl reference electrode (BASi, West Lafayette, IN). The cyclic voltammograms (CVs) reported in this paper were obtained after cycling the potential of each electrode until the CVs did not change from one cycle to the next, typically around 10 cycles.

Chemically functionalized electrodes that did not yield repeatable CVs after 20 cycles were discarded. All CVs were performed at room temperature (approximately 25 °C).

CVs were recorded as a function of scan rate between 10 mV/s and 200 mV/s. The peak currents arising from Faradaic processes were identified by subtracting the non-Faradaic contribution from the total current passed at the electrodes (see Supporting Information for details). For Faradaic peak currents controlled by the diffusion of a redox species from bulk solution to a (stationary) planar electrode, the peak current, I_p, can be calculated from the Randles-Sevcik equation,[38] namely

$$I_p = 0.4463 n^{3/2} \sqrt{\frac{F^3}{RT}} A \mathcal{D}^{1/2} C \nu^{1/2} \tag{2.1}$$

where n is the number of moles of electrons transferred in the reaction, F is the Faraday constant, R is the ideal gas constant, T is the system temperature, A is the surface area of the electrode, $\mathcal{D}$ is the diffusion coefficient of the redox species undergoing reaction, C is the concentration of the redox species in bulk solution, and ν is the scan rate. For Faradaic peak currents that result from redox species adsorbed at an electrode surface, the peak current can be described by the equation:[39]

$$I_p = \left(\frac{n^2 F^2}{4RT}\right) A \nu \Gamma_o \tag{2.2}$$

where Γ_o is the surface concentration of the adsorbed redox species.

2.2.2.4 Quartz crystal microbalance

The quartz crystal microbalance (QCM) experiments were conducted using a Q-Sense E4 instrument (Biolin Scientific, Västra Frölunda, Sweden). In brief, gold-covered quartz crystals were cleaned in alkaline piranha solution (5 parts deionized water, 1 part 30% ammonia hydroxide, 1 part 30% hydrogen peroxide) at 70° C for 10 minutes and then exposed to a UV-ozone environment for ten minutes using a UV/Ozone ProCleaner (BioForce Nanosciences, Ames, IA). The crystals were subsequently sonicated in pure ethanol (without thiols) for five minutes and then immersed in an ethanolic solution of 1 mM 1-dodecanethiol for at least four hours prior to use. The crystals were placed in the Q-sense instrument and then equilibrated by flowing aqueous 100 mM Li_2SO_4 across the crystals at a rate of 50 μL/s at a temperature of 25.0 ± 0.5 °C. Upon reaching steady values of the frequency (fluctuations < 0.5 Hz) and viscous dissipation (fluctuations less than $0.1x10^{-6}$), the flow (50 μL/s) was changed to aqueous 0.1 mM oxidized or reduced FTMA (in 100 mM Li_2SO_4 at pH 5). After reaching a new steady state, the flow was again changed to 1 mM FTMA in the same electrolyte solution. The mass of adsorbed FTMA, Δm, was calculated from the change of frequency by using the Sauerbrey equation:[40]

$$\Delta f = -\frac{2f_o^2}{A\sqrt{\rho_q \mu_q}}\Delta m \qquad (2.3)$$

where f_o is the resonance frequency of the crystal before immersion in FTMA, A is the area of the piezoelectric quartz crystal, ρ_q is the density of quartz, and μ_q is the shear modulus of quartz. The Sauerbrey equation is only valid when the change in viscous dissipation, ΔD, is sufficiently small such that $\Delta D/\Delta f < 4x10^{-7}$ Hz^{-1} for a 5 MHz crystal.[41] This condition is met for all of the measurements reported in this paper; typical values for ΔD/Δf in our measurements were determined to be $2x10^{-8}$ Hz^{-1}.

2.2.2.5 Atomic force microscopy

Interfacial assemblies formed from aqueous solutions of either 1 mM reduced FTMA, 1 mM oxidized FTMA or 20 mM DTAB on HOPG were imaged using AFM. The FTMA solutions were prepared as described above. HOPG was used as a substrate to mimic the hydrophobic character of an alkanethiol monolayer. We did not use alkanethiol-functionalized gold films for imaging because they are too rough to permit molecular-level resolution of an adsorbed surfactant assembly. The HOPG substrates were freshly cleaved, and then incubated in the surfactant solutions for two days before imaging. AFM imaging was performed using a Multimode IIIa instrument (Bruker Nano, Santa Barbara, CA) and a liquid cell. The images were recorded in contact mode using tips with a spring constant of 0.01 N/m (MSCT, Bruker). Images were obtained with scan rates of 7 Hz.

2.3 Results

Prior to functionalizing the gold electrodes with monolayers of alkanethiols, we performed cyclic voltammetry using solutions of FTMA and untreated gold electrodes. In these experiments, we used 1 mM FTMA dissolved in aqueous 100 mM Li_2SO_4 at pH 5. The CVs of FTMA obtained using untreated gold electrodes exhibited two current waves (on both the anodic and cathodic scans; Figure 2.2).[14] By varying the scan rate (see Supporting Information) and making log-log plots of peak current density (I_p) vs. scan rate (ν), we established that the current waves at the least positive potentials on both anodic and cathodic scans scale as $I_p \propto \nu^{\chi}$, where $\chi_a = 0.47 \pm 0.02$ and $\chi_c = 0.47 \pm 0.01$, respectively. These exponents are close to the theoretical values predicted for a Faradaic current limited by the diffusion of FTMA from bulk solution to the electrode (slope of $\chi = 0.5$; see Eq. 2.1). In contrast, the scan-rate dependence of the peaks measured at the more positive potentials were described by exponents of $\chi_a = 1.00 \pm 0.03$ and $\chi_c = 1.03 \pm 0.04$ during the anodic and cathodic scans, respectively. This result indicates that these

current peaks arise from FTMA adsorbed to the electrode surface (see Eq. 2.2). We note that the ratio of peak anodic (I_a) and cathodic (I_c) current (which we define, in this paper, as the current rectification) obtained at the untreated electrode is approximately $I_a/I_c = 2.2$ at a scan rate of 50 mV/s. Below, we contrast these results to those obtained with chemically functionalized electrodes.

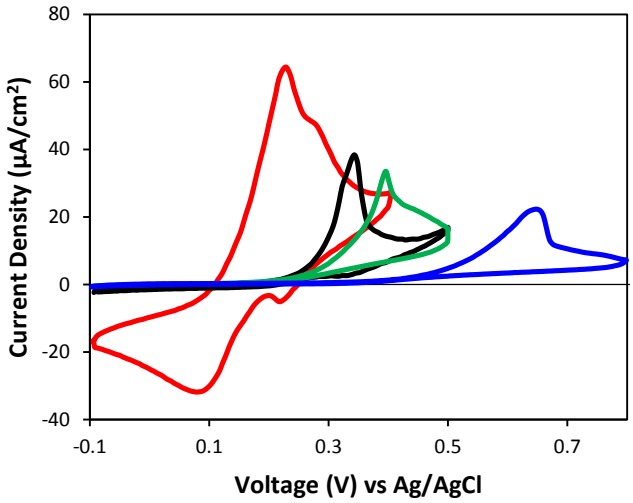

Figure 2.2 CVs of FTMA at alkanethiol functionalized gold electrodes
Cyclic voltammograms of 1 mM FTMA in 100 mM Li_2SO_4 measured at a bare gold electrode (red), a gold electrode functionalized with 1-octanethiol (black), a gold electrode functionalized with 1-dodecanethiol (green), and a gold electrode functionalized with 1-hexadecanethiol (blue). All measurements were performed with a platinum mesh counter electrode and Ag/AgCl reference electrode at a scan rate of 50 mV/s, beginning with an anodic sweep.

To explore the influence of surfactant self-assembly on charge transfer at hydrophobic electrodes, next we used gold electrodes functionalized with alkanethiols. These surfaces have been extensively characterized in past studies and they are known to be hydrophobic (with advancing contact angles of water of about 115° and receding contact angles of about 100°).[42] Fig. 2 shows CVs of aqueous 1 mM FTMA measured at gold electrodes prepared using either octanethiol, dodecanethiol or hexadecanethiol. We make four observations regarding the results

in Fig. 2. First, during anodic scans of the electrode potential, in contrast to untreated gold electrodes, only one wave in Faradaic current is evident at the electrodes (we return to this observation below). Second, the electrode potential at which the peak anodic current density is observed is found to increase with the length of the alkanethiol used to hydrophobize the electrode (200 ± 40 mV vs. Ag|AgCl for untreated gold; 340 ± 10 mV, 380 ± 30 mV, and 670 ± 30 mV on electrodes functionalized with octanethiol, dodecanethiol and hexadecanethiol, respectively). This shift, which we attribute to a chain-length-dependent increase in the electrical resistance of the monolayer, also caused us to vary the range of electrode potentials used to perform the CVs, as shown in Fig 2.2. Specifically, we used potential windows that encompassed the peak in Faradaic current arising from oxidation/reduction of FTMA but avoided oxidation of water (which is suppressed by the alkanethiol monolayers). Third, we measured the anodic peak current to decrease from 73 ± 9 $\mu A/cm^2$ on bare gold electrodes to 43 ± 7, 34 ± 3, and 20 ± 4 $\mu A/cm^2$ when using gold electrodes functionalized with octanethiol, dodecanethiol or hexadecanethiol, respectively. Although this result indicates that the alkanethiol monolayer does resist partially the passage of anodic current, a more striking result is that the peak *cathodic* current density, which was 33 ± 3 $\mu A/cm^2$ on bare gold, was suppressed to less than 4 $\mu A/cm^2$ when using alkanethiol-functionalized electrodes. Specifically, the attenuation of the cathodic current was found to be substantially greater than that of the anodic current, a preliminary result that hinted to us that self-assembly of the amphiphilic redox-mediator at the hydrophobic electrode may be influencing the charge transfer process. Whereas the experiments described above were performed using aqueous solution of reduced FTMA, we also performed CVs using bulk solutions of oxidized FTMA (see Supporting Information Fig. 2.S4). Results obtained using aqueous solutions of oxidized FTMA show that the asymmetry in

the magnitude of anodic and cathodic current passed at the hydrophobic electrode, as detailed above, is not simply a result of differences in the concentrations of the oxidized and reduced forms of the mediator in bulk solution. Below we report further on this asymmetry in charge transfer and provide insight into its origin. We focus (arbitrarily) on measurements that used gold electrodes functionalized using dodecanethiol, although we note that past studies suggest that monolayers formed on gold from dodecanethiol are more densely packed than monolayers formed from octanethiol ,[43] and that use of hexadecanethiol can lead to the deposition of physisorbed layers when the monolayers are formed from ethanol.[44]

To provide insight into the origin of the above-described differences in behavior of the anodic and cathodic peak current densities shown in Fig. 2.2, we explored (and tested) the following three hypotheses:

(i) First, we hypothesized that the current passed at the hydrophobic electrode arises largely from FTMA that diffuses from bulk solution to the electrode, and that the permeability of the alkanethiol monolayer is selective to ferrocene (of reduced FTMA) over ferrocenium (of oxidized FTMA). This hypothesis is based on the observation that ferrocene is electrically neutral and sparingly soluble in water whereas ferrocenium is a cation. This scenario, if correct, predicts that the asymmetry in charge transfer should also be observed for free ferrocene/ferrocenium species (not part of an amphiphilic molecule such as FTMA).

(ii) Second, we hypothesized that the current is dominated by redox-species adsorbed to the hydrophobic electrodes, and that FTMA forms interfacial assemblies in one oxidation state but not the other. This scenario, if underlying the small magnitude of the cathodic current relative to

anodic current that we measure using FTMA, predicts that the amount of reduced FTMA assembled on the hydrophobic electrode would be greater than oxidized FTMA.

(iii) Third, we hypothesized that reduced and oxidized FTMA can both form interfacial assemblies on the electrode, but that these interfacial assemblies do not mix. Specifically, this scenario, if underlying the experimental observations in Fig. 2, would predict that interfacial assemblies of reduced FTMA do not readily incorporate oxidized FTMA, thus forming an effective barrier at the electrode during the cathodic sweep of the potential.

Below we describe experiments that were designed to explore each of these three hypotheses.

2.3.1 Selective Partitioning of Ferrocene and Ferrocenium

As described above, a possible explanation for the asymmetry in the anodic and cathodic peak current density seen in Fig. 2.2 is that the alkanethiol monolayer is permeable to ferrocene but not the ferrocenium ion (hypothesis (i)). To test this possible explanation, we measured CVs using hydroxymethyl ferrocene (HMeFc). We note that HMeFc is not amphiphilic like FTMA and thus, by using HMeFc, we avoid contributions to the CVs that might arise from interfacial self-assembly processes. We also note that ferrocene is not sufficiently soluble in aqueous solution to allow cyclic voltammetry to be performed, whereas HMeFc is readily dissolved. Inspection of Fig. 2.3 shows that we measured an anodic peak current density of $I_a = 8.8 \pm 2.3$ $\mu A/cm^2$ and a cathodic peak current density of $I_c = 5.1 \pm 1.7$ $\mu A/cm^2$ (at 10 mV/s) when using 0.2 mM HMeFc, corresponding to an asymmetry in current of $I_a/I_c = 1.7$. In contrast, the anodic and cathodic peak current densities measured using 1 mM FTMA (scan rate of 10 mV/s) were $I_a = 18 \pm 3$ $\mu A/cm^2$ and $I_c = 1.1 \pm 0.1$ $\mu A/cm^2$, respectively, thus providing a much greater asymmetry ($I_a/I_c = 17$). For HMeFc, we determined that the peak currents depend on scan rate

with exponents $\chi_a = 0.45 \pm 0.05$ and $\chi_c = 0.43 \pm 0.02$ for anodic and cathodic scans, respectively. This lead us to conclude that adsorbed HMeFc does not make a significant contribution to the charge passed at the electrode.

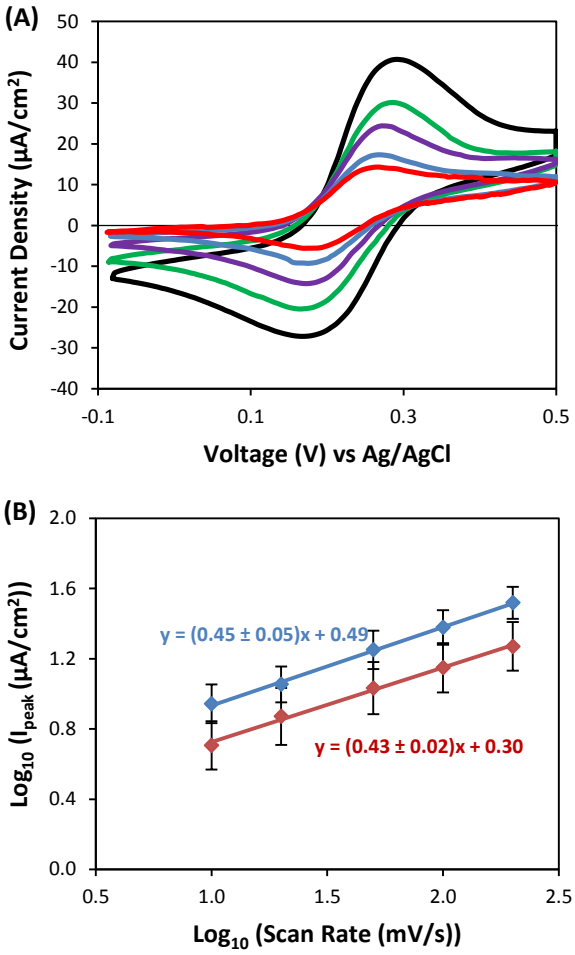

Figure 2.3 CVs of hydroxymethyl ferrocene at dodecanethiol-functionalized gold electrodes **(A)** Cyclic voltammograms of 0.2 mM HMeFc in 100 mM Li_2SO_4 measured at a 1 cm^2 gold electrode functionalized with 1-dodecanethiol. The potential scan rates were 10 (red), 20 (blue), 50 (purple), 100 (green), and 200 (black) mV/s. All voltammograms began with an anodic sweep. **(B)** Scan rate-dependence of anodic peak currents (blue) or cathodic peak currents (red), based on averages obtained from three experiments. The error bars shown represent the standard deviations.

We comment that a past study by Creager *et al.*[45] reported the use of HMeFc as a probe of defects within alkanethiol monolayers (based on the idea that defects would lead to larger

currents). Similar to our measurements, they also observed the attenuation of cathodic currents relative to anodic currents (I_a/I_c = 1.4 for electrodes made with evaporated gold on silicon) but they did not identify the origin of the asymmetry. In another study, Le and Yu[46] investigated the use of ferrocene as a redox mediator at a dodecanethiol monolayer-covered gold electrode in an ionic liquid. They measured peak currents of I_a = 2.0 μA and I_c = 1.1 μA (similar to the asymmetry in our experiments), and suggested that the origin of the asymmetry involves π-π interactions between the ferrocene and ionic liquid. Because the solvent in our experiment is water, the origin of the asymmetry in our CVs does not arise from π-π interactions. Although differences in the permeability of reduced and oxidized HMeFc through the alkanethiol monolayer may underlie the asymmetry measured in our experiments with HMeFc, the magnitude of the asymmetry observed with HMeFc (I_a/I_c = 1.7) is sufficiently small as compared to FTMA (I_a/I_c = 17) that differences in the permeability of oxidized and reduced forms of FTMA do not appear likely to provide the basis of an explanation of the asymmetry measured with FTMA. Furthermore, past studies have determined the dominant mode of electron transfer of the ferrocene moiety (dissolved in water) across dodecanethiol monolayers to be electron tunneling rather than diffusion of the redox species through the monolayer.[47] This conclusion is supported further by results presented below.

2.3.2 Differential Adsorption of Reduced and Oxidized FTMA

The second hypothesis described above regarding the origins of the current rectification measured with FTMA invokes redox-induced changes in the extent of adsorption of FTMA on the hydrophobic electrodes. To investigate the contribution of adsorbed and diffusing FTMA to the measured currents, we performed CVs (Fig. 4) in the presence of FTMA concentrations ranging from 0.01 mM to 1 mM and at scan rates ranging from 10 mV/s to 200 mV/s.

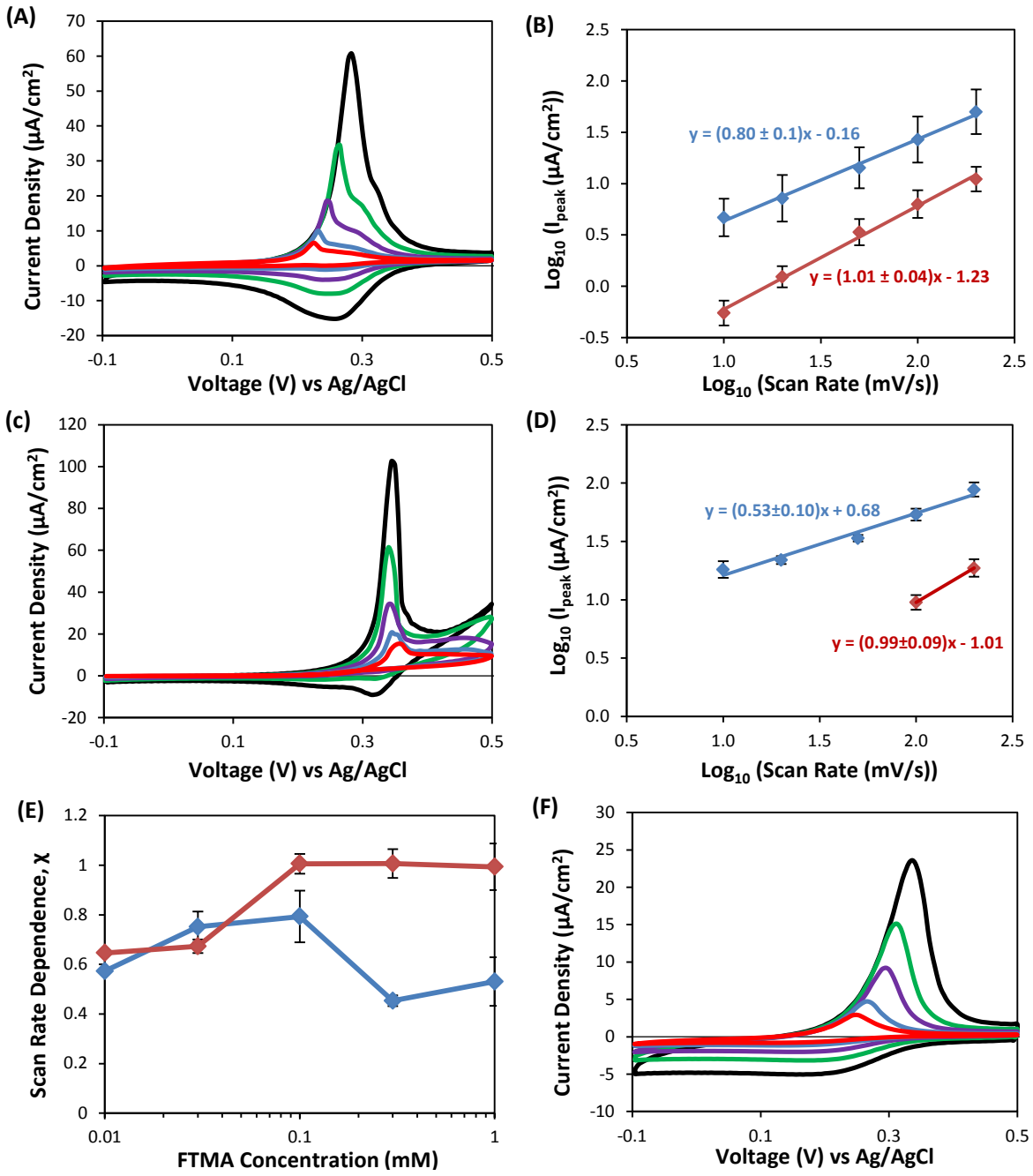

Figure 2.4 CVs of FTMA at dodecanethiol-functionalized gold electrodes
Cyclic voltammograms of 0.1 mM reduced FTMA **(A)** and 1 mM reduced FTMA **(C)**, and 0.1 mM oxidized FTMA **(F)** in 100 mM Li_2SO_4 measured at a 1 cm^2 gold electrode functionalized with 1-dodecanethiol. The potential scan rates were 10 (red), 20 (blue), 50 (purple), 100 (green), and 200 (black) mV/s. All voltammograms began with an anodic sweep. Scan rate-dependence of peak currents using 0.1 mM reduced FTMA **(B)** and 1 mM reduced FTMA, **(D)** anodic peak currents (blue), and cathodic peak currents (red). **(E)** Scan rate-dependence of peak currents for the anodic peak, χ_a, (blue) and cathodic peak, χ_c, (red) as a function of FTMA concentration.

Fig. 2.4A and 2.4C show representative CVs obtained using aqueous solutions of reduced FTMA at concentrations corresponding to the CMC (0.1 mM in aqueous 100 mM Li_2SO_4) and ten times greater than the CMC, respectively. The corresponding log-log plots of peak current density vs. scan rate are shown in Fig 2.4B and 2.4D, and a summary of the values of the exponent (χ) as a function of the concentration of FTMA is shown in Fig 2.4E. First, we discuss the behavior of the anodic currents shown in Fig. 2.4. Inspection of Fig. 2.4E reveals that at low concentrations of FTMA (less than 0.1 mM), χ ranges from 0.6 to 0.8. This range of values of χ indicates that the anodic current passed at low concentrations of FTMA (<CMC) arises from both adsorbed and diffusing species. This conclusion is consistent also with the asymmetric appearance of the anodic wave in Fig. 2.4A (the main peak contains contributions from diffusing species and the minor peak is due to adsorbed species). Here we note that past studies have attributed the more positive redox potential of adsorbed FTMA to a difference in the free energy of adsorption between reduced and oxidized FTMA.[14] When the concentration of FTMA substantially exceeds the CMC, however, as shown in Fig. 2.4C (1mM) and Fig. 2.4E, we measured $\chi_a \approx 0.5$, indicating that the anodic current is dominated by FTMA diffusing from bulk solution to the electrode. Although measurements reported below (using AFM and QCM) clearly demonstrate that reduced FTMA forms interfacial assemblies on the surface of the hydrophobic electrode at concentrations above the CMC (consistent also with the presence of small shoulders in the anodic waves in Fig 2.4C), we conclude that these interfacial assemblies of reduced FTMA do not form substantial barriers to the transport of reduced FTMA from bulk solution to the electrode (in contrast to their influence on oxidized FTMA, as described below).

Next, we turn our attention to the scan rate-dependence of the cathodic currents shown in Fig. 2.4. At low concentrations of FTMA (below 0.1 mM), inspection of Fig. 2.4E reveals that

the peak cathodic current at the hydrophobic electrode also arises from the reduction of both adsorbed and diffusing species (similar to anodic current). Significantly, however, at concentrations of 0.1 mM or greater, inspection of Fig. 2.4B and 2.4E reveals a slope close to $\chi_c \approx 1$, thus indicating that the peak cathodic current in the limit of high FTMA concentration arises largely from adsorbed (oxidized) FTMA species and not oxidized FTMA diffusing from bulk solution. This unexpected result suggests that at high concentrations of FTMA (above the CMC of reduced FTMA), diffusion of oxidized FTMA to the electrode from bulk solution is blocked. Specifically, it is the absence of the diffusive contribution to the cathodic current from oxidized FTMA molecules that leads to the above-described asymmetry in anodic and cathodic currents (i.e. the rectification).

We interpret the results above (see below for additional discussion) to suggest that interfacial assemblies of reduced FTMA block access of oxidized FTMA in bulk solution to the electrode. To provide additional evidence for the presence of interfacial assemblies of FTMA, we measured the mass of adsorbed FTMA using QCM (Fig. 2.5) and imaged FTMA at hydrophobic surfaces using AFM (Fig. 2.6). Inspection of the QCM measurements shown in Fig. 2.5 reveals that FTMA adsorbs onto the hydrophobic monolayers in both redox states. Specifically, at 0.1 mM FTMA, the extent of adsorption of reduced FTMA (the frequency change of ≈ 6 Hz is equivalent to 1.55 ± 0.1 molecules/nm^2) is slightly greater than oxidized FTMA (1.33 ± 0.1 molecules/nm^2). At 1 mM FTMA, however, there is no significant difference between the extent of adsorption of the reduced (1.56 ± 0.2 molecules/nm^2) and oxidized surfactant (1.83 ± 0.2 molecules/nm^2). This set of results, as summarized in Fig. 2.5C, is

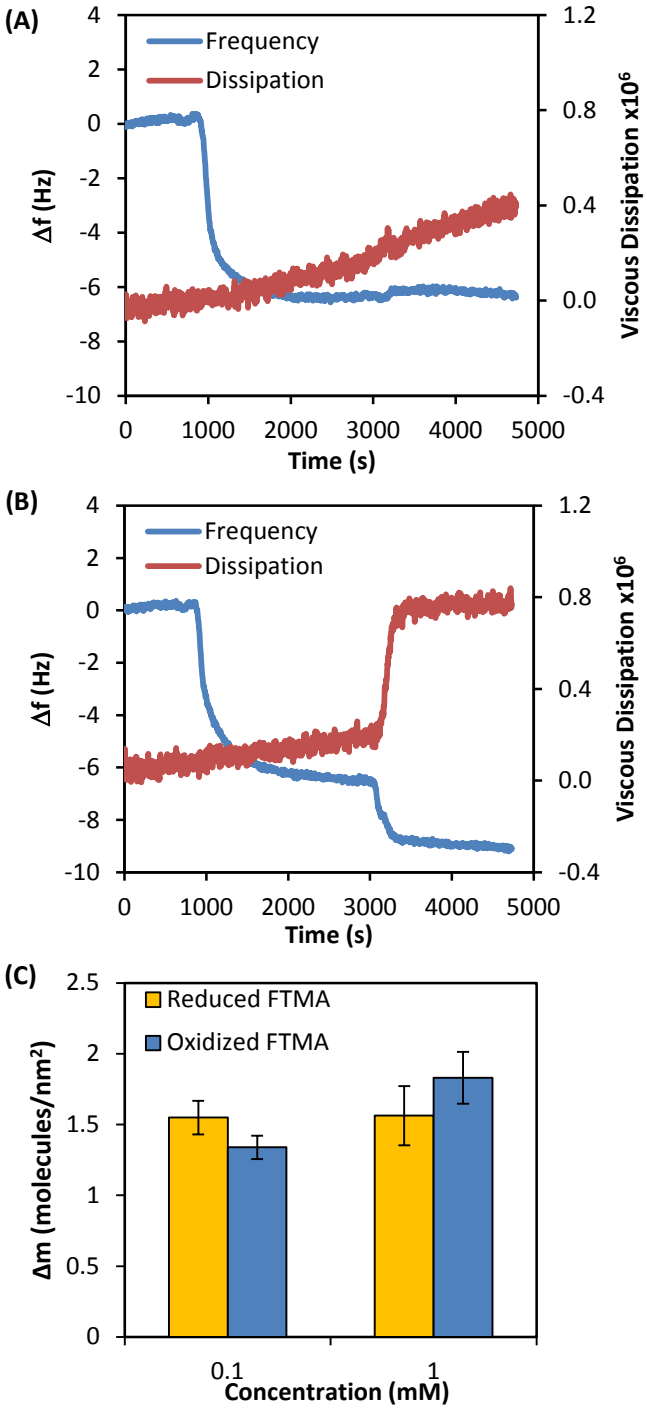

Figure 2.5 QCM of FTMA at dodecanethiol-functionalized gold surfaces
Quartz crystal microbalance measurements performed using a 1-dodecanethiol functionalized gold surface exposed sequentially to 100 mM Li_2SO_4, 0.1 mM surfactant in 100 mM Li_2SO_4 at 1000 s, and 1 mM surfactant in 100 mM Li_2SO_4 at 3000 s, using either **(A)** reduced FTMA, or **(B)** oxidized FTMA. The data shown here are a five point simple moving average. **(C)** Surface density of adsorbed surfactant, obtained from 23 measurements in each redox state at concentrations of 0.1 mM and 1 mM. The error bars are standard deviations.

generally consistent with past studies of the adsorption of FTMA at air-water interfaces.[16] Specifically, the CMC of reduced FTMA is 0.1 mM, beyond which the excess surface concentration of reduced FTMA does not appreciably increase with increase in bulk concentration. In contrast, oxidized FTMA does not aggregate measurably in bulk solution over this concentration range, and its surface excess concentration increases with bulk concentration. Both of these trends are evident in the data shown in Fig. 2.5C.

AFM imaging was performed the using HOPG because HOPG is hydrophobic and atomically flat whereas we found polycrystalline gold films functionalized with alkanthiols to be too rough to permit imaging of surfactants. Images of bare HOPG and DTAB adsorbed on HOPG are shown in Fig. 2.6A and 2.6B, respectively. Consistent with past studies, the AFM image of bare HOPG exhibited a pattern (with period 0.2 ±0.1 nm) with hexagonal symmetry. In contrast, AFM images of DTAB adsorbed on HOPG comprised statistical stripes with a periodicity of 5.4 ±0.1 nm. We note that the symmetries of patterns interpreted from these real-space images were confirmed by Fourier transforms of the images (see insets in Fig. 2.6). Fig. 2.6C reveals that reduced FTMA on HOPG also generates striped patterns in AFM images, although the stripes were not as distinct as those seen for DTAB (see also inset with Fourier transform). The stripes exhibited by reduced FTMA were measured to have widths of 7.2 ±0.1 nm, which is comparable to the widths of striped patterns formed by DTAB on HOPG (periodicity of 5.4 ±0.1 nm in Fig. 2.6B).[32] Guided by past studies of DTAB and hexadecyltrimethylammonium bromide (CTAB) on HOPG, which have interpreted the striped aggregates to correspond to hemi-cylindrical micelles (or cylindrical micelles in the case of mica),[30-32,48] we also interpret Fig. 2.6C to indicate that reduced FTMA likely forms hemi-

cylindrical micelles on HOPG. In contrast, AFM images of oxidized FTMA (Fig. 2.6D) did not exhibit distinguishable striped patterns, although adsorbed surfactant clearly masked the periodicity of the bare HOPG during imaging (Fig. 2.6A). Past studies have suggested that bolaform surfactants form looped configurations at hydrophobic interfaces (e.g., the air-water

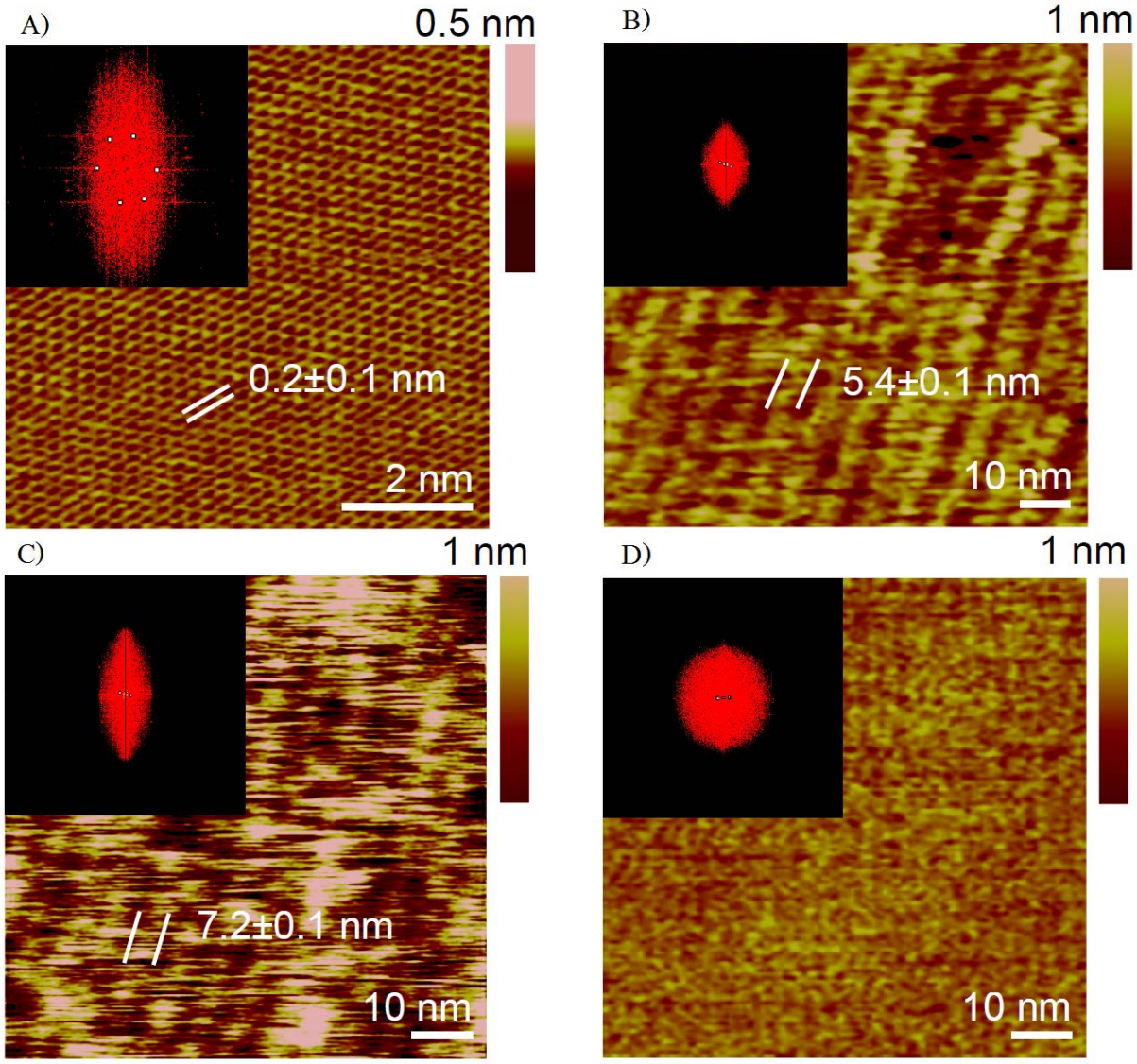

Figure 2.6 AFM images of FTMA assemblies on HOPG
Atomic force micrographs of **(A)** bare HOPG **(B)** 20 mM DTAB on HOPG **(C)** 1 mM reduced FTMA on HOPG and **(D)** 1mM oxidized FTMA on HOPG. All measurements are in aqueous 100 mM Li_2SO_4. The insets show the Fourier transform of the image.

interface).[49,50] The small variation in height of the assemblies formed by oxidized FTMA at the surface of HOPG is potentially consistent with formation of looped configurations, although definitive conclusions regarding the details of the configurations of surfactants are difficult to make using AFM. Importantly, however, in the context of interpreting our CVs of FTMA, AFM does confirm the presence of FTMA assemblies on HOPG in both oxidized and reduced states of the FTMA. We also note that AFM imaging of mobile surfactant assemblies is challenging, and we confirmed that the striped images presented in Fig. 2.6 were not artifacts of the scanning process by rotating the scanned area, changing the scan rate, and by comparing the trace and retrace images (see Supporting Information Fig. 2.S5).

Overall the results of our measurements using QCM and AFM, when combined, lead us to conclude that interfacial assemblies of oxidized and reduced FTMA are present at the surfaces of the hydrophobic electrodes and that the amount of FTMA adsorbed is similar in each of the oxidation states of the surfactant (in 1mM solutions). The results thus lead to the conclusion that the asymmetry of the CVs seen in Fig. 2.2 and Fig. 2.4 does not arise from the inability of one oxidation state of FTMA (oxidized FTMA) to adsorb on the hydrophobic electrode.

2.3.3 Incorporation of reduced and oxidized FTMA into interfacial surfactant assemblies

Although the results above indicate that the amounts of FTMA adsorbed at the hydrophobic electrodes from 1 mM solutions of either reduced or oxidized FTMA are similar, our electrochemical measurements indicate that the anodic current peak contains a significant contribution from diffusing (reduced) FTMA whereas the cathodic current peak is limited to contributions arising from only adsorbed (oxidized) FTMA. Thus, as introduced above in the context of the third hypothesis, we considered it possible that the asymmetry between the anodic

and cathodic peak currents seen in our experiments arises from an adsorbed layer of FTMA that prevents access of oxidized FTMA in bulk solution to the electrode. Here we note again that reduced FTMA has a single ionic head group (similar to a conventional surfactant) whereas oxidized FTMA is a bolaform surfactant with two cationic head groups. Past studies have reported that conventional and bolaform surfactants tend to mix poorly within surfactant assemblies.[22-25]

Prior to exploring ideas related to poor mixing of oxidized and reduced FTMA within interfacial assemblies, we discuss first the processes that we hypothesize to be occurring at the hydrophobic electrode during the cathodic sweep of the potential. At the start of the sweep, based on the results presented above (Fig. 2.5B and Fig. 2.6D), the hydrophobic electrode is decorated with assemblies formed from oxidized FTMA. During the cathodic sweep, by analyzing the change in cathodic peak current with scan rate, we conclude that the cathodic peak current arises largely from reduction of the oxidized FTMA on the electrode surface (Fig. 2.4E). This conclusion is supported by our evaluation of the total charge passed at the electrode during the cathodic sweep. We calculate it to be 10.9 ± 1.6 μC when using 0.1 mM FTMA, which corresponds to an areal density of 0.68 ± 0.1 molecules/nm^2. Our QCM measurements revealed the presence of 1.33 ± 0.1 molecules/nm^2, which is in reasonable agreement with the estimate based on charge passed at the electrode. The key idea that we emphasize here, and which we return to below, is that we interpret our measurements to indicate that an interfacial assembly of reduced FTMA forms on the electrode (during the cathodic sweep) via reduction of oxidized FTMA, and that the FTMA assembly so-formed subsequently serves as a barrier to further reduction of oxidized FTMA (in solution).

To understand better the origin of the above-proposed barrier properties of the adsorbed FTMA assemblies, we measured CVs using a mixed surfactant system containing both FTMA and DTAB. We selected DTAB because it has a molecular architecture similar to reduced FTMA, and thus we predicted that it may also prevent oxidized FTMA from accessing a hydrophobic electrode during a cathodic potential sweep. We performed experiments using 0.1 mM FTMA and 2 mM DTAB to ensure that the interfacial assembly formed at the hydrophobic electrode was primarily DTAB. Inspection of the CV in Fig. 2.7A reveals that the addition of 2 mM DTAB to 0.1 mM FTMA decreased the anodic peak current density (200 mV/s) from I_a = 50 ± 17 μA/cm^2 (no DTAB) to I_a = 8 ± 2 μA/cm^2 while the cathodic peak current density, which was I_c = 10 ± 3 μA/cm^2 prior to addition of DTAB, is suppressed beyond any measurable level by the addition of the DTAB. Furthermore, the scan-rate dependence of the peak anodic current density (χ_a = 0.42 ± 0.05) reveals that the anodic current is dominated by reduced FTMA diffusing from bulk solution, whereas in the absence of DTAB, the scan rate dependence (χ_c = 0.80 ± 0.1; 0.1 mM FTMA in Fig. 2.4E) showed a significant contribution to the anodic current from adsorbed FTMA. These results lead us to conclude that the surface is covered primarily with DTAB but that reduced FTMA is able to readily diffuse to the electrode through the interfacial DTAB assembly whereas oxidized FTMA cannot access the electrode in the presence of DTAB. Because reduced FTMA and DTAB are both conventional surfactants and because oxidized FTMA has a bolaform architecture, we speculate that oxidized FTMA does not mix with DTAB assemblies due to the bolaform architecture of oxidized FTMA.

Next we sought to determine whether the apparent inability of oxidized FTMA to mix with interfacial assemblies of conventional surfactants is due to slow insertion kinetics or thermodynamic immiscibility. We hypothesized that if oxidized FTMA is prevented from mixing

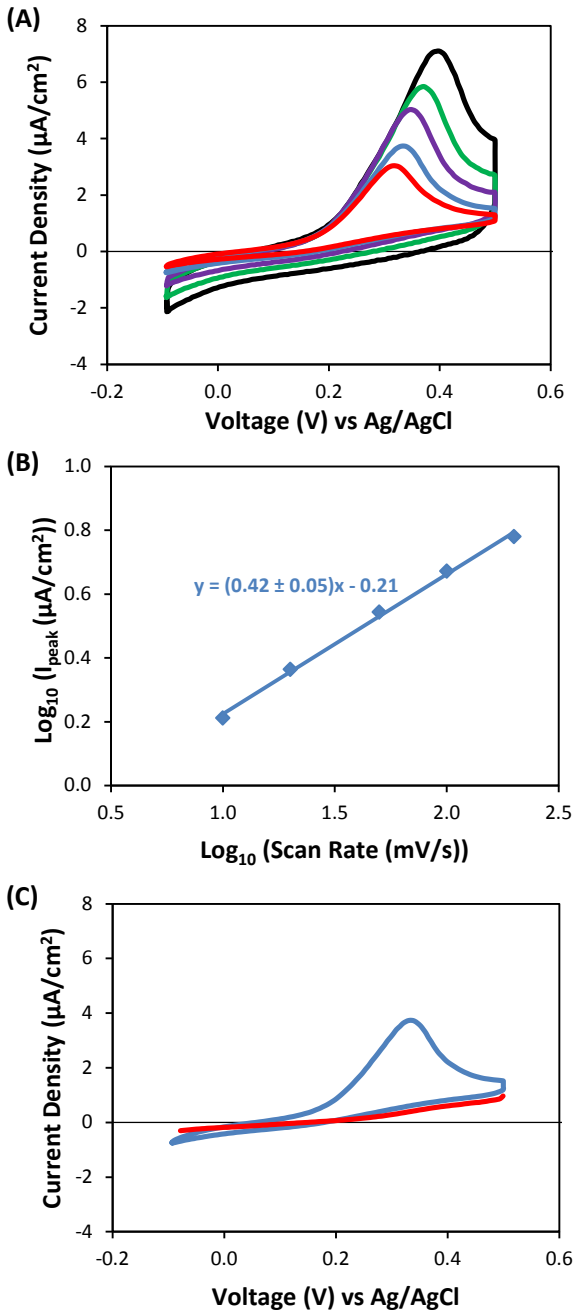

Figure 2.7 CV of FTMA and DTAB at dodecanethiol-functionalized gold electrodes
(A) Cyclic voltammograms of 0.1 mM FTMA and 2 mM DTAB in 100 mM Li_2SO_4 measured using a 1 cm^2 gold electrode functionalized with 1-dodecanethiol. The potential scan rates are 10 (red), 20 (blue), 50 (purple), 100 (green), and 200 (black) mV/s. All voltammograms began with an anodic sweep. **(B)** Scan rate-dependence of the anodic peak currents. **(C)** Linear sweep voltammogram, from +500 mV to -100 mV vs. Ag/AgCl at 20 mV/s with a 5 minute pre-equilibration period at 500 mV (red), compared to a cyclic voltammogram obtained at 20 mV/s (blue). Note that this linear sweep is cathodic.

with interfacial assemblies of DTAB by slow kinetics, equilibrating FTMA and DTAB at a hydrophobic electrode surface at a potential above the formal potential of FTMA would provide oxidized FTMA with sufficient time to mix into interfacial DTAB assemblies. To test this hypothesis, we first equilibrated a dodecanethiol-functionalized electrode against 0.1 mM FTMA and 2 mM DTAB (in 100 mM Li_2SO_4) at 500 mV for 5 minutes. Subsequently, we performed a linear sweep of the electrode potential from +500 mV to -100 mV vs Ag|AgCl. Inspection of Fig. 2.7C shows that the linear sweep does not generate a cathodic peak near 200 mV. This result thus provides support for the hypothesis that the cathodic current is suppressed because oxidized FTMA does not form mixed micelles with interfacial assemblies of reduced FTMA (or DTAB).

2.4 Discussion

The results presented in this paper provide evidence that the self-assembly of redox-mediators can lead to interfacial charge transfer processes that are substantially different from conventional redox mediators. Specifically, our results suggest that FTMA (and other surfactants such as DTAB) can form interfacial assemblies on hydrophobic electrodes that selectively regulate the access of amphiphilic redox-mediators from bulk solution to the electrode. Consistent with our interpretation that interfacial self-assembly processes underlie the asymmetry in the charge transfer that we measure with FTMA, the results shown in Fig. 2.2 obtained with bare gold electrodes do not exhibit the asymmetry (self-assembly is dependent on the surface properties of the electrode). The results shown in Fig. 2.3 with hydrophobic electrodes but non-amphiphilic redox mediators (HMeFc) also do not show the same level of asymmetry in charge transfer as seen with FTMA at hydrophobic electrodes.

We interpret our results to indicate that interfacial assemblies formed from reduced FTMA on hydrophobic electrodes prevent access of oxidized FTMA to the electrode. We propose that this phenomenon reflects the lack of mixing of oxidized and reduced FTMA because of differences in molecular architecture. This proposal finds supported in the results of experiments performed with DTAB, in which we observed interfacial assemblies formed by DTAB to also prevented access of oxidized FTMA to hydrophobic electrodes. The effects of DTAB (and reduced FTMA) on access of oxidized FTMA to the electrode appears to be thermodynamic (not kinetic) in origin. This conclusion is consistent with past studies of the kinetics of insertion of bolaform surfactants into assemblies of conventional surfactants. Although the presence of the two headgroups of a bolaform surfactant constrains the conformation of the surfactant during insertion (relative to a conventional surfactant),[22,51-53] past studies by Zana *et al.*[22-24] report rate constants for the insertion of bolaform alkane-α,ω-bis(trimethylammonium) surfactants to be faster than their analogous alkyl trimethylammonium conventional counterparts of the same chain length.

Past studies do support our proposal that reduced and oxidized FTMA are unlikely to form mixed micelles due to differences in molecular architecture. For example, at concentrations near the critical micelle concentration, mixtures of DTAB and its bolaform variant, dodecyl-1,12-bis(trimethylammonium bromide) (DBTAB), have been shown to not form mixed micelles in aqueous solution.[25] Mixed micellization between alkyltrimethylammonium bromides and alkane-α,ω-bis(trimethylammonium) bromides near the CMC of the conventional surfactant requires that the conventional and bolaform surfactants have specific chain lengths so as to satisfy packing constraints within the micelles. Zana *et al*. determined that for DTAB, a longer bolaform is needed, such as docosyl-1,22-bis(trimethylammonium bromide) for mixed

micelle formation.[54] Given the similarities between reduced FTMA and DTAB and between oxidized FTMA and DBTAB, reduced and oxidized FTMA are not expected to able to form mixed micelles in aqueous solution, a conclusion that is consistent with our experimental observations.

The results reported in this paper reveal that competitive adsorption/assembly of mixtures of reduced FTMA and oxidized FTMA at hydrophobic electrodes can lead to substantial changes in the passage of current at the electrodes. We emphasize, however, that this mechanism represents only one of several that can be envisaged to lead to current rectification when using amphiphilic redox-mediators. For example, we hypothesize that redox-state-dependent self-assembly of amphiphilic redox-mediators in the bulk of an aqueous solution might influence the concentration of redox-mediator adsorbed at the electrode (in the same way that the onset of micellization in bulk solution influences adsorption at aqueous-water interfaces).[55] In this context, we note that methylviologen derivatives have been shown to associate with surfactant micelles in their reduced but not oxidized forms.[56-58] Redox-dependent changes in the relative extent of adsorption of the redox mediator on the electrode (i.e., local concentration) would be expected to lead to changes in the relative rates of the forward and backward reaction of the mediator at the electrode. Alternatively, interfacial assemblies of the redox-mediator might form in both oxidation states, but with distinct organizations, as has been seen in block copolymers containing the ferrocene moiety. [59,60] A change in organization of the interfacial assembly could, for example, impact the distance between the redox-group and the electrode and thus the rate of electron transfer. In future studies, we will report on these physical scenarios by exploring the effects of surfactant molecular architecture and interfacial self-assembly on interfacial charge transfer.

2.5 Conclusions

Overall, this study demonstrates that interfacial self-assembly of an amphiphilic redox-mediator at a hydrophobic electrode substantially influences charge passed at the electrode. Specifically, we measured the Faradaic current passed to/from FTMA at the hydrophobic electrode to differ from that measured using either a non-self-assembling redox-mediator at a hydrophobic electrode or an amphiphilic redox-mediator at an untreated gold electrode. By combining results obtained using CV, QCM and AFM, we conclude that the rectification of current that we measured using FTMA at an alkanethiol-functionalized gold electrode arises from the formation of transient interfacial assemblies of reduced FTMA that block access of oxidized FTMA to the electrode during the cathodic sweep of the electrode potential. This conclusion is supported further by the effects of adding DTAB to the system, as it also forms an interfacial assembly on the hydrophobic electrode that permits transport of reduced FTMA but not oxidized FTMA to the hydrophobic electrode. Overall, our results suggest that the combined use of self-assembling redox-mediators and chemically functionalized electrodes can provide electrode/redox-mediator systems with charge transfer characteristics that differ substantially from systems that do not exhibit interfacial self-assembly. Our results also suggest that interfacial self-assembly processes have the potentially to be broadly useful in a variety of electrochemical contexts in which control over the passage of charge at an interface is needed.

2.6 Acknowledgements

This work was funded by the National Science Foundation through grant CBET-1263970. Partial support is also acknowledged by the ARO (through W911NF-14-1-0140 and W911NF-11-1-0251) and the NSF (DMR-1121288). Use of shared experimental facilities

funding by the Wisconsin MRSEC are also gratefully acknowledged. Professor Joel Pedersen is acknowledged for providing access to QCM.

2.7 References

‡ Portions of this chapter have been previously published as: T.J. Smith, C. Wang, N.L. Abbott; Influence of Self-Assembling Redox Mediators on Charge Transfer at Hydrophobic Electrodes. *Langmuir* **2015**, 31, (39), 10638–10648. Reprinted with permission. Copyright (2015) American Chemical Society.

1. T. Stergiopoulos, P. Falaras, *Adv. Energy Mater.* **2012**, 2 (6), 616-627.

2. A. Hagfeldt, G. Boschloo, L. Sun, L. Kloo, H. Petterson, *Chem. Rev.* **2010**, 110 (11), 6595-6663.

3. G. Boschloo, A. Hagfeldt, *Acc. of Chem. Res.* **2009**, 42 (11), 1819-1826.

4. D. Song, M.-S. Kang, Y.-G. Lee, W. Cho, J. H. Lee, T. Son, K. J. Lee, S. Nagarajan, P. Sudhagar, J.-H. Yum, Y. S. Kang, *Phys. Chem. Chem. Phys.* **2012**, 14 (2), 469-472.

5. S. M. Feldt, E. A. Gibson, E. Gabrielsson, L. Sun, G. Boschloo, A. Hagfeldt, *J. Am. Chem. Soc.* **2010**, 132 (46), 16714-16724.

6. Y. Liu, J. R. Jennings, Y. Huang, Q. Wang, S. M. Zakeeruddin, M. Grätzel, *J. Phys. Chem. C* **2011**. 115 (38), 18847-18855.

7. B. A. Gregg, F. Pichot, S. Ferrere, C. L. Fields, *J. Phys. Chem. B* **2001**, 105 (7), 1422-1429.

8. Z. Zhang, P. Chen, T. N. Murakami, S. M. Zakeeruddin, M. Grätzel, *Adv. Funct. Mater.* **2008**, 18 (2), 341-346.

9. H. Tian, X. Jiang, Z. Yu, L. Kloo, A. Hagfeldt, L. Sun, *Angew. Chem. Int. Ed.* **2010**, 49 (40), 7328-7331.

10. A. Kudo, T. Miseki, *Chem. Soc. Rev.* **2009**, 38, 253–278.

11. F. E. Osterloh, *Chem. Mater.* **2008**, 20, 35–54.

12. L. J. Minggu, W. R. W. Daud, M. B. Kassim, *Int. J. Hydrogen Energy* **2010**, 35, 5233–5244.

13. T. Saji, K. Hoshino, S. Aoyagui, *J. Chem. Soc., Chem. Commun.* **1985**, 13, 865-866.

14. J. P. E. Muller, B. S. Aytar, Y. Kondo, D. M. Lynn, N. L. Abbott, *AIChe J.* **2014**, 60 (4), 1381-1392.

15. B. S. Gallardo, V. K. Gupta, F. D. Eagerton, L. I. Jong, V. S. Craig, R. R. Shah, N. L. Abbott, *Science* **1999**, 283, 57-60.

16. B. S. Gallardo, K. L. Metcalfe, N. L. Abbott, *Langmuir* **1996**, 12 (17), 4116-4124.

17. X. Y. Liu, N. L. Abbott, *J. Colloid Interface Sci.* **2009**, 339 (1), 1-18.

18. N. Aydogan, B. S. Gallardo, N. L. Abbott, *Langmuir* **1999**, 15 (3), 722-730.

19. T. Saji, K. Hoshino, M. Goto, *J. Am. Chem. Soc.* **1991**, 113 (2), 450-456.

20. K. Tsuchiya, H. Sakai, T. Saji, M. Abe, *Langmuir* **2003**, 19 (22), 9343-9350.

21. H. Sakai, H. Imamura, Y. Kondo, N. Yoshino, M. Abe, *Colloids Surf., A.* **2004**, 232, 221–228.

22. S. Yiv, K. M. Kale, J. Lang, R. Zana, *J. Phys. Chem.* **1976**, 80 (24), 2651-2655.

23. S. Yiv, R. Zana, *J. Colloid Interface Sci.* **1980**, 77 (2), 449-455.

24. R. Zana, S. Yiv, K. M. Kale, *J. Colloid Interface Sci.* **1980**, 77 (2), 456-465.

25. R. Zana, In *Mixed Surfactant Systems*, Proceedings of the American Chemical Society Division of Colloid and Surface Chemistry at the 65th Colloid and Surface Science Symposium, Norman, Oklahoma, June 17-19, 1991 ; Paul M. Holland, Donn N. Rubingh, Eds.; American Chemical Society: Washington, DC., **1992;** 501, pp. 292-300.

26. T. W. Davey, W. A. Ducker, A. R. Hayman, *Langmuir* **2000,** 16, 2430-2435.

27. G. Mao, Y.-H. Tsao, M. Tirrell, H. T. Davis, V. Hessel, H. Ringsdorf, H. *Langmuir* **1993**, 9, 3461-3470.

28. G. Mao, Y.-H. Tsao, M. Tirrell, H. T. Davis, V. Hessel, J. van Esch, H. Ringsdorf, *Langmuir* **1994**, 10, 4174-4184.

29. G. Mao, Y.-H. Tsao, M. Tirrell, H. T. Davis, V. Hessel, H. Ringsdorf, *Langmuir* **1995**, *11*, 942-952.

30. W. A. Ducker, E. J. Wanless, *Langmuir* **1996**, 12, 5915-5920.

31. H. N. Patrick, G. G. Warr, S. Manne, I. A. Aksay, *Langmuir* **1999**, 15 (5), 1685-1692.

32. J. F. Liu, W. A. Ducker, *J. Phys. Chem. B* **1999**, 103 (40), 8558-8567.

33. K. Hoshino, K. Suga, T. Saji, *Chem. Lett.* **1986**, 15, 979-982.

34. T. Komura, T. Yamaguchi, K. Noda, S. Hayashi, *Electrochim. Acta* **2002**, 47, 3315-3325.

35. K. Tsuchiya, H. Sakai, T. Saji, M. Abe, *Langmuir* **2003**, 19, 9343-9350.

36. X. Liu, M. D. Graham, N. L. Abbott, *Langmuir* **2007**, 23, 9578-9585.

37. W. L. Deng, D. B. Yang, Y. Fang, C. L. Bai, *Sci. China Ser. B* **1996**, 39 (3), 225-234.

38. A. J. Bard, L. R. Faulkner, *Electrochemical Methods: Fundamentals and Applications*; 2nd Edition, Wiley: New York, NY, **2004;** p. 231.

39. A. J. Bard, L. R. Faulkner, *Electrochemical Methods: Fundamentals and Applications*; 2nd Edition, Wiley: New York, NY, **2004;** p. 591.

40. G. Sauerbrey, *Z. Phys.* **1959**, 155 (2), 206-222.

41. I. Reviakine, D. Johannsmann, R. P. Richter, *Anal. Chem.* **2011**, 83, 8838–8848.

42. J. P. Folkers, P. E. Laibinis, G. M. Whitesides, *J Adhesion Sci, Technol.* **1992**, 6 (12), 1397-1410.

43. F. Schreiber, *Prog. Surf. Sci.* **2000**, 65, 151-256.

44. D. J. Lavrich, S. M. Wetterer, S. L. Bernasek, G. Scoles, *J. Phys. Chem. B* **1998**, 102, 3456-3465.

45. S. E. Creager, L. A. Hockett, G. K. Rowe, *Langmuir* **1992**, 8 (3), 854-861.

46. A. D. Le, L. Yu, *J. Electrochem. Soc.* **2011**, 158 (1), F10-F14.

47. J. F. Smalley, M. D. Newton, S. W. Feldberg, *J. Electroanal. Chem.* **2006**, 589, 1–6.

48. W. A. Ducker, E. J. Wanless, *Langmuir* **1999**, 12, 5915-5920.

49. F. M. Menger, S. Wrenn *J. Phys. Chem.* **1974**, 78 (74), 1387-1390.

50. N. Aydogan, N. L. Abbott, *J. Colloid Interface Sci.* **2001**, 242, 411-418.

51. E. A. G. Aniansson, S. N. Wall, *J. Phys. Chem.* **1974**, 78 (10), 1024-1030.

52. E. A. G. Aniansson, S. N. Wall, *J. Phys. Chem.* **1975,** 79 (8), 857-858.

53. E. A. G. Aniansson, S. N. Wall, M. Almgren, H. Hoffman, I. Kielmann, W. Ulbricht, R. Zana, J. Lang, C. Tondre, *J. Phys. Chem.* **1976**, 80 (9), 905-922.

54. R. Zana, Y. Muto, K. Esumi, K. Meguro, *J. Colloid Interface Sci.* **1988**, 123 (2), 502-511.

55. P. C. Hiemenz, R. Rajagopalan, *Principles of Colloid and Surface Chemistry*; 3rd Edition, Taylor & Francis Group: Boca Raton, FL, **1997**; p. 330.

56. P. Brugger, M. Grätzel, *J. Am. Chem. Soc.* **1980**, 102, 2461-2463.

57. M. Grätzel, *Farad. Discuss.* **1980**, 70, 359-374.

58**.** K. Monserrat, M. Grätzel, *J. Chem. Soc., Chem. Commun.* **1981**, 4, 183-187**.**

59. H. B. Eitouni, N. P. Balsara, *J. Am. Chem. Soc.* **2004**, 126, 7446-7447.

60. H. B. Eitouni, N. P. Balsara, *J. Am. Chem. Soc.* **2006**, *128*, 16248-16252.

2.8 Supporting Materials

Figure 2.8 shows the cyclic voltammogram of 1 mM FTMA in 100 mM Li_2SO_4 on a bare gold electrode surface. Similar to the result reported on bare platinum by Muller *et al.*,[1] two peaks are seen on both the anodic and cathodic scans (one corresponding to a diffusing species and the other to an adsorbed species).

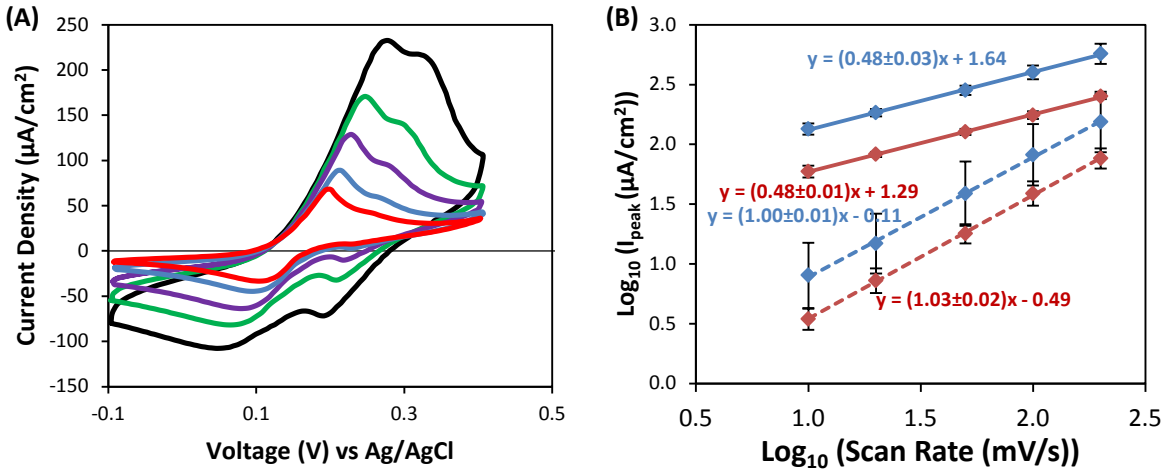

Figure 2.8 CV of FTMA at bare gold electrodes
(A) Cyclic voltammetry of 1 mM FTMA in 100 mM Li_2SO_4 on a 1 cm^2 bare gold electrode at scan rates 10 (red), 20 (blue), 50 (purple), 100 (green), and 200 (black) mV/s. All voltammograms began with an anodic sweep. **(B)** Scan rate dependence for anodic peaks (blue), cathodic peaks (red), the peak at lower potential (solid) and the peak at higher potential (dotted). Note the scan rate dependence is to the ~0.5 power for the first peak and ~1 power for the second.

Figure 2.9 shows a cyclic voltammogram measured using 0.1 mM FTMA in 100 mM Li_2SO_4 and a 1-dodecanethiol covered gold surface at a scan rate of 200 mV/s. In addition, a cyclic voltammogram recorded using 100 mM Li_2SO_4 (no FTMA) is shown. The Faradaic current is evaluated as the difference between the two currents. The differential capacitance, C_d, of the 1-dodecanethiol monolayer can be calculated from the equation:[2]

$$\Delta I_e = C_d v \tag{2.4}$$

where ΔI_e is the capacitive current, which is evaluated on a cyclic voltammogram of 100 mM Li_2SO_4 in the absence of FTMA. We evaluate the differential capacitance to be 13.2 μF/cm^2. This value is similar to estimates obtained from past electrochemical studies performed with 1-dodecanethiol monolayers.[2,3]

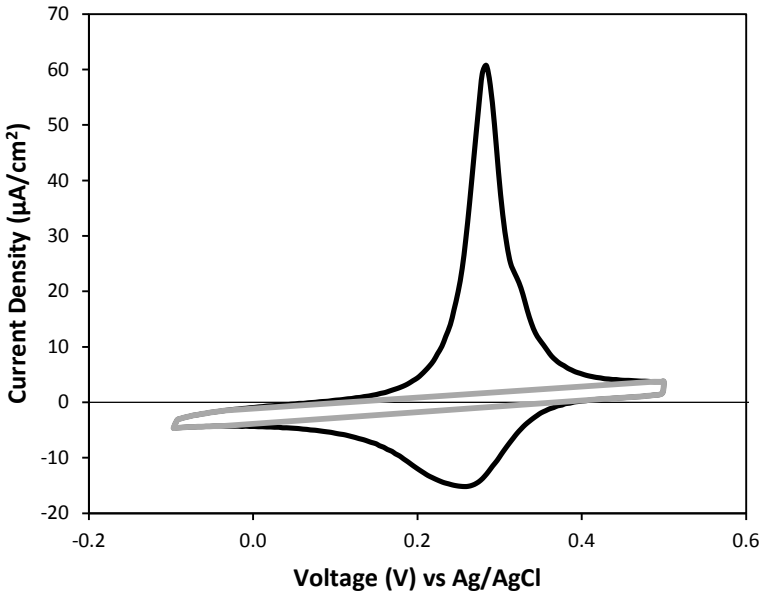

Figure 2.9 CV of FTMA showing a baseline estimate used to calculate faradaic currents
The total (black) current measured during a cyclic voltammogram of 0.1 mM FTMA in 100 mM Li_2SO_4 on a 1 cm^2 1-dodecanethiol functionalized gold electrode at a scan rate of 200 mV/s. In addition, a cyclic voltammogram (grey) recorded using 100 mM Li_2SO_4 (no FTMA) is shown. Both voltammograms began with an anodic sweep.

Figure 2.10 shows cyclic voltammograms measured using 0.01 mM, 0.03 mM, and 0.3 mM FTMA in 100 mM Li_2SO_4 on a 1-dodecanethiol covered gold surface.

Figure 2.11 shows the cyclic voltammogram of 1 mM, 0.3 mM, and 0.1 mM oxidized FTMA in 100 mM Li_2SO_4 on a 1-dodecanethiol covered gold surface. Similar to reduced FTMA, significant current rectification is seen with $I_a/I_c = 21$ (10 mV/s, 1 mM).

Figure 2.12 shows additional AFM images of reduced FTMA on HOPG. The striped pattern with a periodicity of 7.2 ± 0.1 nm is visible throughout.

Figure 2.13 shows an AFM image of a bare gold substrate prepared as described in the methods section of this paper.

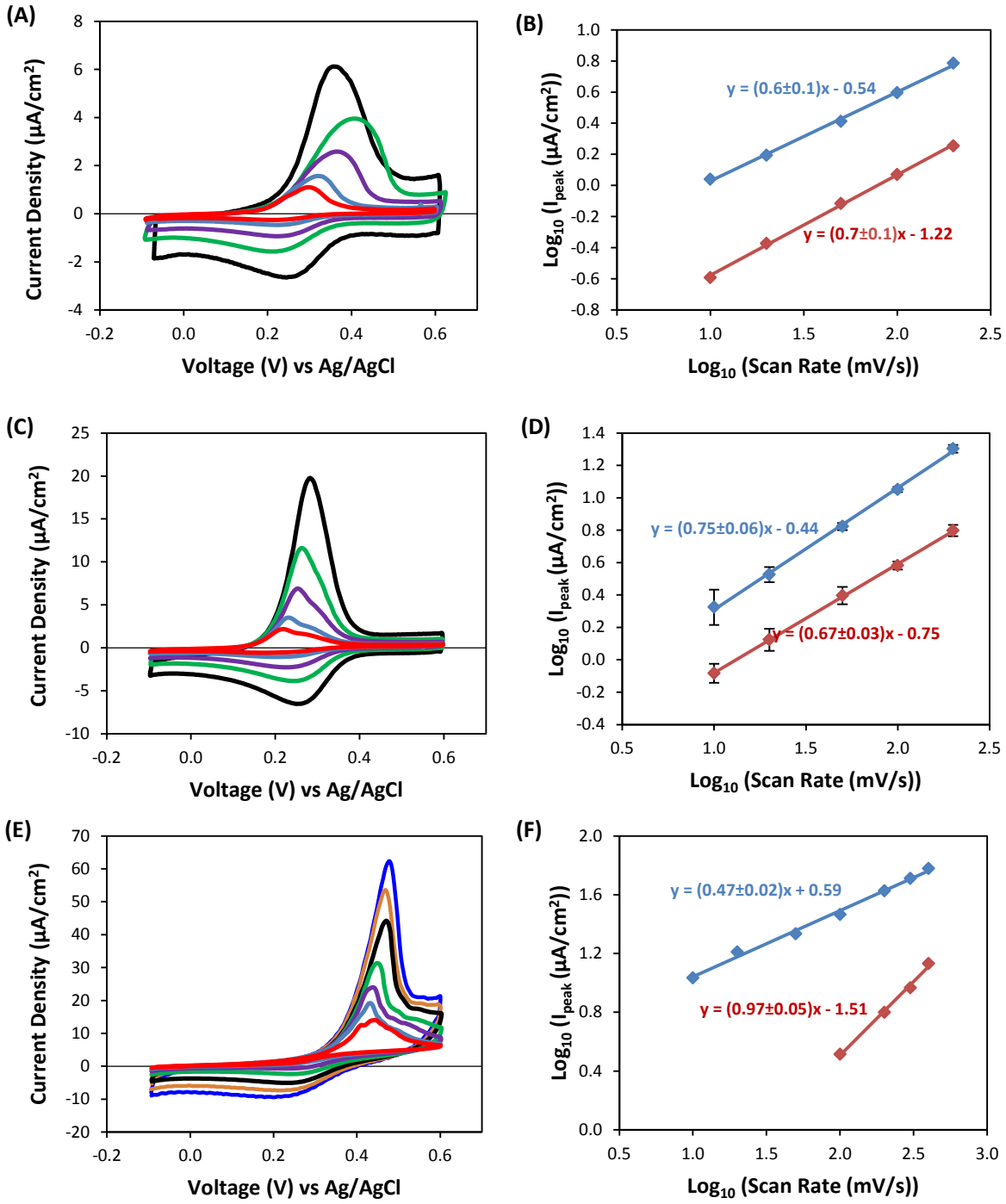

Figure 2.10 CVs of FTMA at varying concentration
Cyclic voltammograms of 0.01**(A)**, 0.03 **(C)**, and 0.3 **(E)** mM FTMA in 100 mM Li_2SO_4 on a 1 cm^2 gold electrode covered in a 1-dodecanethiol monolayer at scan rates 10 (red), 20 (blue), 50 (purple), 100 (green), 200 (black), 300 (orange), and 400 (blue) mV/s. All voltammograms began with an sweep. Scan rate dependence for 0.01 **(B)**, 0.03 **(D)**, and 0.3 **(F)** mM of the anodic peak (blue) and the cathodic peak (red).

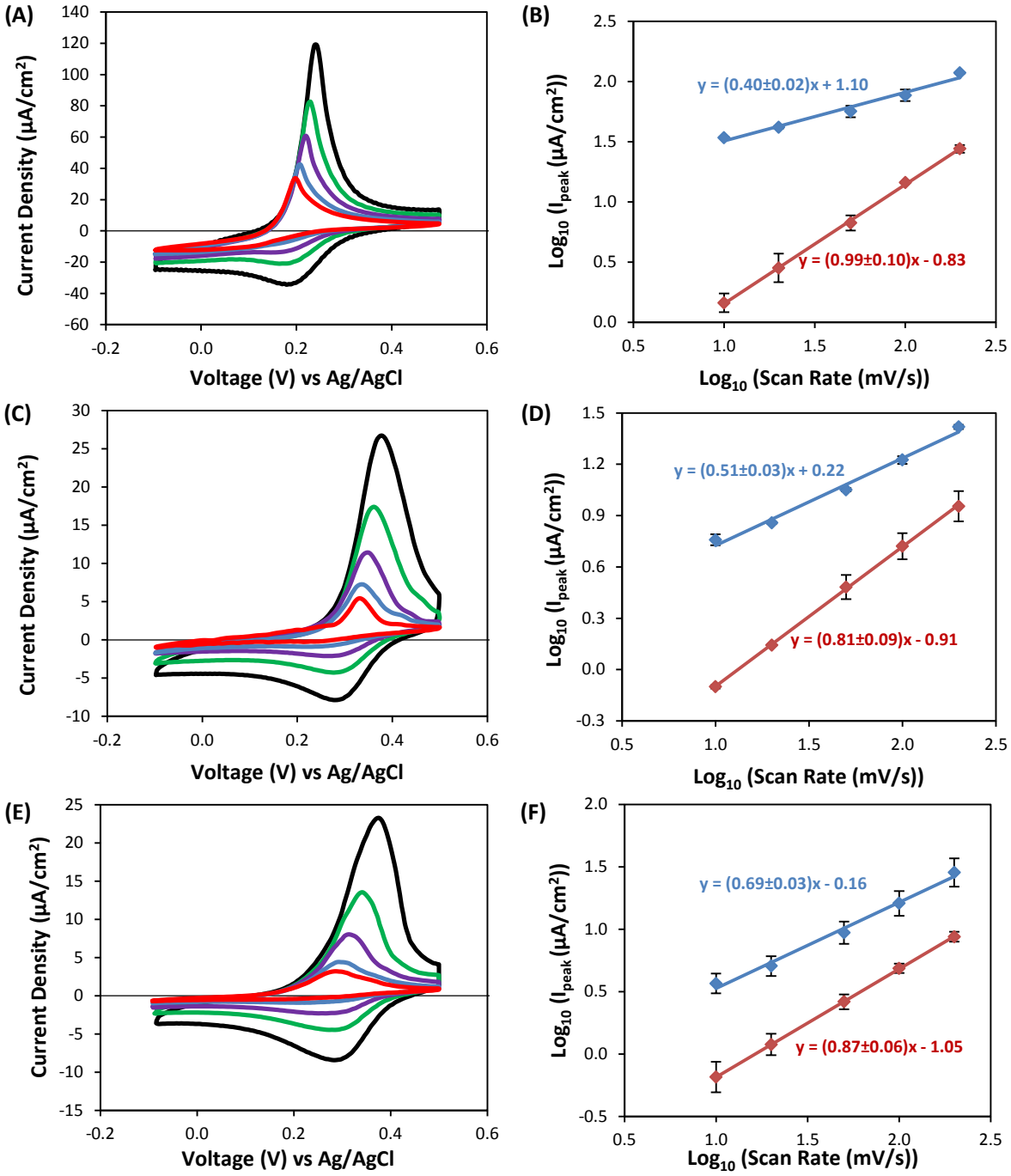

Figure 2.11 CVs of solutions containing oxidized FTMA
Cyclic voltammogram 1 mM **(A)**, 0.3 mM **(C)**, and 0.1 mM **(E)** oxidized FTMA in 100 mM Li_2SO_4 on a 1 cm^2 gold electrode covered in a 1-dodecanethiol monolayer at scan rates 10 (red), 20 (blue), 50 (purple), 100 (green), and 200 (black) mV/s. All voltammograms began with a cathodic sweep. Scan rate dependence for 1 mM **(B)**, 0.3 mM **(D)**, and 0.1 mM **(F)** oxidized FTMA anodic peak (blue) and the cathodic peak (red).

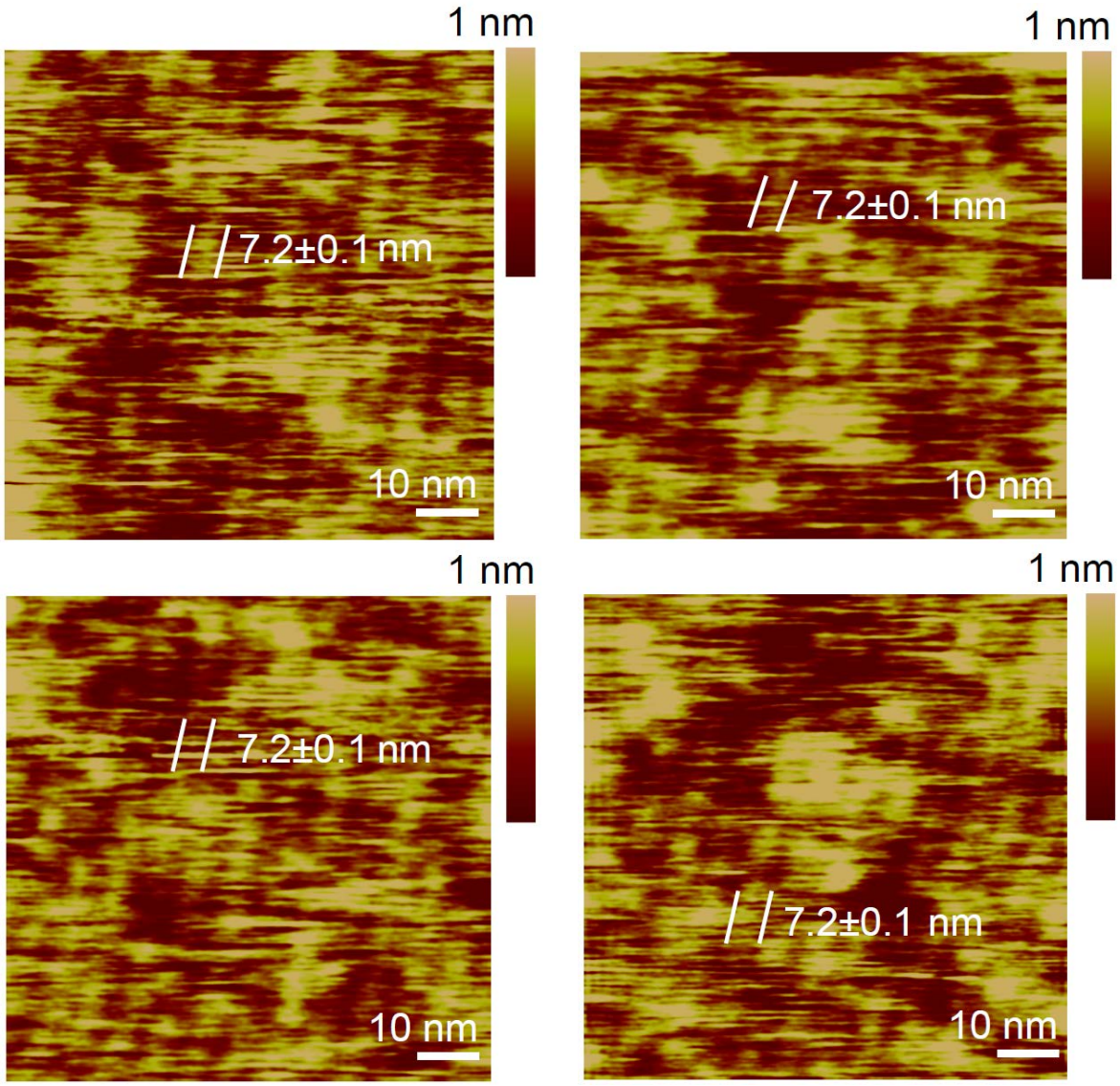

Figure 2.12 Additional AFM images of 1 mM reduced FTMA on HOPG
Atomic force micrographs of 1 mM reduced FTMA on HOPG.

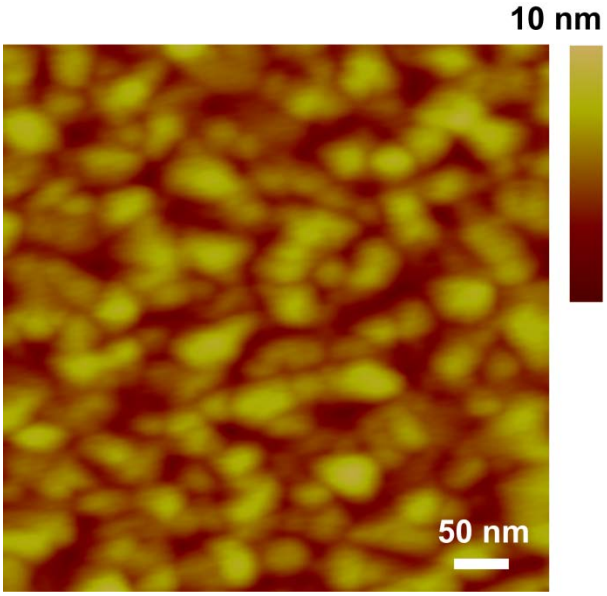

Figure 2.13 AFM image of a bare gold electrode
Atomic force micrograph of a bare gold electrode. The root-mean-square roughness value is 1.4 ± 0.1 nm (calculated using a scanned area of 500 nm x 500 nm).

2.9 Supporting References

1. J. P. E. Muller, B. S. Aytar, Y. Kondo, D. M. Lynn, N. L. Abbott, *AIChe J.* **2014**, 40 (4), 1381-1392.

2. M. A. Rampi, O. J. A. Schueller, G. M. Whitesides, *Appl. Phys. Lett.* **1998**, 72 (14), 1781-1783.

3. M. D. Porter, T. B. Bright, D. L. Allara, C. E. D. Chidsey, *J. Am. Chem. Soc.* **1987**, 109, 3559-3568

Chapter 3 : Redox-Triggered Mixing and Demixing of Surfactants within Assemblies Formed in Solution and at Surfaces‡

3.1 Introduction

Surfactant mixtures are widely used to tune the structure and properties of micellar assemblies formed by surfactants in bulk solution or at interfaces.[1-12] Surfactant mixtures can form assemblies with a range of morphologies, including vesicles (e.g., by binary mixtures of conventional cationic and anionic surfactants),[1-5] various lyotropic liquid crystalline phases,[6,7] and giant worm-like micelles.[8-10] Surfactant mixtures can be exploited also to design systems that minimize the concentration of surfactant monomer present in bulk solution through favorable interactions between unlike surfactants in the mixture (i.e., minimizing the critical aggregation concentration (CAC)).[11] Alternatively, the interactions between some surfactant mixtures can be sufficiently unfavorable that the surfactants form two coexisting micelle populations that do not mix.[13-17] For example, mixtures of conventional (hydrogenated) and fluorinated surfactants,[13,14] ternary mixtures of cationic, anionic and nonionic surfactants,[15] or mixtures of conventional and bolaform surfactants can form coexisting populations of micelles.[16,17] In this study, we report on the mixing of surfactants that contain the redox-active group ferrocene. Specifically, we test the hypothesis that redox-triggered changes in molecular architecture can be used to control the mixing of these surfactants within micellar assemblies formed in bulk solution and at interfaces.

The properties of switchable surfactants containing the ferrocene moiety have been explored in a number of past studies.[18-21] These past investigations revealed that oxidation of ferrocene to ferrocenium changes the properties of aqueous solutions of ferrocenyl surfactants in a manner that is strongly dependent on whether the ferrocene moiety is located near the head

group or the terminus of the tail of the surfactants.[22-24] Herein we focus on the mixing behavior of two ferrocenyl surfactants (Fig. 3.1): 11-ferrocenylundecyl trimethylammonium bromide (FTMA) and *N*,*N*-dimethylferrocenylmethyldecyl ammonium bromide (DMFA). Both surfactants possess cationic head groups (trimethylammonium), but the ferrocene of FTMA is located at the terminus of the aliphatic tail whereas the ferrocene of DMFA is located adjacent to the head group.[25] Upon oxidation of ferrocene to ferrocenium, FTMA is transformed to an ionic bolaform surfactant. Past measurements at the air-water interface of solutions of FTMA have shown that this transformation can lead to an increase in surface tension of as much as 23 mN/m.[22] In contrast, because the ferrocene group of DMFA is located adjacent to the trimethylammonium head group of the surfactant, oxidation of ferrocene in DMFA results in the formation of a surfactant with a conventional architecture and divalent head group. Past measurements performed with DMFA at the air-water interface have revealed the surface tensions of aqueous solutions of DMFA to increase by only 3 mN/m when DMFA is oxidized.[23]

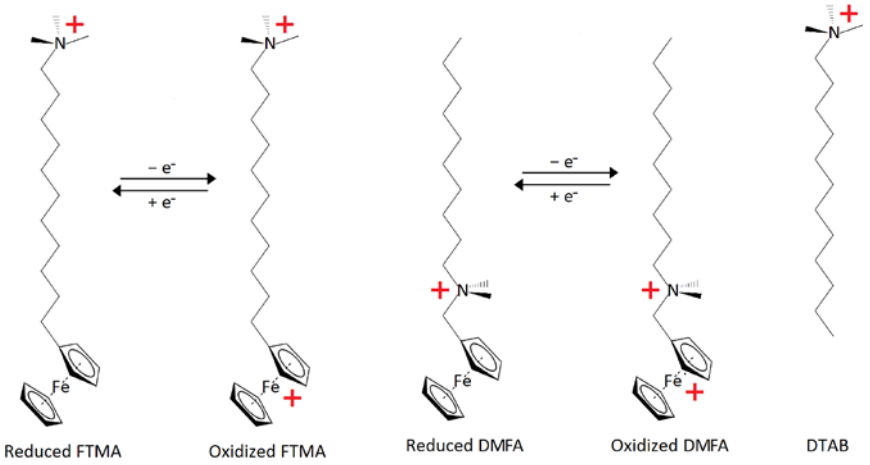

Figure 3.1 Molecular structures of FTMA, DMFA, and DTAB
Molecular structures of surfactants used in this study.

In this paper, we contrast the behavior of FTMA and DMFA in the context of understanding how redox-triggered changes in molecular architecture affect their tendency to form mixed assemblies in solution and at interfaces.

As context to the study reported herein, we note that prior studies have proposed mixing rules for conventional and bolaform surfactants within micellar assemblies. For example, the formation of mixed micelles in bulk solution by conventional and bolaform surfactants was investigated by Zana *et al*.,[16,17] using mixtures of alkyltrimethylammonium bromide (C_nTAB) and alkane-α-ω-bis(trimethylammonium) bromide ($TABC_mTAB$) amphiphiles. These studies concluded that, due to chain packing constraints, mixed micelles only form with C_nTAB and $TABC_mTAB$ when the values of *m* and *n* satisfy $2n - 5 \approx m$. This conclusion was also supported by studies of the dynamics of micellization of bolaform surfactants,[26-28] which conclude that bolaform surfactants adopt a looped configuration in mixed micelles. In this paper, we explore the applicability of these mixing rules to ferrocenyl surfactants such as FTMA and DMFA. For example, if reduced FTMA behaves as a conventional surfactant ($n \approx 14$), the above-described mixing rules predict that reduced FTMA will not form mixed micelles with oxidized FTMA ($m = 11$). We note, however, that the applicability of these mixing rules to a ferrocenyl surfactant such as reduced FTMA was not obvious to us in advance of this study. For example, reduced FTMA differs from conventional surfactants such as DTAB because the ferrocene group is bulkier and more polarizable than a methyl group (terminus of a conventional surfactant).[29,30] Both of these factors can impact chain-packing statistics.

Zana and coworkers proposed that the mixing rules outlined above arise from constraints on the packing of surfactant chains in micellar assemblies. Accordingly, the applicability of the mixing rules is predicted to depend on the morphology of the assembly, as the morphology of an

assembly impacts chain packing statistics. In this paper, we explore mixing within surfactant assemblies formed in three environments: (i) in bulk solution, (ii) at the air/water interface, and (iii) at hydrophobic solid surfaces. Past studies have found that reduced FTMA forms micellar and hemimicellar assemblies in bulk solution[31,32] and at hydrophobic solid surfaces, respectively.[33] This behavior is similar to DTAB. In contrast, at the surface of water, reduced FTMA has been inferred to form a monolayer comprised of molecules in a looped configuration whereas DTAB forms a monolayer within which the molecules adopt an extended configuration.[34,35]

We end this Introduction by noting that the results of our investigation of redox-triggered changes in the mixing of surfactants in solution and at interfaces is broadly relevant to the development of self-assembling redox mediators.[33, 36] Specifically, we recently reported that the charge-transfer characteristics of electrodes can be substantially tuned by using redox-mediators that undergo redox-dependent self-assembly at the electrodes.[33] As discussed below, we use the results of the study reported in this paper to advance our understanding of the design of self-assembling redox-mediators as well as to provide insight into the factors that broadly control the mixing of surfactants.

3.2 Materials and Methods

3.2.1 Materials

DTAB and Li_2SO_4 were purchased from Sigma Aldrich (St. Louis, MO). FTMA was purchased from Dojindo Molecular Technologies (Rockville, MD). All materials were used as received. DMFA was synthesized as described elsewhere.[24] Unless otherwise stated, oxidized FTMA or DMFA solutions were electrochemically oxidized in a three-electrode cell, as

described previously.[36] Surface tension measurements were performed using solutions of oxidized FTMA that were prepared by the addition of $Fe_2(SO_4)_3$ in a stoichiometric ratio of one Fe^{3+} ion per ferrocene group, as detailed previously.[22] Oxidized DMFA was used immediately following preparation.[24] All surfactant mixtures were investigated in aqueous solutions containing 100 mM Li_2SO_4, adjusted to a pH of 5 by the addition of H_2SO_4. AFM tips (MSCT model) and highly-oriented pyrolytic graphite sheets (HOPG) were purchased from Bruker Nano Company (Santa Barbara, CA). Deionized water with a resistivity of 18.2 MΩ-cm from a Synergy Ultrapure Water System (Millipore, Darmstadt, Germany) was used to form all aqueous solutions.

3.2.2 Experimental methods

3.2.2.1 Surface Tension Measurements

Surface tensions were measured using a KSV NIMA PS4 pressure sensor (NIMA Technology, Coventry, United Kingdom) and a paper Wilhelmy plate. The Wilhelmy plate was immersed in the solution and allowed to equilibrate for approximately ten minutes before measurement. The surface tension, γ, was determined by measuring the change in force on the plate immediately before and after removal from solution, F, and using F in the Wilhelmy equation:[37]

$$\gamma = \frac{F}{\ell \cos \theta} \tag{3.1}$$

where ℓ is the wetted perimeter (21 mm) and θ is the contact angle, which is zero for a paper plate.[38]

We calculated the limiting surface excess concentration (Γ_{lim}) for a solution containing a single surfactant in the presence of a swamping electrolyte, at concentrations just below the CAC from the Gibbs adsorption isotherm:[39]

$$\Gamma_{lim} = -\frac{1}{kT}\frac{d\gamma}{d \ln C} \tag{3.2}$$

where k is the Boltzmann constant, T is the temperature, and C is the surfactant concentration. The minimum area per molecule (A_{min}) was calculated from Γ_{lim} as $A_{min} = 1/\Gamma_{lim}$.

For a multi-component surfactant system, assuming the activity coefficient of each component to be unity, the Gibbs adsorption equation can be written:[40]

$$-d\gamma = RT \sum_i \Gamma_i \, d \ln C_i \tag{3.3}$$

For the case of a binary mixture of cationic surfactants 1 and 2 where the two surfactants are added to bulk solution at a constant ratio, the overall surface excess (Γ_{Total}) can be calculated as (see Supporting Information for derivation):

$$\Gamma_{Total} = \Gamma_1 + \Gamma_2 = -\frac{1}{kT}\frac{d\gamma}{d \ln C_1} \tag{3.4}$$

We used Eq. 3.4 to determine Γ_{Total} for binary surfactant mixtures in swamping electrolyte.

3.2.2.2 Static Light Scattering

Static light scattering measurements were performed using a Brookhaven BI 200-SM goniometer (Holtsville, NY) with a 532 nm laser. Surfactant solutions were filtered using a Millex-GV 0.22 μm-pore polyvinylidene fluoride filter (Millipore, Darmstadt, Germany) prior to measurement. Borosilicate glass culture tubes (12 x 75 mm; Fisher, Waltham, MA) were rinsed

in hexane (Sigma Aldrich, St. Louis, MO) and dried immediately before filling with sample for measurement. Culture tubes that did not produce constant intensities of scattered light (within 20%) upon rotation were discarded. All intensities of scattered light were measured at θ = 90° and analyzed using the equation[41]:

$$\frac{KC}{\Delta R_{90^\circ}} = \frac{1}{M^*} + 2B^*C \tag{3.5}$$

where C is the solute concentration, M* is the apparent molecular weight of the aggregates, B* is the apparent second Virial coefficient, K is an optical constant, and ΔR_{90° is the excess Rayleigh ratio of the sample. The optical constant K was calculated as:

$$K = \frac{4\pi^2 n^2_{cac}(dn/dC)^2}{N_A \lambda^4} \tag{3.6}$$

where n_{cac} is the refractive index of the aqueous solution at its CAC, dn/dC is the refractive index increment with respect to concentration, which is approximated as 0.18 cm^3/g for surfactant micelles,[42] N_A is Avogadro's number, and λ is the wavelength of the laser (532 nm). The excess Rayleigh ratio was evaluated for each sample as:

$$\Delta R_{90^\circ} = \left(\frac{I - I_s}{I_T}\right)\left(\frac{n}{n_T}\right)^2 R_{90^\circ,T} \tag{7}$$

where I is the intensity of light scattered by the sample, I_s is the intensity of light scattered by a 100 mM aqueous Li_2SO_4 solution free of surfactant, I_T is the intensity of light scattered by toluene, n is the refractive index of the sample, n_T is the refractive index of toluene, and $R_{90^\circ,T}$ is the Rayleigh ratio of toluene for a 532 nm laser at 25°C, which is measured to be 2.803 x 10^{-5}

cm^{-1}.[42] For micellar solutions, the concentration in Eq. 3.5 is based on the surfactant within aggregates, giving:

$$\frac{K(C - C_{cac})}{\Delta R_{90^\circ}} = \frac{1}{M^*} + 2B^*(C - C_{cac}) \quad (3.8)$$

3.2.2.3 Quartz Crystal Microbalance

Quartz crystal microbalance with viscous dissipation (QCM-D) measurements were performed using a Q-Sense E4 instrument (Biolin Scientific, Västra Frölunda, Sweden), as described in detail previously.[33] For the adsorption of films where the viscous dissipation, ΔD, and the change in frequency, Δf, satisfy $\Delta D/\Delta f < 4x10^{-7}$ Hz^{-1} using a 5 MHz crystal, the adsorbed mass, Δm, can be calculated from the Sauerbrey equation:[43]

$$\Delta f = -\frac{2f_o^2}{A\sqrt{\rho_q \mu_q}} \Delta m \quad (3.9)$$

where f_o is the resonant frequency of the crystal before immersion into solution, A is the area of the piezoelectric quartz crystal, ρ_q is the density of quartz, and μ_q is the shear modulus of quartz.

3.2.2.3 Atomic Force Microscopy

Atomic force microscopy (AFM) was used to image interfacial assemblies formed by mixtures of 2 mM DTAB and 0.1 mM FTMA (oxidized or reduced), as well as 20 mM DTAB. All measurements were performed in 100 mM Li_2SO_4 on highly-oriented pyrolytic graphite (HOPG). The AFM images were acquired using a Multimode IIIa instrument (Bruker Nano, Santa Barbara, CA), using methods detailed elsewhere.[33] HOPG was selected as the substrate because alkanethiol-functionalized gold substrates are too rough to allow high-resolution AFM imaging and HOPG is also a hydrophobic surface.

3.3 Results

3.2.1 Assemblies Formed in Bulk Aqueous Solution

The first experiments reported in this paper were performed to address the question of whether or not reduced FTMA (structure shown in Fig. 3.1) forms mixed micelles with oxidized FTMA in bulk solution. To this end, we measured surface tensions of reduced and oxidized FTMA dissolved in aqueous solutions containing 100 mM Li_2SO_4. Inspection of Fig. 3.2A reveals that the solutions containing reduced FTMA alone exhibit a logarithmic decrease in surface tension with increasing FTMA concentration until reaching a threshold concentration beyond which the surface tension is constant. This break (at 0.072 ± 0.003 mM) indicates the CAC of reduced FTMA (in 100 mM Li_2SO_4).[22,34] In contrast, the addition of oxidized FTMA to the aqueous electrolyte had no measurable effect on surface tensions at concentrations below 0.1 mM. In addition, there is no evidence of a CAC in the surface tension measurements of oxidized FTMA.

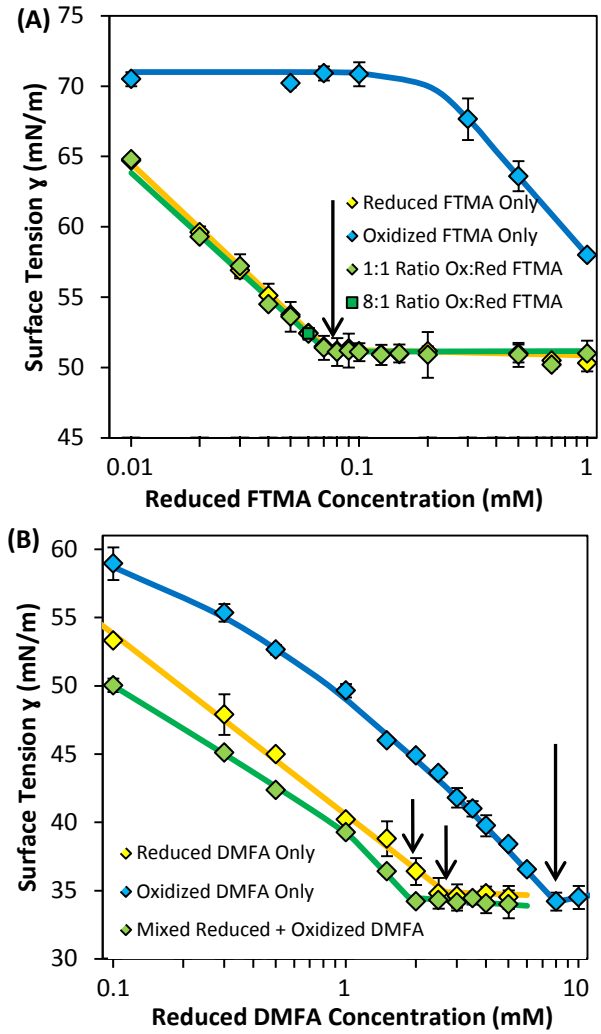

Figure 3.2 Surface tension of mixtures of reduced and oxidized FTMA and DMFA
Surface tension measurements of aqueous solutions (100 mM Li_2SO_4) containing either (i) reduced ferrocenyl surfactant, (ii) oxidized ferrocenyl surfactant, or (iii) a mixture of reduced and oxidized ferrocenyl surfactant (1:1 ratio), where the ferrocenyl surfactant is **(A)** FTMA or **(B)** DMFA. A single data point corresponding to a 8:1 ratio of oxidized FTMA to reduced FTMA (0.06 mM reduced FTMA and 0.5 mM oxidized FTMA) is also shown in (A). The concentration shown on the x-axis is that of reduced ferrocenyl surfactant except for the samples containing oxidized surfactant only, in which case the oxidized surfactant concentration is shown. The error bars indicate the standard deviation between at least 3 independent experiments. The breaks in the surface tension vs. concentration curves are indicated by arrows and listed in Table 3.1.

(A)

Surfactant(s)	Break in Curve (mM of Reduced FTMA)	Limiting Area ($Å^2$/molecule)
Reduced FTMA Only	0.072 ± 0.003	62 ± 2
Oxidized FTMA Only	N/A	58 ± 6
Reduced and Oxidized FTMA	0.071 ± 0.003	64 ± 7

(B)

Surfactant(s)	Break in Curve (mM DMFA)	Limiting Area ($Å^2$/molecule)
Reduced DMFA Only	2.6 ± 0.1 (reduced DMFA)	69 ± 2
Oxidized DMFA Only	7.8 ± 0.2 (oxidized DMFA)	53 ± 1
Reduced and Oxidized DMFA	2.0 ± 0.1 (reduced DMFA)	56 ± 4

(C)

Surfactant(s)	Break(s) in Curve (mM DTAB)	Limiting Area ($Å^2$/molecule)
DTAB Only	4.0 ± 0.2	29 ± 4
DTAB and Reduced FTMA	0.95 ± 0.08 2.5 ± 0.2	55 ± 5
DTAB and Oxidized FTMA	4.0 ± 0.2	40 ± 2

Table 3.1 Summary of CMC values of surfactant mixtures
Surface tensions and values of the limiting area per molecule for **(A)** mixtures of reduced and oxidized FTMA, **(B)** mixtures of reduced and oxidized DMFA, and **(C)** mixtures of DTAB and each redox state of FTMA. The surface tension plots of the data in (A) and (B) are shown in Figure 3.2 and the plots for (C) are shown in Figure 3.3.

Fig. 3.2A also shows surface tensions of solutions containing 1:1 mixtures of oxidized and reduced FTMA (plotted as a function of the concentration of reduced FTMA in the solution). Inspection of Fig. 3.2A reveals that the addition of the oxidized FTMA to a solution of reduced FTMA has no measureable effect on either the surface tension of the aqueous solution or the CAC of FTMA. Specifically, if oxidized and reduced FTMA formed mixed micelles, we would observe a lowering of the CAC of the mixture relative to reduced FTMA alone. Here we note that the addition of millimolar concentrations of oxidized FTMA does not significantly change

the ionic strength of a solution containing 100 mM Li_2SO_4. Overall, these results indicate that reduced FTMA and oxidized FTMA do not form mixed micelles in bulk solution at the concentrations investigated. The results are consistent also with reduced FTMA behaving as a conventional surfactant and oxidized FTMA behaving as a bolaform surfactant when forming mixed micelles in bulk solution (i.e., the two oxidation states of FTMA do not form mixed micelles; see Introduction).

To test further if the absence of mixing of reduced and oxidized FTMA within micelles formed in bulk solution reflects a redox-induced change in the molecular architecture of FTMA, next we measured the mixing behavior of the reduced and oxidized states of DMFA. As noted above, because the ferrocene of DMFA is adjacent to the quaternary ammonium head group, unlike FTMA, oxidation of ferrocene to ferrocenium within DMFA does not generate a surfactant with a bolaform architecture. Accordingly, an observation of mixing of reduced and oxidized DMFA within micelles in bulk solution would provide additional support for the hypothesis that the absence of mixing of reduced and oxidized FTMA within micelles is due to the distinct architectures of reduced (conventional) and oxidized (bolaform) FTMA. Surface tension measurements of aqueous solutions containing either reduced DMFA or oxidized DMFA in 100 mM Li_2SO_4 (Fig. 3.2B) reveal CACs of 2.6 ± 0.1 mM and 7.8 ± 0.2, respectively. Inspection of Fig. 3.2B also reveals that a 1:1 mixture of reduced and oxidized DMFA exhibits a CAC of 2.0 ± 0.1 mM (concentration of reduced DMFA), a value that is lower than that of either reduced DMFA alone (2.6 ± 0.1 mM) or oxidized DMFA alone (7.8 ± 0.2 mM). These results indicate that, unlike FTMA, reduced and oxidized DMFA form mixed assemblies in bulk solution. Significantly, these results also support our hypothesis that the absence of mixing of reduced and oxidized FTMA is primarily a consequence of the redox-induced change in

molecular architecture (classical versus bolaform) and not simply a consequence of the increase in net charge of the surfactant (as the latter is the same for both DMFA and FTMA).

To provide an additional test of the role of the redox-controlled change in surfactant architecture on mixing within micellar assemblies, we examined mixtures of DTAB and either reduced or oxidized FTMA (we hypothesized that DTAB would form mixed micelles with reduced FTMA but not with oxidized FTMA). Fig. 3.3A shows measurements of surface tensions of solutions containing DTAB, or mixtures of DTAB with FTMA in a 15:1 ratio (Fig. 3.3A). This ratio was selected so that each surfactant has an appreciable effect on surface tension over the concentration range investigated. For DTAB alone, we measured a CAC (in 100 mM Li_2SO_4) of 4.0 ± 0.2 mM.[44,45] Inspection of Fig. 3.3A reveals that the addition of oxidized FTMA to DTAB has no measurable effect on the CAC of the DTAB, which suggests that oxidized FTMA and DTAB do not form mixed aggregates in bulk solution under the conditions investigated.

We now turn our attention to mixtures of reduced FTMA and DTAB. Fig. 3.3A reveals a break in the surface tension vs. concentration plot for solutions of DTAB and reduced FTMA (with a 15:1 ratio) at a mixture containing 2.5 ± 0.3 mM DTAB and 0.17 ± 0.02 mM reduced FTMA. We also note, however, that 0.17 ± 0.02 mM FTMA is already above the CAC of reduced FTMA alone (see Fig. 3.2A). Because we do not expect DTAB to suppress the aggregation of reduced FTMA, we hypothesized that micelles are already present in solution prior to the break seen at 2.5 mM DTAB/0.17 mM FTMA and that this break corresponds to a change in micelle composition. To test this hypothesis, we performed both surface tension measurements and static light scattering measurements of solutions containing a 15:1 ratio of DTAB to reduced FTMA over a wider concentration range. Inspection of Fig. 3.3B reveals that

indeed two breaks exist in the surface tension vs. concentration curve. The first break at 0.063 ± 0.006 mM FTMA/0.95 ± 0.08 mM DTAB is slightly below the CAC of reduced FTMA in the absence of DTAB. That is, the presence of DTAB decreases the CAC of reduced FTMA from 0.071 ± 0.003 mM (no DTAB) to 0.063 ± 0.006 mM FTMA, thus indicating that reduced FTMA forms mixed micelles with DTAB in bulk solution.

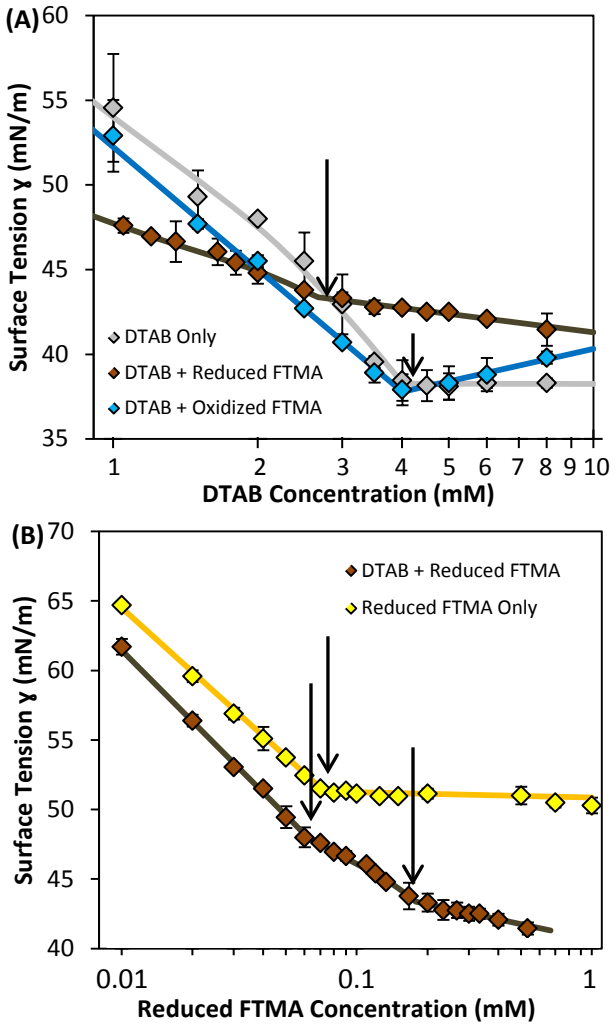

Figure 3.3 Surface tensions of FTMA and DTAB mixtures
(A) Surface tensions of aqueous solutions (100 mM Li_2SO_4) of DTAB, a 15:1 ratio of DTAB to reduced FTMA, and a 15:1 ratio of DTAB to oxidized FTMA. **(B)** Surface tensions of aqueous solutions (100 mM Li_2SO_4) of reduced FTAM, and a 15:1 ratio of reduced FTMA to DTAB. The error bars indicate the standard deviation between at least 3 independent measurements. The measured breaks in the surface tension vs. concentration curves are indicated by arrows and listed in Table 3.1.

To gain further insight into the second break in surface tension mentioned above and to test the hypothesis that it corresponds to a change in micelle composition, we performed static light scattering measurements on the mixed surfactant system. The light scattering (Fig. 3.4) was performed at a constant detector angle of $\theta = 90°$ with a 532 nm laser. Since the radii of the micelles are less than 10 nm,[32] we neglected the angular dependence of the Zimm equation, as described in Eq. 3.5. Fig. 3.4A shows $KC/\Delta R_{90°}$ plotted as a function of overall surfactant concentration in solution, where K is the optical constant defined in Eq. 3.6, C is the surfactant concentration, and $\Delta R_{90°}$ is the Rayleigh ratio calculated using Eq. 3.7. Four regimes of behavior are apparent in Fig. 3.4A: First, at very low concentrations, $KC/\Delta R_{90°}$ is constant as a function of concentration. This regime corresponds to a surfactant mixture below its CAC and its upper concentration limit (~0.9 mM DTAB) matches the CAC measured for the mixture of reduced FTMA and DTAB using surface tension (Fig. 3.3B; 0.95 ± 0.08 mM DTAB). Second, at concentrations above the CAC, we observe a linear increase in $KC/\Delta R_{90°}$ with concentration. Third, we observe a second linear regime with a distinct slope beginning at 2.5 mM DTAB, which corresponds to the concentration at which the second break in the γ vs log C curve in Fig. 3.3B was observed. Fourth, at the highest surfactant concentrations, the relationship between $KC/\Delta R_{90°}$ and concentration becomes non-linear as higher-order interaction terms make significant contributions to the light scattering.

In Fig. 3.4B, we replot the scattering data for the two linear regimes as $K(C-C_{cac})/\Delta R_{90°}$ versus $C-C_{cac}$ in order to determine the molecular weight of the aggregates, as described in Eq. 3.8. We sought to demonstrate a change in micelle size with concentration, consistent with a change in micelle composition. Between 0.95 and 2.5 mM DTAB, the intercept indicates micelles with an effective mass of 19.7 kDa, which corresponds to 41-64 surfactant molecules

per micelle (depending on the composition of FTMA and DTAB in the micelle). Above 2.5 mM DTAB, we find that the micelles have shrunk to 10.2 kDa, corresponding 22-33 molecules per micelle (depending on the composition of FTMA and DTAB in the micelle). As reduced FTMA has a lower CAC than DTAB, we infer that the micelles formed at lower concentrations in the mixed system are predominantly composed of reduced FTMA. Previous dynamic light scattering studies have found that reduced FTMA (without DTAB) forms micelles with a hydrodynamic diameter of 5.7 nm[32] and that DTAB (without reduced FTMA) forms micelles with a hydrodynamic diameter of 4.4 nm.[46] Consistent with our measurements of aggregation numbers, the larger micelles measured at low concentrations in the mixed system are likely rich in reduced FTMA whereas the smaller micelles at higher concentrations are rich in DTAB. More broadly, the static light scattering results support our conclusion that reduced FTMA and DTAB form mixed micelles with compositions that change with the overall surfactant concentration in solution. We also note, however, that light scattering measurements alone cannot eliminate the possibility that reduced FTMA and DTAB form two separate coexisting micelle populations and that the breaks observed in the static light scattering plots corresponding to the CAC of each surfactant. As discussed earlier, however, the addition of reduced FTMA leads to the disappearance of the break in the γ vs. log C curve at 4 mM DTAB. If DTAB and reduced FTMA were forming coexisting micelles, we would not expect the concentration at which DTAB forms micelles to be impacted by the presence of reduced FTMA. Overall, our results provide strong support for the conclusion that reduced FTMA and DTAB form mixed micelles.

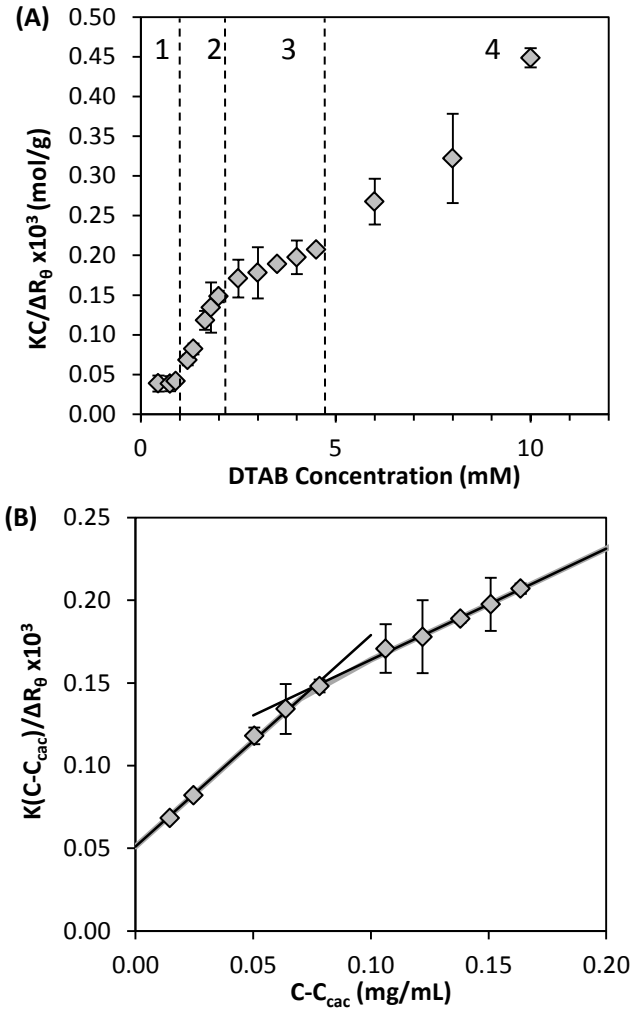

Figure 3.4 Static light scattering of mixtures of reduced FTMA and DTAB
Static light scattering from an aqueous solution (100 mM Li_2SO_4) containing a 15:1 ratio of DTAB to reduced FTMA. **(A)** KC/ ΔR_{90} over the entire concentration range measured. The vertical dashed lines and numbered regions are discussed in the text. **(B)** Debye plot for micelles of DTAB and reduced FTMA. The error bars represent the standard deviation calculated from at least three independent measurements.

In summary, our experimental measurements obtained using DTAB, FTMA, DMFA and their mixtures support the hypothesis that redox-induced changes in the molecular architecture of FTMA can be used to manipulate the extent to which FTMA forms mixed micelles in binary surfactant systems in bulk solution. For example, upon oxidation of FTMA, the surfactant transforms from having a conventional surfactant architecture to a bolaform architecture, which

in turn renders oxidized FTMA unable to mix with reduced FTMA or DTAB in micelles formed in bulk solution. In contrast, reduced DMFA and oxidized DMFA, both of which possess conventional architectures, are able to mix with each other in micelles in bulk solution. Similarly, reduced FTMA and DTAB are also able to form mixed micelles in bulk solution.

3.2.2 Mixing within Monolayers Formed at the Surface of Water

To address the mixing behavior of reduced and oxidized FTMA within monolayers at the air/water interface, we return to the surface tension measurements shown in Fig. 3.2A. Specifically, we compare the surface tensions measured for aqueous solutions containing reduced FTMA alone with those containing the 1:1 mixture of reduced and oxidized FTMA. Inspection of Fig. 3.2A reveals the addition of the oxidized FTMA to have no measurable effect on the surface tension of the reduced FTMA solution. In particular, at concentrations above ~0.2 mM FTMA, where oxidized FTMA measurably lowers the surface tension of water in the absence of reduced FTMA, the lack of difference between surface tensions of solutions of reduced FTMA or mixtures of reduced and oxidized FTMA suggests that oxidized FTMA does not co-adsorb with reduced FTMA at the surface of water. To provide additional support for this conclusion, we performed experiments using aqueous solutions containing 0.06 mM reduced FTMA (below its CAC) and 0.5 mM oxidized FTMA (which, alone, causes a surface tension of 64 ± 1 mN/m), and measured the mixture surface tension to be 52.3 ± 0.4 mN/m. Despite the 0.5 mM oxidized FTMA having a significant effect on the surface tension of aqueous solutions in the absence of reduced FTMA, the surface tension of the mixture was indistinguishable from that of 0.06 mM reduced FTMA without oxidized FTMA (γ = 52.5 ± 0.1). The lack of effect of oxidized FTMA on the surface tension of solutions containing reduced FTMA supports our

conclusion that oxidized FTMA is not mixed substantially with reduced FTMA at the surfaces of these solutions. We analyze further the results in Fig. 3.2A in the Discussion.

Next, we consider the behavior of reduced and oxidized DMFA within monolayers at the air/water interface by using the surface tension measurements of aqueous solutions containing reduced DMFA, oxidized DMFA, and a 1:1 mixture of reduced and oxidized DMFA (Fig. 3.2B). Below the CAC, we observed the solution containing the mixture to possess a surface tension that is lower than solutions of either reduced or oxidized DMFA alone. In addition, by using the Gibb's adsorption equation at a bulk concentration of 1 mM of surfactant (below any CACs), we calculate the surface area per molecule to be 69 ± 2, 70 ± 2, and 56 ± 4 $Å^2$/molecule for reduced DMFA, oxidized DMFA, and the mixture, respectively. Both results above lead us to conclude that oxidized and reduced DMFA co-adsorb within monolayers formed on the surface of water. Additional comments regarding the surface area occupied by molecules of DMFA can be found in the Supporting Information.

Insights into the mixing of reduced FTMA and DTAB at the surface of water can be obtained from the measurements in Fig. 3.3, which show the surface tensions of solutions containing DTAB alone and DTAB mixed with reduced FTMA (in a 15:1 ratio in the mixture). Below concentrations at which aggregation occurs in bulk solution (1 mM DTAB and 0.06 mM reduced FTMA), the surface tension of the mixture is lower than that measured for either component individually. This suggests that, at these low concentrations, both surfactants in the mixture co-adsorb at the air/water interface and lower the surface tension below that measured for each individually. At higher concentrations, DTAB alone has a limiting surface tension of 38 mN/m whereas reduced FTMA has a limiting surface tension of 51 mN/m. Although the surface tension of the mixture is measured to lie between these values, an interpretation of this

observation is not simple because reduced FTMA and DTAB form mixed micelles in bulk solution at these high concentrations (the mixed assemblies impact the chemical potential of the surfactants in bulk solution, and thus their adsorption at interfaces).

Next we consider the mixing behavior of DTAB and oxidized FTMA at the air/water interface (Fig. 3.3A). The addition of oxidized FTMA (in a 15:1 DTAB: oxidized FTMA ratio) has two noteworthy effects on the surface tension of aqueous solutions containing DTAB. First, below the CAC of DTAB in the bulk solution, the surface tension of the mixture decreases by up to 3 mN/m (as compared to the surface tension of DTAB alone). We attribute the decrease in surface tension below the CAC to co-adsorption of oxidized FTMA along within DTAB within the monolayer formed at the surface of the water. Using Eq. 3.2 and Eq. 3.4 at a bulk concentration of 3 mM (at a concentration below the CAC), we evaluated the surface excess concentration of surfactants within the monolayers to be 29 ± 4 and 40 ± 2 $Å^2$/molecule for DTAB and the mixture (with respect to all surfactant molecules on the surface), respectively. Interestingly, the results above suggest that addition of oxidized FTMA results in a decrease in surface concentration of surfactant along with a decrease in surface tension. This result reflects the relatively large area occupied by oxidized FTMA molecules at the air-water interface (see below). More importantly, these results suggest that oxidized FTMA co-adsorbs at the air/water interface in the presence of DTAB, despite their absence of mixing in micelles in bulk solution.

A second interesting observation regarding mixtures of DTAB and oxidized FTMA is made by inspection of Fig. 3.3A at concentrations greater than the CAC of DTAB (4.0 mM). Specifically, we measured the surface tension to increase with addition of DTAB and oxidized FTMA, which suggests a change in the composition of surfactant within the monolayer formed at the surface of water. Because oxidized FTMA and DTAB do not mix within micelles formed

in bulk solution, we interpret the result to indicate that addition of DTAB and oxidized FTMA to solution at concentrations greater than the CAC of DTAB results in an increase in the chemical potential of oxidized FTMA in solution whereas the chemical potential of DTAB remains largely fixed at the value corresponding to the CAC. The increase in chemical potential of oxidized FTMA in solution results in the competitive displacement of DTAB from the air/water interface, which in turn leads to the change in surface tension.

In summary, the results above, obtained with FTMA, DMFA, DTAB and their mixtures lead us to conclude that within monolayers formed at the surface of water (i) oxidized and reduced FTMA do not co-adsorb, (ii) oxidized and reduced DMFA do co-adsorb, (iii) reduced FTMA and DTAB do co-adsorb, and (iv) oxidized FTMA and DTAB do co-adsorb. Here we note that this behavior is similar to that of the surfactants in bulk solution for each mixture investigated except for the mixture of oxidized FTMA and DTAB. We return to these observations in the Discussion.

3.2.3 Assemblies Formed at Hydrophobic Solid Surfaces

To gain insight into the mixing/demixing of interfacial assemblies of FTMA and DTAB formed at hydrophobic solid surfaces, we used both QCM-D and AFM. We performed QCM-D measurements using gold films functionalized with 1-dodecanethiol that were supported on a quartz crystal. In brief, our experimental protocol involved the sequential exposure of the hydrophobic surfaces to (i) aqueous 100 mM Li_2SO_4, (ii) 2 mM DTAB in 100 mM Li_2SO_4, and (iii) 2 mM DTAB and 0.1 mM of either reduced or oxidized FTMA in 100 mM Li_2SO_4 (Fig. 3.5). This experimental design allowed us to monitor dynamic changes in both the adsorbed mass as well as the viscous dissipation, the latter being a measure of the rigidity and thus morphology

of the adsorbed layer. We note that we measured the viscous dissipation to satisfy $\Delta D/\Delta f < 4x10^{-7}$ Hz^{-1} for all of our experiments, thus allowing us to estimate the mass of adsorbed surfactant using the Sauerbray equation (Eq. 3.9).

For 2 mM DTAB alone (with no FTMA), we measured surfactant adsorption to cause a ~3 Hz change in frequency (over 2-3 mins), corresponding to 54 ± 7 ng/cm^2 DTAB or 1.07 ± 0.07 molecules/nm^2.[47] This surface coverage is similar to that concluded from in our surface tension measurements (Fig. 3.3A), where we calculate, using the Gibbs adsorption isotherm (Eq. 3.2), approximately 50 ng/cm^2 of DTAB to adsorb at the air/water interface from a 2 mM solution of DTAB. The measured increase in viscous dissipation (0.19 ± 0.05) x10^{-6} was similar to that reported previously for surfactants adsorbed to non-polar surfaces.[48-50] The subsequent introduction of a mixture of 2 mM DTAB and 0.1 mM reduced FTMA (Fig. 3.5A), which is above the CAC of the mixture, caused a further increase in frequency of ~10 Hz, signifying a threefold increase in mass of adsorbed surfactant (166 ± 14 ng/cm^2). Interestingly, introduction of the surfactant mixture was accompanied by a transient spike in both the frequency and viscous dissipation (~over 5 minutes). We speculate that this spike is caused by the adsorption of micelles containing DTAB and reduced FTMA, which then undergo a rearrangement on the surface. This response is analogous to but less pronounced than spikes in frequency and dissipation that have been seen in past studies of the adsorption of vesicles and their subsequent rearrangement into a planar bilayer (~1 Hz here vs. ~30 Hz for liposomes).[51] The total mass of the DTAB/FTMA mixture adsorbed to the alkanethiol monolayer is larger than the limiting excess concentration of reduced FTMA (107 ng/cm^2) or DTAB (130 ng/cm^2) calculated from surface tension measurements at the air/water interface, consistent with co-adsorption to the surface.

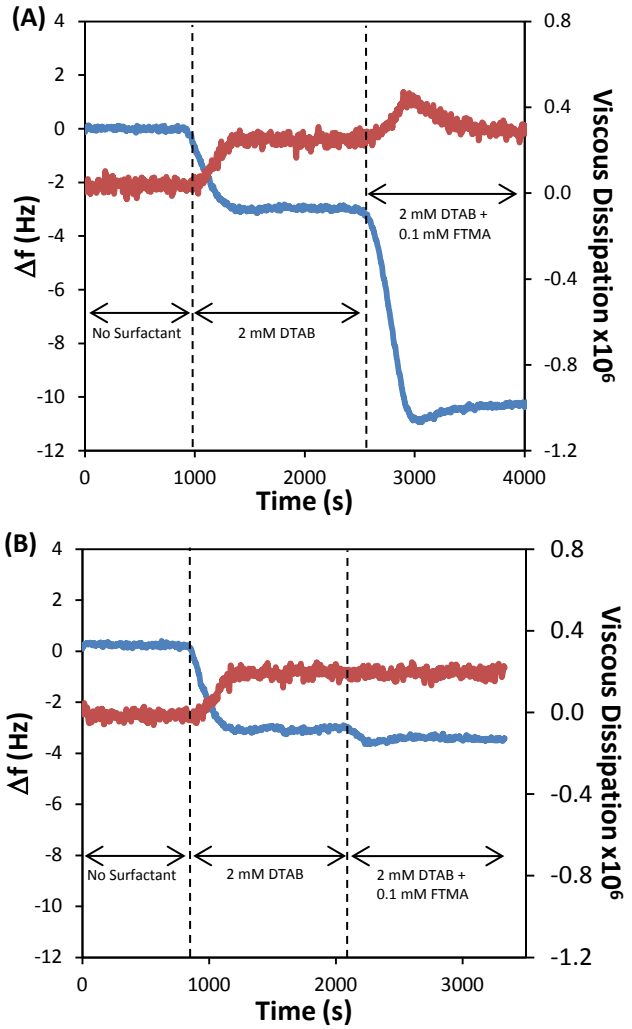

(C)

Surfactant Concentration	Δm (ng/cm^2)	ΔD x10^6
2 mM DTAB only	54 ± 7	0.19 ± 0.05
2 mM DTAB with 0.1 mM reduced FTMA	166 ± 14	0.29 ± 0.05
2 mM DTAB with 0.1 mM oxidized FTMA	65 ± 12	0.21 ± 0.06

Figure 3.5: QCM of mixtures of DTAB and FTMA at hydrophobic surfaces
Quartz crystal microbalance results obtained using a 1-dodecanethiol-treated gold-coated crystal exposed sequentially to (i) aqueous 100 mM Li_2SO_4, 2 mM DTAB in 100 mM Li_2SO_4, and then 2 mM DTAB and 0.1 mM of either **(A)** reduced FTMA or **(B)** oxidized FTMA in 100 mM Li_2SO_4. The data plotted here is a 7-point moving average to minimize noise. **(C)** Table of averaged adsorbed mass and viscous dissipation, calculated from two independent experiments for reduced and oxidized FTMA.

In contrast to the observations above using reduced FTMA, when a surface equilibrated against DTAB was exposed to a mixture of 2 mM DTAB and 0.1 mM oxidized FTMA (Fig. 3.5B), there was no statistically significant increase in the mass of adsorbed surfactant (54 ± 7 ng/cm^2 versus 65 ± 12 ng/cm^2). We also note that the mass of surfactant adsorbed to the surface from the solution containing the mixture of oxidized FTMA and DTAB was less than the mass of adsorbed surfactant when using oxidized FTMA alone (106 ± 7 ng/cm^2).[33] This result suggests that the presence of DTAB on the surface inhibits the adsorption of oxidized FTMA at the hydrophobic solid surface, leading to the conclusion that oxidized FTMA and DTAB are unable to mix at the surface and that DTAB is more strongly bound to the surface than oxidized FTMA. Also, in contrast to the systems containing reduced FTMA, no significant change in viscous dissipation was observed (0.19 ± 0.05 vs 0.21 ± 0.06) between DTAB alone and the mixture of DTAB and oxidized FTMA (respectively). Furthermore, no temporary spike in frequency and dissipation was observed following the introduction of oxidized FTMA. These results suggest that the presence of oxidized FTMA does not significantly alter the interfacial hemimicelles that are known to be formed by DTAB at the hydrophobic solid surface.[52]

In order to gain additional insight into the interfacial morphologies of the assemblies formed by DTAB and FTMA at hydrophobic solid surfaces, we imaged DTAB mixed with FTMA in both redox states on HOPG surfaces by using AFM (Fig. 3.6). As noted above, HOPG was used for the AFM measurements because alkanethiol monolayers adsorbed to polycrystalline gold films are too rough to permit imaging of surfactant assemblies. In order to confirm that the features presented in Fig. 3.6 were not artifacts of the scanning process, we performed extensive control experiments. Specifically, we rotated the scanned area, changed the scan rate, and compared the trace and retrace images. The trace and retrace images are included

in the Supporting Information Fig. 3.8. Fig. 3.6A shows the presence of a striped surfactant assembly on the surface equilibrated against DTAB and reduced FTMA. The spacing of the stripes was 6.5 ± 0.1 nm, calculated as a numerical average from the real-space images and confirmed by Fourier transforms of the real-space images (see the insets in Fig. 3.6). We interpret these results in light of our previous paper,[33] which reported striped aggregates to be formed by reduced FTMA (in the absence of DTAB) with a spacing of 5.4 ± 0.1 nm and aggregates formed by DTAB (in the absence of FTMA) to have a spacing of 7.2 ± 0.1 nm. Striped patterns observed by AFM imaging of adsorbed alkyltrimethylammonium surfactants on HOPG have been assigned in past studies to correspond to hemicylindrical micelles (or cylindrical micelles when adsorbed to mica).[52,53-55] Our AFM results suggest that mixtures of DTAB and reduced FTMA form mixed interfacial hemicylindrical hemimicelles, similar to DTAB and reduced FTMA alone, except that the mixed micelles exhibit a periodicity intermediate to that measured for DTAB and reduced FTMA alone.

Oxidized FTMA and DTAB also form a striped interfacial assembly on HOPG with a spacing of 5.6 ± 0.1 nm (Fig. 3.6B). The presence of oxidized FTMA, however, has no statistically significant effect on the spacing of the striped aggregates formed by DTAB on HOPG in the absence of FTMA (5.4 ± 0.1 nm). Based on past interfacial studies of bolaforms[56,57] and past AFM images of oxidized FTMA on HOPG,[33] oxidized FTMA is proposed to adopt a looped configuration within a flat monolayer rather than hemicylindrical hemimicelles when adsorbed to hydrophobic interfaces. We interpret the AFM image of DTAB and oxidized FTMA to be consistent with adsorbed interfacial hemicylindrical hemimicelles of DTAB with which oxidized FTMA does not mix. When combined, the QCM and AFM results described above suggest that, similar to micelles formed in bulk solution, DTAB is able to form

mixed interfacial hemimicellar assemblies at hydrophobic solid surfaces with reduced FTMA but not with oxidized FTMA.

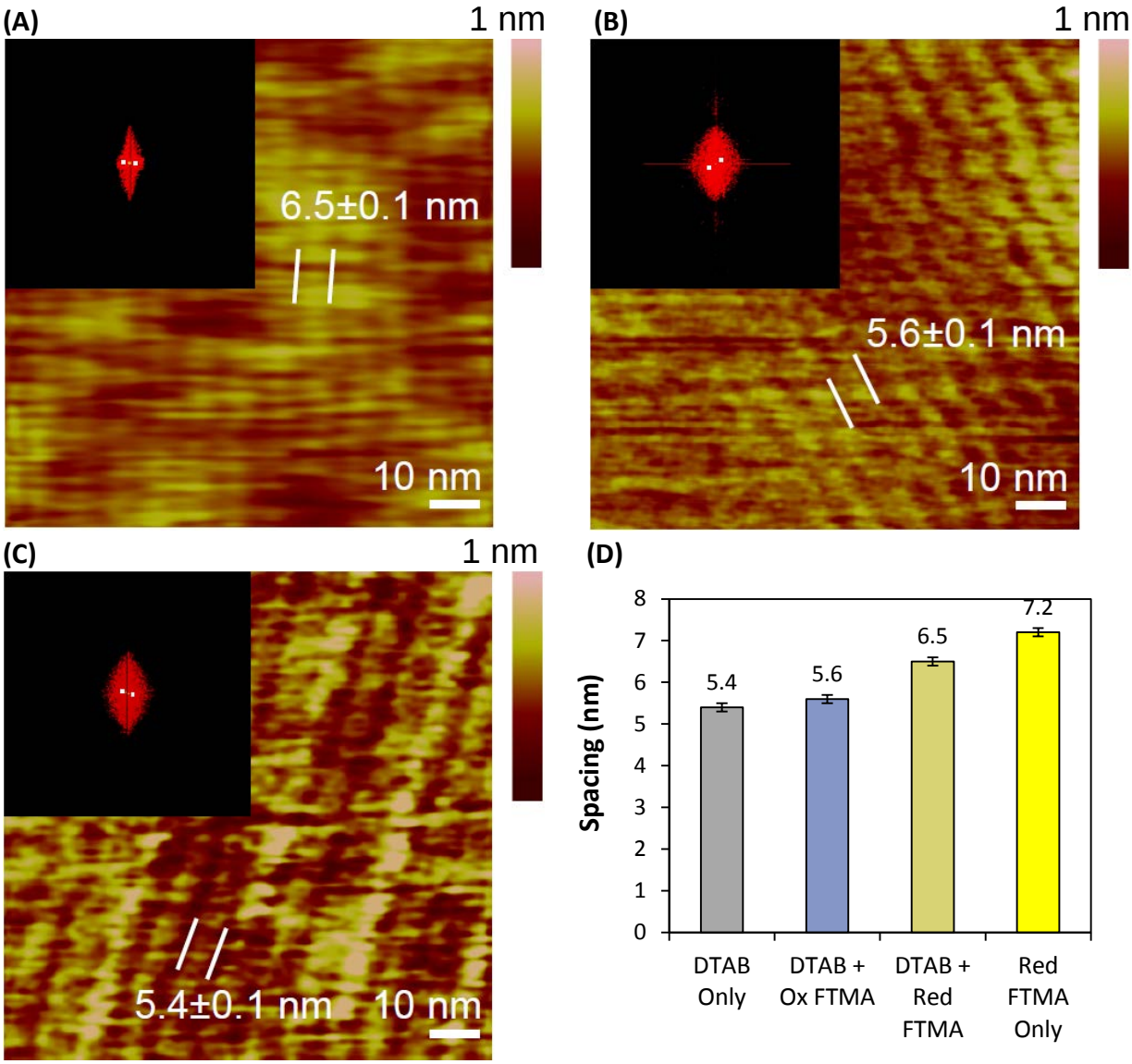

Figure 3.6 AFM of DTAB and FTMA assemblies on HOPG
Atomic force microscopy of HOPG in contact with aqueous solutions (100 mM Li_2SO_4) containing 2 mM DTAB and either **(A)** 0.1 mM reduced FTMA or **(B)** 0.1 mM oxidized FTMA. The insets show the Fourier transform of each image. **(C)** AFM image of HOPG in contact with an aqueous solution (100 mM Li_2SO_4) of 20 mM DTAB (without FTMA). **(D)** Spacing between the stripes shown in the micrographs in (A) and (B) compared to those seen for DTAB and reduced FTMA alone. The error bars show the standard deviation of the stripe spacing measured at 300 randomly selected locations in the image.

3.4 Discussion

The results presented in this paper lead to two broad insights into redox-triggered changes in the extent of mixing of binary systems containing ferrocenyl surfactants. First, the measurements test the hypothesis that redox-driven changes in extent of mixing can be understood in terms of redox-driven changes in molecular architecture, which in turn can be manipulated via the position of the ferrocene group within the redox surfactant. Second, the measurements address the question of how the mixing/demixing of surfactant mixtures differs between assemblies formed in bulk solution, at hydrophobic solid surfaces, and at the air/water interface.

We interpret our measurements to support the hypothesis that redox-triggered changes in the molecular architectures of surfactants can be used to control the extent of mixing in molecular assemblies formed in bulk solution, as summarized in Fig. 3.7. We noted that, as discussed above, within micelles formed by reduced FTMA in bulk solution, reduced FTMA behaves as a surfactant with a conventional architecture (the ferrocene is part of the hydrophobic tail). Consistent with previously described mixing rules for conventional and bolaform surfactants reported by Zana et al,[16] reduced FTMA does not mix with oxidized FTMA within micelles in bulk solution. For DMFA, in contrast, which does not undergo a change in molecular architecture (from conventional to bolaform) upon oxidation, the reduced and oxidized states of DMFA are able to form mixed micelles. We emphasize that the results obtained with DMFA provide key evidence that it is the transformation of FTMA from conventional to bolaform architecture that leads to reduced and oxidized FTMA being unable to mix with each other within assemblies formed in bulk solution.

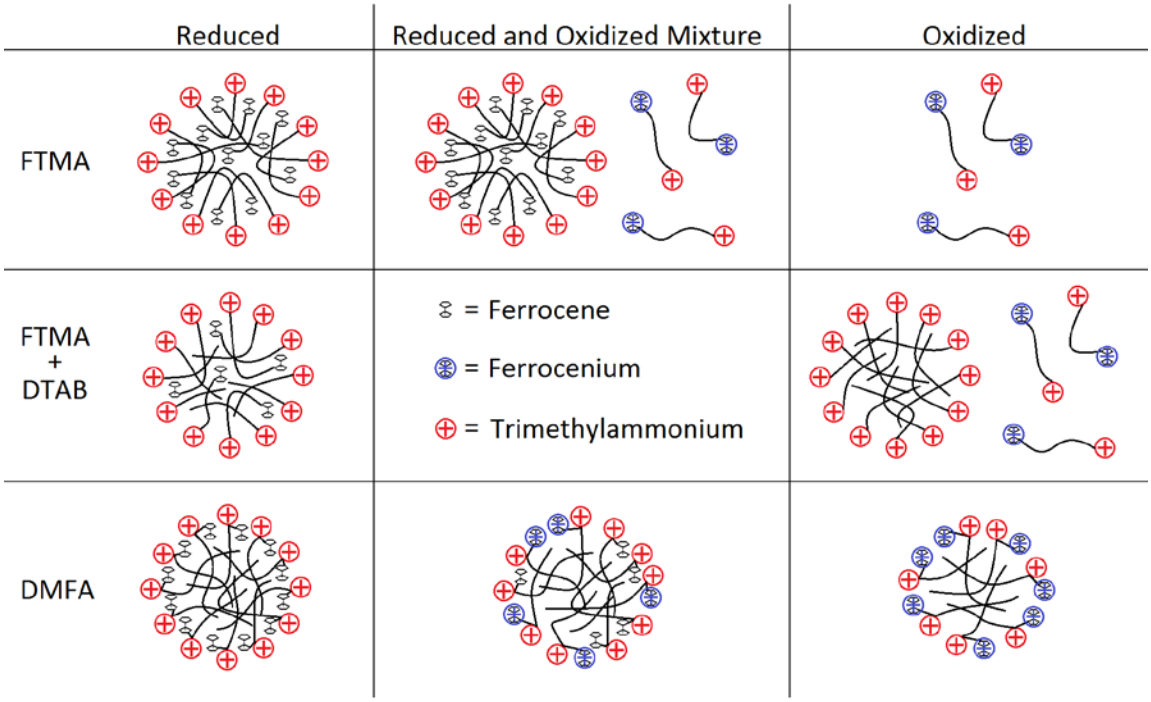

Figure 3.7 Schematic of mixed micellization between FTMA, DTAB, and DMFA
Schematic illustration of micellization in bulk solution of mixtures of (top) reduced and oxidized FTMA, (middle) FTMA and DTAB, and (bottom) reduced and oxidized DMFA **(bottom)**. Reduced FTMA alone forms micelles. Oxidized FTMA, a bolaform, is unable to mix with reduced FTMA micelles. Reduced FTMA is able to form mixed micelles with DTAB, but oxidized FTMA does not form mixed micelles with DTAB. Reduced and oxidized DMFA can each form micelles and they form mixed micelles.

Our results suggest that the above-described mixing rules for ferrocenyl surfactant-containing mixtures in bulk solution apply also to hemimicelles formed at hydrophobic solid surfaces. This result is significant in the context of a recent electrochemical study[33] which led to the proposal that oxidized FTMA was unable to mix with interfacial assemblies of reduced FTMA or DTAB at hydrophobic electrodes. This absence of mixing was inferred from the observation that assemblies of FTMA that formed on hydrophobized electrodes allowed oxidation of FTMA but inhibited reduction of oxidized FTMA (i.e., current rectification). The study led to the hypothesis that current rectification arises from the presence of interfacial

hemimicelles of reduced FTMA that block oxidized FTMA in bulk solution from accessing the electrode. The results hinted that charge transfer at interfaces can be controlled by the ability or inability of a redox mediator to self-assemble (and mix) into interfacial mixed hemimicelles. The study also found that the addition of DTAB further enhanced current rectification. The results presented in this paper provide supporting evidence that DTAB and reduced FTMA indeed can form mixed interfacial hemimicelles at hydrophobic surfaces but that DTAB and oxidized FTMA do not. More broadly, the conclusion that the extent of mixing of ferrocenyl and conventional surfactants within micellar assemblies is dependent on the molecular architectures of the ferrocenyl surfactants suggests general principles for the design of interfacial assemblies that can reorganize in response to a redox-trigger to modulate charge transfer in useful ways.

In contrast to the mixing behaviors observed in micellar and hemimicellar assemblies formed in bulk solution and at hydrophobic solid surfaces, respectively, the results reported in this paper suggest that different mixing rules may control co-adsorption of the surfactants at the air/water interface. As detailed below, we hypothesize that the different mixing behaviors measured within micelles and within monolayers formed at the surface of water reflect the fact that the surfactants adopt distinct conformations in their different environments. First, we address the behavior of the monolayers containing reduced FTMA. Specifically, we interpret our experimental measurements to conclude that reduced FTMA does not co-adsorb with oxidized FTMA but does co-adsorb with DTAB. While these two observations would appear, at first inspection, to be consistent with the effects of molecular architecture on mixing of surfactants, measurements of the area per molecule occupied by reduced FTMA at the surface of water hint that the situation is more complicated. By using the Gibbs adsorption equation (Eq. 3.2) for reduced FTMA, we calculate (A_{min}) to be 62 ± 2 $Å^2$/molecule. This value of A_{min} is

significantly greater than that reported for conventional surfactants (e.g., sodium dodecyl sulfate (SDS)[58] and C_{16}TAB[59] form monolayers with limiting molecular surface areas of 25-35 $Å^2$/molecule in the presence of swamping concentrations of electrolyte). These measurements are also consistent with prior reports[34,35] that have concluded that FTMA in both redox states adopts a looped configuration within monolayers formed at the air/water interface. If both oxidized and reduced FTMA adopt a looped configuration at the surface of water, the absence of co-adsorption of mixtures of oxidized and reduced FTMA cannot be attributed to a difference in their configurations. Similarly, if DTAB and reduced FTMA adopt distinct configurations within mixed monolayers (as they are thought to do when adsorbed as single components), their co-adsorption at the air/water interface cannot be understood on the basis of similar configurations. We caution, however, that the configurations adopted by FTMA may depend on the environment of the surfactant, and that it is possible that reduced FTMA changes its configuration at the surface of water in the presence of DTAB and/or oxidized FTMA. For example, for mixtures of reduced FTMA and DTAB, our measurements reveal the presence of the two species on the interface. Although the limiting area per molecule within the mixed monolayer at the surface of water (55 ± 5 $Å^2$/molecule) is less than the limiting area per molecule for reduced FTMA alone (62 ± 2 $Å^2$/molecule), it is possible that the decrease in area per molecule reflects the incorporation of DTAB into the interface via a change in conformation of FTMA. In short, our measurements of coadsorption of mixtures of reduced FTMA and DTAB may reflect FTMA adopting an extended (non-looped) conformation within the mixed monolayer. However, it is difficult to imagine oxidized FTMA, which also coadsorbs with DTAB, to adopt an extended conformation at the surface of water given the ionic nature of the ferrocenium cation. Overall,

we conclude that the mixing rules that apply to micelles and hemimicelles (as detailed above) do not extend in an obvious manner to monolayers formed at the surface of water.

3.5 Conclusion

Overall, the key findings reported in this paper are twofold. First, by using redox-active surfactants containing ferrocene, we show that redox-driven changes in molecular architecture can be used to control the mixing/demixing of surfactants within molecular assemblies. Second, we demonstrate that the extent of mixing/demixing of the ferrocenyl surfactants differs between assemblies formed in bulk solution, at hydrophobic solid surfaces, and at the air/water interface.

The above-stated conclusions are supported by experiments testing the hypothesis that redox-driven changes in molecular architecture can be manipulated via the position of the ferrocene group within a redox surfactant, which in turn impacts the mixing/demixing of the surfactants in assemblies. Specifically, we report measurements of the redox-dependent mixing/demixing of cationic surfactants with a ferrocene group located either at the surfactant terminus (FTMA) or adjacent to the head group (DMFA).[22-25] By comparing FTMA to DMFA, we conclude that the absence of mixed micelles and hemimicelles formed from oxidized and reduced FTMA stems not from increased electrostatic repulsion associated with the increase in charge upon oxidation but from its change in molecular architecture from a conventional to a bolaform surfactant. Past studies have reported that conventional and bolaform surfactants with specific chain lengths do not mix within micelles formed bulk solution.[16,25] Our results go beyond these past studies by demonstrating that redox-induced changes in surfactant architecture (from conventional to bolaform) can be used to manipulate the extent of mixing within assemblies. In addition, we find similar mixing rules to describe micelles in bulk solution and

hemimicelles at hydrophobic surfaces. The mixing behavior within monolayers formed at the surface of water, however, was found to be distinct, potentially reflecting differences in conformations/chain packing in the distinct assemblies. Additional studies are needed to fully elucidate the thermodynamics of the mixed assemblies formed by ferrocenyl surfactants (such as their composition, and entropy and enthalpy of mixing).[60]

We conclude by commenting that the insights obtained from this study have the potential to aid in the future design of interfacial assemblies of surfactant that can be used to control interfacial charge transfer.[33,36] In addition to the mixtures of surfactants presented here, we envision several other scenarios in which differences in molecular architectures of surfactants might be leveraged to control their organization at interfaces. On the basis of the results presented in this paper with hemimicellar assemblies, we predict that addition of a redox-inactive bolaform surfactant to a solution of oxidized FTMA will allow reduction of oxidized FTMA but not oxidation of reduced FTMA at hydrophobic electrodes. Alternatively, we predict that an oxidized ferrocenyl surfactant with a hydrocarbon chain containing approximately 19 methylene groups will mix with DTAB assemblies adsorbed at an electrode, thus allowing the reduction of the oxidized ferrocenyl surfactant but not oxidation of the reduced surfactant. In future studies we will report on these and other scenarios by which the demixing of conventional and bolaform surfactants can be exploited to manipulate current rectification.

3.6 Acknowledgements

This work was primarily funded by the National Science Foundation through grant CBET- 1263970. Partial support is also acknowledged by the ARO (through W911NF-14-1-

0140 and W911NF-15-1-0568). The authors acknowledge the use of instrumentation supported by the Wisconsin Materials Research Science and Engineering Center (DMR-1121288).

3.7 References

‡ Portions of this chapter have been previously published as: T.J. Smith, C. Wang, N.L. Abbott; Redox-Triggered Mixing and Demixing of Surfactants within Assemblies Formed in Solution and at Surfaces. *J. Colloid Interface Sci.* **2017**, 502, 122–133. Reprinted with permission. Copyright (2017) Elsevier.

1. K. L. Herrington, E. W. Kaler, D. D. Miller, J. A. Zasadzinski, S. Chiruvolu, *J. Phys. Chem.* **1993**, 97 (51), 13792–13802.

2. A. Shiloach, D. Blankschtein, *Langmuir* **1998**, 14 (7), 1618–1636.

3. R. Zana, H. Levy, D. Danino, Y. Talmon, K. Kwetkat, *Langmuir* **1997**, 13 (3), 402–408.

4. L. Jiang, M. Deng, Y. Wang, D. Liang, Y. Yan, J. Huang, *J. Phys. Chem. B* **2009**, 113 (21), 7498–7504.

5. A. A. McLachlan, D. G. Marangoni, *J. Colloid Interface Sci.* **2006**, 295 (1), 243-248.

6. G. J. T. Tiddy, *Phys. Rep.* **1980**, 57 (1), 1–46.

7. X. Mulet, B. J. Boyd, C. J. Drummond, *J. Colloid Interface Sci.* **2013**, 393, 1–20.

8. D. P. Acharya, H. Kunieda, *Adv. Colloid Interface Sci.* **2002**, 123, 401–413.

9. S. R. Raghavan, G. Fritz, E. W. Kaler, *Langmuir* **2002**, 18, 3797–3803.

10. V. Croce, T. Cosgrove, C. A. Dreiss, G. Maitland, T. Hughes, G. Karlsson, *Langmuir* **2004**, 20 (19), 7984–7990.

11. J. F. Scamehorn, An Overview of Phenomena Involving Surfactant Mixtures. In *Phenomena in Mixed Surfactant Systems*; ACS Symposium Series; American Chemical Society: Washington, DC, **1986**; Vol. *311*, pp 1−27.

12. Y. C. Yu, T. Pakalns, Y. Dori, J. B. McCarthy, M. Tirrell, G. B. Fields, *Solid Phase Pept. Synth.* **1997**, 289, 571−587.

13. P. Mukerjee, A. Y. S. Yang, *J. Phys. Chem.* **1976**, 80 (12), 1388–1390.

14. P. Barthélémy, V. Tomao, J. Selb, Y. Chaudier, B. Pucci, *Langmuir* **2002**, 18, 2557–2563.

15. M. B. Ghoulam, N. Moatadid, A. Graciaa, *J. Colloid Interface Sci.* **1998**, 200, 74–80.

16. R. Zana, Y. Muto, K. Esumi, K. Meguro, *J. Colloid Interface Sci.* **1988**, 123, (2), 502–511.

17. R. Zana, Mixed Micelles with Bolaform Surfactants. In *Mixed Surfactant Systems*, Proceedings of the American Chemical Society Division of Colloid and Surface Chemistry at the 65th Colloid and Surface Science Symposium, Norman, Oklahoma, June 17-19, 1991 ; Paul M. Holland, Donn N. Rubingh, Eds.; American Chemical Society: Washington, DC., **1992;** 501, pp. 292–300.

18. C. Rosslee, N. L. Abbott, *Curr. Opin. Colloid Interface Sci.* **2000**, 5, 81–87.

19. P. Brown, C. P. Butts, J. Eastoe, J., *Soft Matter*, **2013**, 9, 2365-2374.

20. X. Liu, N. L. Abbott, N.L., *J. Colloid Interface Sci.* **2009**, 339 (1), 1-18.

21. B. S. Gallardo, V. K. Gupta, F. D. Eagerton, L. I. Jong, V. S. Craig, R. R. Shah, N. L. Abbott, *Science* **1999**, 283, 57-60.

22. B. S. Gallardo, M. J. Hwa, N. L. Abbott, *Langmuir*, **1995**, 11, 4209–4212.

23. K. Tajima, T. Huxur, Y. Imai, I. Motoyama, A. Nakamura, M. Koshinuma, *Colloids Surf., A* **1995**, 94, 243–251.

24. N. Aydogan, C. A. Rosslee, N. L. Abbott, *Colloids Surf. A* **2002**, 201, 101–109.

25. T. Saji, K. Hoshino, S. Aoyagui, *J. Chem. Soc., Chem. Commun.* **1985**, 13, 865–866**.**

26. S. Yiv, K. M. Kale, J. Lang, R. Zana, *J. Phys. Chem.* **1976**, 80 (24), 2651–2655.

27. S. Yiv, R. Zana, *J. Colloid Interface Sci.* **1980**, 77 (2), 449–455.

28. R. Zana, S. Yiv, K. M. Kale, *J. Colloid Interface Sci.* **1980**, 77 (2), 456–465.

29. G. Calvaruso, F. P. Cavasino, C. Sbriziolo, M. L. T. Liveri, *J. Colloid Interface Sci.* **1994**, 164 (1), 35–39.

30. N. L. Abbott, G. M. Whitesides, *Langmuir* **1994**, 10 (5), 1493–1497.

31. N. Aydogan, N. L. Abbott, *Langmuir* **2001**, 17 (19), 5703–5706.

32. X. Liu, M. D. Graham, N. L. Abbott, *Langmuir* **2007**, 23 (19), 9578–9585.

33. T. J. Smith, C. Wang, N. L. Abbott, *Langmuir* **2015**, 31 (39), 10638–10648.

34. B. S. Gallardo, K. L. Metcalfe, N. L. Abbott, *Langmuir* **1996**, 12, 4116–4124.

35. N. Aydogan, B. S. Gallardo, N. L. Abbott, *Langmuir* **1999**, 15, 722–730.

36. J. P. E. Muller, B. S. Aytar, Y. Kondo, D. M. Lynn, N. L. Abbott, *AIChe J.* **2014**, 40 (4), 1381–1392.

37. P. C. Hiemenz, R. Rajagopalan, *Principles of Colloid and Surface Chemistry*; 3rd Edition, Taylor & Francis Group: Boca Raton, FL, **1997**; p. 330.

38. G. L. Gaines, *J. Colloid Interface Sci.* **1977**, 62 (1), 191–192.

39. D. K. Chattoraj, K. S. Birdi, Adsorption and the Gibbs Surface Excess; Plenum Press: New York, NY, **1984**; p. 40.

40. J. Eastoe, *Graduate teaching books: surfactant chemistry*; Wuhan University Press: Wuhan, Hubei, China, **1991**, p.18.

41. W. H. Stomckmayer, *J. Chem. Phys.* **1950**, 18 (1), 58–61.

42. C. A. Gracia, S. Gómez-Barreiro, A. González-Pérez, J. Nimo, J. R. Rodríguez, *J. Colloid Interface Sci.* **2004**, 276, 408–413.

43. G. Sauerbrey, *Eur. Phys. J. A* **1959**, 155 (2), 206–222.

44. A. A. Ansari, M. Kamil, Kabir-ud-Din, *J. Dispersion Sci. Technol.* **2013**, 34, 722–730.

45. E. J. Acosta, A. Mesbah, T. Tsui, *J. Surfactants Deterg.* **2006**, 9, 367–376.

46. S. J. Candau, E. Hirsch, R. Zana, R., *J. Physique* **1984**, 45 (7), 1263–1270.

47. L. Mivehi, R. Bordes, K. Holmberg, *Langmuir***2011**, 27 (12), 7549–7557.

48. E. M. Song, D. W. Kim, J. C. Lim, *J. Ind. Eng. Chem.* **2015**, 28, 351–358.

49. R. Bordes, F. Höök, *Anal. Chem.* **2010**, 82, 9116–9121.

50. J. J. R. Stålgren, J. Eriksson, K. Boschkova, *J. Colloid Interface Sci.* **2002**, 253 (1), 190–195.

51. R. P. Richter, R. Bérat, A. R. Brisson, *Langmuir* **2006**, 22 (8), 3497–3505.

52. J. F. Liu, W. A. Ducker, *J. Phys. Chem. B* **1999**, 103 (40), 8558–8567.

53. W. A. Ducker, E. J. Wanless, *Langmuir* **1996**, 12, 5915–5920.

54. H. N. Patrick, G. G. Warr, S. Manne, I. A. Aksay, *Langmuir* **1999**, 15 (5), 1685–1692.

55. W. A. Ducker, E. J. Wanless, *Langmuir* **1999**, 12, 5915–5920.

56. N. Aydogan, N. L. Abbott, *J. Colloid Interface Sci.* **2001**, 242, 411–418.

57. F. M. Menger, S. Wrenn, *J. Phys. Chem.* **1974**, 78 (74), 1387–1390.

58. K. Ananda, O. P. Yadav, P.P. Singh, *Colloids Surf.* **1991**, 55, 345–358.

59. K. Szymczyk, B. Jańczuk, *Colloids Surf., A* **2007**, 293, 39–50.

60. C. M. Nguyen, J. F. Rathman, J. F. Scamehorn, *J. Colloid Interface Sci.* **1986**, 112 (2), 438–446.

3.8 Supporting Information

3.8.1 Derivation of the Gibbs Adsorption Equation for Binary Surfactant Mixtures

For a multi-component surfactant system, assuming the activity coefficient of each component to be unity, the Gibbs adsorption equation can be written (see Eq. 3.3):

$$-d\gamma = RT \sum_i \Gamma_i \, d \ln C_i \tag{3.3}$$

For the case of a binary mixture of cationic surfactants 1 and 2 with the counterion X^- immersed in an electrolyte solution containing the ions M^+ and Y^{2-}, Eq. 3.3 becomes:

$$-d\gamma = RT \left[\Gamma_1 \frac{dC_1}{C_1} + \Gamma_2 \frac{dC_2}{C_2} + \Gamma_{x-} \frac{dC_{x-}}{C_{x-}} + \Gamma_{M+} \frac{dC_{M+}}{C_{M+}} + \Gamma_{y2-} \frac{dC_{y2-}}{C_{y2-}} \right] \tag{3.10}$$

where Γ_i and C_i are the surface excess and bulk concentrations of each component, respectively. Since the concentration of M^+ and Y^{2-} is constant, the last two terms of Eq. 3.10 are zero. The condition of charge neutrality for the interface is:

$$\Gamma_1 + \Gamma_2 + \Gamma_{M+} = \Gamma_{x-} + 2\Gamma_{y2-} \tag{3.11}$$

For the case of a swamping electrolyte ($C_{electrolye} >> C_{surfactant}$), we would expect $\Gamma_{y2-} >> \Gamma_{x-}$, and therefore $\Gamma_1, \Gamma_2 >> \Gamma_{x-}$. Thus, Eq. 3.11 becomes:

$$-d\gamma = RT \left[\Gamma_1 \frac{dC_1}{C_1} + \Gamma_2 \frac{dC_2}{C_2} \right] \tag{3.12}$$

If the two surfactants are added to bulk solution at a constant ratio, the overall surface excess (Γ_{Total}) can be calculated as:

$$\Gamma_{Total} = \Gamma_1 + \Gamma_2 = -\frac{1}{kT}\frac{d\gamma}{d \ln C_1} \quad (3.4)$$

We used Eq. 3.4 to determine Γ_{Total} for binary surfactant mixtures in swamping electrolyte.

3.8.2 Configuration of DMFA at the Air/Water Interface

We calculated A_{min} using Eq. 2 (for single surfactant systems) and Eq. 4 for mixtures. First, we consider the case of reduced and oxidized DMFA mixtures (Fig. 2B) where both surfactants have a conventional molecular architecture. The corresponding limiting areas for reduced DMFA alone, oxidized DMFA alone, and the mixture are 69 ± 2, 53 ± 1, and 56 ± 4 $Å^2$/molecule, respectively. While the values of A_{min} are larger than those of conventional surfactants such as DTAB (29 ± 1 $Å^2$/molecule), to we do not interpret this result to indicate that DMFA assumes a looped configuration at the air/water interface due to its conventional architecture (see Tajima *et al.*[23] for additional discussion).

3.8.2 AFM Trace and Retrace Images

Figure 3.8 shows the trace and retrace AFM images of DTAB and **(A)** reduced FTMA or **(B)** oxidized FTMA or **(C)** in the absence of other surfactant, in 100 mM Li_2SO_4 on HOPG. The striped pattern is seen in both the trace and retrace in all three sets of images.

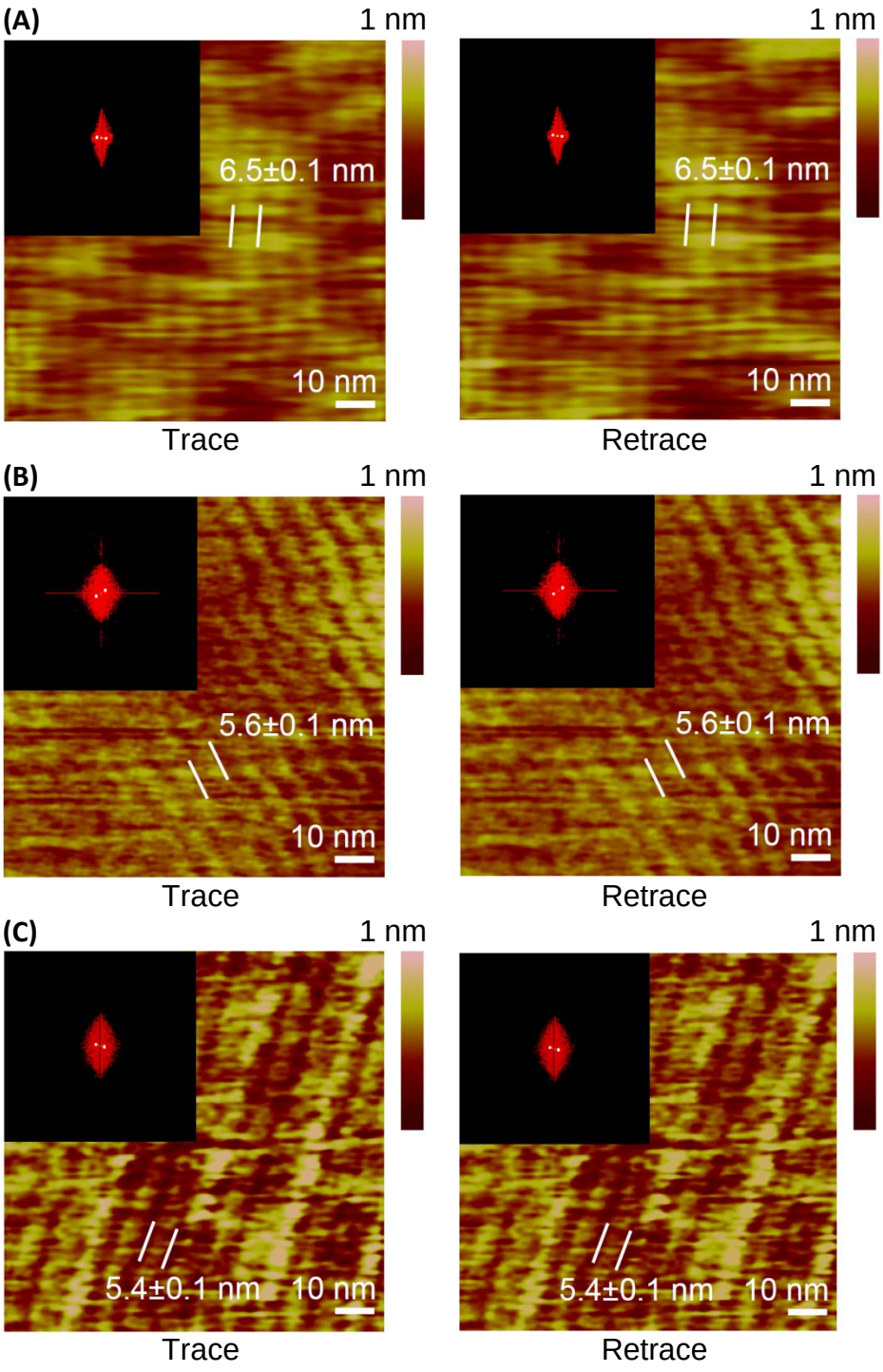

Figure 3.8 Trace and retrace AFM images of FTMA and DTAB assemblies on HOPG
Atomic force micrographs obtained using HOPG, 2 mM DTAB and either **(A)** 0.1 mM reduced FTMA, or **(B)** 0.1 mM oxidized FTMA, or **(C)** 20 mM DTAB all in 100 mM aqueous Li_2SO_4. The trace (left) and retrace (right) are shown for each.

Chapter 4 : Effect of Surface Charge on Interfacial Self-Assembly of Amphiphilic Redox Mediators‡

4.1 Introduction

Recent studies have revealed that amphiphilic redox mediators form interfacial self-assemblies at hydrophobic electrode surfaces that can selectively block electron transfer in one direction while allowing it in the reverse direction (i.e. current rectification). In particular, amphiphiles containing ferrocene, which undergo self-assembly in a manner that is dependent on the redox state of ferrocene,[1-5] have served as a useful model system to elucidate the physical mechanisms through which interfacial self-assembly can influence charge transfer. For example, in a previous study,[6] we reported that current rectification can be achieved using 11-ferrocenyltrimethylammonium bromide (FTMA) at hydrophobic electrodes (see Fig. 4.1A). In general, however, we predict that the self-assembly of a redox mediator into interfacial assemblies, and thus its interfacial electrochemical properties, will depend on the surface chemistry of the electrode. In this paper, we investigate the role of electrode surface chemistry, with a particular focus on the presence of charged groups attached to the electrode, in directing the self-assembly of redox surfactants and influencing interfacial charge transfer.

Our study is broadly motivated by the utility of interfaces that rectify the passage of current between a solid electrode and redox mediator in solution, including in contexts such as efficient and cost-effective dye sensitized solar cells[7-11] and solar water splitters.[12-15] Currently, dye-sensitized solar cells use the redox pair iodide (I^-)/triiodide (I_3^-), which is corrosive[3,8] and thus restricts the materials that can be used for other components of the device. Alternative strategies that have been explored for controlling charge transfer at interfaces include the

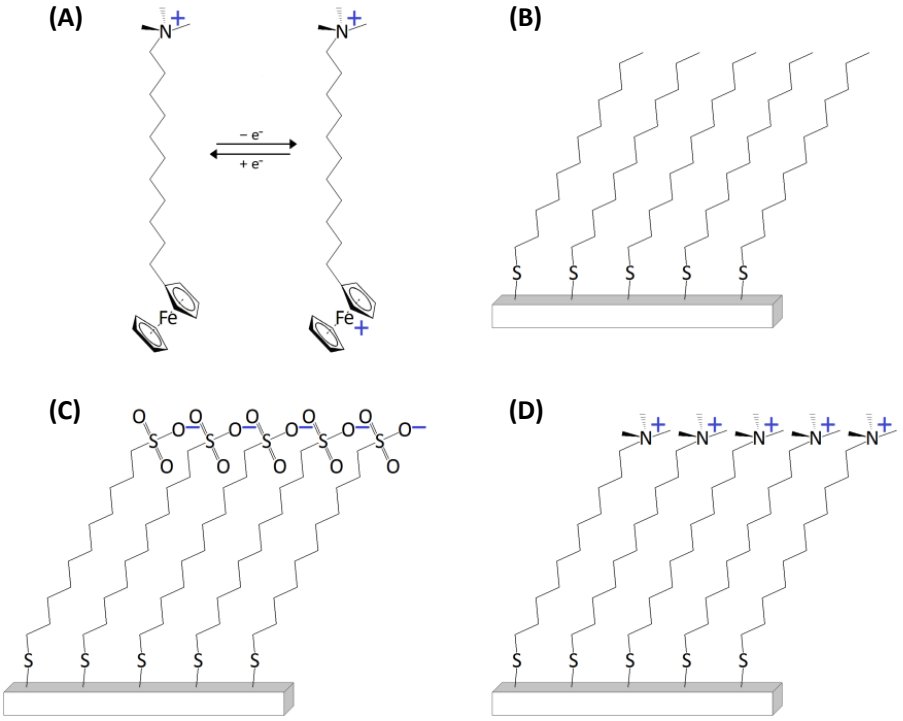

Figure 4.1 Molecular structures of FTMA and thiol monolayers
Molecular structures **(A)** of 11-ferrocenylundecultrimethylammonium bromide (FTMA), **(B)** a monolayer dodecanethiol (DT) on a gold surface, **(C)** a monolayer of Sodium 11-mercapoundecanesulfonate (MUS) on a gold surface, and **(D)** a monolayer of N,N,N-trimethyl-(11-mercaptoundecyl)ammonium (TMUA) chloride on a gold surface. Counterions not shown.

deposition of chemically functionalized layers on electrode surfaces, such as silanes[16] or metal oxides.[17,18] These strategies affect charge transfer at the electrode through many mechanisms, such as by altering the conduction band of the semiconductor electrode,[19] or by creating an insulating layer that slows unwanted reactions.[20] In this paper, we explore the role of electrode surface chemistry in guiding the self-assembly and charge transfer properties of amphiphilic redox mediators.

Past studies have established that current rectification observed with FTMA at hydrophobic electrodes arises from the formation of hemimicelles of reduced FTMA that block oxidized FTMA from accessing the electrode.[33] This blocking occurs because (i) oxidized

FTMA does not displace reduced FTMA from the electrode and (ii) oxidized and reduced FTMA do not mix within micellar assemblies. Specifically, whereas reduced FTMA has the architecture of a conventional surfactant with a single charged headgroup, when oxidized, it assumes the architecture of a bolaform surfactant with a charged headgroup at both ends of its hydrocarbon chain (Fig. 4.1A). A number of past studies have established that conventional and bolaform surfactants do not generally form mixed micelles.[21,22]

While our previous study reported current rectification at hydrophobic electrodes,[33] many technologically relevant surfaces (e.g. titania) have more complex and heterogeneous surface chemistry when placed into contact with aqueous solutions at neutral pH.[23] As described above, the factors that cause a self-assembling redox mediator to cause current rectification at a hydrophobic electrode are dependent on the presence of hemimicelles formed by the self-assembling redox mediator, which in turn depends on the surface chemistry of the electrode. In this paper, we investigate the role of electrode surface chemistry on charge transfer between a self-assembling redox mediator in solution in contact with a solid electrode. To investigate the effects of surface chemistry on interfacial self-assembly and charge transfer processes involving redox surfactants, we employ cyclic voltammetry (CV), a quartz crystal microbalance (QCM), and atomic force microscopy (AFM). In our electrochemical measurements, we use gold electrodes functionalized with 1-dodecanethiol (DT) as a model nonpolar surface (Fig. 4.1B), 11-mercaptoundecansulfonate (MUS) as a model negatively-charged electrode surface (Fig. 4.1C), and N,N,N-trimethyl-(11-mercaptoundecyl)ammonium (TMUA) as a model electrode with positively-charged surface groups (Fig. 4.1D).

4.2 Experimental section

4.2.1 Materials

Dodecyltrimethylammonium bromide (DTAB), Li_2SO_4, hydroxymethyl ferrocene (HMeFc), and 1-dodecanethiol were purchased from Sigma Aldrich (St. Louis, MO). FTMA was purchased from Dojindo Molecular Technologies (Rockville, MD). N,N,N-trimethyl-(11-mercaptoundecyl)ammonium chloride and sodium 11-mercaptoundecansulfonate were purchased from ProChimia Surfaces (Gdansk, Poland). These materials were used as received without further purification. AFM tips (MSCT model) and mica, were purchased from Bruker Nano Company (Santa Barbara, CA). Aqueous surfactant solutions were prepared using deionized water with a resistivity of 18.2 MΩ-cm purified by a Synergy Ultrapure Water System (Millipore, Darmstadt, Germany) and adjusted to pH 5 by the addition of sulfuric acid. These solutions were degassed by bubbling a gaseous stream of nitrogen for approximately an hour prior to use.

4.2.2 Experimental methods

4.2.2.1 Functionalized Surfaces

Gold substrates were made by depositing 10 nm titanium (at a deposition rate of 0.2 Å/s) and 100 nm gold (at a deposition rate of 1 Å/s) on to a silicon wafer surface using an e-beam evaporator. The silicon wafers were used as received from the manufacturer. The gold substrates were subsequently functionalized with either DT, TMUA, or MUS by their immersion in ethanolic solutions containing 1 mM thiol. After immersion overnight, the functionalized gold electrodes were removed from the ethanolic thiol solution, rinsed with pure ethanol to remove excess thiols, and dried under nitrogen. The formation of thiol monolayers was confirmed using

ellipsometry. We measured film thicknesses of 17.1 ± 0.4 Å, 17.8 ± 0.2 Å, and 18.0 ± 1.0 Å for gold surfaces functionalized with DT, MUS, and TMUA, respectively. These film thicknesses are indicative of a thiol monolayer and are consistent with a literature value of 16.9 Å.[24]

4.2.2.2 Cyclic Voltammetry

The cyclic voltammograms (CVs) presented here were performed according to the procedure described in detail elsewhere.[33] Of particular importance in our analysis here is the dependence of peak current, I_p, on scan rate, ν:

$$I_p \sim \nu^{\chi} \tag{4.1}$$

The exponent in Eq. 4.1, χ, is calculated for these systems and compared to the expected value for current limited by the diffusion of a reacting species from bulk solution to the electrode, where $\chi = 0.5$ and the peak current can be modeled by the Randle-Sevcik Equation,[25]

$$I_p = 0.4463 n^{3/2} \sqrt{\frac{F^3}{RT}} A \mathcal{D}^{1/2} C \nu^{1/2} \tag{4.2}$$

and the expected value of $\chi = 1$ for a system where the redox species is adsorbed on the electrode's surface:[26]

$$I_p = \left(\frac{n^2 F^2}{4RT}\right) A \nu \Gamma_o \tag{4.3}$$

In Eq. 4.2 and Eq. 4.3, n is the number of moles of electrons transferred in the reaction, F is the Faraday constant, R is the ideal gas constant, T is the system temperature, A is the surface area of the electrode, $\mathcal{D}$ is the diffusion coefficient of a redox species diffusing from bulk solution, C is the concentration of the redox species in bulk solution, and Γ_o is the surface concentration of adsorbed redox species.

4.2.2.3 Quartz Crystal Microbalance

A Q-Sense E4 instrument (Biolin Scientific, Västra Frölunda, Sweden) was used to perform Quartz crystal microbalance (QCM) measurements as described in detail previously.[33] We calculate the adsorbed mass, Δm, of surfactant films where the viscous dissipation, ΔD, is sufficiently small compared to the change in frequency, Δf, defined as $\Delta D/\Delta f < 4x10^{-7}$ Hz^{-1} using a 5 MHz crystal, using the Sauerbrey equation:[27]

$$\Delta f = -\frac{2f_o^2}{A\sqrt{\rho_q \mu_q}} \Delta m \tag{4.4}$$

where f_o is the resonance frequency of the crystal before immersion in FTMA, A is the area of the piezoelectric quartz crystal, ρ_q is the density of quartz, and μ_q is the shear modulus of quartz.

4.2.2.4 Atomic Force Microscopy

Atomic force microscopy (AFM) was used to image interfacial assemblies formed from aqueous solutions of either 1 mM reduced FTMA, 1 mM oxidized FTMA or 20 mM DTAB on mica. Because thiol-functionalized gold films are too rough to permit molecular-level resolution of an adsorbed surfactant assembly, we used mica as a substrate to mimic the negatively-charged character of an MUS monolayer. The mica substrates were freshly cleaved, and then incubated in the surfactant solutions for two days before imaging. The AFM imaging was done using a Multimode IIIa instrument (Bruker Nano, Santa Barbara, CA) with a procedure detailed elsewhere.[33]

4.3 Results

4.3.1 Adsorbed Assemblies of FTMA at Negatively-Charged Surfaces

We first turn our attention to the interfacial self-assembly of FTMA at gold electrodes functionalized with the negatively-charged MUS monolayer. As discussed in the Introduction, our prior study[33] found that, at (hydrophobic) DT-functionalized electrodes, reduced FTMA forms adsorbed hemimicelles that prevent oxidized FTMA in bulk solution from accessing the electrode surface. Oxidized FTMA in solution is unable to access hydrophobic electrodes because it is unable to mix with hemimicelles of reduced FTMA that are adsorbed to the electrode and is unable to displace reduced FTMA from the surface. Based on prior AFM studies of assemblies formed by conventional cationic surfactants such as DTAB[28,29] on negatively-charged surfaces, we anticipated that reduced FTMA would form adsorbed micelles on MUS monolayers. From the molecular architecture of reduced and oxidized FTMA, we anticipated that, like its demixing with adsorbed hemimicelles of reduced FTMA at hydrophobic surfaces, oxidized FTMA would also be unable to mix with adsorbed micelles of reduced FTMA at negatively-charged surfaces. However, we also predicted the adsorption of cationic surfactant at a negatively-charged surface would be impacted by electrostatic interactions that are much stronger than those present between cationic surfactants and hydrophobic surfaces. Thus, we hypothesized that, unlike at a hydrophobic electrode, at negatively-charged electrodes oxidized FTMA would be able to displace reduced FTMA from the electrode surface through competitive adsorption.

First, we used AFM to determine whether reduced and oxidized FTMA form micellar assemblies at a negatively-charged surface. We note past AFM studies have observed that the

morphology of interfacial assemblies formed by cationic surfactants vary with the surface charge of the substrate.[30] Because thiol-functionalized gold substrates are too rough to permit AFM of surfactant assemblies, we instead used (negatively charged) mica substrates. We note that the surface charge density of mica (in air) is one negative charge per every 48 $Å^2$,[31] whereas we the MUS monolayer has approximately one negative charge per every 25.4 $Å^2$ (the approximate cross-sectional area of the methyl chain). In order to ensure the images we obtained are not artifacts of the scanning process, we imaged the bare mica surface (Fig. 4.2A), changed our scanning rate, rotated the scanning direction, and compared the trace and retrace images (see Fig. 4.11). For the purpose of comparison, both with the assemblies observed in previous studies and with those formed here by FTMA, we imaged assemblies formed by DTAB on mica when the mica was contacted with an aqueous solution containing 20 mM DTAB and 100 mM Li_2SO_4 (Fig. 4.2B). DTAB forms striped interfacial aggregates with a spacing of 4.6 ± 0.1 nm between stripes, consistent with past studies that have reported a spacing of 4.8 ± 0.2 nm.[28,29] A second direction of orientational ordering is also observed along the length of the stripes with a spacing of 16.8 ± 0.5 nm, which has also been reported in past studies. These studies have interpreted the striped aggregates to be cylindrical micelles. We imaged interfacial assemblies at mica substrates formed by 1 mM oxidized FTMA (Fig. 4.2C) and 1 mM reduced FTMA (Fig. 4.2D) in aqueous solutions also containing 100 mM Li_2SO_4. The image of the mica surface in contact with a solution containing oxidized FTMA did not exhibit any distinguishable patterns, although the adsorbed surfactant masks the pattern observed in images of bare mica (Fig. 4.2A). We interpret this image to suggest that oxidized FTMA forms adsorbed assemblies with no apparent long-range order.

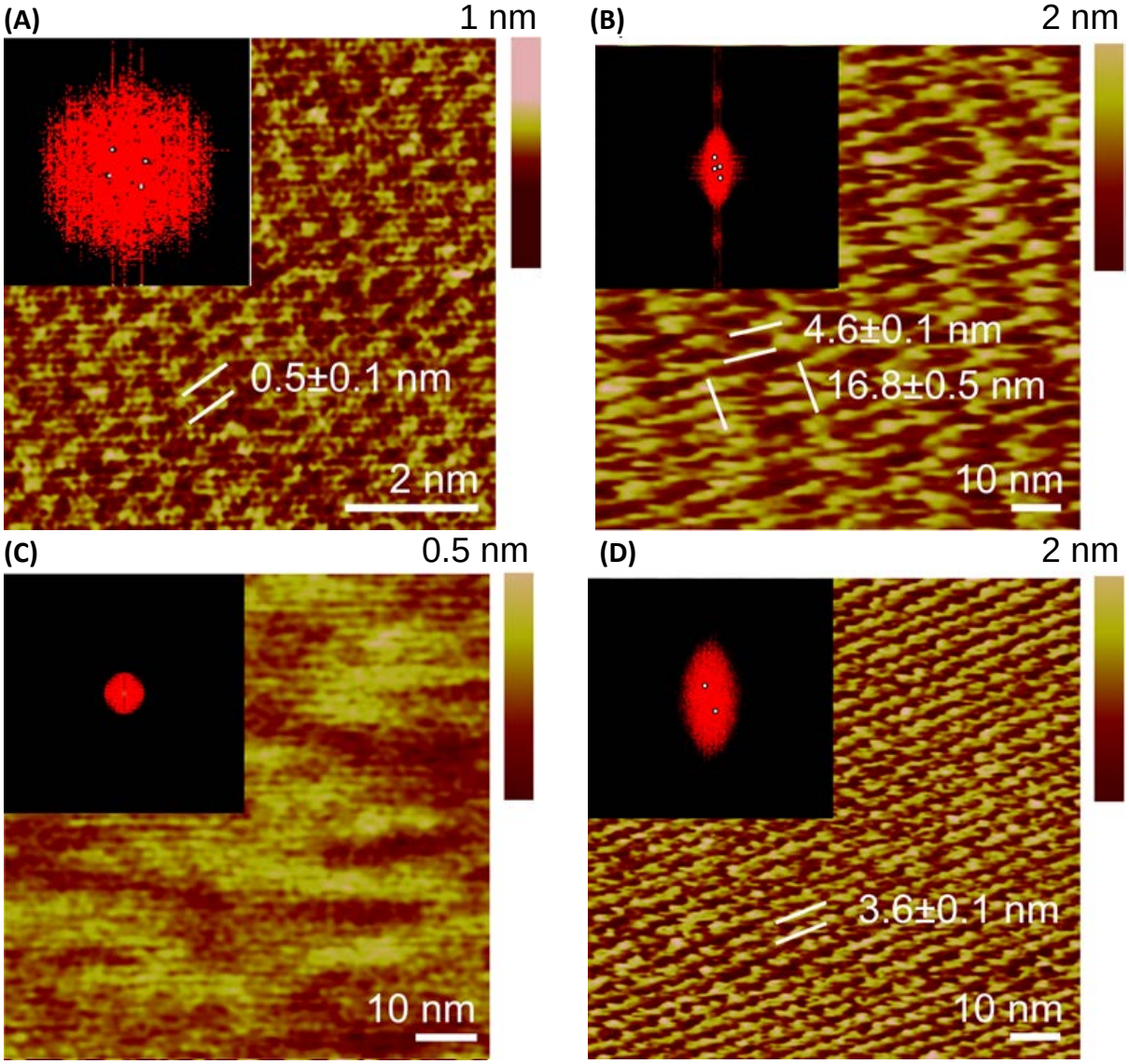

Figure 4.2 AFM images of FTMA and DTAB assemblies on mica
Atomic force microscopy results on mica for **(A)** bare mica and **(B)** 20 mM DTAB on mica showing striped aggregates with order in two dimensions, one with a width of 4.6 ± 0.1 nm and the other 16.8 ± 0.5 nm, consistent with previous AFM images of DTAB on mica.[28,29] AFM images of **(C)** 1 mM oxidized FTMA and **(D)** 1 mM reduced FTMA both in an aqueous 100 mM Li_2SO_4 solution on mica. FTMA forms striped aggregates with a spacing of 3.6 ± 0.1 nm in its reduced redox state and surface aggregates without long range order in its oxidized state. The insets show the Fourier transfer of the image.

In contrast to the assemblies formed by oxidized FTMA, AFM images of reduced FTMA assemblies on mica (Fig. 4.2D) show striped aggregates with a spacing of 3.6 ± 0.1 nm between stripes. We compare the striped aggregates formed by reduced FTMA at mica surfaces with

striped aggregates seen in past AFM studies[33] of reduced FTMA assemblies at (hydrophobic) highly-oriented pyrolytic graphite (HOPG) substrates, and we note two differences. First, the height of the interfacial aggregates formed at mica substrates is 2 nm, compared to 1 nm at HOPG substrates. This is consistent with the formation of hemimicellar aggregates at the (hydrophobic) HOPG surface and micellar aggregates at the (negatively charged) mica surface. Second, the spacing between striped FTMA aggregates is 3.6 ± 0.1 nm at the mica substrate, compared to 7.2 ± 0.1 nm at HOPG. The spacing between adsorbed DTAB aggregates also exhibits a smaller spacing (4.6 ± 0.1 nm) on mica than on HOPG (5.4 ±0.1 nm). The smaller spacing between adsorbed assemblies of reduced FTMA or DTAB on mica than on HOPG results from greater adsorption at mica than at HOPG. Examples of this phenomenon can be found in past studies that have seen a decrease in spacing between adsorbed SDS hemicylindrical hemimicelles on HOPG with increasing SDS concentration.[32] Overall, while we note that it is difficult to make conclusions about the configuration of surfactant assemblies from AFM images, the images are consistent with the formation of adsorbed micelles by reduced FTMA but not by oxidized FTMA. Although the AFM images of reduced FTMA assemblies on negatively-charged surfaces show adsorbed micelles rather than adsorbed hemimicelles, we would not predict that oxidized FTMA will mix with adsorbed micelles either, because past studies have shown that oxidized FTMA does not mix with reduced FTMA micelles in bulk solution.[21,33]

We sought to determine if mixing occurs between the two redox states of FTMA within interfacial assemblies and to provide insight into their competitive adsorption, by performing QCM on solutions containing reduced FTMA, oxidized FTMA, and mixtures of reduced and oxidized FTMA. First we used QCM to quantify the amount of adsorbed FTMA in each redox state in the absence of the other redox state at an MUS monolayer. The QCM results for FTMA

on an MUS monolayer formed on a gold coated crystal are shown in Fig. 4.3A-B. The crystals, functionalized with an MUS monolayer prior to use, were initially equilibrated with aqueous. solutions containing 100 mM Li_2SO_4. Next, the flow was switched to 0.1 mM FTMA in either redox state in aqueous 100 mM Li_2SO_4 solution. Finally, the flow was switched back to aqueous 100 mM Li_2SO_4 (without surfactant) in order to measure the desorption of FTMA. Our QCM measurements show an adsorbed mass, calculated using the Sauerbrey equation (Eq. 4.4), of 2.6 ± 0.4 molecules/nm^2 for 0.1 mM reduced FTMA and 0.9 ± 0.2 molecules/nm^2 for 0.1 mM oxidized FTMA at an MUS monolayer. Further discussion of the difference in the amount of adsorption of FTMA between the two redox states can be found below. Curiously, the viscous dissipation goes *down* upon the adsorption of FTMA in either redox state, suggesting that the adsorption of FTMA stabilizes the MUS monolayer. Previous studies have found the adsorption of ions to stabilize surfactant films;[34] for example, counterion adsorption has been shown to decrease the viscous dissipation seen of adsorbed (positively-charged) pectin multilayers in QCM-D experiments when exposed to buffer solution.[35]

Next, we performed QCM experiments (Fig. 4.3C) in which we equilibrated the MUS monolayer with an aqueous solution containing 0.1 mM reduced FTMA in 100 mM Li_2SO_4 (after prior adsorption of reduced FTMA), and then we switched the flow to an aqueous solution containing 0.1 mM reduced FTMA and 0.1 mM oxidized FTMA in 100 mM Li_2SO_4. We predicted that oxidized FTMA, which has a +2 charge, would displace reduced FTMA which only has a +1 charge, from the negatively-charged MUS surface. Surprisingly, we observed no significant changes in either the frequency or viscous dissipation upon the exposure of the adsorbed reduced FTMA assembly to oxidized FTMA in solution (2.6 ± 0.4 and 2.6 ± 0.3 for reduced FTMA alone and a solution containing both reduced and oxidized FTMA, respectively).

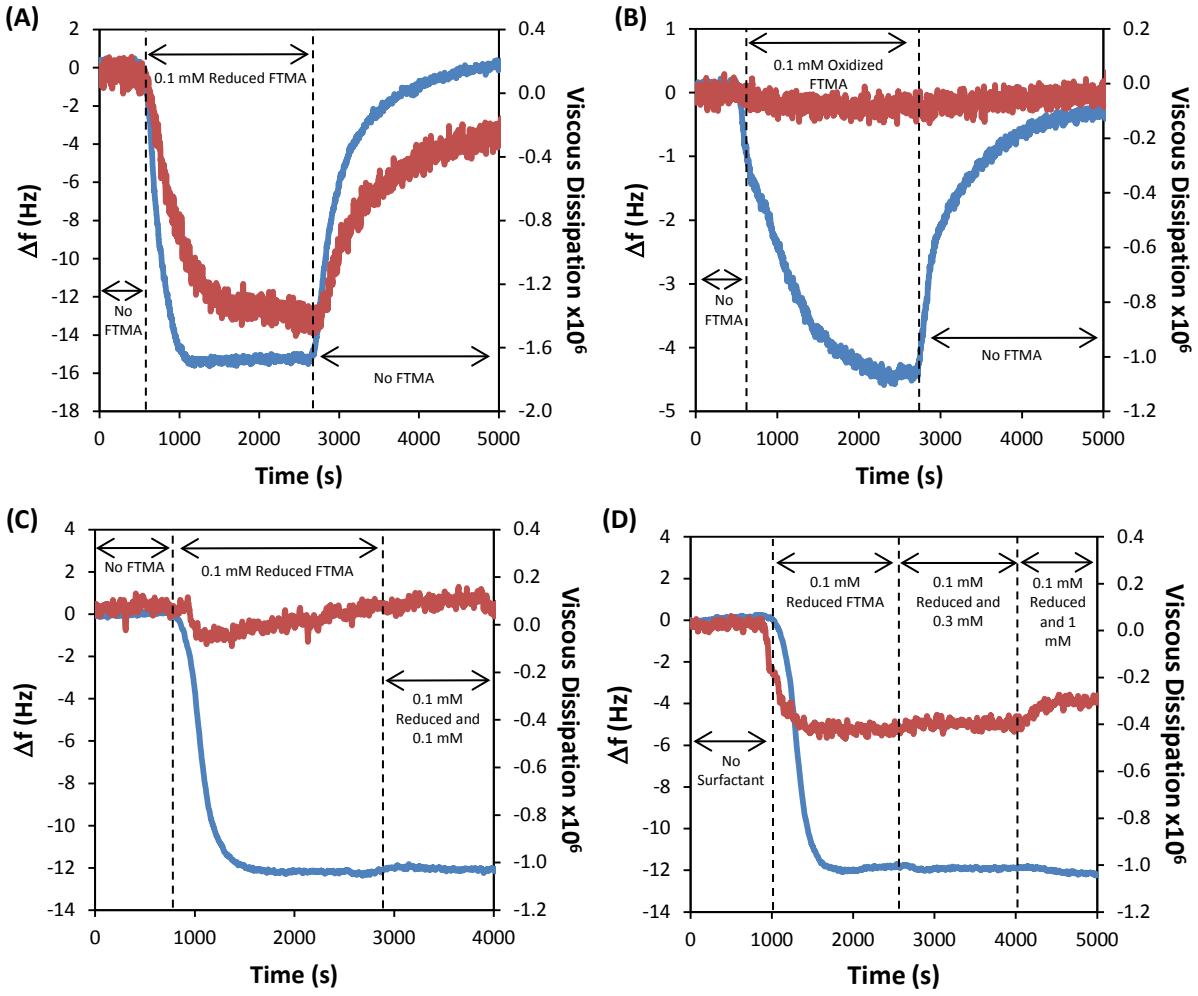

(E)

Surfactant Concentration	Δm (molecules/nm^2)	ΔD x10^6
0.1 mM Reduced FTMA	2.6 ± 0.4	-0.2 ± 0.4
0.1 mM Oxidized FTMA	0.9 ± 0.2	-0.1 ± 0.2
0.1 mM Red/0.1 mM Ox	2.6 ± 0.3	0.0 ± 0.3
0.1 mM Red/0.3 mM Ox	2.5 ± 0.3	-0.2 ± 0.3
0.1 mM Red/1.0 mM Ox	2.6 ± 0.4	-0.1 ± 0.3

Figure 4.3 QCM of mixtures of reduced and oxidized FTMA on MUS monolayers
Quartz crystal microbalance results on a 11-mercaptoundecansulfonate covered gold substrate with 100 mM Li_2SO_4 flowing through a cell initially, switching to **(A)** 0.1 mM reduced FTMA or **(B)** 0.1 mM oxidized FTMA in 100 mM Li_2SO_4 around 1000 s, and again switching around 3000 s back to 100 mM Li_2SO_4 in the absence of surfactant. In **(C)** and **(D)** the substrate was initially equilibrated with 100 mM Li_2SO_4 in the absence of surfactant, followed by 0.1 mM reduced FTMA, and then switched to solutions containing both 0.1 mM reduced FTMA and either **(C)** 0.1 mM oxidized FTMA or **(D)** 0.3 mM oxidized FTMA followed by 1 mM oxidized FTMA (all in 100 mM Li_2SO_4). The data shown here were smoothed using a five-point simple moving average. **(E)** Table of averaged adsorption mass and viscous dissipation for each reduced and oxidized FTMA.

To further confirm that reduced FTMA competitively adsorbs over oxidized FTMA, we exposed an MUS monolayer equilibrated with 0.1 mM reduced FTMA in 100 mM Li_2SO_4 to solutions containing 0.1 mM reduced FTMA and 0.3 mM oxidized FTMA in 100 mM Li_2SO_4, and, finally, 0.1 mM reduced FTMA and 1 mM oxidized FTMA in 100 mM Li_2SO_4 (Fig. 4.3D). No change in the adsorbed mass was observed. This result leads to two notable conclusions. First, the absence of any measurable indication of coadsorption shows that adsorbed assemblies of reduced and oxidized FTMA on MUS monolayers do not mix. Second, contrary to our predictions prior to this experiment, at the concentrations used, oxidized FTMA is unable to displace reduced FTMA from the MUS surface. We interpret the inability of oxidized FTMA to displace reduced FTMA assemblies from the MUS surface to be a result of the formation of adsorbed reduced FTMA micelles (see the AFM images in Fig. 4.2C-D). Whereas oxidized FTMA monomers have a charge of +2, the total charge of a reduced FTMA micelle is significantly greater, which leads to increased electrostatic attraction with a negatively-charged surface and, thus, the preferential adsorption of reduced FTMA.

4.3.2 FTMA Electrochemistry at Negatively-Charged Electrodes

The results described above lead to the conclusion that reduced FTMA forms adsorbed micelles at negatively-charged surfaces with which oxidized FTMA can neither mix with nor displace from the surface (at 0.1 mM of surfactant). From these conclusions, we then hypothesized that adsorbed micelles of reduced FTMA would prevent oxidized FTMA in solution from accessing an electrode functionalized with MUS. To test this hypothesis, we performed CVs using aqueous solutions containing 0.1 mM FTMA and 100 mM Li_2SO_4 at MUS-functionalized gold electrodes (Fig. 4.4A). We evaluated the rectifying behavior of these surfaces by comparing the ratio of the peak current on the anodic and cathodic scans (I_a/I_c).

Unexpectedly, we observed that CVs performed at MUS-functionalized gold electrodes (10 mV/s) exhibited little current rectification (I_a/I_c = 3.4 ± 1.2) in comparison to those performed at hydrophobized (DT) gold electrodes (I_a/I_c = 8 ± 2).[33] This loss in current rectification results from an increase in cathodic current at the MUS electrode (3.9 ± 0.5 μA) compared to the DT electrode (0.7 ± 0.1 μA). Below, we perform additional experiments to understand why reduced FTMA hemimicelles adsorbed at hydrophobic electrodes are able to prevent oxidized FTMA from accessing the electrode more effectively than reduced FTMA micelles adsorbed to negatively-charged electrodes.

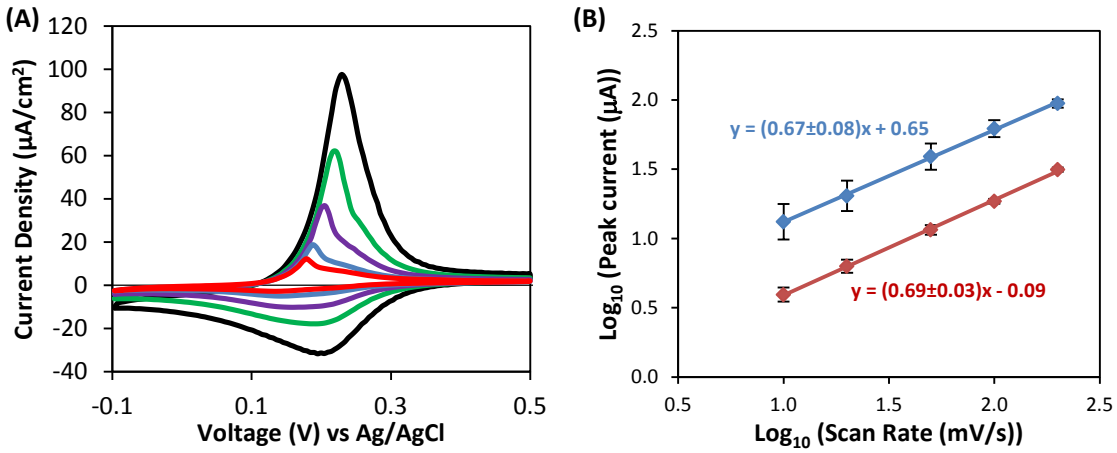

Figure 4.4 CV of FTMA at an MUS-functionalized gold electrode
(A) Cyclic voltammogram of 0.1 mM FTMA in the absence of other surfactant in 100 mM Li_2SO_4 at an 11-mercapoundecanesulfonate (MUS)-functionalized gold electrode at scan rates 10 (red), 20 (blue), 50 (purple), 100 (green), and 200 (black) mV/s. **(B)** Scan rate dependence for the anodic peak (blue) and cathodic peak (red).

To characterize the charge transfer mechanism between FTMA and the negatively-charged MUS-functionalized electrode, we first performed CVs with a varying scan rate (Fig. 4.4A). Varying the scan rate allows us to distinguish between current arising from FTMA adsorbed to the electrode surface (χ = 1) and FTMA diffusing to the electrode from bulk solution

($\chi = 0.5$). The anodic sweep of the CVs reveals a prominent current peak with shoulder. We calculated the scan rate dependence of the main peak to be $\chi_a = 0.67 \pm 0.08$, which suggests both adsorbed and diffusing FTMA make significant contributions to the anodic current since it is $0.5 < \chi < 1$. We modeled the anodic faradaic current measured during the CVs as the sum of current from FTMA diffusing to the electrode surface and current from adsorbed FTMA (see Fig. 4.4C). The current from FTMA diffusing to the electrode surface was fit to the form for a diffusing Nernstian redox mediator (see Supporting Information for details).[25] The current arising from adsorbed FTMA was approximated by a Gaussian curve.[36] Notably, we observe an absence of anodic current characteristic of a diffusing Nernstian redox mediator at potentials beyond the peak potential, which means the reaction of reduced FTMA in bulk solution is suppressed at potentials beyond the peak potential. This suppression of the anodic current beyond the peak potential is indicative of the electrode being covered by a layer of adsorbed oxidized FTMA that prevents reduced FTMA in solution from accessing the electrode. We note that while reduced FTMA is able to displace oxidized FTMA from the electrode surface when the two redox states are present at equal concentrations, at the end of an anodic sweep of a CV, a depletion layer of reduced FTMA forms at the electrode surface. Importantly, our CV indicates that reduced FTMA adsorbs at an MUS functionalized electrode, which is consistent with our AFM and QCM results, and is able to access the electrodes from bulk solution at the potential at which the peak current occurs during an anodic scan.

During the cathodic sweep, we also observe a single prominent peak current with a small shoulder, which is only distinguishable on the scan performed at 10 mV/s. We calculate the scan rate dependence of the main cathodic peak, χ_c, to be 0.69 ± 0.03, suggesting that both adsorbed and diffusing FTMA make significant contributions to the cathodic current. This result stands in

contrast to the behavior observed at hydrophobic electrodes where no contribution was seen from oxidized FTMA in bulk solution diffusing to the electrode (χ_c = 1.01 ± 0.04).[33] At the DT-functionalized electrodes, the observed current rectification (I_a/I_c = 8 ± 2) occurred due to adsorbed hemimicelles of reduced FTMA that blocked access of oxidized FTMA in bulk solution to the electrode (see Introduction). In contrast, at the MUS-functionalized electrode, oxidized FTMA in bulk solution is able to access the electrode from bulk solution and thus significantly less rectification of current during the anodic and cathodic scans is measured. Below we discuss why reduced FTMA hemimicelles that form on DT monolayers block oxidized FTMA from the electrode but reduced FTMA micelles on MUS monolayers do not.

In order to gain insight into the behavior of FTMA in interfacial assemblies on the MUS-functionalized electrode surface, we again considered the QCM results in Fig. 4.3A-B. We measured 2.6 ± 0.4 molecules/nm^2 for 0.1 mM reduced FTMA and 0.9 ± 0.2 molecules/nm^2 for 0.1 mM oxidized FTMA at an MUS monolayer, whereas at a DT monolayer, only a small difference is measured between the amount of adsorbed surfactant in each redox state (1.55 ± 0.1 molecules/nm^2 vs 1.33 ± 0.1 molecules/nm^2 for reduced and oxidized FTMA, respectively).[33] At the beginning of the cathodic scan of the CVs in Fig. 4.4, our QCM measurements suggest the electrode surface is decorated by 0.9 ± 0.2 molecules/nm^2 of adsorbed oxidized FTMA. Consistent with our findings that reduced FTMA will preferentially adsorb to an MUS surface over oxidized FTMA, we would predict adsorbed oxidized FTMA to be reduced before oxidized FTMA in solution. However, this only accounts for 0.9 ± 0.2 molecules/nm^2 of reduced FTMA adsorbed to the electrode surface, whereas our QCM measurements in Fig. 4.3A show that the equilibrium amount of adsorbed reduced FTMA at an MUS surface contacted with 0.1 mM reduced FTMA is 2.6 ± 0.4 molecules/nm^2. Thus, an additional 1.7 molecules/nm^2 of FTMA

must be recruited from bulk solution in order to form the adsorbed micellar assemblies of reduced FTMA we observe via QCM and AFM. Further support for this interpretation can be found by comparing the integrated faradaic current passed during the cathodic scans of CVs performed using 0.1 mM FTMA at MUS monolayers (Fig. 4.5A). The integrated current in both the anodic and cathodic scans decreases with increasing scan rate, suggesting that newly reduced FTMA diffuses away from the electrode during the cathodic scan. As an approximation of the amount of amount of reduced FTMA needed to form a micellar assembly that blocks oxidized FTMA from the surface, we calculate the cathodic current passed (26 ± 5 μC) during the fastest scan rate used in the CV (200 mV/s), which is selected to minimize the contribution from to the current from FTMA that diffuses away from the electrode. This corresponds to the reaction of 2.5 ± 0.4 molecules of FTMA per nm^2 of electrode surface being needed to form a blocking layer, which is in good agreement with the amount of adsorbed reduced FTMA we measure using QCM (2.6 ± 0.4 molecules/nm^2). Together, these observations suggest the ability of oxidized FTMA in bulk solution to access electrodes functionalized with a negatively-charged monolayer comes is due to more reduced FTMA being needed to form a micellar assembly able to block oxidized FTMA from the electrode than can be generated by reducing the adsorbed assembly of oxidized FTMA.

The proposed mechanism described above requires that an incomplete layer of reduced FTMA (i.e. one formed by 0.9 ± 0.2 molecules/nm^2) adsorbed to an MUS-functionalized electrode is insufficient to block oxidized FTMA from the electrode. We interpret our results in the context of past studies that have reported the structure of adsorbed assemblies of cationic surfactants such as CTAB and DTAB (which, like reduced FTMA, have the molecular architecture of a conventional surfactant) form flat, incomplete bilayers on negatively charged

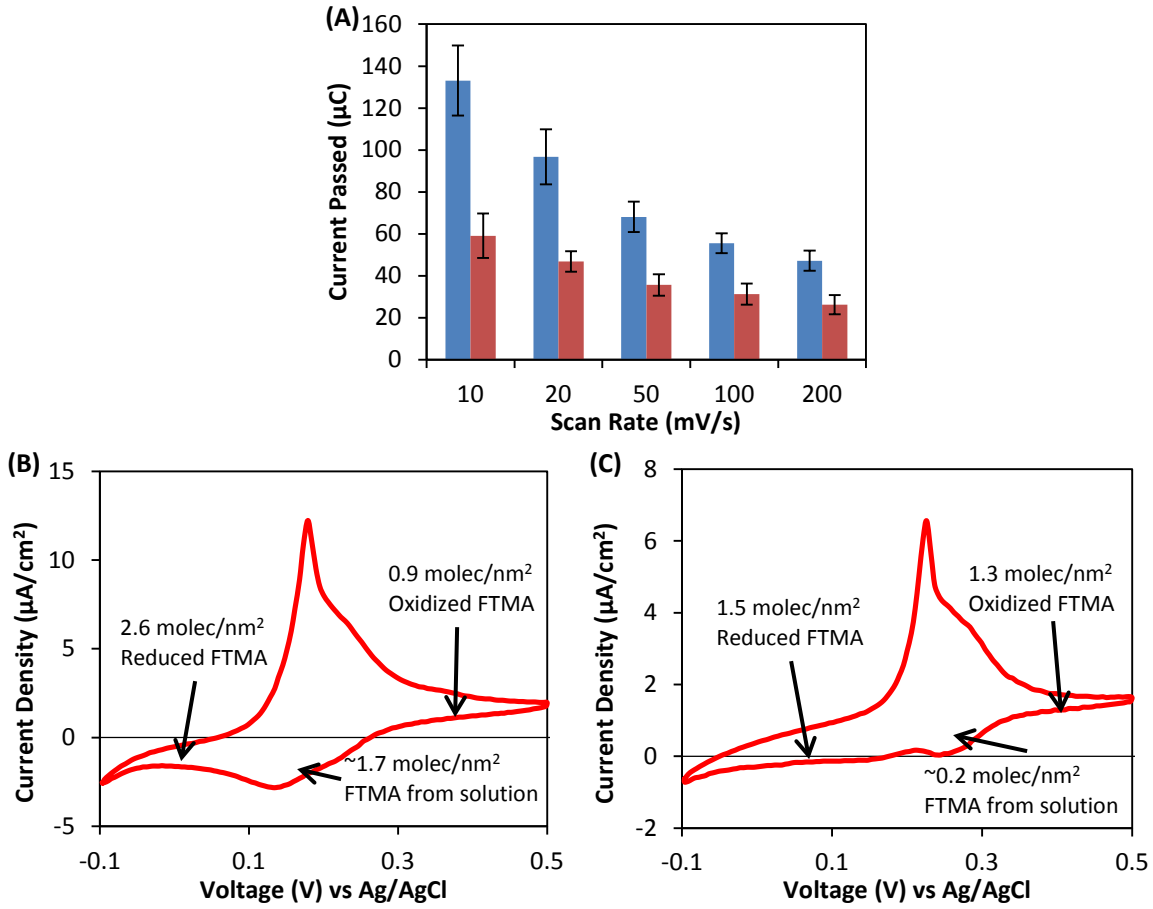

Figure 4.5 Integrated current during CVs of FTMA at an MUS electrode
(A) Total faradaic charge transferred during the anodic (blue) and cathodic (red) scans of the cyclic voltammograms of 0.1 mM FTMA in the absence of other surfactant in 100 mM Li_2SO_4 at an 11-mercapoundecanesulfonate (MUS)-functionalized gold electrode in Fig. 4.2. **(B)** CV of 0.1 mM FTMA at an MUS-functionalized electrode (10 mV/s) with the adsorbed masses calculated using QCM noted. **(C)** CV of 0.1 mM FTMA at a DT-functionalized electrode (10 mV/s) with the adsorbed masses calculated using QCM noted.

surfaces at low bulk concentrations that undergo a transformation to adsorbed micelles at concentrations near their cmc.[37,38] Importantly, these studies found that at lower surface coverages of CTAB or DTAB, adsorbed micellar aggregates of CTAB or DTAB do not form on negatively-charged substrates. Here we note that the concentration of FTMA used in our experiments (0.1 mM) is above the critical micelle concentration (cmc) of reduced FTMA but below the cmc of oxidized FTMA[21,39] These studies are consistent with our interpretation of our

QCM and AFM results that adsorbed oxidized FTMA (0.9 ± 0.2 molecules/nm^2) likely forms an adsorbed assembly without long-range order on the electrode surface (such as an incomplete monolayer or bilayer) but that reduced FTMA forms an adsorbed micellar structure (2.6 ± 0.4 molecules/nm^2). Furthermore, they suggest that at lower surface coverages of reduced FTMA (such as the 0.9 molecules/nm^2 that can be generated through the reduction of adsorbed oxidized FTMA), the adsorbed micellar structure of reduced FTMA, which we predict blocks oxidized FTMA in solution from reaching the electrode, may not form.

From the interpretation described above, we hypothesized that the addition of DTAB (at a concentration near its cmc) would form interfacial micelles that would be able to prevent oxidized FTMA in bulk solution from reaching an MUS-functionalized electrode. Past studies have found DTAB to form mixed micelles with reduced FTMA but not oxidized FTMA,[33,21] and, because DTAB is redox-inactive at the potentials used in our CVs, its adsorbed assemblies are not replaced on the electrode surface during a CV. As described above, AFM images of adsorbed DTAB assemblies (Fig. 4.2B) and images of reduced FTMA assemblies (Fig. 4.2D) on negatively-charged surfaces are both consistent with cylindrical micelles. We performed CV on an aqueous solution containing 0.1 mM FTMA, 2 mM DTAB, and 100 mM Li_2SO_4 at an MUS functionalized gold electrode (Fig. 4.6). Inspection of Fig. 4.6 reveals the inhibition of all measurable cathodic faradaic current (I_a/I_c > 80), which is the same degree of current rectification seen for CVs performed with solutions containing 0.1 mM FTMA and 2 mM DTAB at DT functionalized gold electrodes.[33] Importantly, this result demonstrates that significant current rectification can be achieved using FTMA at electrodes functionalized with a negatively-charged monolayer by adding DTAB.

From the above results, we conclude that while CVs of FTMA performed at MUS-functionalized electrodes show less current rectification than those performed at DT-functionalized electrodes, this current rectification can be recovered by the addition of DTAB. The loss of current rectification observed with FTMA (in the absence of DTAB) at a negatively-charged electrode compared to a hydrophobic electrode is likely caused by the increased amount of reduced FTMA needed to form adsorbed micelles that block oxidized FTMA in solution from reaching the electrode. Overall, these results suggest that surfaces functionalized with negatively charged groups may be used in rectifying devices that make use of a FTMA as a self-assembling redox mediator in the presence of DTAB.

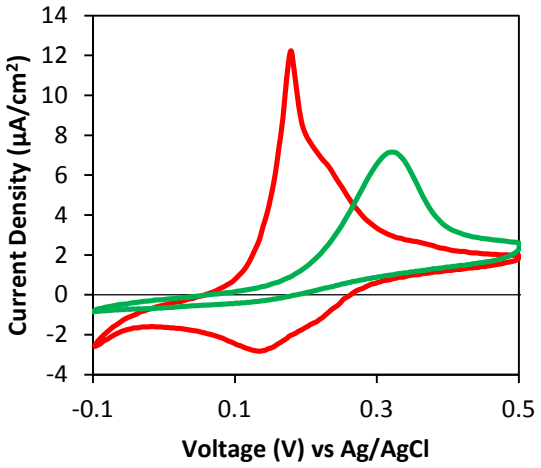

Figure 4.6 CV of FTMA and DTAB at an MUS-functionalized gold electrode
Cyclic voltammogram of 0.1 mM FTMA, in the absence of (red) and in the presence of 2 mM DTAB (green) in 100 mM Li_2SO_4 at an 11-mercapoundecanesulfonate (MUS)-functionalized gold electrode at a scan rate of 10 mV/s.

4.3.3 FTMA Electrochemistry at Positively-Charged Electrodes

We now turn our attention to the behavior of FTMA at the (positively charged) TMUA-functionalized electrode. As noted above, CVs of 0.1 mM FTMA in 100 mM Li_2SO_4 performed

at TMUA-functionalized gold electrodes yield $I_a/I_c = 1.4 \pm 0.1$, compared to $I_a/I_c = 8 \pm 2$ at DT-functionalized gold electrodes and $I_a/I_c = 3.4 \pm 1.2$ at negatively-charged MUS-functionalized gold electrodes. To characterize the physical processes underlying charge transfer between FTMA and a TMUA-functionalized gold electrode, we varied the scan rate of CVs performed on aqueous solutions containing 0.1 mM FTMA and 100 mM Li_2SO_4 at a TMUA SAM functionalized electrode (Fig. 4.7A). We calculated the anodic scan rate dependence of the CV in Fig. 4.7A to be $\chi_a = 0.52 \pm 0.01$ and the cathodic scan rate dependence to be $\chi_c = 0.44 \pm 0.01$. These values of χ_a and χ_c suggest that the charge transfer occurring in the CVs of FTMA is limited by the diffusion of FTMA to the electrode from bulk solution. Importantly, no detectable contribution can be seen to either the anodic or cathodic current from FTMA adsorbed to the electrode surface.

In order to determine whether FTMA adsorbs at a TMUA SAM in each redox state, we performed QCM experiments (Fig. 4.8) in which we sequentially exposed gold-coated quartz crystal sensors functionalized with a TMUA SAM (see Methods) to aqueous solutions containing 100 mM Li_2SO_4, first in the absence of FTMA, then in the presence of 0.1 mM FTMA in either redox state, and then finally in the absence of FTMA. We measured an adsorbed mass of 0.4 ± 0.1 molecules/nm^2 when exposed to 0.1 mM reduced FTMA and 0.15 ± 0.05 molecules/nm^2 when exposed to 0.1 mM oxidized FTMA. Compared to the adsorbed masses of 2.6 ± 0.4 molecules/nm^2 and 0.9 ± 0.2 molecules/nm^2 for 0.1 mM FTMA in its reduced and oxidized states, respectively, at an MUS SAM, significantly less adsorbed mass was measured at a TMUA SAM. We conclude that the decrease in adsorption of FTMA at a TMUA-functionalized electrode likely leads to little impact of self-assembly on charge transfer.

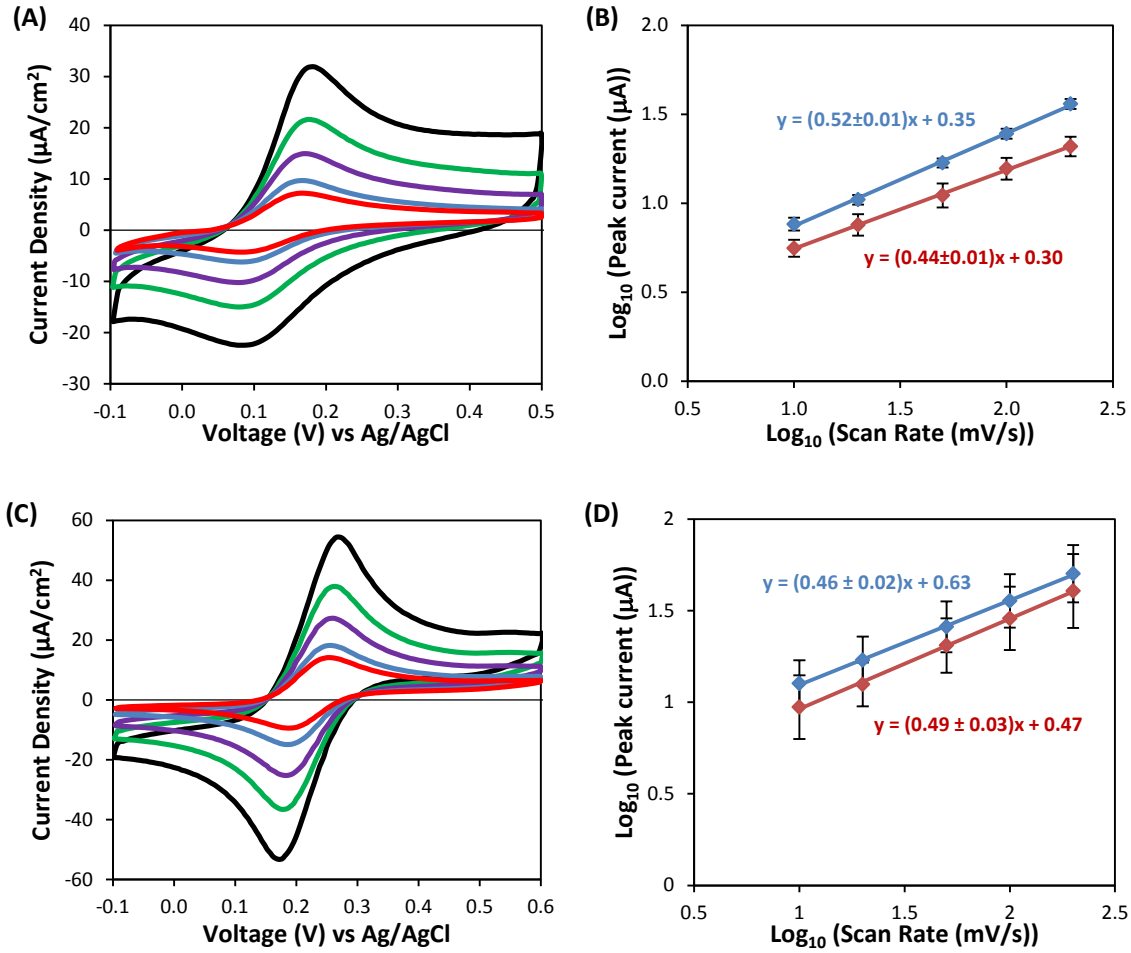

Figure 4.7 CVs of FTMA and HMeFc at TMUA-functionalized gold electrodes
Cyclic voltammogram of **(A)** 0.1 mM FTMA and **(C)** 0.2 mM Hydroxymethyl Ferrocene, both in aqueous 100 mM Li_2SO_4 solutions at an N,N,N-trimethyl-(11-mercaptoundecyl)ammonium-functionalized gold electrode at scan rates 10 (red), 20 (blue), 50 (purple), 100 (green), and 200 (black) mV/s. Scan rate dependence for the anodic peak (blue) and cathodic peak (red) for the CVs of **(B)** 0.1 mM FTMA and **(D)** 0.2 mM Hydroxymethyl Ferrocene.

We further speculated that if FTMA self-assembly does not affect its charge transfer, then the small degree of current rectification (I_a/I_c = 1.4 ± 0.1) observed in the CV of FTMA at a TMUA functionalized electrode may be due to increased electrostatic repulsion between oxidized FTMA and the positively charged SAM relative to the electrostatic repulsion between reduced FTMA and the TMUA SAM. To test this idea, we performed a CV of HMeFc (Fig.

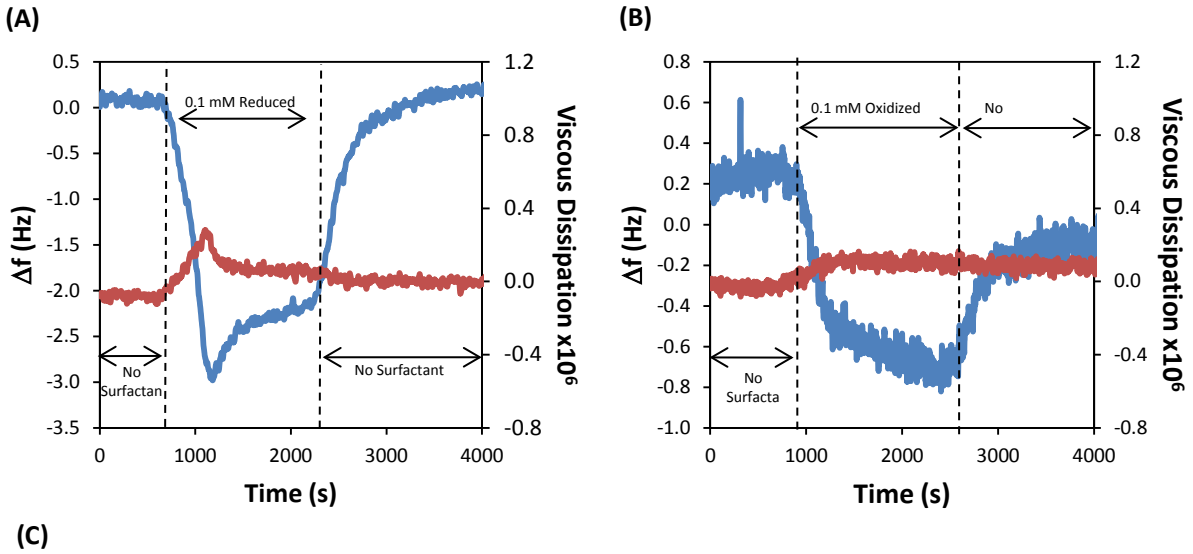

(C)

Surfactant Concentration	Δm (molecules/nm^2)	ΔD x10^6
0.1 mM Reduced FTMA	0.4 ± 0.1	0.1± 0.1
0.1 mM Oxidized FTMA	0.15 ± 0.05	0.07± 0.04
Desorbed Reduced FTMA	0.1 ± 0.2	0.1± 0.2
Desorbed Oxidized FTMA	0.0 ± 0.1	0.6± 0.3

Figure 4.8 QCM of FTMA at a TMUA-functionalized gold surface
Quartz crystal microbalance results on a 1- N,N,N-trimethyl-(11-mercaptoundecyl)ammonium covered gold substrate with 100 mM Li_2SO_4 flowing through a cell initially, switching to 0.1 mM of either **(A)** Reduced FTMA or **(B)** Oxidized FTMA in 100 mM Li_2SO_4 around 1000 s, and switching back to 100 mM Li_2SO_4 in the absence of surfactant around 2500 s. The data shown here are a simple five-point moving average. **(C)** Table of averaged adsorption mass and viscous dissipation over six runs for each reduced and oxidized FTMA.

4.7C), which is a ferrocenyl compound that does not self-assemble, at a TMUA-functionalized gold electrode. If charge repulsion alone were sufficient to explain the current rectification then we would predict the CV of HMeFc to show the same rectification seen with FTMA. The CV of HMeFc at a TMUA SAM shows $I_a/I_c = 1.4 \pm 0.1$, which is identical to the value of I_a/I_c measured in CVs of FTMA at the TMUA SAM. The scan rate dependence ($\chi_a = 0.46 \pm 0.02$ and $\chi_c = 0.49 \pm 0.03$) shows both peaks on the HMeFc CV are limited by diffusion, as anticipated for a non-self-assembling mediator. Overall, we conclude that at an electrode functionalized with a

positively-charged monolayer, FTMA behaves similarly to a non-self-assembling redox mediator.

Together, these results lead us to conclude that while FTMA self-assembly at electrodes functionalized with either hydrophobic or negatively-charged monolayers may be used to elicit current rectification, at electrodes functionalized with positively-charged monolayers no current rectification occurs. This lack of current rectification likely stems from the decrease in adsorption of FTMA at a positively-charged surface compared to negatively-charged and hydrophobic surfaces.

4.4 Conclusions

Overall, this study explores the role played by the surface chemistry of functionalized electrodes on the interfacial self-assembly and charge transfer exhibited by amphiphilic redox mediators. Through the use of AFM we found that reduced FTMA forms micellar assemblies adsorbed to negatively-charged surfaces. Our QCM measurements show that, despite oxidized FTMA having a +2 charged and reduced FTMA having a +1 charge, reduced FTMA adsorbs competitively over oxidized FTMA to negatively-charged surfaces exposed to a solution containing 0.1 mM of each. We also found no evidence of mixing between reduced and oxidized FTMA in micellar assemblies formed on negatively-charged electrodes. This behavior can be explained by the differences in molecular architecture between reduced FTMA (conventional architecture) and oxidized FTMA (bolaform architecture). These conclusions led us to predict that adsorbed assemblies of reduced FTMA would be able to inhibit the reduction of oxidized FTMA at negatively-charged electrodes.

However, we found that a lesser degree of current rectification in CVs performed with FTMA at (negatively-charged) MUS-functionalized electrodes (I_a/I_c = 3.4 ± 1.2) than at (hydrophobic) DT-functionalized electrodes (I_a/I_c = 8 ± 2). In contrast to CVs at DT-functionalized electrodes, at which only current due to the reduction of adsorbed oxidized FTMA contributes to cathodic faradaic current, we found that oxidized FTMA in bulk solution is able to access MUS-functionalized electrodes. Our QCM measurements suggest that the amount of reduced FTMA needed to form a micellar assembly that blocks oxidized FTMA (2.6 ± 0.4 molecules/nm^2) is greater than the amount of oxidized FTMA that adsorbs to the electrode (0.9 ± 0.2 molecules/nm^2), which thus requires the recruitment of oxidized FTMA from bulk solution and leads to a loss in current rectification. We then added DTAB to our CVs because it forms a micellar assembly that does not undergo an electrochemical reaction. We found that the addition of DTAB as a co-surfactant leads to the formation of a micellar assembly that inhibits all measurable cathodic faradaic current at MUS-functionalized electrodes. At positively charged electrodes, we observed only slight current rectification (I_a/I_c = 1.4 ± 0.1) with FTMA. We found that self-assembly at positively-charged surfaces plays no apparent role in the observed charged transfer.

We found that electrodes functionalized with either a negatively-charged monolayer or hydrophobic monolayer (though not a positively-charged monolayer) may be used in the design of rectifying devices that make use of a cationic self-assembling redox mediator. The findings of this paper point toward two strategies for the design of electrodes in rectifying devices that use a self-assembling redox mediator. One strategy is to modify the electrode surface with thin films of a preferred chemistry, such as alkyl silanes, phosphonates, and polymers. Another is to make use of the native surface chemistry of semiconductors themselves, which, the findings of this

paper suggest could be used to elicit current rectification with a self-assembling redox mediator when combined with a non-redox-active co-surfactant. In future studies, we will report on the fabrication of rectifying devices made using the insights described in this paper.

4.5 Acknowledgements

This work was primarily funded by the National Science Foundation through grant CBET- 1263970. Partial support is also acknowledged by the ARO (through W911NF-14-1-0140 and W911NF-15-1-0568). The authors acknowledge the use of instrumentation supported by the Wisconsin Materials Research Science and Engineering Center (DMR-1121288).

4.6 References

‡ Portions of this chapter will be submitted as: T. J. Smith, C. X. Wang and N. L. Abbott, *Effect of Surface Charge on Interfacial Self-Assembly of Amphiphilic Redox Mediators*, In Preparation, (2017)

1. T. Saji, K. Hoshino, S. Aoyagui, *J. Chem. Soc., Chem. Commun.* **1985**, 13, 865-866**.**
2. T. Saji, K. Hoshino, M. Goto, *J. Am. Chem. Soc.* **1991**, 113 (2), 450-456.
3. B. S. Gallardo, K. L. Metcalfe, N. L. Abbott, *Langmuir* **1996**, 12 (17), 4116-4124.
4. P. Brown, C. P Butts, J. Eastoe, J *Soft Matter* **2013**, *9* (8), 2365–2374.
5. X. Y. Liu, N. L. Abbott, *J. Colloid Interface Sci.* **2009**, 339 (1), 1-18.
6. T. J. Smith, C. Wang, N. L. Abbott, *Langmuir* **2015**, *31* (39), 10638–10648.
7. G. Boschloo, A. Hagfeldt, *Acc. of Chem. Res.* **2009**, 42 (11), 1819-1826.
8. A. Hagfeldt, G. Boschloo, L. Sun, L. Kloo, H. Petterson, *Chem. Rev.* **2010**, 110 (11), 6595-6663.
9. Z. Zhang, P. Chen, T. N. Murakami, S. M. Zakeeruddin, M. Grätzel, *Adv. Funct. Mater.* **2008**, 18 (2), 341-346.
10. Y. Liu, J. R. Jennings, Y. Huang, Q. Wang, S. M. Zakeeruddin, M. Grätzel, *J. Phys. Chem. C* **2011**. 115 (38), 18847-18855.

11. T. Stergiopoulos, P. Falaras, *Adv. Energy Mater.* **2012**, 2 (6), 616-627.

12. L. J. Minggu, W. R. W. Daud, M. B. Kassim, *Int. J. Hydrogen Energy* **2010**, 35, 5233–5244.

13. F. E. Osterloh, *Chem. Mater.* **2008**, 20, 35–54.

14. W. J. Youngblood S.-Y. A. Lee, K. Maeda, T. E. Mallouk, *Acc. Chem. Res.* **2009**, *42* (12), 1966-1973.

15. A. Kudo, T. Miseki, *Chem. Soc. Rev.* **2009**, *38*, 253–278.

16. B. A. Gregg, F. Pichot, S. Ferrere, C. L. Fields, *J. Phys. Chem. B* **2001**, 105 (7), 1422-1429.

17. B. C. O'Regan, S. Scully, A. C. Mayer, E. Palomares, J. Durrant, *J. Phys. Chem. B* **2005**, *109* (10), 4616–4623.

18. S. G. Chen, S. Chappel, Y. Diamant, A. Zaban, *Chem. Mater.* **2001**, *13* (12), 4629–4634.

19. Z. P. Zhang, S. M. Zakeeruddin, B. C. O'Regan, R. Humphry-Baker, M. Gratzel, *J. Phys. Chem. B* **2005**, *109* (46), 21818–21824.

20. T. W. Hamann, O. K. Farha, J. T. Hupp, *J. Phys. Chem. C* **2008**, *112* (49), 19756–19764.

21. T. J. Smith, C. Wang, N. L. Abbott, *J. Colloid Interface Sci.* **2017**, *502*, 122–133.

22. R. Zana, S. Yiv, K. M. Kale, *J. Colloid Interface Sci.* **1980**, 77 (2), 456-465.

23. H. Geng, Q. Qu, C. Chen, H. Wu, M. Wang, *J. Electron. Mater.* **2010**, *39* (1), 1–7.

24. W. L. Deng, D. B. Yang, Y. Fang, C. L. Bai, *Sci. China Ser. B* **1996**, *39* (3), 225-234.

25. A. J. Bard, L. R. Faulkner, *Electrochemical Methods: Fundamentals and Applications*; 2nd Edition, Wiley: New York, NY, **2004;** p. 231.

26. A. J. Bard, L. R. Faulkner, *Electrochemical Methods: Fundamentals and Applications*; 2nd Edition, Wiley: New York, NY, **2004;** p. 591.

27. G. Sauerbrey, *Z. Phys.* **1959**, 155 (2), 206-222.

28. H. N. Patrick, G. G. Warr, S. Mann, I. A. Aksay, *Langmuir* **1999**, *15* (5), 1685–1692.

29. W. A. Ducker, E. J. Wanless, *Langmuir* **1996**, *12*, 5915–5920.

30. J. F. Liu, W. A. Ducker, *J. Phys. Chem. B* **1999**, *103* (40), 8558–8567.

31. N. Güven, *Z. Kristallogr.* **1971**, *134*, 196–212.

32. B. J. Micklavzina, S. Zhang, H. He, M. L. Longo, *Langmuir* **2017**, *33* (9), 2122–2132.

33. X. Liu, M. D. Graham, N. L. Abbott, *Langmuir* **2007**, *23* (19), 9578–9585.

34. R. A. Böckmann, A. Hac, T. Heimburg, H. Grubmüller, *Biophys. J.* **2003**, *85* (3), 1647–1655.

35. A. Krzeminski, M. Marudova, J. Moffat, T. R. Noel, R. Parker, N. Wellner, S. G. Ring, *Biomacromolecules* **2006**, *7*, 498-506.

36. G. K. Rowe, M. T. Carter, J. N. Richardson, R. W. Murray, *Langmuir* **1995**, 11 (5), 1797–1806.

37. E. S. Pagac, D. C. Prieve, R. D. Tilton, *Langmuir*, **1998**, *14* (9), 2333–2342.

38. C. P. Whitby, P. J. Scales, F. Grieser, T. W. Healy, S. Nishimura, H. Tateyama, *J. Colloid Interface Sci.* **2001**, 235, 350–357.

39. B. S. Gallardo, M. J. Hwa, N. L. Abbott, *Langmuir*, **1995**, *11*, 4209–4212.

4.7 Supporting Information

4.7.1 Cyclic Voltammetry of Hydroxymethyl Ferrocene at MUS-functionalized Electrodes

Figure 4.9 shows a CV performed on an aqueous solution containing 0.1 mM hydroxymethyl ferrocene and 100 mM Li_2SO_4 at an MUS functionalized gold electrode. This experiment showed $I_a/I_c = 1.3 \pm 0.2$ at 10 mV/s.

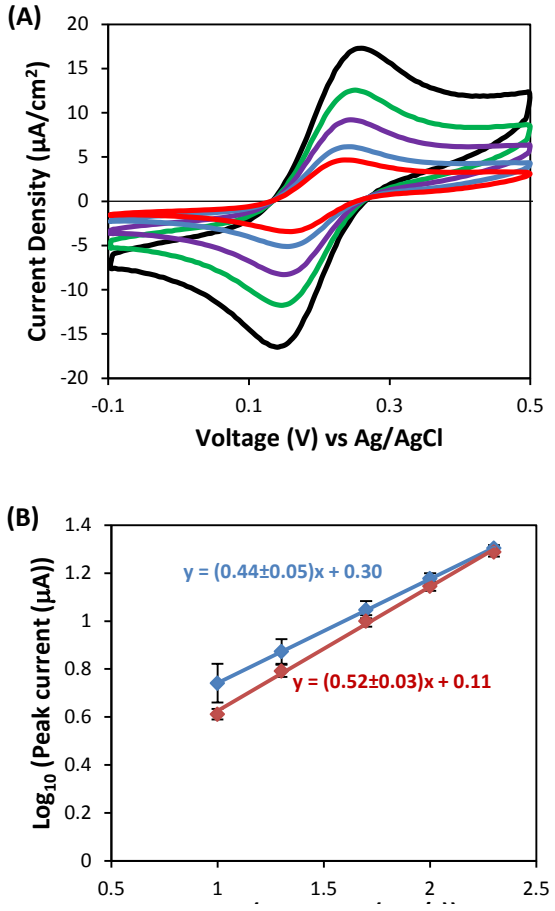

Figure 4.9 CV of HMeFc at an MUS-functionalized electrode
(A) Cyclic voltammogram of 0.2 mM Hydroxymethyl Ferrocene in 100 mM Li_2SO_4 at an 11-mercapoundecanesulfonide-functionalized gold electrode at scan rates 10 (red), 20 (blue), 50 (purple), 100 (green), and 200 (black) mV/s. **(B)** Scan rate dependence for the anodic peak (blue) and cathodic peak (red).

4.7.2 Quantification of Adsorbed and Diffusing Contributions of Anodic Current

Figure 4.10 shows statistical analysis performed on the anodic sweep of the CV shown in Fig. 4.2 of the main text. For each anodic sweep, the baseline current was calculated as shown and subtracted to find the faradaic current. We fit the faradaic current on each anodic scan, I_{farad}, to the sum of a peak due to adsorbed surfactant, I_{ads}, and a peak following the form of a diffusing redox mediator, I_{dif}. The current, I_{ads}, due to adsorbed FTMA can be approximated by a Gaussian curve:[28]

$$I_{ads}(E) = A \exp\left[-\frac{(E - E_o)^{½}}{2\sigma^2}\right] \tag{4.5}$$

where E is the applied potential, A is proportional to the amount of adsorbed FTMA, E_o is the formal potential of adsorbed reduced FTMA, and σ^2 is the variance of distribution. The current due to reduced FTMA diffusing to the electrode, I_{dif}, can be characterized by the form derived in *Bard & Faulkner*:[25]

$$I_{dif}(E) = nFAC, (\pi\mathcal{D}\sigma)^{½}\,\chi(E - E_o) \tag{4.6}$$

where n is the number of moles of electrons transferred in the reaction, F is the Faraday constant, A is the electrode area, C is the concentration of the redox species in bulk solution, $\mathcal{D}$ is the diffusion coefficient of a redox species diffusing from bulk solution, $\sigma = nF\nu/RT$, and $\chi(E - E_o)$ is a numerically calculated parameter characterizing the shape of a curve for current of a diffusing Nernstian redox mediator.

As discussed in the main text, we observe an absence of the anodic current at potentials beyond the peak potential characteristic of a diffusing Nernstian redox mediator. While the analysis suggests the peak at lower potential is due to adsorbed surfactant and the peak at higher potential

is due to reduced FTMA diffusing to the electrode from bulk solution, it does not give sufficient resolution to conclusively determine which peak occurs at a lower potential.

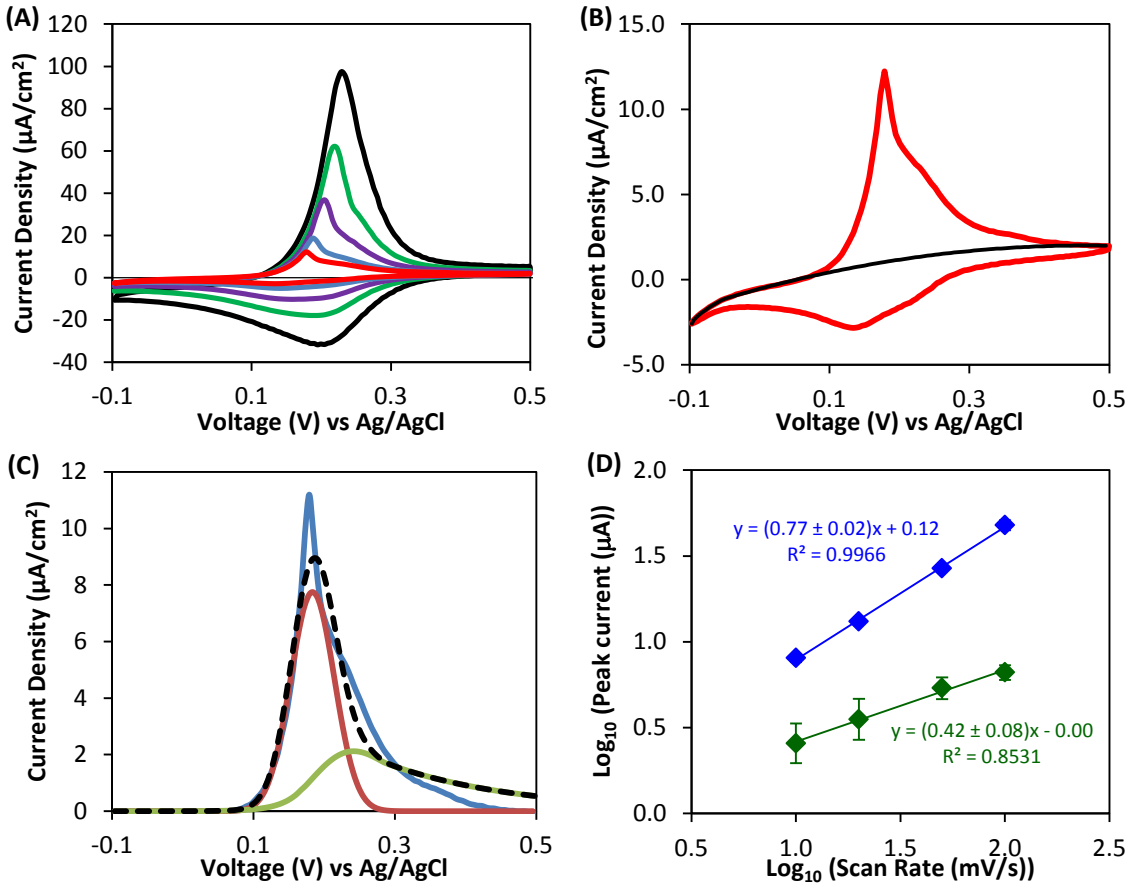

Figure 4.10 Analysis of anodic current in CVs of FTMA at an MUS electrode
(A) Cyclic voltammogram of 0.1 mM FTMA in the absence of other surfactant in 100 mM Li_2SO_4 at an 11-mercapoundecanesulfonide (MUS)-functionalized gold electrode at scan rates 10 (red), 20 (blue), 50 (purple), 100 (green), and 200 (black) mV/s. **(B)** Cyclic voltammogram at 10 mV/s shown in (A) (red) with baseline shown (black). **(C)** Faradaic current from the anodic sweep of (B) (blue) shown with best-fit Gaussian curve (red) and diffusion-based anodic wave (green) corresponding to the main peak and shoulder, and their sum (black dotted). **(D)** Scan rate dependence for the Gaussian anodic peak (blue) and diffusing anodic peak (green) calculated from the scan rates 10, 20, 50, and 100 mV/s.

4.7.3 Trace and Retrace AFM Images

Figure 4.11 shows the trace and retrace AFM for DTAB, oxidized FTMA, and reduced FTMA. The striped pattern observed can be seen in both the trace and retrace images of assemblies formed by DTAB and reduced FTMA.

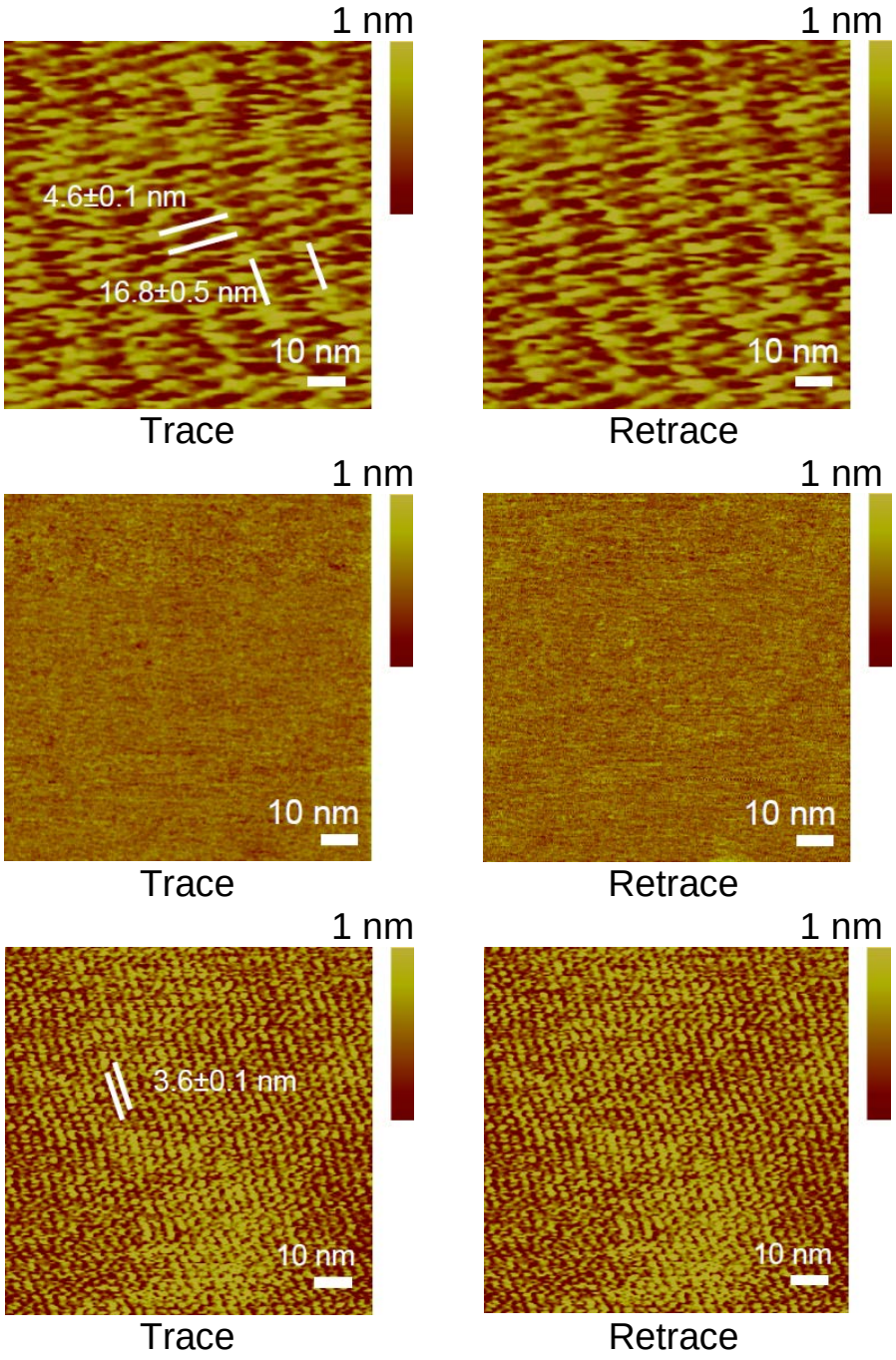

Figure 4.11 Trace and retrace AFM images of FTMA and DTAB on mica
Atomic force microscopy results on mica for 20 mM DTAB (top), 1 mM oxidized FTMA (middle), and 1 mM reduced FTMA (bottom) all in 100 mM aqueous Li_2SO_4. The trace (left) and retrace (right) are shown for each.

4.7.4 Desorption Kinetics of Reduced and Oxidized FTMA

Figure 4.12 shows QCM experiments performed to measure the kinetics of the replacement of a layer of adsorbed oxidized FTMA by reduced FTMA on MUS- and DT-functionalized gold surfaces. A statistically significant difference was not found between the amount of time needed to replace oxidized FTMA on a DT- or MUS-surface. The timescales identified in these QCM experiments suggest that kinetics should not hinder the competitive adsorption of reduced and oxidized FTMA during the CVs in Fig. 4.2 of the main text.

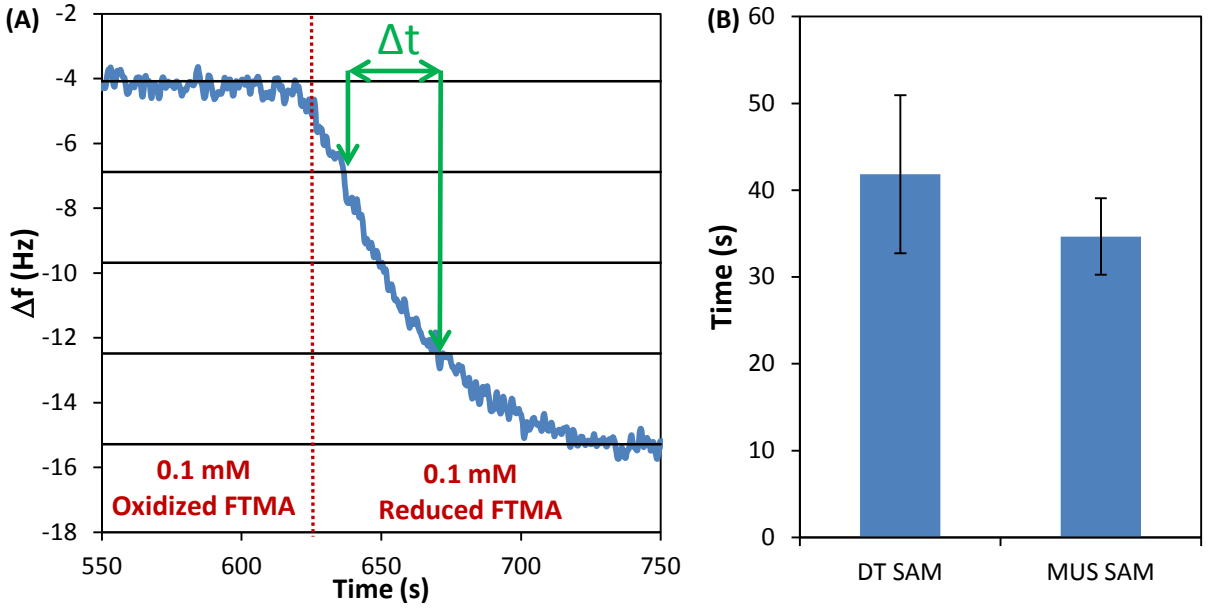

Figure 4.12 QCM of adsorption kinetics of reduced and oxidized FTMA at MUS surface
QCM measurements showing the kinetics of the replacement of a layer of adsorbed oxidized FTMA by reduced FTMA on MUS- and DT-functionalized gold surfaces. Thiol-functionalized gold QCM crystals were initially equilibrated with aqueous solutions containing 100 mM Li_2SO_4 moving past the crystal with a volumetric flow rate of 500 μL/min (the QCM experiments in the main text used a flow rate of 50 μL/min). The flow was subsequently switched to 0.1 mM oxidized FTMA and the crystals were equilibrated. **(A)** Next, the flow was switched to 0.1 mM reduced FTMA and the change in adsorbed mass was monitored. The timescale of the replacement of oxidized FTMA by reduced FTMA on the surface was characterized by calculating the average elapsed time between 25% and 75% of the mass change occurring. (B) The average and standard deviation of the timescale calculated in (A) for QCM crystals functionalized by DT and MUS monolayers.

Chapter 5 : Influence of Self-Assembly of a Redox Mediator on Dye Sensitized Solar Cells[‡]

5.1 Introduction

Control of charge transfer at the interface of a solid electrode and a redox mediator in liquid solution underlies the performance of many energy harvesting and storage devices, such as dye-sensitized solar cells[1-21] and solar water splitters.[22-25] In dye-sensitized solar cells, the design of efficient devices hinges upon the ability of the redox mediator to allow electrons to readily pass from the mediator solution to oxidized adsorbed dye while blocking the flow of electrons from the electrode back to the redox solution (so-called recombination reactions). A range of strategies have been explored to inhibit recombination reactions including the use mediators that form adsorbed radical cations,[4] two electron pathways with slow kinetics,[9-11] tuning the steric hindrance of the mediator through the addition of bulky organometallic ligands,[12,13] and adsorbed interfacial barrier layers.[14,15] More recently, electrochemical studies[26,27] have reported that amphiphilic redox mediators can exhibit asymmetrical charge transfer that results from their self-assembly performed at functionalized gold electrodes. Herein we investigate the redox state-dependent self-assembly of redox mediators to inhibit recombination reactions and improve the efficiency of photo-induced charge separation in dye-sensitized solar cells

We compare dye-sensitized solar cells containing 11-ferrocenyltrimethylammonium bromide (FTMA; Fig. 5.1A), a redox mediator that forms interfacial self-assemblies on an electrode surface that depend on the oxidation state of FTMAto cells containing (2-methyl-1-ferrocenylmethyl) trimethylammonium iodide (MFMT; Fig. 5.1B), a redox mediator that we

show does not self-assemble in our experiments. Our use of FTMA was guided by past

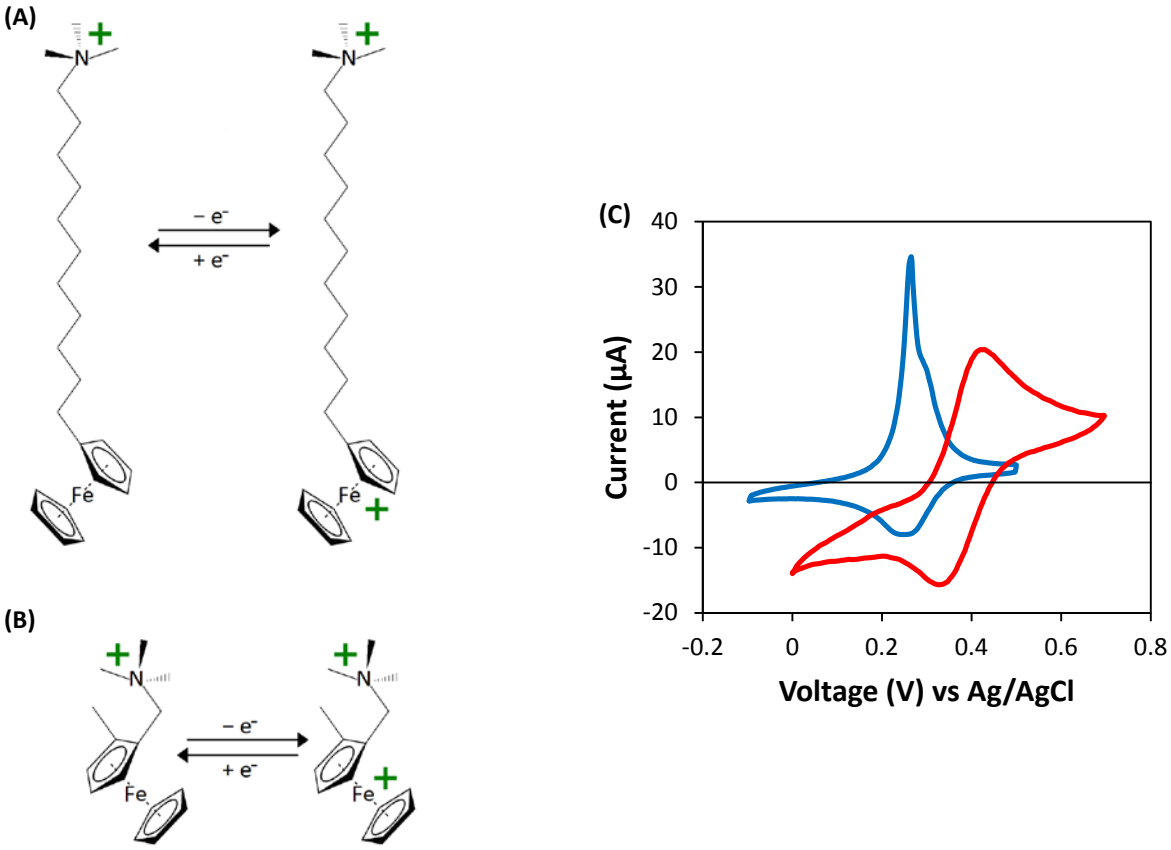

Figure 5.1 Molecular structures and Cyclic Voltammetry of FTMA and MFMT
Molecular structures of **(A)** 11-ferrocenylundecyltrimethyl ammonium bromide (FTMA) and **(B)** (2-methyl-1-ferrocenylmethyl) trimethylammonium iodide (MFMT). Counter ions not shown. **(C)** Cyclic voltammograms performed on aqueous solutions containing 100 mM Li_2SO_4 and either 0.1 mM FTMA (blue) or 0.1 mM MFMT after the removal of iodide (red) at 1-dodecanethiol-functionalized gold electrode at a scan rate of 100 mV/s. We measure the redox potential of MFMT to be 0.37 ± 0.02 V vs. Ag/AgCl and the redox potential of FTMA to be 0.23 ± 0.02 V vs. Ag/AgCl. The iodide ion in the MFMT solution used in this cyclic voltammogram was exchanged for sulfate (see Supporting Information Fig. 5.8).

studies,[26,27] showing reduced FTMA forms hemimicelles on the surfaces of (hydrophobic) alkanethiol-functionalized gold electrodes that block oxidized FTMA in bulk solution from accessing the electrode, leading to the passage of anodic current and inhibition of cathodic current (Fig. 5.2A). The asymmetry in charge transfer arises because reduced FTMA competitively adsorbs in preference to oxidized FTMA onto hydrophobic interfaces and oxidized

FTMA does not mix into assemblies of reduced FTMA due to differences between the molecular

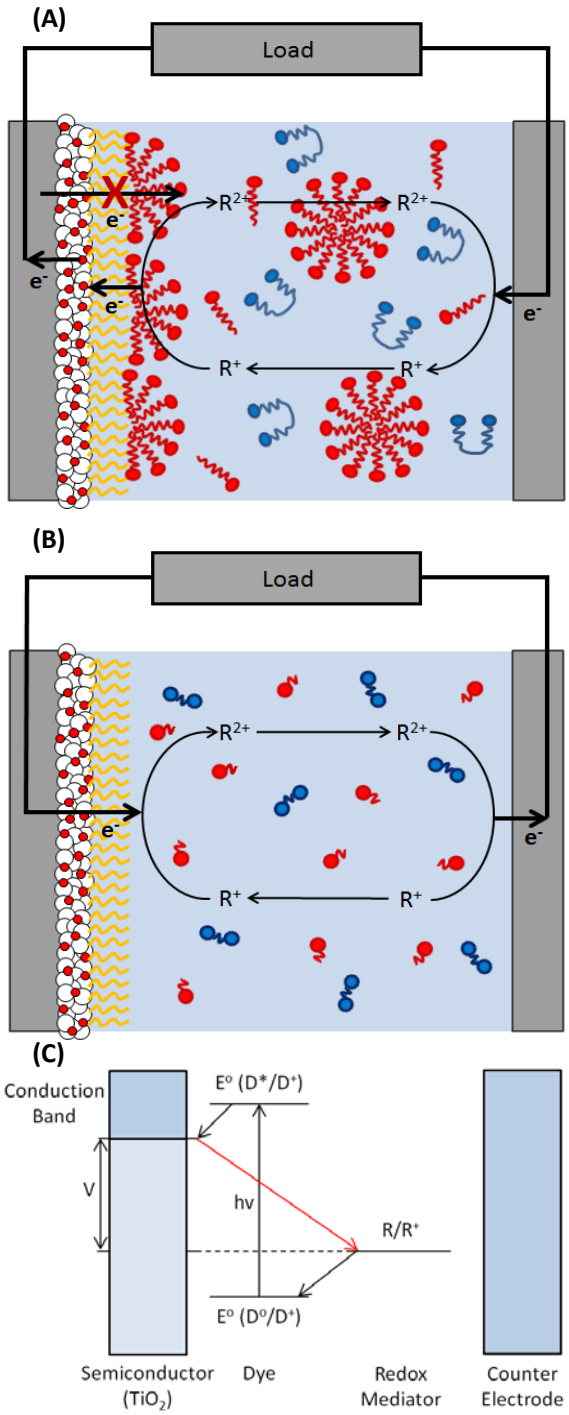

Figure 5.2 Schematics of dye-sensitized solar cells with a self-assembling redox mediator
Diagrams showing a dye-sensitized solar cell as fabricated in this study with **(A)** a self-assembling redox mediator such as FTMA and **(B)** a non-self-assembling redox mediator such as MFMT. The cell in (A) is shown generating power whereas the cell in (B) is shown dissipating power. **(C)** Diagram showing the energy levels of cell components under an applied voltage of V. The recombination reaction we desire to block is shown in red.

architectures of reduced and oxidized FTMA (reduced FTMA behaves as a classical surfactant whereas oxidized FTMA has the molecular architecture of a bolaform).[28]

While past studies of FTMA as a self-assembling redox mediator used alkanethiol-functionalized gold electrodes, the self-assembly of FTMA and its charge transfer behavior depend on the surface chemistry of the electrode.[27] Dye-sensitized solar cells typically use titania as a semiconducting electrode. Herein we report an investigation of the use of a self-assembling redox mediator to influence recombination reactions in a dye-sensitized solar cell with titania electrodes that have been functionalized by a hydrophobic monolayer to facilitate the self-assembly of FTMA. We hypothesized that in cells containing FTMA as their redox mediator, reduced FTMA would form hemimicelles on the hydrophobized titania electrode to prevent oxidized FTMA from reaching the electrode. In contrast, we hypothesized that both redox states of MFMT would readily access the titania electrode in MFMT-based cells (see Fig. 5.2B). These differences, we predicted, would lead to greater efficiency when using FTMA compared to MFMT. We comment that the experiments reported herein were designed as a proof of concept and do not represent a system optimized for application.

5.2 Experimental section

5.2.1 Materials

MFMT, dodecylphosphonic acid, cis-bis(isothiocyanato) bis(2,2'-bipyridyl-4,4'-dicarboxylato) ruthenium(II) (N3) dye, Li_2SO_4 ,H_2SO_4, LiBr and Ag_2SO_4, were purchased from Sigma Aldrich (St. Louis, MO). Fluorine-doped tin oxide electrodes with a layer of titania deposited upon them were purchased from Solaronix (Aubonne, Switzerland). FTMA was purchased from Dojindo Molecular Technologies (Rockville, MD). NaI was purchased from

Thermo Fisher Scientific (Waltham, MA). All materials were used as received except for MFMT (see MFMT Ion Exchange below). All aqueous solutions containing 100 mM Li_2SO_4 were prepared using deionized water with a resistivity of 18.2 MΩ from a Synergy Ultrapure Water System (Millipore, Darmstadt, Germany), adjusted to a pH of 5 by the addition of H_2SO_4.

5.2.2 Experimental methods

5.2.2.1 Fabrication of Photoelectrochemical Cells. Working electrodes consisting of nanoporous titania films screen printed onto a fluorine-doped tin oxidize substrate were washed with pure ethanol, dried under nitrogen, and then immersed in an ethanolic solution containing 355 μg N3 dye per mL of solution overnight. The electrodes were then removed from the dye solution, washed with pure ethanol, and dried under nitrogen. Gold counter electrodes were prepared by depositing films of gold (thickness of 100 nm deposited at a rate of 1 nm/s) onto glass slides (with a 10 nm-thick titanium adhesion layer deposited at a rate of 0.2 nm/s) using an electron-beam evaporator (Tek-Vac Industries, Brentwood, NY). The dye-sensitized solar cells were then fabricated by placing three pieces of double-sided adhesive tape (3M Corporation; Maplewood, MN), used as 300 μm spacers, between the treated titania and gold electrodes. The active electrode area of both the working and counter electrodes was 4 cm^2. Finally, 100 μL of the relevant redox solution was injected between the electrodes immediately prior to testing.

5.2.2.2 Phosphonate Functionalization. In cells with a dodecylphosphonate film deposited on the titania surface, subsequent to the adsorption of the dye, the titania films were immersed in an ethanolic solution containing 2 mM dodecylphosphonic acid for 48 hours at room temperature. The films were removed and placed immediately in a 60°C temperature-controlled oven overnight without washing. Prior studies have reported the formation of alkylphosphonate

monolayers under these conditions.[29] The presence of the dodecylphosphonate monolayer on titania substrates was confirmed via ellipsometry (see below).

5.2.2.3 Ellipsometry. The ellipsometric thickness of dodecylphosphonate films was measured using a Rudolph Research AutoEL-II ellipsometer (Flanders, NJ) with a 632.8 nm laser and an angle of incidence of 70°. The ellipsometry was performed on titanium substrates (thickness of 100 nm) that were deposited onto glass slides via electron-beam evaporation. A layer of titania forms on the surface of the substrate upon exposure to ambient oxygen. We measured a refractive index of 2.2 and an extinction coefficient of 3.0 for the titanium substrate, which is consistent with reported values.[30] We approximated the refractive index of the dodecylphosphonate film as 1.46 in order to calculate its thickness.

5.2.2.4 Dye-Sensitized Cell Testing. The solar cells were tested by applying a linear voltage sweep between the working and counter electrodes (in a two electrode configuration) from 0 to 500 mV using a Metrohm Autolab (Herisau, Switzerland) PGSTAT302N potentiostat. Samples were illuminated using a 12BR3041K light-emitting diode lamp (TCP Lighting, Inc.; Cleveland, OH). The irradiance at the position of the cells was measured with a Traceable Dual-Range Light Meter (Thermo Fisher Scientific; Waltham, MA) to be 138 mW/cm^2.The white-light spectral output of the lamp is shown in the Supporting Information Fig. 5.6.

5.2.2.5 Surface Tension Measurements. The surface tension of aqueous solutions containing MFMT and FTMA were measured using a paper Wilhelmy plate and a KSV NIMA PS4 pressure sensor (NIMA Technology, Coventry, United Kingdom) as described in detail previously.[21] Each measurement was made by immersing the Wilhelmy plate and allowing it to equilibrate until the surface tension became constant (which occurred within five minutes). Surface tensions were

measured from the change in force on a plate immediately before and after removal from solution using the Wilhelmy equation.[31] The contact angle was taken to be zero for a paper plate.[32] The surface excess concentration (Γ) for a solution containing a single surfactant in the presence of a swamping electrolyte, at a bulk concentration below the critical micelle concentration of the solute, can be calculated using the Gibbs adsorption isotherm:[33]

$$\Gamma = \frac{1}{kT}\frac{d\gamma}{d\ln C} \quad (1)$$

where k is the Boltzmann constant, T is the temperature, and C is the solute concentration. The maximum surface excess concentration of a component occurs at concentrations immediately below its critical micelle concentration.

5.2.2.6 Cyclic Voltammetry. The cyclic voltammograms presented in this paper were performed using a Pine Instruments (Grove City, PA) AFCBP1 bipotentiostat. We used a standard three-electrode configuration with a 1-dodecanethethiol-functionalized gold film (working electrode), a platinum wire mesh (counter electrode), and a Ag/AgCl reference electrode (BASi, West Lafayette, IN). The gold working electrode was functionalized with 1-dodecanethethiol as described in detail elsewhere.[26,27] The cyclic voltammograms presented here were obtained after cycling the applied potential until the measured current did not change from one cycle to the next, typically around 10 cycles.

5.3 Results and Discussion

Our first measurements were performed to demonstrate that MFMT does not self-assemble in aqueous solution under the condition of our experiments. To this end, we performed surface tension measurements on aqueous solutions containing MFMT and FTMA, both in their

reduced redox states (Fig. 5.3). We measured the surface tension of aqueous solutions (also containing 100 mM Li_2SO_4 adjusted to pH 5 by the addition of H_2SO_4) of MFMT (Fig. 5.3; red data) at concentrations ranging from 0.1 to 30 mM using the Wilhelmy plate method (see Methods). We observed an approximately linear decrease in surface tension with increasing MFMT concentration characteristic of a non-self-assembling organic solute (see inset of Fig. 5.3).[34] Specifically, we observed no break or plateau in the surface tension vs. concentration curve indicating the onset of self-assembly. In contrast, the surface tension vs. concentration curve for FTMA, which is consistent with prior reports,[28] has a break around ~0.1 mM FTMA and a plateau in surface tension at approximately 50 mN/m at concentrations of FTMA beyond ~0.1 mM, indicating self-assembly in bulk solution. Using Eq. 1, we calculate the maximum surface excess concentration of FTMA at the air/water interface to be 1.45 molecules/nm^2. Because FTMA self-assembles in bulk solution, its adsorption to the air/water interface does not appreciably increase beyond its critical micelle concentration. From these results, we chose to use 20.9 mM of either FTMA or MFMT as the redox mediator in our dye-sensitized solar cells. This concentration was selected because 20.9 mM FTMA self-assembles in aqueous 100 mM Li_2SO_4 solutions but 20.9 mM MFMT does not. From Eq. 1, we calculate the surface excess concentration of MFMT at 20.9 mM to be 2.59 molecules/nm^2, indicating greater adsorption of MFMT than FTMA at the air/water interface under the solution conditions used in experiments reported below.

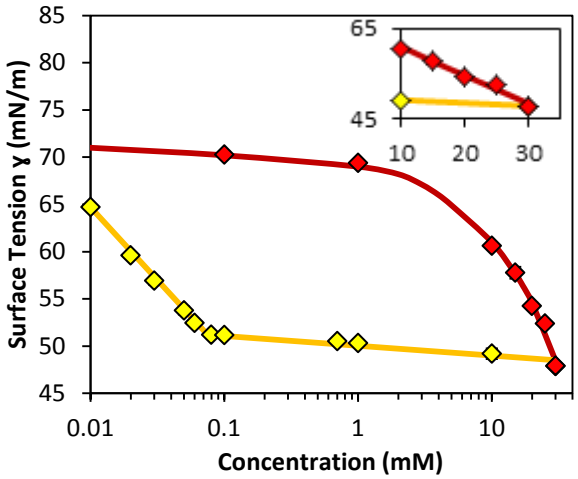

Figure 5.3 Surface tension of FTMA and MFMT
Surface tension measurements of aqueous solutions of either MFMT (red) or FTMA (yellow), each in their reduced redox state, in 100 mM Li_2SO_4. Surface tension measurements were made using a paper Wilhelmy Plate. The error bars are of the standard deviation between at least three measurements at each point. A clear break can be seen in the surface tension curve vs. concentration curve for FTMA but not for MFMT, suggesting that FTMA self-assembles in bulk solution at 20.9 mM but MFMT does not. The inset shows the surface tension data as a function of concentration with a linear scale from 10-30 mM.

Motivated by prior studies[26,27] that found a hydrophobic electrode to facilitate the self-assembly of FTMA in ways that lead to the inhibition of cathodic current in cyclic voltammograms, we functionalized the surface of the titania electrodes in our dye-sensitized solar cells with a dodecylphosphonate monolayer. Phosphonate chemistry was selected as a method of hydrophobizing titania surfaces due the ability of alkyl phosphonates to readily form an ordered hydrocarbon film on titania.[29,35-37] We used elliposometry (see Methods) to measure dodecylphosphonate films on titania substrates that were prepared by physical vapor deposition (nanoporous titania films are too rough to permit elliposometric methods). We measured a film thickness of 13 ± 2 Å, consistent with past studies[38] that have measured the ellipsometric thickness of a dodecylphosphonate monolayer to be 13 ± 1 Å. We also prepared cells without a dodecylphosphonate monolayer for comparison (see Fig. 5.4B).

Next, we performed cyclic voltammetry on aqueous solutions containing 100 mM Li_2SO_4 and 0.1 mM of either FTMA or MFMT (Fig. 5.1C). The cyclic voltammogram of FTMA (Fig. 5.1C; blue data) reveals the presence of current peaks on both the anodic and cathodic scans. On the anodic scan, we measure a prominent current peak (35 ± 4 μA) with a noticeable shoulder, which is indicative of adsorbed FTMA assemblies influencing the electron transfer process. On the cathodic scan, we observe a single cathodic peak current with a magnitude of (11 ± 4 μA), which is less than a third of the magnitude of the anodic peak. By averaging the positions of the anodic and cathodic current peaks, we determine the redox potential of FTMA to be 0.23 ± 0.02 V vs. Ag/AgCl. From the scan-rate dependence of the anodic and cathodic peak current (see Supporting Information Fig. 5.7), we can determine that adsorbed interfacial assemblies make a significant contribution to the faradaic current. These results are consistent with cyclic voltammograms of FTMA observed in past studies[26,27] and indicate an ability of FTMA to inhibit cathodic current while transmitting anodic current. In contrast, the cyclic voltammogram of MFMT (Fig. 5.1C; red data) reveals anodic and cathodic peak currents of comparable magnitude (22 ± 3 μA and 20 ± 2 μA for the anodic and cathodic peaks, respectively). Unlike FTMA, the scan-rate dependence of the current peaks observed with MFMT is consistent with a diffusion-limited charge transfer process (see Supporting Information Fig. 5.7). Overall, these measurements lead to two important observations. First, the cyclic voltammograms indicate that FTMA, which self-assembles, is able to inhibit cathodic reactions at a hydrophobized electrode and MFMT, which does not self-assemble, is not. Second, the redox potential of MFMT (0. 37 ± 0.02 V) is more positive than that of FTMA, which suggests that dye-sensitized solar cells that use N3 dye with MFMT as their redox mediator have the potential for a wider operating voltage range than those that use FTMA.

We measured the dark current passed in the test cells containing an aqueous redox solution with 100 mM Li_2SO_4 and 20.9 mM of either FTMA or MFMT by applying a linear potential sweep from 0 to 500 mV at the counter electrode relative the working electrode at a scan rate of 10 mV/s using a potentiostat (Fig. 5.4A). This potential window was selected to minimize the current transmitted across the aqueous 100 mM Li_2SO_4 electrolyte solution in the absence of redox mediator (see Fig. 5.4A; gray data). In the absence of illumination, the applied potential is reducing at the working electrode and oxidizing at the counter electrode. Current measured under these conditions (called dissipative current) arises from charge transfer processes equivalent to the recombination reaction shown in red in Fig. 5.2C. Throughout this paper, we plot dissipative current as negative. Inspection of Fig. 5.4A reveals that little dark current is transmitted by FTMA-based and MFMT-based cells at applied potentials less than 300 mV. The absence of dark current likely results from the bulk redox solution consisting of entirely reduced mediator (i.e. without generating oxidized mediator via photoreaction, none is present to transport electrons toward the counter electrode). In a dye-sensitized solar cell, the potential of the counter electrode is fixed by the potential of the redox solution (because no reference electrode is used). This results in the absolute potential of cells containing different redox solutions to differ despite the application of the same voltage difference between the working and counter electrodes. Because the redox potential of MFMT is 0.37 ± 0.02 V vs. Ag/AgCl and the redox potential of FTMA is 0.23 ± 0.02 V vs. Ag/AgCl (measured via cyclic voltammetry; see Fig. 5.1C), the onset of dark current occurs in cells with FTMA at a lower applied voltage difference between the working and counter electrodes than the applies voltage difference at which dark current is generated in MFMT-based cells. In addition to the redox mediator itself, reduction of water may make a significant contribution to the dark current we measure. We

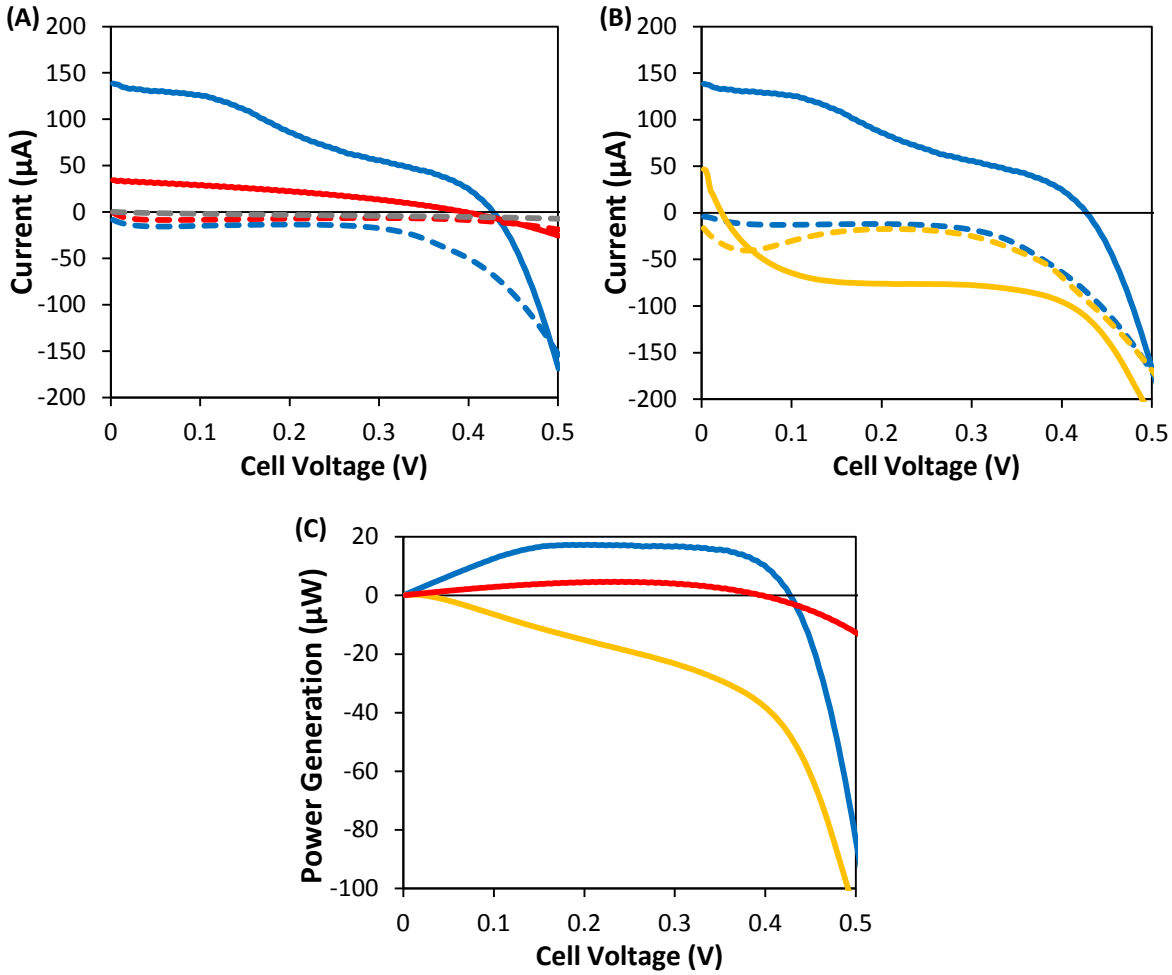

Figure 5.4 Cell Performance with 20.9 mM FTMA or MFMT
(A) Current vs voltage curves for dye-sensitized solar cells consisting of a titania working electrode functionalized by a dodecylphosphonate monolayer, adsorbed N3 dye, a gold counter electrode, and an aqueous redox solution containing 100 mM Li_2SO_4 either alone (gray), or 20.9 mM FTMA (blue) or 20.9 mM MFMT (red), both in the dark (dotted lines) and under a 138 mW/cm^2 lamp (solid lines). **(B)** Current vs voltage curves for the same solar cells with 20.9 mM (blue) compared to otherwise identical cells with titania electrodes that were not functionalized by dodecylphosphonate. **(C)** The power generated by the cells in cells shown in (A) as a function of applied cell voltage.

comment that although the more positive redox potential of MFMT allows for an MFMT-based cell to more effectively block dissipative currents transmitted in the dark, to which water reduction may significantly contribute, that does not mean an MFMT-based cell will also more effectively inhibit recombination reactions when oxidized mediator is generated at the titania

electrode while the cell is producing photocurrent. The more favorable redox potential of MFMT does give it an advantage over FTMA in power generation because a greater voltage difference can be applied to the cell before significant dissipative current is transmitted.

We next performed a linear potential sweep under illumination by a 138 mW/cm^2 lamp on the cell containing MFMT (Fig. 5.4A; red data). Under illumination, dye molecules adsorbed to the titania working electrode absorb photons and release electrons into the titania conduction band. For the cell to generate power, the reaction at the working electrode must involve reduction of oxidized dye by the redox mediator in solution. This current, called photocurrent, corresponding to power generation, is plotted as positive throughout this paper. In order to generate photocurrent, the cell must also be able to prevent electron transfer from the conduction band of the titania (and the excited dye) electrode to the oxidized mediator. At the onset of the applied potential sweep, the cell containing MFMT generates 30 ± 7 μA of short circuit current (current at zero applied voltage). As an increasingly reducing potential is applied at the working electrode during the potential sweep, the photocurrent is eventually overcome by the dissipative current from the applied potential. Once a potential of 365 ± 50 mV is reached, the total current becomes zero. At applied potentials beyond the open circuit voltage, the cell dissipates power rather than generating it. The power generated at each point along the linear sweep can be seen in Fig. 5.4C. From these results, we are able to determine the maximum power generation of the cell to be 3 ± 2 μW.

In contrast, when a linear potential sweep is performed on the FTMA-based cells (Fig. 5.4A; blue data) under illumination, the cell generates a short circuit current of 138 ± 5 μA, compared to the 30 ± 7 μA generated by the MFMT-based cell. We note that our surface tension measurements (Fig. 5.3) suggested that more MFMT adsorbs to the air/water interface under the

solution conditions used in our solar cells. While a hydrophobic solid surface is not the same as the air/water interface, we would also anticipate that more MFMT adsorbs to the electrode than FTMA. However, the FTMA cell, despite a lower expected density of mediator on the electrode surface, is able to generate more than four times as much photocurrent than the MFMT at an applied voltage of zero. We attribute the decrease in photocurrent seen in MFMT cells compared to FTMA cells to recombination reactions between the electrode and MFMT, newly oxidized by the excitation of the dye under illumination. The additional photocurrent generated in the FTMA-based cell also results in the generation of a maximum power of 17.5 ± 0.2 μW, which is greater than the 3 ± 2 μW of power generated by the MFMT cell. Despite its less optimal redox potential and greater dark current, the FTMA-based cell exhibits an open circuit voltage of 432 ± 2 mV, which is greater than the open circuit voltage of the MFMT cells (365 ± 50 mV). Overall, these measurements indicate that FTMA is able to facilitate photo-induced charge-separation as a redox mediator in dye-sensitized solar cells more effectively than MFMT. We interpret our measurements of the FTMA cells in the context of past studies,[26-28] which have shown that the ability of FTMA to rectify current at an electrode in contact with an aqueous FTMA solution to result from the formation of hemimicellar reduced FTMA assemblies on the electrode surface that expel oxidized FTMA. We attribute the inhibition of recombination reactions observed in the FTMA-based cells to result from the expulsion of oxidized FTMA from the electrode by interfacial reduced FTMA assemblies. In contrast, MFMT does not self-assemble and is unable to inhibit recombination reactions. As a result, we observe less power generation in MFMT-based cells.

We note that the counterions of each of these compounds, iodide in the case of MFMT and bromide in the case of FTMA, can function as redox mediators in dye-sensitized solar

cells.[39] Past studies have shown that iodide is significantly more effective than bromide at reducing ruthenium-based dyes such as N3 dye, which was used in these experiments, due to the more positive redox potential of bromide than iodide (+0.84 V vs Ag/AgCl rather than +0.32 V vs. Ag/AgCl for bromide and iodide respectively).[39,40] Specifically, past studies[40] found that the photocurrent generated by bromide-based cells with a ruthenium-based dye is less than 2% of that generated by iodide-based cells. Thus, the improved performance of FTMA-based cells (with bromide as the counterion) over MFMT-based cells (with iodide as the counterion) result from the self-assembly behavior of FTMA rather than from bromide. To confirm that the difference in counterion is not responsible for the difference in behavior of MFMT and FTMA based cells, we exchanged the iodide in MFMT (as purchased) for bromide and found a decrease in the power generated by MFMT cells (see Supporting Information Fig. 5.8-5.9).

From our conclusion that the self-assembly of FTMA causes it to block recombination reactions in dye-sensitized solar cells (with dodecylphosphonate-functionalized titania electrodes) more effectively than MFMT, we hypothesized that the performance of FTMA-based cells would be dependent on the surface chemistry of the working electrode. We were motivated by past studies[26,27] that found the presence of a hydrophobized layer on the electrode to be necessary for the formation of adsorbed hemimicelles that block oxidized FTMA in bulk solution from accessing the electrode. In order to investigate the role of a hydrophobized layer in facilitating interfacial self-assemblies of FTMA to inhibit recombination reactions in dye-sensitized cells, we fabricated cells without dodecylphosphonate. We measured the performance of cells without dodecylphosphonate with an aqueous redox solution containing 100 mM Li_2SO_4 and 20.9 mM FTMA (Fig. 5.4B; yellow data) and found them to yield a maximum power output of 0.4 ± 0.3 μW (compared to 17.5 ± 0.2 μW generated by FTMA cells with a

dodecylphosphonate monolayer) with a short circuit current of 50 ± 20 μA and an open circuit voltage of 30 ± 10 mV. However, despite the decrease in power generation seen in the cells without dodecylphosphonate compared to those with dodecylphosphonate, we do not observe a significant change in their dark current. We interpret these results to suggest that without the presence of a hydrophobic film on the electrode surface, the formation of reduced FTMA hemimicelles that are able to expel oxidized FTMA (thus inhibiting recombination reactions) does not occur. In addition, this results shows that changes in surface chemistry lead to changes in the cell performance, giving further evidence that the self-assembly of FTMA underlies the ability of FTMA-based cells (with a dodecylphosphonate film on the titania electrode) to inhibit recombination reactions and generate photocurrent.

5.4 Conclusions

Overall, the study reported in this paper demonstrates that a self-assembling redox mediator can be used to improve the efficiency of photo-induced charge separation in a dye-sensitized solar cell. We found that FTMA-based cells were able to generate significantly more photocurrent than MFMT-based cells when illuminated by a white-light lamp despite MFMT having a more optimal redox potential. From these results we concluded that FTMA, which self-assembles, is more effective than MFMT, which does not at inhibiting recombination reactions in dye-sensitized cells in which the titania electrode surface is functionalized with a dodecylphosphonate monolayer despite MFMT having a more optimal redox potential for the cells used. We interpret our results to suggest that reduced FTMA forms hemimicelles on the surface of the hydrophobized titania electrode that expel oxidized FTMA from the assembly, and thus leading to the inhibition of recombination reactions whilst allowing for ample reduced FTMA in the vicinity of the electrode to replenish electrons to the oxidized dye. Further evidence

of the role of self-assembly in the ability of FTMA to inhibit recombination reactions can be seen in experiments demonstrating that without hydrophobization of the titania electrode, the cells do not generate significant power. Together, the results reported in this paper demonstrate that self-assembly can be used in the design of dye-sensitized solar cells capable of rectifying current and generating power. In future studies we will employ strategies that rely on self-assembly to improve upon the performance of the cells described here, such as adding redox-inactive surfactants to influence the micellar assemblies formed on the electrode.

5.5 Acknowledgements

This work was primarily funded by the National Science Foundation through grant CBET- 1263970. Partial support is also acknowledged by the ARO (through W911NF-14-1-0140 and W911NF-15-1-0568). The authors acknowledge the use of instrumentation supported by the Wisconsin Materials Research Science and Engineering Center (DMR-1121288). The authors also thank Prof. George Huber for potentiostat access and Dr. Ryan Clark for assistance in attaining the irradiance and spectral output of the lamp used in this work.

5.6 References

‡ Portions of this chapter will be submitted as: T. J. Smith, C. X. Wang and N. L. Abbott, *Influence of Self-Assembly of a Redox Mediator on Dye Sensitized Solar Cells*, In Preparation, (2017).

1. S. Y. Huang, G. Schlichthörl, A. J. Nozik, M. Grätzel, A. J. Frank, *J. Phys. Chem. B* **1997**, *101* (14), 2576–2582.

2. Q. Wang, J. E. Moser, M. Grätzel, *J. Phys. Chem. B* **2005,** 109 (31), 14945–14953.

3. Q. Wang, S. Ito, M. Grätzel, F. Fabregat-Santiago, I. Mora-Seró, J. Bisquert, T. Bessho, H. Imai, *J. Phys. Chem. B* **2006,** 110 (50), 25210–25221.

4. G. Boschloo, A. Hagfeldt, *Acc. Chem. Res*., **2009**, *42* (11), 1819–1826.

5. S. A. Haque, Y. Tachibana, R. L. Willis, J. E. Moser, M. Grätzel, D. R. Klug, J. R.; Durrant, *J. Phys. Chem. B* **2000**, *104* (3), 538–547.

6. S. Ito, P. Liska, P. Comte, R. L. Charvet, P. Péchy, U. Bach, L. Schmidt-Mende, S. M. Zakeeruddin, A.; Kay, M. K. Nazeeruddin, M. Grätzel, *Chem. Commun.*, **2005**, *34*, 4351–4353.

7. A. C. Fisher, L. M Peter, E. A. Ponomarev, A. B. Walker, K. G. U. Wijayantha, *J. Phys. Chem. B* **2000**, *104* (5), 949–958.

8. J. Bisquert, F. Fabregat-Santiago, I. Mora-Seró, G. Garcia-Belmonte, S. Giménez, *J. Phys. Chem. C* **2009**, *113* (40), 17278–17290.

9. E. Palomares, J. N. Clifford, S. A. Haque, T. Lutz, J. R. Durrant, *J. Am. Chem. Soc.* **2003**, *125* (2), 475-482.

10. M. Wang, N. Chamberland, L. Breau, J.-E. Moser, R. Humphrey-Baker, B. Marsan, S. M. Zakeeruddin, M. Grätzel, *Nat. Chem.* **2010**, *2* (5), 385-389.

11. H. Tian, X. Jiang, Z. Yu, L. Kloo, A. Hagfeldt, L. Sun, *Angew. Chem. Int. Ed.* **2010**, *49* (40), 7328-7331.

12. S. M. Feldt, E. A. Gibson, E. Gabrielsson, L. Sun, G. Boschloo, A. Hagfeldt, *J. Am. Chem. Soc.* **2010**, *132* (46), 16714-16724.

13. Y. Liu, J. R. Jennings, Y. Huang, Q. Wang, S. M. Zakeeruddin, M. Grätzel, *J. Phys. Chem. C* **2011**. *115* (38), 18847-18855.

14. B. A. Gregg, F. Pichot, S. Ferrere, C. L. Fields, *J. Phys. Chem. B* **2001**, *105* (7), 1422-1429.

15. Z. Zhang, P. Chen, T. N. Murakami, S. M. Zakeeruddin, M.; Grätzel, *Adv. Funct. Mater.* **2008**, *18* (2), 341-346.

16. C. H. Law, S. C. Pathirana, X. Li, A. Y. Anderson , P. R. F. Barnes, A. Listorti, T. H. Ghaddar, B. C. O ′ Regan, *Adv. Mater.* **2010**, *22* (40), 4505–4509.

17. H.-L. Lu, T. F.-R. Shen, S.-T. Huang, Y.-L. Tung, T. C.-K. Yang, *Sol. Energy Mater Sol. Cells* **2011**, *95* (7), 1624–1629.

18. Y.-S. Jung, B. Yoo, M. K. Lim, S. Y. Lee, K.-J. Kim, *Electrochimica Acta* **2009**, *54* (26), 6286–6291.

19. C. H. Law, O. Moudam, S. Villarroya-Lidon, B. C. O'Regan, *J. Mater. Chem.* **2012**, *22* (44), 23387–23394.

20. H. Zhang, L. Qiu, D. Xu, W. Zhang, F. Yan, *J. Mater. Chem. A* **2014**, *2* (7), 2221–2226.

21. T. Daeneke, Y. Uemura, N. W. Duffy, A. J. Mozer, N. Koumura, U. Bach, L. Spiccia, *Adv. Mater.* **2012**, *24* (9), 1222–1225.

22. F. E. Osterloh, *Chem. Mater.* **2008**, *20*, 35–54.

23. A. Kudo, T. Miseki, *Chem. Soc. Rev.* **2009**, *38*, 253–278.

24. W. J. Youngblood, S.-Y. A. Lee, K. Maeda, T. E. Mallouk, *Acc. Chem. Res.* **2009**, *42* (12), 1966-1973.

25. L. J. Minggu, W. R. W. Daud, M. B. Kassim, *Int. J. Hydrogen Energy* **2010**, *35*, 5233–5244.

26. T. J. Smith, C. Wang, N. L. Abbott, *Langmuir* **2015**, 31 (39), 10638–10648.

27. T. J. Smith, C. Wang, N. L. Abbott. *In Preparation*.

28. T. J. Smith, C. Wang, N. L. Abbott, *J. Colloid Interface Sci*. **2017**, *502*, 122–133.

29. E. S. Gawalt, M. J. Avaltroni, N. Koch, J. Schwartz, *Langmuir* **2001**, *17*, 5736–5738.

30. D. M. Spori, N. V. Venkataraman, S. G. P. Tosatti, F. Durmaz, N. D. Spencer, S. Zürcher, *Langmuir* **2007**, *23* (15), 8053–8060.

31. P. C. Hiemenz, R. Rajagopalan, *Principles of Colloid and Surface Chemistry*; 3rd Edition, Taylor & Francis Group: Boca Raton, FL, **1997**; p. 330.

32. G. L. Gaines, *J. Colloid Interface Sci.* **1977**, *62* (1), 191–192.

33. D. K. Chattoraj, K. S. Birdi, K.S., *Adsorption and the Gibbs Surface Excess*; Plenum Press: New York, NY, **1984**; p. 40.

34. P. C. Hiemenz, R. Rajagopalan, *Principles of Colloid and Surface Chemistry*; 3rd Edition, Taylor & Francis Group: Boca Raton, FL, **1997**; p. 328.

35. R. Helmy, A. Y. Fadeev, *Langmuir* **2002**, *18*, 8924–8928.

36. S. Tosatti, R. Michel, M. Textor, N. D. Spencer, *Langmuir* **2002**, *18*, 3537–3548.

37. M.-A. Neouze, U. Schubert, *Monatsh Chem* **2008** *139*, 183–195.

38. D. M. Spori, N. V. Venkataraman, S. G. P. Tosatti, F. Durmaz, N. D. Spencer, S. Zürcher, *Langmuir* **2007**, *23* (15), 8053–8060.

39. A. Hagfeldt, G. Boschloo, L. Sun, L. Kloo, H. Pettersson, *Chem. Rev.* **2010**, *110*, 6595–6663.

40. G. Wolfbauer, A. M. Bond, J. C. Eklund, D. R. MacFarlane, *Sol. Energy Mater Sol. Cells* **2001**, *70* (1), 85–101.

5.7 Supporting Information

5.7.1 Additional Samples of FTMA-based Solar Cells

Figure 5.5 shows additional current vs voltage curves for dye-sensitized solar cells consisting of a titania working electrode functionalized by a dodecylphosphonate monolayer, adsorbed N3 dye (before functionalization), a gold counter electrode, and an aqueous redox solution containing 20.9 mM FTMA and 100 mM Li_2SO_4 both in the dark (dotted lines) and under a 138 mW/cm^2 lamp (solid lines). These results demonstrate the reproducibility of the power generation in FTMA-based solar cells presented in this paper.

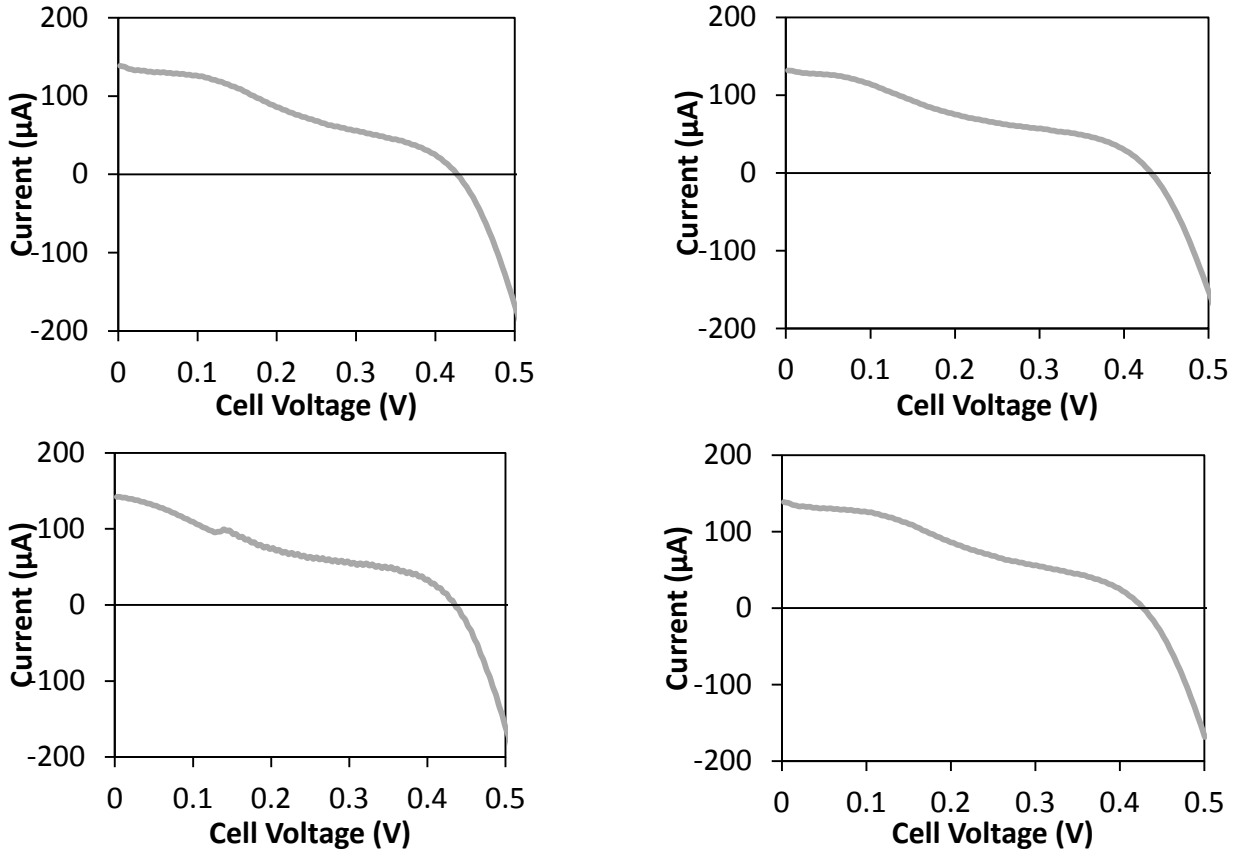

Figure 5.5 Currents vs voltage plots for illuminated DSCs with FTMA
Current vs voltage curves for dye-sensitized solar cells consisting of a titania working electrode functionalized by a dodecylphosphonate monolayer, adsorbed N3 dye (before functionalization), a gold counter electrode, and an aqueous redox solution containing 20.9 mM FTMA and 100 mM Li_2SO_4 under illumination by a 138 mW/cm^2 lamp.

5.7.2 Spectral Output of Lamp used to Test Solar Cells

Figure 5.6 shows the spectral output of the lamp used to test the solar cells in this paper as measured with a Vernier Go Direct SpectroVis Plus Spectrophotometer.

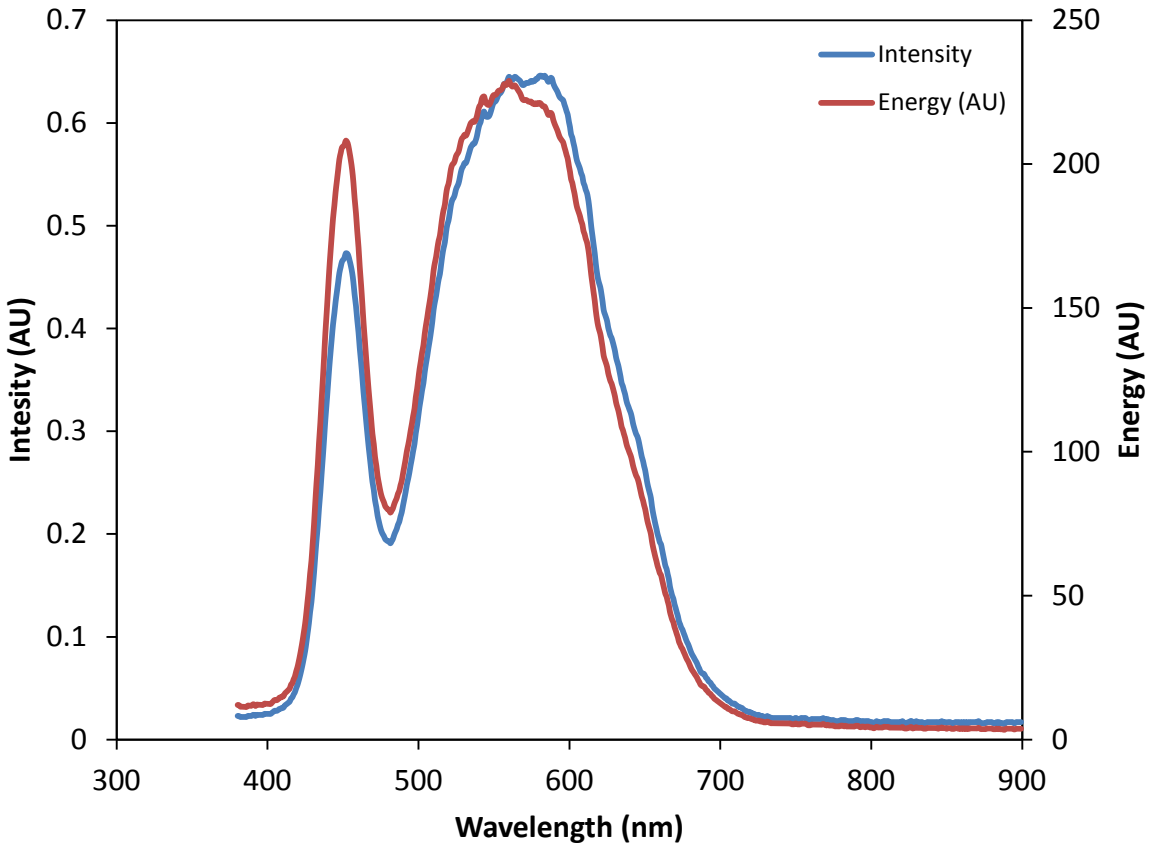

Figure 5.6 Spectral output of lamp used to test DSCs
Spectral output of the lamp used to test the solar cells in this paper as measured with a Vernier Go Direct SpectroVis Plus Spectrophotometer.

5.7.3 Scan-rate Dependence of MFMT and FTMA Cyclic Voltammograms

Figure S3 shows the scan-rate dependence of cyclic voltammograms performed on aqueous solutions containing 100 mM Li_2SO_4 and 20.9 mM of either MFMT or FTMA. From the dependence of peak current, I_p, on scan rate, ν:

$$I_p \sim \nu^{\chi} \tag{5.2}$$

we can gain insight into the processes underlying electron transfer in a cyclic voltammogram. In particular, the exponent in Eq. 5.2, χ, is calculated for cyclic voltammograms of FTMA and MFMT, and compared to the expected value for current limited by the diffusion of a reacting species from bulk solution to the electrode, where $\chi = 0.5$ and the peak current can be modeled by the Randle-Sevcik Equation,[1]

$$I_p = 0.4463 n^{3/2} \sqrt{\frac{F^3}{RT}} A \mathcal{D}^{1/2} C \nu^{1/2} \tag{5.3}$$

and the expected value of $\chi = 1$ for a system where the redox species is adsorbed on the electrode's surface:[2]

$$I_p = \left(\frac{n^2 F^2}{4RT}\right) A \nu \Gamma_o \tag{5.4}$$

In Eq. 5.3 and Eq. 5.4, n is the number of moles of electrons transferred in the reaction, F is the Faraday constant, R is the ideal gas constant, T is the system temperature, A is the surface area of the electrode, $\mathcal{D}$ is the diffusion coefficient of a redox species diffusing from bulk solution, C is the concentration of the redox species in bulk solution, and Γ_o is the surface concentration of adsorbed redox species.

From this analysis, we can determine that the electron transfer seen with MFMT is characteristic of a diffusion-limited electron transfer process and that both diffusing and adsorbed FTMA contribute significantly to its electron transfer processes. This behavior is consistent with the self-assembly of FTMA affecting its charge transfer, whereas in contrast, MFMT does not self-assemble.

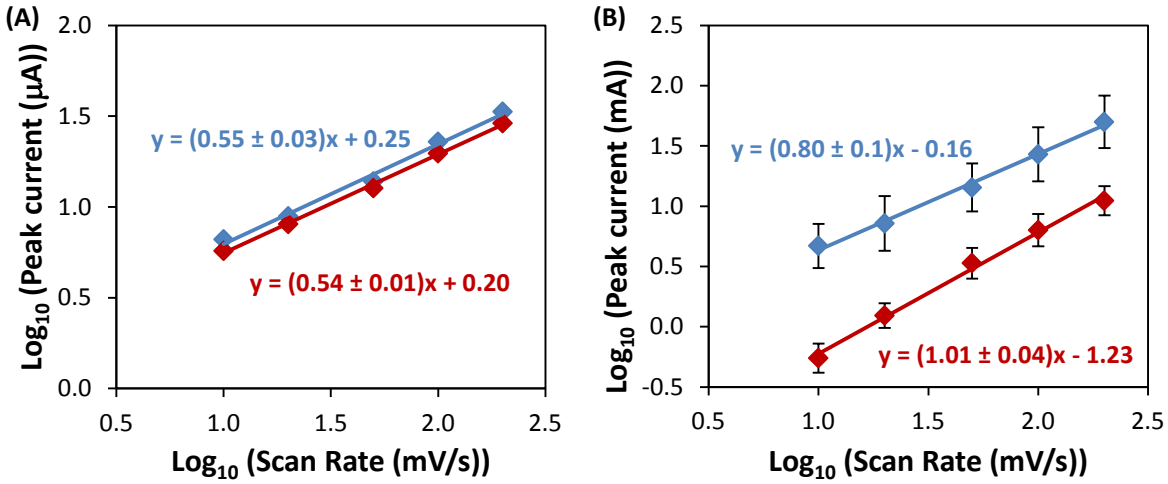

Figure 5.7 Scan-rate Dependence of Cyclic Voltammograms of MFMT and FTMA
Scan rate dependence of cyclic voltammograms performed on aqueous solutions containing 100 mM Li_2SO_4 and 20.9 mM of either **(A)** MFMT or **(B)** FTMA. The anodic peak current is shown in blue and the cathodic peak in red.

5.7.4 MFMT Ion Exchange

To confirm that the improvement in power generation observed in FTMA-based solar cells over those using MFMT was not a result of MFMT having an iodide counterion and FTMA having a bromide counterion, we performed an ion exchange on MFMT solutions. First, aqueous solutions containing 26.1 mM MFMT (with iodide) and 100 mM Li_2SO_4 were prepared. 14.4 mM Ag_2SO_4 was added and the solutions were subsequently sonicated for 15 minutes to allow for mixing. The resulting mixtures were then centrifuged using an Eppendorf 5417R centrifuge (Hamburg, Germany) at 12,000 rpm for 15 minutes. The supernate was drawn off and, because the addition of Ag_2SO_4 was found to partially oxidize the MFMT solution, the solution was electrochemically reduced as described previously.[3] Cyclic voltammetry was performed (see Fig. 5.8) to confirm the successful replacement of iodide with sulfate as the counter ion of MFMT. The resulting MFMT solution was then diluted in LiBr to yield a solution containing 20.9 mM MFMT, 20.9 mM bromide, and 100 mM Li_2SO_4. Dye-sensitized solar cells containing the resulting solution were fabricated and compared to those containing MFMT with iodide counterions (see Fig. 5.9).

Figure 5.8 shows cyclic voltammograms performed on aqueous solutions containing 100 mM Li_2SO_4 and 20.9 mM MFMT prior to (orange) and after (blue) the exchange of iodide counter ions for sulfate ions. A cyclic voltammogram of 20.9 mM NaI is shown in gray as a comparison. These cyclic voltammograms provide confirmation that the replacement of iodide with sulfate in MFMT was successful.

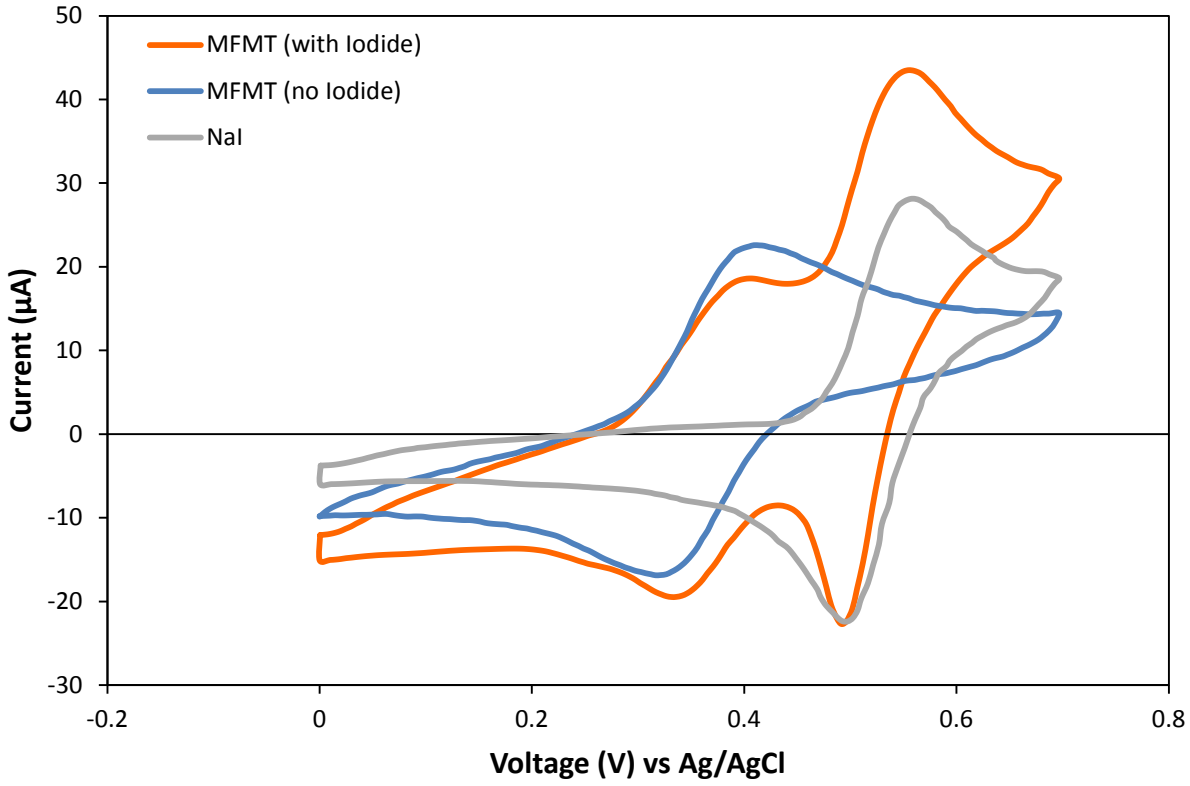

Figure 5.8 CV of MFMT solutions before and after removal of iodide
Cyclic voltammograms performed with a dodecanethiol-functionalized gold electrode, platinum mesh counter electrode, and Ag/AgCl reference electrode on aqueous solutions containing 100 mM Li_2SO_4 and either 0.1 mM MFMT with iodide counter ions (orange), MFMT with the iodide counter ions replaced by sulfate as described in the main text (blue), or 0.1 mM NaI. The scan rate was 100 mV/s.

Figure 5.8 shows the current vs. voltage curves MFMT-based cells with either bromide or iodide as their counterion. These results demonstrate that the presence of bromide does not improve the performance of MFMT cells, thus suggesting that the increased photocurrent seen in FTMA-based cells occurs due to the self-assembly of FTMA rather than the presence of bromide counterions.

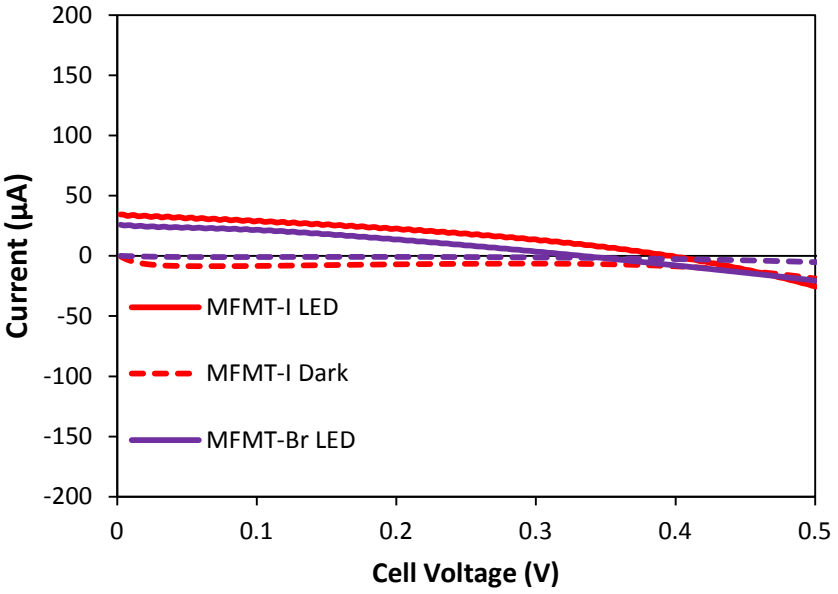

Figure 5.9 Performance of MFMT Cells with Bromide or Iodide as Counterions
Current vs voltage curves for dye-sensitized solar cells consisting of a titania working electrode functionalized by a dodecylphosphonate monolayer, adsorbed N3 dye (before functionalization), a gold counter electrode, and an aqueous redox solution containing 20.9 mM MFMT, either with iodide counterions (red) or bromide counterions (purple),
and 100 mM Li_2SO_4, both in the dark (dotted lines) and under a 138 mW/cm^2 lamp (solid lines).

2.9 Supporting References

1. A. J. Bard, L. R. Faulkner, *Electrochemical Methods: Fundamentals and Applications*; 2nd Edition, Wiley: New York, NY, **2004;** p. 231, p. 231.

2. A. J. Bard, L. R. Faulkner, *Electrochemical Methods: Fundamentals and Applications*; 2nd Edition, Wiley: New York, NY, **2004;** p. 231, p. 591.

3. X. Liu, M. D. Graham, N. L. Abbott, *Langmuir* **2007**, *23* (19), 9578–9585.

Chapter 6 : Redox-Triggered Transformations of Liposomes into Cubosomes‡

6.1 Introduction

Lyotropic liquid crystalline (LC) dispersions are widely regarded as a promising potential means for non-invasive drug delivery.[1-6] Past studies have shown that solutes (i.e. drugs, proteins, or peptides) can be encapsulated in lyotropic LC dispersions and released upon external stimuli, such as a change in temperature,[7] pH,[8,9] or activation by electromagnetic radiation.[10] Essential to these controlled release strategies is a phase transformation of the lyotropic LC dispersion. Lyotropic LCs form a number of distinct phases including lamellar, inverse bicontinuous cubic (with multiple geometries), inverse hexagonal, and inverse discontinuous micellar cubic.[11,12] Solutes (such as drugs) can be encapsulated in these aggregates and their diffusion (ie. release) depends greatly on the phase of the aggregates.[13] In this paper, we investigate a redox-triggered phase change in aqueous lyotropic LC dispersions with redox-active surfactant doped into the dispersion. Our objective in this study was to demonstrate how lyotropic LC dispersions could be controlled by redox reaction.

Lyotropic LC dispersions can be formed in aqueous solution by a variety of amphiphilic compounds, such as phytantriol,[60,14,15] oleines,[16-18] and phospholipids.[19] In this paper, we selected phytantriol as an amphiphilic molecule that forms lyotropic LC dispersions when mixed with water. The phase behavior of phytantriol/water systems has been well characterized in past studies.[60,14,15] Aqueous dispersions of phytantriol in the absence of other surfactants containing 10 wt% lipid are known to form an inverse bicontinuous cubic phase (called “cubosomes” when dispersed) with Pn3m (double diamond) symmetry at 25°C (see Fig. 6.1). The phase behavior of

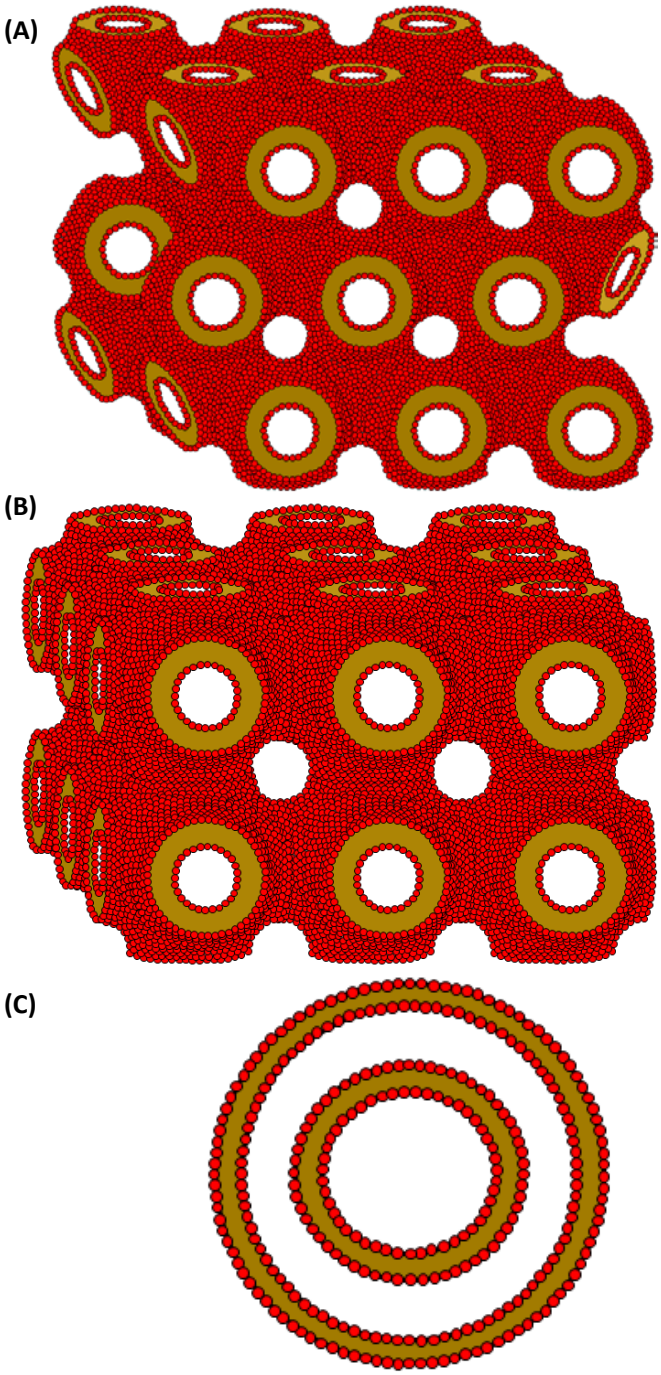

Figure 6.1 Schematics of cubic and lamellar lyotropic LC phases
Schematics showing the structure of three phases formed by the lyotropic dispersions discussed in this paper: two inverse bicontinuous cubic geometries: **(A)** Pn3m and **(B)** Im3m, and a **(C)** lamellar phase.

phytantriol has been found to be sensitive to solutes, such as Vitamin E,[15] or conventional surfactants.[20,21] Past studies have shown that phytantriol/water dispersions that also contain linear or double-tailed cationic surfactants, such as didodecyldimethylammonium bromide (DDAB)[20] or dodecyltrimethylammonium bromide (DTAB),[21] form lamellar phases (called "liposomes" when dispersed). From these past studies, we hypothesized that the incorporation of linear cationic ferrocenyl surfactants, such as 11-ferrocenyl trimethylammonium bromide (FTMA; Fig. 6.2), into phytantriol aggregates would also lead to changes in packing geometry, and thus phase changes.

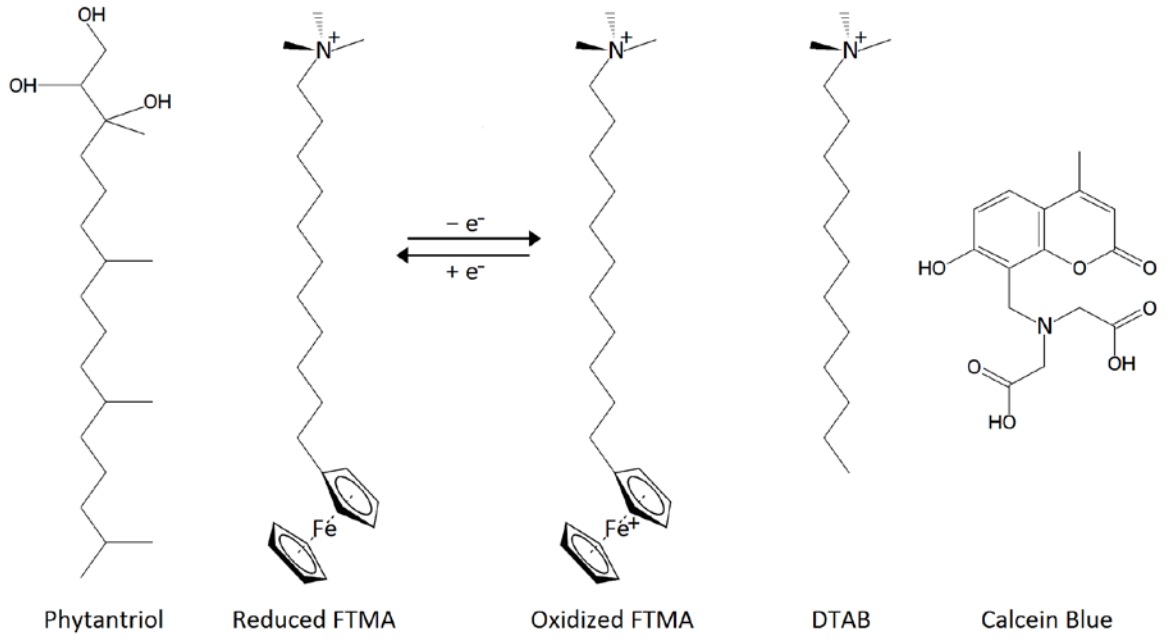

Figure 6.2 Molecular structures of phytantriol, FTMA, DTAB, and calcein blue
Molecular Structures of Phytantriol, Reduced 11-ferrocenylundecyltrimethyl ammonium bromide (FTMA), Oxidized FTMA, dodecyltrimethylammonium bromide (DTAB), and calcein blue. Bromide ions not shown.

These effects on the phase behavior of phytantriol/water systems are thought to occur because of changes in the packing geometry of mixed aggregates due to the introduction of DDAB and DTAB. The behavior of a amphiphiles in a self-assembly can be described using a critical packing parameter:[22,23]

$$cpp = v/a_o\ell_c \tag{6.1}$$

where a_o is the optimal area of the surfactant headgroups, v is the volume of the hydrophobic surfactant tail, and ℓ_c is the critical chain length of the hydrophobic surfactant tail, which is the longest the tail can extend without suffering a significant entropic penalty. The packing parameter allows us to understand the relationship between the architecture of the surfactants in an assembly and the curvature of the self-assembly. Inverse phases, such as cubosomes and hexasomes, are able to form when cpp > 1. Lamellar phases form when ½ < cpp < 1. Reduced FTMA[24] and DTAB,[25] which have a single, unbranched hydrocarbon chain, form globular micellar aggregates in water (in the absence of other surfactant) with cpp ≈ ⅓. Phytantriol, on the other hand, has a branched hydrocarbon tail resulting in the formation of aggregates with cpp > 1, which gives rise to the lyotropic LC phases described above. We anticipate that the addition of FTMA and DTAB will lead to a decrease in the cpp of phytantriol-based aqueous dispersions, thus leading to changes in their phase behavior.

Ferrocenyl surfactants have been used in numerous systems because of their redox-driven changes in aggregation in bulk solution and at interfaces. For example, past studies involving the ferrocenyl surfactant bis(*n*-ferrocenylundecyl)dimethylammonium bromide (BFDMA) have been shown to form multilamellar complexes with DNA that can be exploited to transfect DNA into

cells when the BFDMA is in its reduced redox state but not when BFDMA is in its oxidized state.[26,27] As an example of a redox-active surfactant that can be added to phytantriol/water dispersions, we selected 11-ferrocenyltrimethylammonium bromide (FTMA). FTMA is a redox-active surfactant containing the ferrocene moiety at one end of a hydrocarbon chain and a trimethylammonium group at the other end.[28] FTMA forms globular micelles in bulk solution in its reduced state and these micelles reversibly dissociate when FTMA is oxidized and becomes an asymmetric bolaform surfactant. We anticipated that this change in FTMA behavior upon oxidation would lead to a phase change in phytantriol/FTMA dispersions upon oxidation and sought to exploit it by the addition of a redox agent. Specifically, we made dispersions of phytantriol, FTMA, and DTAB in 1 mM aqueous Li_2SO_4 to test the concepts outlined below.

In this paper, we investigated the following key questions using the principles described above: (i) how the addition of FTMA (in each redox state) affects the phase behavior of phytantriol in an aqueous dispersion, (ii) whether we can trigger a phase transformation in the phytantriol/FTMA dispersions by changing the oxidation state of FTMA, and (iii) whether the system can be used to release an encapsulated solution upon a redox trigger.

6.2 Experimental section

6.2.1 Materials

DTAB, Li_2SO_4, Pluronic F-127, and calcein blue were purchased from Sigma Aldrich (St. Louis, MO). $Fe_2(SO_4)_3$ was purchased from Acros chemicals (Geel, Belgium). FTMA was purchased from Dojindo Molecular Technologies (Rockville, MD). Phytantriol was purchased from DSM Nutritional Products (Singapore). All materials were used as received. Aqueous solutions were prepared using deionized water with a resistivity of 18.2 MΩ-cm that had been

purified by a Millipore Synergy Ultrapure Water System (Darmstadt, Germany). An Osmonics Inc. (Penang, Malaysia) 50 nm polycarbonate membrane filter was used for filtration of samples containing calcein blue during the triggered release experiments.

6.2.2 Experimental methods

6.2.2.1 Sample Preparation

Aqueous solutions of 1 mM Li_2SO_4 were prepared by dissolving Li_2SO_4 in deionized water and adjusting to pH 5 by the addition of sulfuric acid. DTAB, Pluronic F-127, and reduced FTMA were dissolved in aqueous Li_2SO_4 solutions directly. Samples containing oxidized FTMA were either oxidized electrochemically as described previously,[29] or prepared as solutions of reduced FTMA and subsequently oxidized by the addition of $Fe_2(SO_4)_3$. The aqueous solutions were then mixed with phytantriol and dispersed using a tip sonicator.

6.2.2.2 Small Angle X-Ray Scattering (SAXS)

The geometry of the structures of the aggregates in the dispersions was analyzed using Small Angle X-ray Scattering (SAXS). SAXS measurements were performed using the SAXS/WAXS beamline at the Australian Synchrotron (Clayton, VIC). Two-dimensional SAXS patterns were collected with a Pilatus 1 M detector (170 mm x 170 mm) that was 900 mm from the samples with an exposure time of 1s. The structure of the dispersions was analyzed from the ratio of the scattering vector, *q*, values of the Bragg reflections seen in SAXS. From the *q* of the Bragg scattering data, the lattice spacing, *d*, of lyotropic phases in the dispersion can be calculated by:

$$d = 2\pi\sqrt{h^2 + k^2 + l^2}/q \qquad (6.2)$$

SAXS was used to perform two types of experiments on these dispersions: equilibrium measurements and dynamic activation experiments.

Equilibrium SAXS measurements were performed by mounting glass capillary tubes, filled with samples of the dispersion, in the beam path. The temperature of the capillary holder was maintained using a hot water bath. SAXS was performed on these samples at temperatures varying from 25°C to 80°C in 5°C increments. Measurements were performed under temperature equilibrium conditions.

In addition to equilibrium measurements, SAXS measurements were also used to detect phase changes when exposed to a stimulus in real time. A schematic of the experimental setup of our dynamic activation experiments is shown in Figure 6.3. Dispersions containing phytantriol, reduced FTMA, and DTAB were initially placed in a reaction vessel with a magnetic stir bar on a magnetic stir plate. SAXS measurements were taken by wicking some of the dispersion through a capillary tube in the path of the x-ray beam. After a 1s exposure, the sample was reinjected to the vessel. A second remotely activated syringe was used to inject $Fe_2(SO_4)_3$ to the vessel in order to oxidize the FTMA and trigger a phase change. Subsequent SAXS measurements were made to measure the phase change over time.

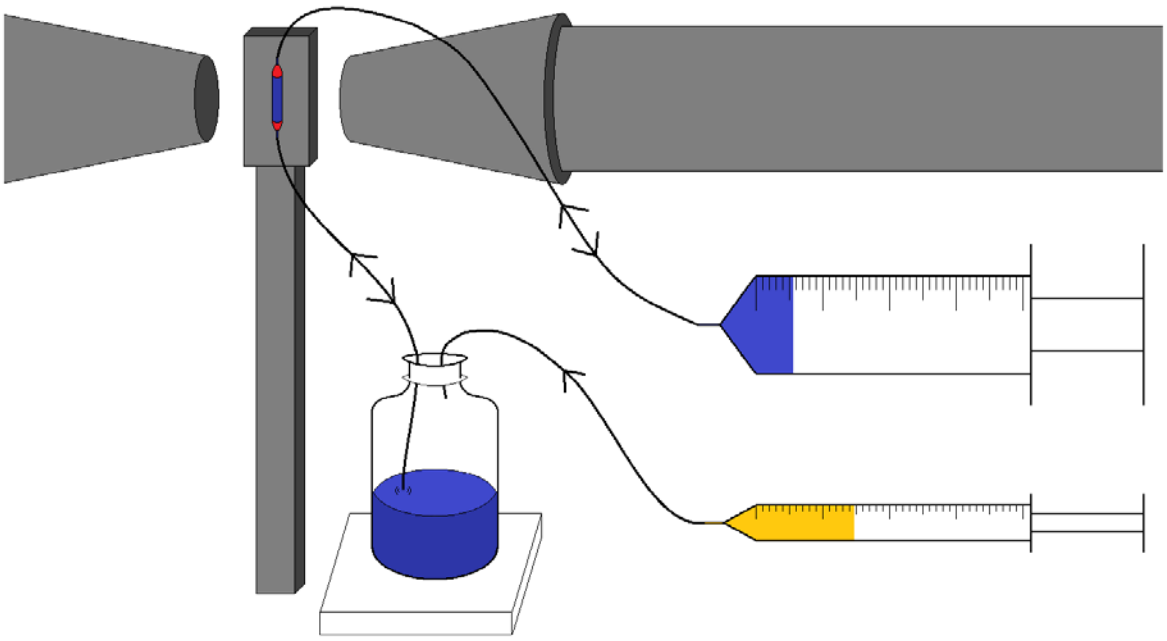

Figure 6.3 Experimental setup used in dynamic activation experiments
Experimental setup used in dynamic activation experiments performed using SAXS with a synchrotron source. The lyotropic liquid crystalline solution was initially placed in a vial with a magnetic stir bar on a magnetic stir plate. Two capillary tubes were run into the reaction vessel. One capillary tube was connected to a quartz capillary suspended in the path of the x-ray beam line. Each time a measurement was taken by SAXS, some of the lyotropic LC sample was drawn into the quartz capillary using a motor-controlled syringe. The second capillary was used to inject redox trigger into the reaction vessel from a second motor-controlled syringe.

6.2.2.3 Cryogenic Transmission Electron Microscopy (Cryo-TEM)

Dispersions containing 10% FTMA (in each redox state), 2% DTAB, and 88% Phytantriol in aqueous 1 mM Li_2SO_4 with 10 mg Pluronic F-127 polymer as a stabilizer were prepared as described above. 2 μL of each of these dispersions was placed on a carbon film-coated TEM grid, blotted using an FEI Vitrobot. The grid with the sample was then rapidly plunged into liquid ethanol, and then subsequently transferred to a TEM (Tecnai 12) with cryogenic capability. The TEM imaging was performed at 120 keV. The sample was kept below

-170 °C during imaging using a Gatan cryo-TEM holder. A Gatan ultrascan CCD (charge-coupled device**)** camera was used to collect TEM images.

6.2.2.4 Triggered Release

The dispersions used for triggered release experiments were prepared as described above except that calcein blue dye was dissolved in phytantriol before the samples were dispersed, resulting in the formation of liposomes loaded with calcein blue. In order to remove the calcein blue from the continuous phase, the loaded liposomes were passed through a size-exclusion column loaded with Sephadex G-50 (Pharmacia Fine Chemicals; Piscataway, NJ). Loaded liposomes were collected in the eluate. 2.5 mL of the eluate was added to a reaction vessel with 225 μg of $Fe_2(SO_4)_3$ as a redox trigger. Fractions of the sample were collected at 5, 30, 60, and 120 minutes after the addition of $Fe_2(SO_4)_3$, diluted by a factor of three with aqueous 1 mM Li_2SO_4, and filtered with 50 nm polycarbonate filter paper via an Emerson vacuum pump (St. Louis, MO) to remove the liposomes or cubosomes, which are approximately 100-200 nm in size. Another fraction was collected from the eluate, filtered, and then had 45 μg of $Fe_2(SO_4)_3$ added. This fraction was used to establish the background amount of calcein blue in the continuous phase of the dispersion after passing through a size-exclusion column. A final fraction was taken at the end of the timed release experiment and diluted in methanol in order to disrupt all aggregates and release any remaining calcein blue. The calcein blue content of these fractions was measured using UV-visible absorption spectroscopy with a Cary 100 scan UV-Visible Spectrophotometer (Agilent Technologies; Santa Clara, CA).

6.3 Results and Discussion

6.3.1 Incorporation of FTMA into Phytantriol Assemblies

We began by investigating how the addition of FTMA (in each redox state) affects the phase behavior of phytantriol in an aqueous dispersion. Our dispersions contained 88% Phytantriol, 10% FTMA (in either redox state), and 2% DTAB in aqueous 1 mM Li_2SO_4 (Fig. 6.4). Pluronic F-127 was used as a dispersing agent. We prepared the dispersions by mixing an aqueous 1 mM Li_2SO_4 solution containing FTMA, DTAB, and F-127 with phytantriol, and then dispersing the mixture using a tip sonicator. We prepared two dispersions with oxidized FTMA: one in which the FTMA had been oxidized electrochemically and the other in which the FTMA was oxidized chemically by $Fe_2(SO_4)_3$. The chemically oxidized sample was oxidized by the addition of $Fe_2(SO_4)_3$ until the concentration reached the amount needed to fully oxidize the FTMA (5.2 mM), assuming the reaction went to completion. Photographs of these samples can be seen in Fig. 6.4A. The sample containing reduced FTMA appears yellow and clear while, in contrast, the sample containing oxidized FTMA appears blue and cloudy. The color change in FTMA solutions from yellow to blue when oxidized has been well-documented in past studies.[28] The sample containing reduced FTMA has a noticeably higher viscosity than the sample containing oxidized FTMA. Both the viscosity and turbidity differences between the samples suggest that the sample containing reduced FTMA may be in a lamellar phase and the sample containing oxidized FTMA may be in a cubic or hexagonal phase.

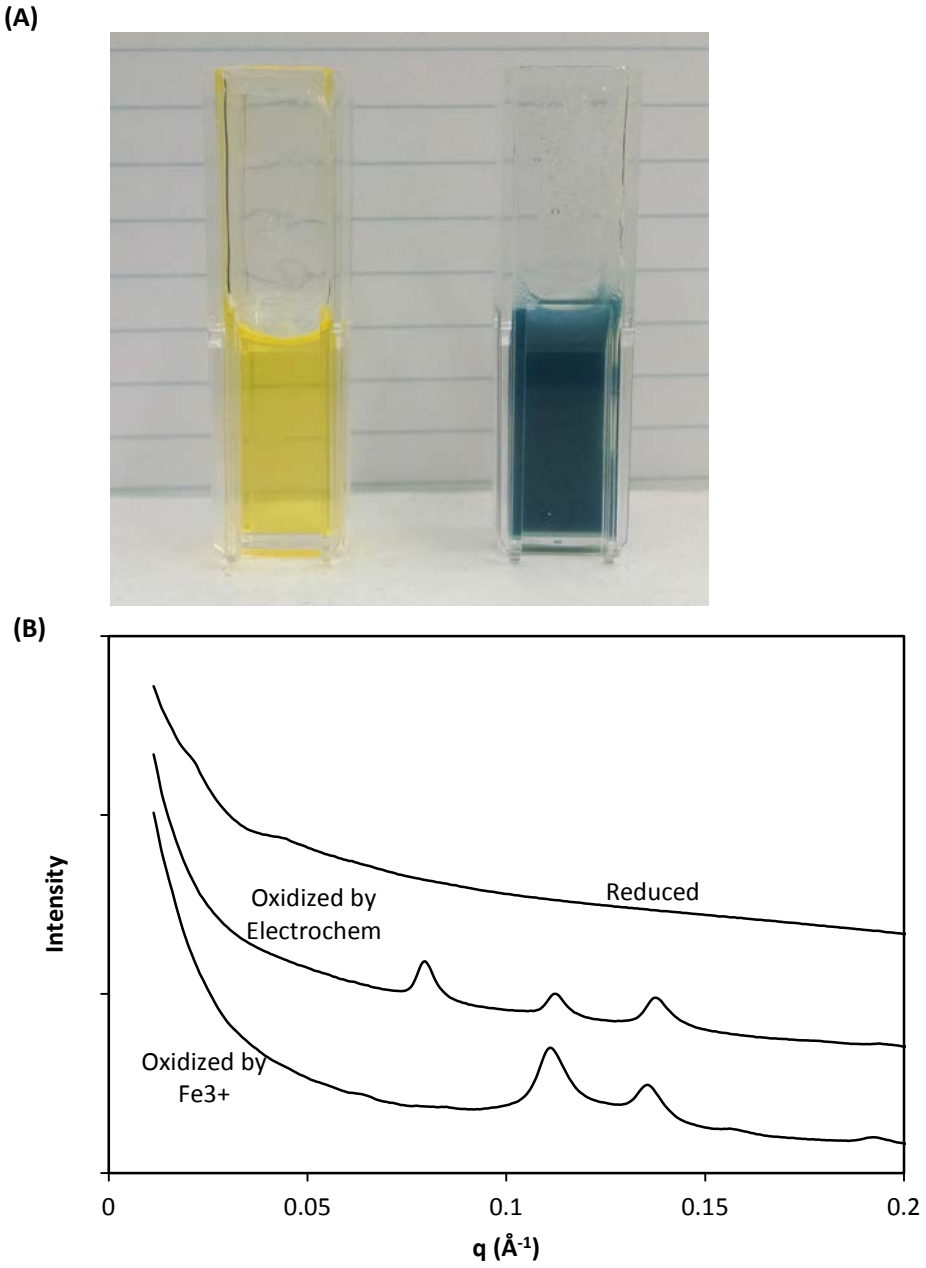

Figure 6.4 Pictures and SAXS diffractograms of FTMA/phytantriol dispersions
(A) Pictures of dispersions with 88% Phytantriol, 2% DTAB and 10% either reduced FTMA (left) or oxidized FTMA (right). **(B)** SAXS diffractograms of dispersions with 88% Phytantriol, 10% FTMA (reduced or oxidized either electrochemically or with $Fe_2(SO_4)_3$), and 2% DTAB in 1 mM Li_2SO_4. Each peak is labelled according to its relative position.

In order to determine the geometry of the phases formed by the samples described above, we performed SAXS (Fig. 6.4B). The sample containing reduced FTMA has two apparent peaks in its SAXS diffractogram at q = 0.02 Å^{-1} and q = 0.04 Å^{-1}. Since the second peak is at twice as large of a q as the first peak, these peaks can be interpreted as scattering from the diffraction planes {*hkl*} = {100} and {200}. The lattice spacing, *d*, calculated from the diffractograms by $d = 2\pi\sqrt{h^2 + k^2 + l^2}/q$ is 300 Å. Combined with the observations of the reduced sample described above (high viscosity and low turbidity), the SAXS diffractogram leads us to the conclusion that the dispersion containing reduced FTMA forms a multilamellar structure ("liposomes"). This result can be interpreted by considering the molecular packing of FTMA and phytantriol within their assemblies. As described in the introduction, the molecular packing of surfactants in assemblies can be described by their cpp (Eq. 6.1).[22,23] Phytantriol in the absence of other surfactant has a cpp > 1 at 25 °C in aqueous solution and forms an inverse cubic phase with Pn3m symmetry.[60] In contrast, reduced FTMA forms assemblies with cpp ≈ ⅓ in aqueous assemblies without additional surfactant. Thus, we would predict that if a sufficient amount of reduced FTMA is included in the phytantriol/FTMA assembly, the packing factor would be low enough for the self-assembly to be lamellar, as seen in the dispersion containing reduced FTMA in Fig. 6.4. This is in agreement with the behavior seen in prior studies of DDAB/Phytantriol and DTAB/Phytantriol systems.[20,21]

In contrast, a simple explanation for the behavior of the oxidized FTMA/phytantriol dispersions is less apparent. The SAXS diffractogram (Fig. 6.4B) of the electrochemically oxidized sample has Bragg reflections with relative positions, *q*, corresponding to multiples of $\sqrt{2}$, $\sqrt{4}$, $\sqrt{6}$. These correspond to the diffraction planes {*hkl*} = {110}, {200}, and {211}. This diffractogram is consistent with cubosomes that have Im3m symmetry and a lattice spacing of

112 Å, calculated using Eq. 6.2. The SAXS diffractogram of the sample oxidized with $Fe_2(SO_4)_3$ has peaks with the relative positions $\sqrt{2}$, $\sqrt{3}$, $\sqrt{4}$, $\sqrt{6}$. These correspond to the diffraction planes {*hkl*} = {110}, {111}, {200}, and {211}. This diffractogram is consistent with cubosomes that have Pn3m symmetry and a lattice spacing of 80 Å, calculated using Eq. 6.2. Consistent with our expectations from the visual appearance of the samples, we conclude that both dispersions containing oxidized FTMA are cubosomes. However, the geometry of the inverse cubic phase is dependent on whether the FTMA was oxidized electrochemically or by the addition of $Fe_2(SO_4)_3$. One possible explanation for this difference is that the introduction of additional sulfate ions when $Fe_2(SO_4)_3$ is added increase in charge screening between cationic headgroups in the dispersion. Since the effective size of ionic headgroups of amphiphiles in aggregates is dependent on charge screening, the addition of counterions can decrease the effective headgroup size and alter the optimal packing structure of the aggregate. A decrease in the effective headgroup size of oxidized FTMA is consistent with our observation that the cubosomes formed in dispersions containing chemically oxidized FTMA have a smaller lattice spacing than those formed by electrochemically oxidized FTMA.

Because oxidized FTMA has two headgroups, the phase behavior of the dispersions containing phytantriol and oxidized FTMA defies a simple interpretation using the packing parameter described above. Here, we note two considerations that differ from the system with reduced FTMA. First, oxidized FTMA cannot be assumed from the outset to enter into the phytantriol assembly. Past studies have suggested that oxidized FTMA does not form mixed aggregates with conventional surfactants such as reduced FTMA and DTAB.[30] Second, if oxidized FTMA does enter the phytantriol/DTAB assemblies, it is unclear what configuration

oxidized FTMA would adopt within the assembly. For example, one can envision oxidized FTMA adopting a folded configuration or bridging the lipid bilayer between water channels.

To elucidate the behavior of oxidized FTMA in aqueous dispersions with phytantriol, we prepared dispersions varying the amount of oxidized FTMA present. For comparison, we also made dispersions with matching amounts of reduced FTMA. We investigated the phase behavior of FTMA/phytantriol aqueous dispersions as a function of the FTMA content using SAXS. We used samples containing 0%, 5%, 10%, and 20% FTMA (in either redox state) with the remainder of lipid phytantriol. In order to understand the system's phase behavior, we collected diffractograms on each sample at temperatures ranging from 25°C to 80°C in 5° increments. A summary of these experiments can be seen in Figure 6.5 and each diffractogram used in the summary can be seen in the Supporting Information (see Fig. 6.9-6.10). Dispersions of phytantriol (in the absence of other surfactant) have a SAXS diffractogram consistent with a cubic phase with double diamond (Pn3m) symmetry at 25°C. This behavior is consistent with past studies.[60] The addition of reduced FTMA (Fig. 6.5A) leads to a transition to Im3m at 5% reduced FTMA, and to a lamellar phase at 10% reduced FTMA. These transitions can be explained by the addition of reduced FTMA leading to an increase in the relative headgroup size of the surfactant in the aggregates due to charge repulsion and hydration. This increase in headgroup size leads to an increase in lattice parameter, a transition to Im3m, and eventually a transition to a lamellar phase. The addition of 10% oxidized FTMA (Fig. 6.5B) leads to an increase in lattice parameter and a transition to Im3m. Fig. 6.5C shows the lattice parameter measured by SAXS of phytantriol/oxidized FTMA dispersions. The lattice parameter decreases with increasing temperature, which is consistent with previous studies that have observed a similar relationship between lattice parameter and temperature, which can be attributed to an

(A)

Reduced FTMA Content	0%	5%	10%	20%
Appearance	Cloudy	Cloudy	Clear	Clear
SAXS (25 °C)	Pn3m	Im3m	L_α	L_α
SAXS (60 °C)	H_{II}	Im3m + H_{II}	L_α	L_α
Lattice Param, 25 °C (Å):	65	102		

(B)

Oxidized FTMA Content	0%	5%	10%	20%
Appearance	Cloudy	Cloudy	Cloudy	Cloudy
SAXS (25 °C)	Pn3m	Pn3m	Im3m	??
SAXS (60 °C)	H_{II}	Pn3m	Im3m	Im3m
Lattice Param, 25 °C (Å):	65	70	110	

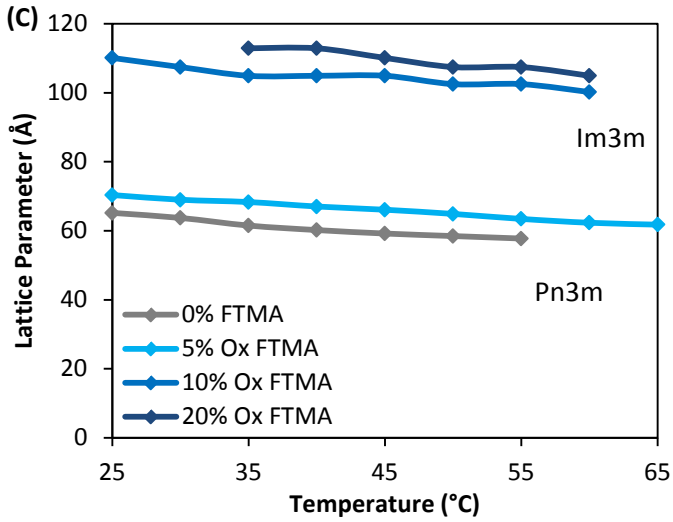

Figure 6.5 Summary of phase behavior of FTMA/phytantriol dispersions
Tables summarizing the phase behavior of dispersions containing phytantriol and **(A)** reduced FTMA or **(B)** oxidized FTMA in aqueous 1 mM Li_2SO_4. **(C)** The lattice parameter determined from SAXS of dispersions containing phytantriol and oxidized FTMA in aqueous 1 mM Li_2SO_4 at temperatures from 25°C to 65°C. The temperature was varied in 5 °C increments and measured at equilibrium. The percentage of oxidized FTMA shown in the legend is the weight fraction of amphiphile (oxidized FTMA and phytantriol) that is oxidized FTMA.

increase in kinks in alkyl chains.[16,31] Since the lattice parameter of these dispersions changes with oxidized FTMA content, we conclude that oxidized FTMA does enter the lyotropic phase with phytantriol. From these results, we conclude that the addition of FTMA (in either redox state) leads to an increase in the relative headgroup size of the surfactant in the aggregates due to charge repulsion and hydration. This increase in headgroup size leads to an increase in lattice parameter, a transition to an Im3m phase, and, for reduced FTMA, eventually a transition to the lamellar phase.

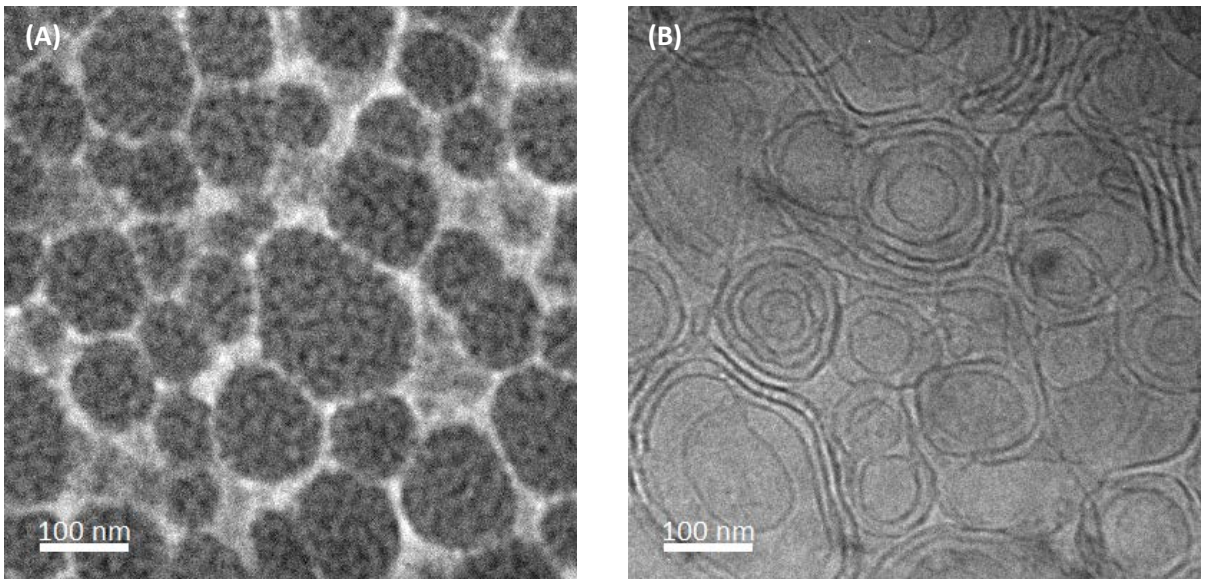

Figure 6.6 Cryo-TEM images of FTMA/phytantriol dispersions
Cryo-TEM images of dispersions containing **(A)** 10% Oxidized FTMA and **(B)** 10% Reduced FTMA with 2% DTAB and 88% Phytantriol in aqueous 1 mM Li_2SO_4 with 10 mg Pluronic F-127 polymer as a stabilizer. The image of the system containing oxidized FTMA is consistent with cubosomes and the image of the system containing reduced FTMA is consistent with liposomes.

To provide an independent characterization of the structures formed by these dispersions, we imaged them using Cryo-TEM. Cryo-TEM images of a dispersion containing 10% Oxidized FTMA, 2% DTAB, and 88% Phytantriol in aqueous 1 mM Li_2SO_4 are shown in Fig. 6.6A. Additional Cryo-TEM images of dispersions containing oxidized FTMA can be seen in the

Supporting Information (Fig. 6.12).The dispersed phase appears to form approximately 100-200 nm aggregates that have a visible internal structure. While the geometry of the structure cannot be determined from the Cryo-TEM images, when considered in combination with SAXS, they point to the formation of cubosomes. Images of dispersions containing reduced FTMA (10% FTMA, 2% DTAB, 88% Phytantriol in aqueous 1 mM Li_2SO_4) are shown in Fig. 6.6B. These images show multilamellar liposomes with dimeters of 100-400 nm.

In addition to the above described experiments performed on dispersions that are prepared in their final state using FTMA solutions that remain in their initial redox state throughout the experiment, we next investigated how changes in the redox state of FTMA can lead to changes in the lyotropic phase.

6.3.2 Dynamic Activation

In order to characterize the dynamic phase behavior of a lyotropic system containing FTMA and phytantriol, we chemically oxidized the incorporated FTMA by the addition of $Fe_2(SO_4)_3$. We used a synchrotron x-ray source for SAXS, which allows for characterization of lyotropic phases in seconds. We placed our dispersion (initially liposomes containing reduced FTMA) in a reaction vessel as shown in Fig. 6.3. To perform SAXS measurements on the dispersion, we drew up ~300 μL with a syringe pump so that the dispersion filled a capillary tube in the beamline. After a 1 s acquisition time, the dispersion was reinjected into the reaction vessel using the syringe pump. A second syringe pump was used to inject an aqueous solution of 20.9 mM $Fe_2(SO_4)_3$ into the dispersion in order to oxidize it. This configuration allowed for dynamic SAXS measurements to be performed on the dispersions while they were being oxidized.

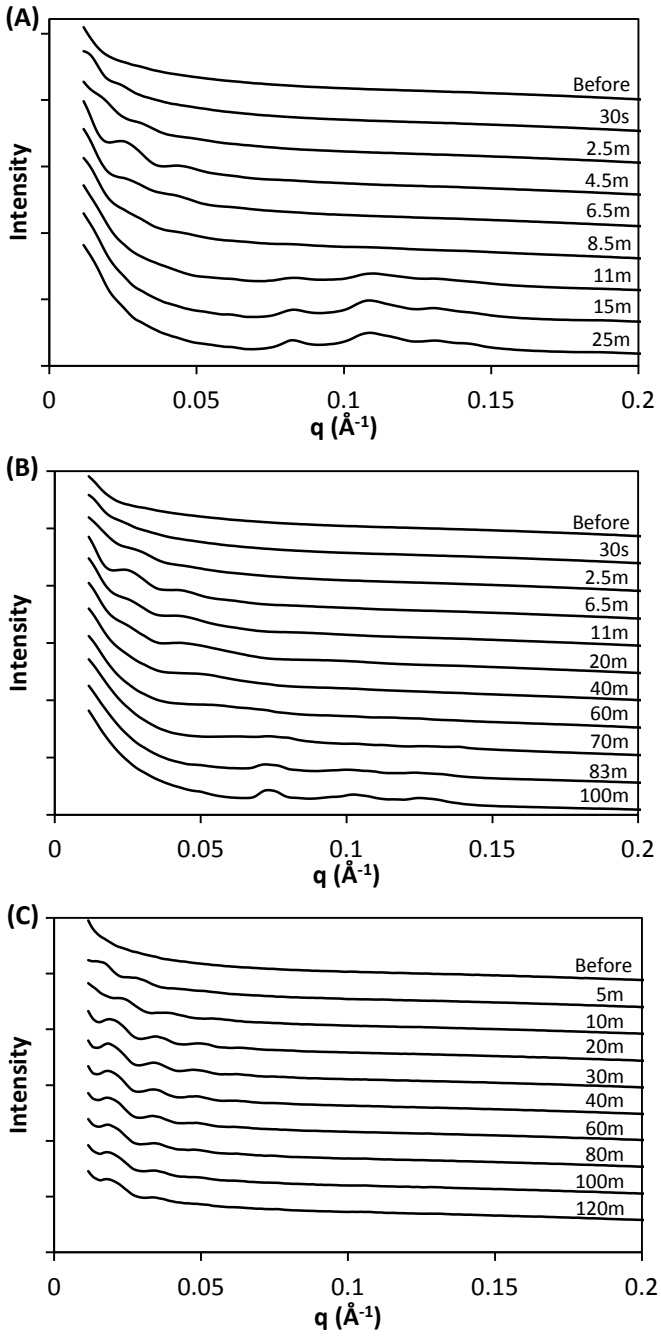

Figure 6.7 SAXS diffractograms of dynamic changes in FTMA/phytantriol phases
SAXS diffractogram showing the dynamic phase transition of dispersions initially containing **(A)** and **(C)** 88% Phytantriol, 10% Reduced FTMA, and 2% DTAB in 0.5 mM Li_2SO_4, and **(B)** 85% Phytantriol, 10% FTMA, and 5% DTAB in 1.5 mM Li_2SO_4. In (A), 50 μL of 20.9 mM $Fe_2(SO_4)_3$ was injected into the dispersion at t = 0,2,4,6, and 8 min. In (B), 50 μL of 20.9 mM $Fe_2(SO_4)_3$ was injected into the dispersion at t = 0,2,4,6, and 8 min and 100 μL of 20.9 mM $Fe_2(SO_4)_3$ was injected into the dispersion at t = 67 min. In (C), 250 μL of 62.7 mM Li_2SO_4 was injected into the dispersion at t = 0. The diffractogram of the initial state in all three samples is consistent with a dispersion of liposomes. The diffractogram of the final state is consistent with cubosomes in (A) and (B). (C) remains lamellar 120 min after the addition of Li_2SO_4.

The first system we explored using the setup described above was a dispersion containing 88% Phytantriol, 10% FTMA, and 2% DTAB in 0.5 mM Li_2SO_4 (Fig. 6.7A). The FTMA in the sample was initially reduced. 50 μL of 20.9 mM $Fe_2(SO_4)_3$ was injected at times t = 0, 2, 4, 6, and 8 minutes. SAXS measurements were performed between injections as noted in Fig. 6.7A. The diffractogram of the initial dispersion is consistent with liposomes, as predicted from the equilibrium experiments described above. As $Fe_2(SO_4)_3$ is added, the lattice parameter shrinks. Once 250 μL of 20.9 mM $Fe_2(SO_4)_3$ was added, we begin to see peaks appear in the SAXS diffractogram around $q \approx 0.1$ Å^{-1}. 250 μL of 20.9 mM $Fe_2(SO_4)_3$ corresponds to the concentration needed to oxidized 50% of the FTMA in the sample. The peaks that appear can be understood as two sets of peaks, one with the relative positions: $\sqrt{2}$, $\sqrt{4}$, $\sqrt{6}$, corresponding to the $\{hkl\}$ = {110}, {200}, and {211} diffraction planes, respectively, of an Im3m structure with a lattice spacing of 107 Å (relative peak positions denoted in blue), and the other with relative positions relative positions $\sqrt{2}$ and $\sqrt{3}$, which correspond to the $\{hkl\}$ = {110}, {111} planes, respectively, of a Pn3m structure with a lattice spacing of 82 Å (relative peak positions denoted in red).

We also performed a dynamic activation experiment (monitored using SAXS) on a dispersion containing 85% Phytantriol, 10% FTMA (initially reduced), and 5% DTAB in aqueous 1.5 mM Li_2SO_4 (Fig. 6.7B). At the beginning of the experiment, the SAXS diffractogram and visual appearance of the sample are consistent with liposomes. In the same fashion as with the previous experiment, 50 μL of 20.9 mM $Fe_2(SO_4)_3$ was added to the sample at time t = 0, 2, 4, 6, and 8 minutes. As described above, the lattice parameter shrinks upon addition of Fe(III), but here no transition to a cubic phase was seen with the quantity of Fe(III) needed to oxidize 50% of the FTMA. After 67 minutes, 100 μL more of 20.9 mM $Fe_2(SO_4)_3$ was

added to the dispersion (the quantity of Fe(III) needed to oxidize 70% of the FTMA). Over the next half hour, the diffractogram began to show peaks around q ≈ 0.1 $Å^{-1}$. These peaks have the relative positions of: $\sqrt{2}$, $\sqrt{4}$, $\sqrt{6}$, corresponding to the {*hkl*} = {110}, {200}, and {211} diffraction planes, respectively, of an Im3m structure with a lattice spacing of 122 Å.

We note that there are two differences between the experiment in Fig. 6.7B and the experiment in Fig. 6.7A: the amount of DTAB and the Li_2SO_4 concentration. Since we would expect an increase in Li_2SO_4 to screen electrostatic interactions and therefore decrease the effective headgroup size of DTAB and FTMA in the liposomes, we would not expect an increase in Li_2SO_4 from 0.5 mM to 1.5 mM to cause the increased preference for a lamellar phase seen in Fig. 6.7B (compared to Fig. 6.7A). Thus, from the experiment in Fig. 6.7B, we conclude that increasing the amount of DTAB present inhibits the transition from liposomes to cubosomes, manifested by a higher fraction of the FTMA needing to be oxidized in order for the transition to occur.

We also considered the effect of electrolyte strength on the phase transformations seen in our dynamic activation experiments. Since increasing electrolyte strength decreases the effective headgroup size of ionic surfactants, increasing the electrolyte strength could also lead to a phase transition from lamellar to cubic. We also considered the possibility that the phase transition observed above from lamellar to cubic upon the addition of $Fe_2(SO_4)_3$ could also be explained by an increase in electrolyte strength rather than the oxidation of FTMA. We prepared a dispersion containing 88% Phytantriol, 10% FTMA, and 2% DTAB in 0.5 mM Li_2SO_4 (the same system as in Fig. 6.7A) and performed a dynamic activation experiment on it (Fig. 6.7C). However, instead of adding $Fe_2(SO_4)_3$ as we did in the experiments above, we added 250 μL of 62.7 mM aqueous

Li_2SO_4 at t = 0. The concentration was selected to match the final concentration of SO_3^{2-} ions in the experiment in Fig. 6.7A. The initial SAXS diffractogram of the dispersion in Fig. 6.7C is consistent with the dispersion being in a lamellar phase. After Li_2SO_4 is added, the lattice spacing shrinks, and no sign of cubic symmetry can be seen during the duration of the experiment. A control dispersion (10% Red FTMA, 2% DTAB, 7.41 mM Li_2SO_4) prepared a week before the beam time see Supporting Information (Fig. 6.11) also does not show a transition to a cubic structure. Therefore, we conclude that the transition seen from liposome to cubosome in dispersions containing FTMA and DTAB upon the addition of $Fe_2(SO_3)_4$ occurs due to oxidation of FTMA rather than an increase in electrolyte strength.

6.3.2 Controlled Release from Liposomes via Redox Trigger

Based on the phase transition of FTMA/phytantriol/DTAB-based dispersions described above from liposomes to cubosomes upon the addition of $Fe_2(SO_3)_4$, we next sought to demonstrate that these transitions could be used for the controlled release of an encapsulated solute. The scheme we selected to investigate the use of redox-triggered phase changes in FTMA-doped lyotropic dispersions was to load liposomes with calcein blue, a variant of calcein, which is a water-soluble dye commonly used encapsulated in liposomes for controlled release studies,[32-35] and release the calcein upon a transition to cubosomes that occurs when $Fe_2(SO_3)_4$ is added. Calcein blue has UV absorption peak at 340 nm,[36] which allows for its detection using UV-visible absorption spectroscopy.

We prepared liposomes loaded with calcein blue containing 80% phytantriol, 10% reduced FTMA, and 10% DTAB as described in Methods. The DTAB content was increased compared to that used in our SAXS experiments because calcein blue was found to inhibit the formation of liposomes. The loaded dispersions were subsequently passed through a size-

exclusion column to separate the liposomes (in the eluate) from free calcein in the continuous phase. The controlled release was performed by adding 225 μg of $Fe_2(SO_4)_3$ as a redox trigger. Fractions of the sample were collected at 5, 30, 60, and 120 minutes after the addition of $Fe_2(SO_4)_3$ and passed through a 50 nm polycarbonate filter to remove the aggregates. One fraction was separated and filtered before the addition of $Fe_2(SO_4)_3$ in order to establish the background amount of calcein blue in the continuous phase of the dispersion after passing through a size-exclusion column. 45 μg of $Fe_2(SO_4)_3$ was added to this fraction (so that it had the same Fe^{3+} content as the other fractions analyzed) in order to account for any effects of iron on calcein blue absorption.[36] Another fraction was collected at the end of the timed release experiment and diluted in methanol in order to disrupt all aggregates and release any remaining calcein blue. This fraction was subsequently filtered. UV-visible absorption spectroscopy was used to quantify the presence of calcein blue in each fraction. The percentage of encapsulated calcein blue released at each time point (see Fig. 6.8) was calculated using the baseline established by the sample that was filtered prior to the addition of $Fe_2(SO_4)_3$ and the total quantity of calcein blue found in the sample that was diluted in methanol prior to filtration. Additional information on the calculation of the percentage of calcein blue released in this experiment can be found in the Supporting Information (see Fig. 6.15-6.16).

Inspection of Fig. 6.8 shows that significantly more calcein blue is detected in all samples filtered after the addition of $Fe_2(SO_4)_3$ than in the sample that was filtered before the addition of $Fe_2(SO_4)_3$. This suggests that calcein blue was successfully encapsulated in the liposomes and that the addition of $Fe_2(SO_4)_3$ led to its release. The sample collected 5 minutes after the addition of $Fe_2(SO_4)_3$ showed that 70 ± 4% of the encapsulated calcein blue was released. By the time 120

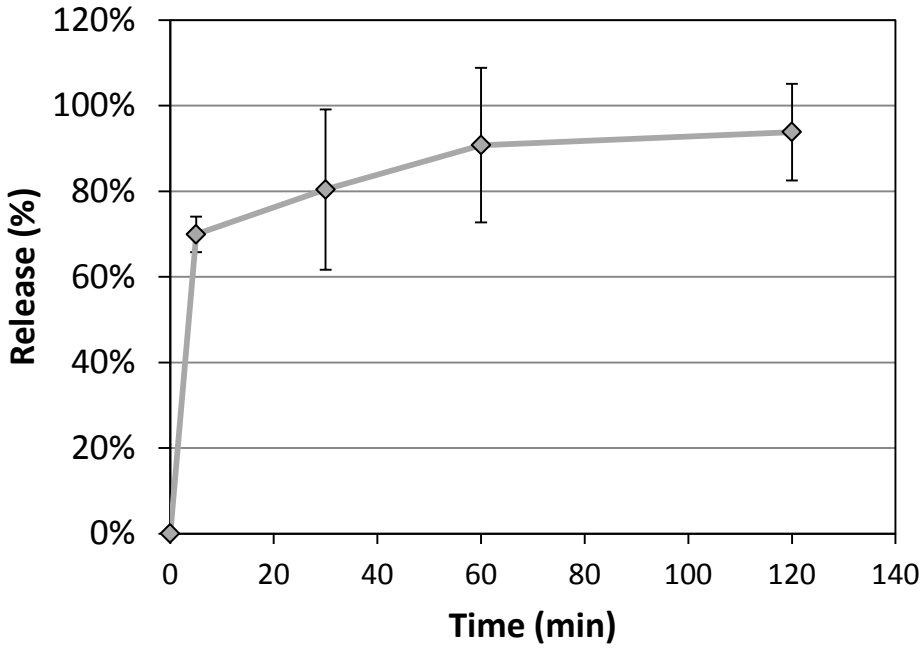

Figure 6.8 Triggered release of calcein blue from FTMA/phytantriol dispersions
Percentage of calcein blue released from liposomes, loaded with calcein blue, made from a dispersion containing containing 10% Reduced FTMA with 10% DTAB and 80% Phytantriol in aqueous 1 mM Li_2SO_4 with 10 mg Pluronic F-127 polymer as a stabilizer and 3 mg calcein blue. The dispersion was passed through a size exclusion column to remove free calcein blue from the continuous phase while liposomes loaded with calcein blue were obtained in the eluate. $Fe_2(SO_4)_3$ was added to the sample at time = 0 to trigger a phase transformation from liposomes to cubosomes and release calcein blue. Fractions were removed from the sample and passed through 50 nm pore polycarbonate filter paper. The calcein blue content in each fraction was calculated using UV-Visible absorption spectrometry. The percentage of calcein blue released was calculated by comparing the calculated amount in each fraction to the amount of calcein blue in a fraction filtered before the addition of $Fe_2(SO_4)_3$ and a fraction to which methanol had been added prior to filtration in order to disassemble any aggregates.

minutes had elapsed, the amount of calcein blue released increased to 94 ± 11%. While the release we observed occurs too fast to allow the calculation of diffusion information, we note that the system we investigated here was not optimized. Importantly, from these results, we conclude that calcein blue dye was released upon the oxidation of FTMA within the Phytantriol/FTMA/DTAB assemblies.

The results in this paper provide a proof-of-concept design for a system that releases a solute via a redox trigger. In future studies, we plan to investigate the use of other chemical redox agents as triggers, such as ascorbic acid and glutathione, for phase changes in lyotropic LC dispersions with redox-active surfactants incorporated. We also plan to investigate the use of non-ionic redox surfactants, such as ethoxylated ferrocenyl surfactants, as a means to achieve phase transitions independent of electrolyte strength such as can be used in biological systems. These studies will help to guide the application of redox-triggered lyotropic LC phase changes as a means of triggered release of encapsulated solutes.

6.4 Conclusions

Overall, the study reported in this paper demonstrates that lyotropic LC dispersions can be designed to undergo phase changes upon a redox trigger. Phytantriol-based aqueous dispersions were made redox-active by the incorporation of FTMA into surfactant assemblies. Assemblies where the surfactant consisted of 10% reduced FTMA and 90% phytantriol adopted lamellar configurations; in contrast, mixtures containing 10% oxidized FTMA and 90% phytantriol formed cubosomes when dispersed. Next, we showed that liposomes (88% Phytantriol, 10% Reduced FTMA, and 2% DTAB) could be transformed into cubosomes by the oxidation of FTMA through the addition of $Fe_2(SO_4)_3$ as a redox trigger. We found that the time necessary for this transition to occur is controllable by altering the amount of DTAB in the sample. Finally, we demonstrated that a solute (calcein blue) could be encapsulated in FTMA/DTAB/Phytantriol liposomes and released upon the addition of $Fe_2(SO_4)_3$ as a redox trigger. The insights obtained from this study have the potential to aid in the design of redox-triggered controlled release schemes for drug delivery.

6.5 Acknowledgements

This work was primarily funded by the National Science Foundation through grant CBET- 1263970. Partial support is also acknowledged by the ARO (through W911NF-14-1-0140 and W911NF-15-1-0568). The authors acknowledge the use of instrumentation supported by the Wisconsin Materials Research Science and Engineering Center (DMR-1121288). SAXS studies were conducted on the SAXS/WAXS beamline at the Australian Synchrotron, Victoria, Australia.

6.6 References

‡ Portions of this chapter will be submitted as: T. J. Smith, R. Suketana, X. Wang, N. A. Alcaraz, B. J. Boyd and N. L. Abbott, *Redox-Triggered Transformations of Liposomes into Cubosomes*, In Preparation, (2017).

1. S. Phan, W.-K. Fong, N. Kirby, T. Hanley, B. J. Boyd, *Int. J. Pharm.* **2011**, *421*, 176–182.

2. R. Negrini, R. Mezzenga, *Langmuir* **2012**, 28, 16455−16462.

3. X. Mulet, B. J. Boyd, C. J. Drummond, *J. Colloid Interface Sci.* **2013**, *393*, 1–20.

4. S. Akbar, A. Anwar, A. Ayish, J. M. Elliott, A. M. Squires, *Eur. J. Pharm. Sci.* **2017**, *101*, 31–42.

5. C. Y. Guo, J. Wang, F. L. Cao, R. J. Lee, G. X. Zhai, *Drug Discov. Today* **2010**, *15* (23–24), 1032–1040.

6. A. Zabara, R. Mezzenga, *J. Control. Release* **2014**, *188*, 31–43.

7. Y.-D. Dong, A. W. Dong, I. Larson, M. Rappolt, H. Amenitsch, T. Hanley, B. J. Boyd, *Langmuir* **2008**, *24* (13), 6998-7003.

8. G. Milkereit, M. Morr, J. Thiem, V. Vill, *Chem. Phys. Lipids* **2004**, *127* (1), 47–63.

9. R. Negrini, R.; Mezzenga, *Langmuir*, **2011**, *27* (9), 5296–5303.

10. K. J. Tangso, W.-K. Fong, T. Darwish, N. Kirby, B. J. Boyd, T. L. Hanley, *J. Phys. Chem. B* **2013**, *117* (35), 10203−10210.

11. K. Larsson, *J. Phys. Chem.* **1989**, *93* (21), 7304–7314.

12. G. J. T. Tiddy, *Phys. Rep.* **1980**, *57* (1), 1-46.

13. W.-K. Fong, T. Hanley, B. J. Boyd, *J. Control Release* **2009**, *135* (3), 218-226.

14. J. Barauskas, T. Landh, *Langmuir* **2003**, *19* (23), 9562–9565.

15. Y.-D. Dong, I. Larson, T. Hanley, B. J. Boyd, *Langmuir* **2006**, *22* (23), 9512–9518.

16. L. de Campo, A. Yaghmur, L. Sagalowicz, M. E. Leser, H. Watzke, O. Glatter, *Langmuir* **2004**, *20* (13), 5254–5261.

17. P. B. Geraghty, D. Attwood, J. H. Collett, Y. Dandiker, *Pharm. Res.* **1996**, *13* (8), 1265–1271.

18. D. Libster, A. Aserin, N. Garti, *J. Colloid Interface Sci.* **2011**, *356* (2), 375–386.

19. I. Martiel, L. Sagalowicz, R. Mezzenga, *Adv. Colloid Interface Sci.* **2014**, *209*, 127-143.

20. Q. Liu, Y.-D. Dong, T. L. Hanley, B. J. Boyd, *Langmuir* **2013**, *29*, 14265–14273.

21. S. J. Fraser, X. Mulet, A. Hawley, F. Separovic, A. Polyzos, *J. Colloid Interface Sci.* **2013**, *408*, 117–124.

22. J. N. Israelachvili, D. J. Mitchell, B. W. Ninham, *J. Chem. Soc. Faraday Trans.* **1976**, *72*, 1525-1568.

23. J. N. Israelachvili, *Intermolecular and Surface Forces: With Applications to Colloidal and Biological Systems*; 3rd Edition, Academic Press: San Diego, CA, **2011**; p. 536.

24. X. Liu, M. D. Graham, N. L. Abbott, *Langmuir* **2007**, *23* (19), 9578–9585.

25. K. L. Herrington, E. W. Kaler, D. D. Miller, J. A. Zasadzinski, S. Chiruvolu, *J. Phys. Chem.*, **1993**, *97* (51), 13792−13802.

26. C. L. Pizzey, C. M. Jewell, M. E. Hays, D. M. Lynn, N. L. Abbott, Y. Kondo, S. Golan, Y. Tahnon, *J. Phys. Chem. B* **2008**, *112* (18), 5849−5857.

27. B. S. Aytar, J. P. E. Muller, S. Golan, S. Hata, H. Takahashi, Y. Kondo, Y. Talmon, N. L. Abbott, D. M. Lynn, *J. Control Release* **2012**, *157* (2), 249-259.

28. T. Saji, K. Hoshino, S. Aoyagui, *J. Chem. Soc., Chem. Commun.* **1985**, *13*, 865-866.

29. J. P. E. Muller, B. S. Aytar, Y. Kondo, D. M. Lynn, N. L. Abbott, *AIChe J.* **2014**, *40* (4), 1381–1392.

30. T. J. Smith, C. Wang, N. L. Abbott, *J. Colloid Interface Sci.* **2017**, *502*, 122–133.

31. B. Geil, T. Feiweier, E.-M. Pospiech, J. Eisenblätter, F. Fujara, R. Winter, *Chem. Phys. Lipids* **2000**, *106* (2), 115–126.

32. C. Kayalar, N. Düzgüneç, *Biochim. Biophys. Acta* **1986**, *860* (1), 51–56.

33. R. J. Lee, P. S. Low, *Biochim. Biophys. Acta* **1995**, *1233* (2), 134–144.

34. M. H. Gaber, N. Z. Wu, K. Hong, S. K. Huang, M. W. Dewhirst, D. Papahadjopoulos, *Int. J. Radiat. Oncol.* **1996**, *36* (5), 1177–1187.

35. P. Pradhan, J. Giri, F. Rieken, C. Koch, O. Mykhaylyk, M. Doblinger, R. Banerjee, D. Bahadur, C. Plank, *J. Control Release* **2010**, *142* (1), 108–121.

36. D. Seto, T. Maki, N. Soh, K. Nakano, R. Ishimatsu, K. Imato, *Talanta* **2012**, *94*, 36–43.

6.7 Supporting Information

Figure 6.9 shows SAXS diffractograms of samples containing 0%, 5%, 10%, and 20% reduced FTMA (Fig. 6.5). Increased reduced FTMA content (>5%) leads to the formation of liposomes.

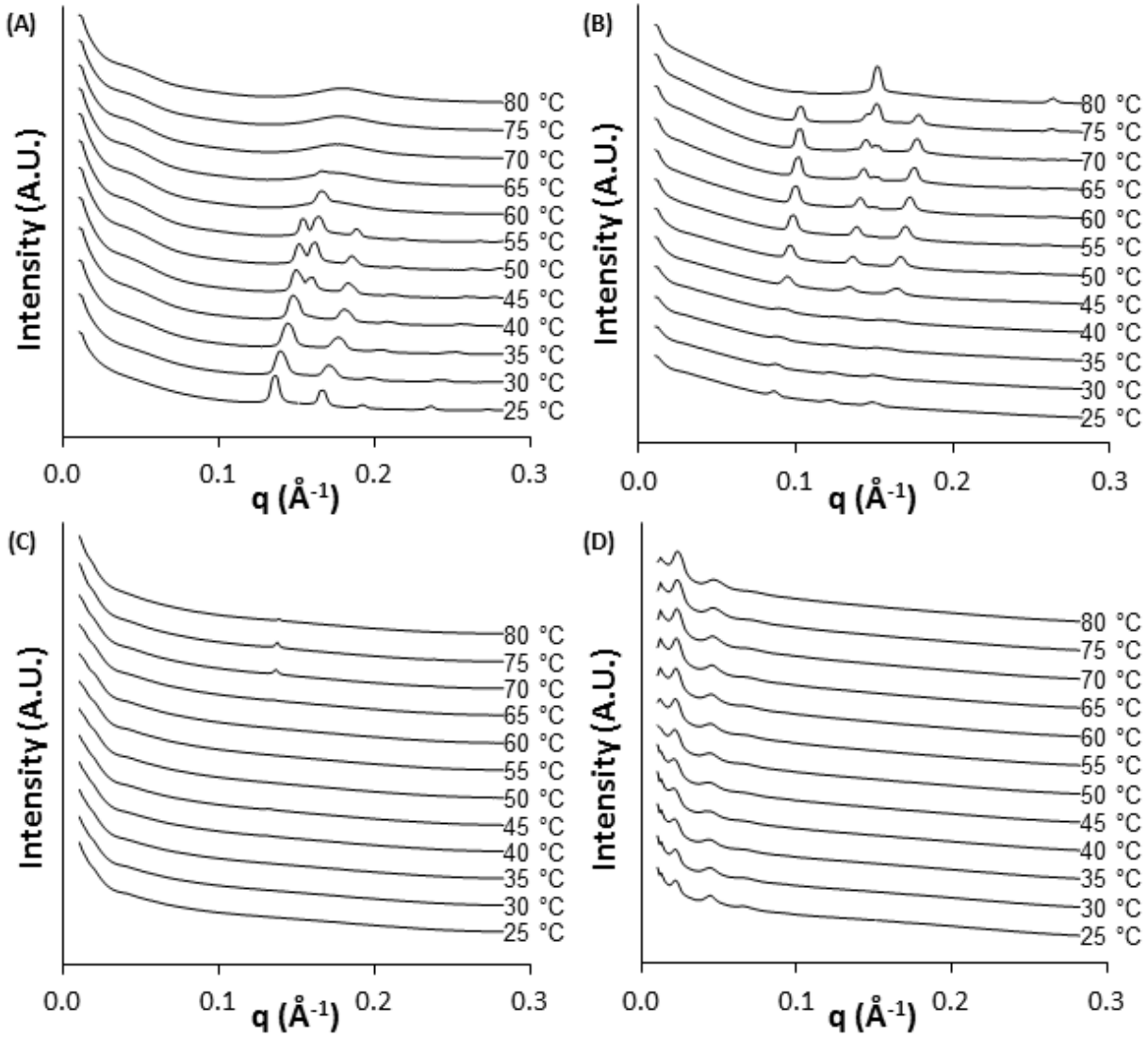

Figure 6.9 SAXS of dispersions with varying reduced FTMA concentration
SAXS diffractograms of dispersions containing **(A)** 0%, **(B)** 5%, **(C)** 10%, and **(D)** 20% reduced FTMA and the balance phytantriol, with the exception of (C) which also had 1% DTAB. (A) shows Bragg reflections consistent with Pn3m symmetry at T < 60 °C and H_{II} symmetry at 40 °C < T < 70 °C. (B) shows Bragg reflections consistent with Im3m symmetry at T < 80 °C and H_{II} symmetry at T > 60 °C. (C) does not show Bragg reflections at T < 70 °C, which is consistent with a lamellar phase, and reflections at T > 65 °C that are consistent with H_{II}. (D) shows Bragg reflections consistent with a lamellar phase at all temperatures measured.

Figure 6.10 shows SAXS diffractograms of samples containing 0%, 5%, 10%, and 20% oxidized FTMA (see Fig. 6.5). Unlike the samples containing reduced FTMA, Bragg reflections that suggest the presence of cubic phases remain visible even in the sample containing 20% oxidized FTMA.

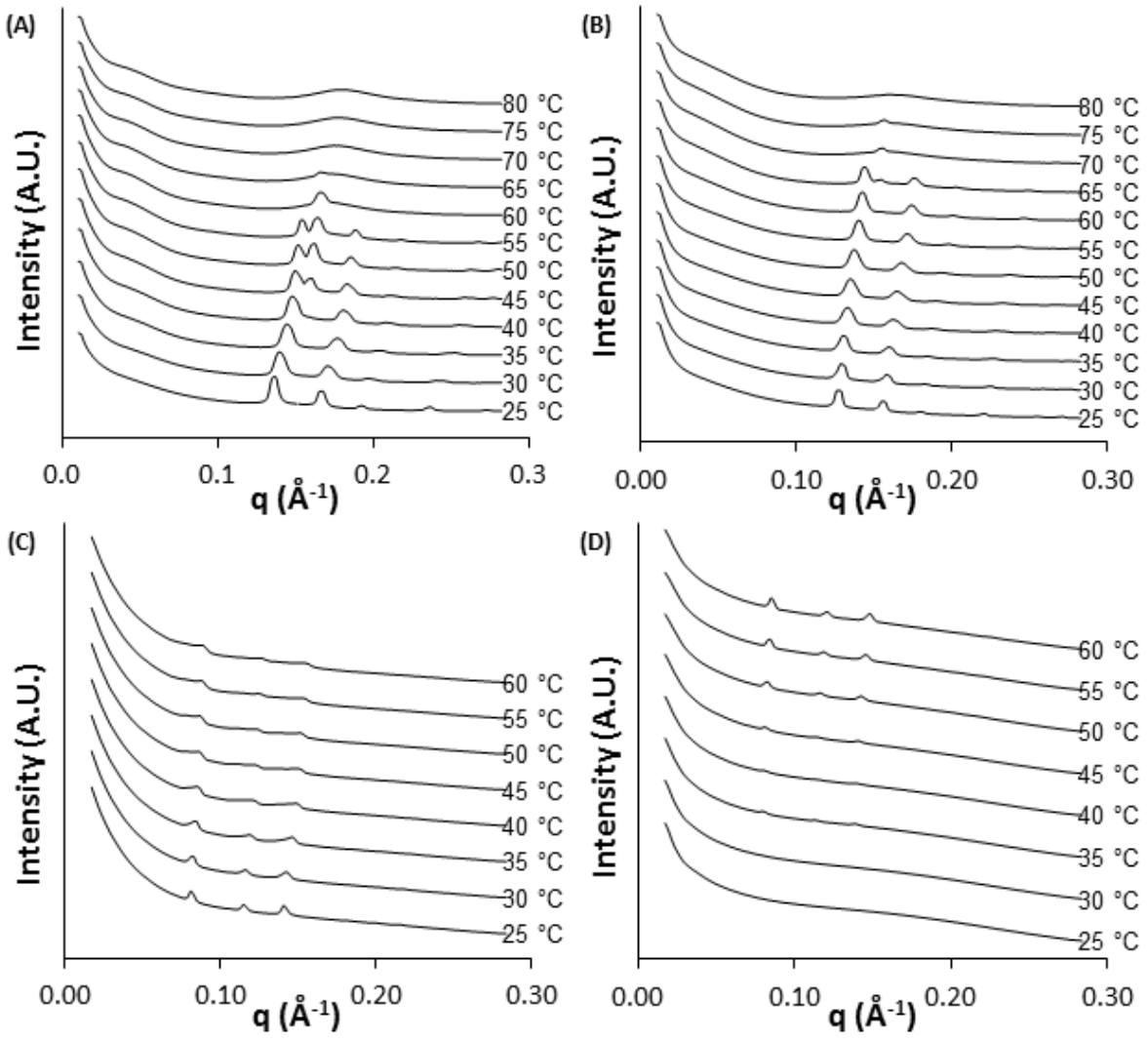

Figure 6.10 SAXS of dispersions with varying oxidized FTMA concentration
SAXS diffractograms of dispersions containing (A) 0%, (B) 5%, (C) 10%, and (D) 20% oxidized FTMA and the balance phytantriol. (A) shows Bragg reflections consistent with Pn3m symmetry at T < 60 °C and H_{II} symmetry at 40 °C < T < 70 °C. (B) shows Bragg reflections consistent with Pn3m symmetry at T < 70 °C and H_{II} symmetry at 60 °C < T < 80 °C. (C) shows Bragg reflections consistent Im3m symmetry at all temperatures measured. (D) shows Bragg reflections consistent with Im3m symmetary at T > 30 °C. No Bragg reflections are visible in (D) below 35 °C, which may suggest the formation of a lamellar phase.

Figure 6.11 shows the SAXS diffractogram of an aqueous dispersion containing 88% Phytantriol, 10% reduced FTMA and 2% DTAB in 7.41 mM Li_2SO_4. The sample was prepared a week before SAXS was performed in order to ensure it remains lamellar. No peaks suggestive of a cubic structure can be seen.

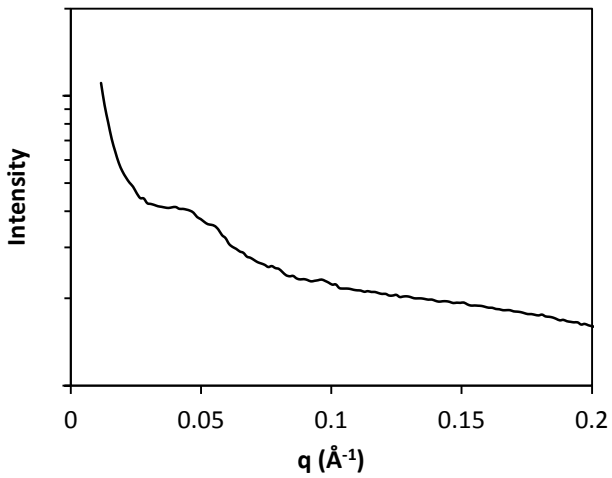

Figure 6.11 SAXS of FTMA/phytantriol dispersion with increased salt
SAXS diffractogram of a dispersion with 88% Phytantriol, 10% reduced FTMA and 2% DTAB in 7.41 mM Li_2SO_4. SAXS was performed one week after the sample was prepared. No peaks suggestive of a cubic structure can be seen.

Figure 6.12 shows additional cryo-TEM images taken of aqueous dispersions containing 10% Oxidized FTMA, 2% DTAB, and 88% Phytantriol in aqueous 1 mM Li_2SO_4 with 10 mg Pluronic F-127 polymer as a stabilizer. These images support the conclusions drawn from Fig. 6A that these dispersions form cubosomes.

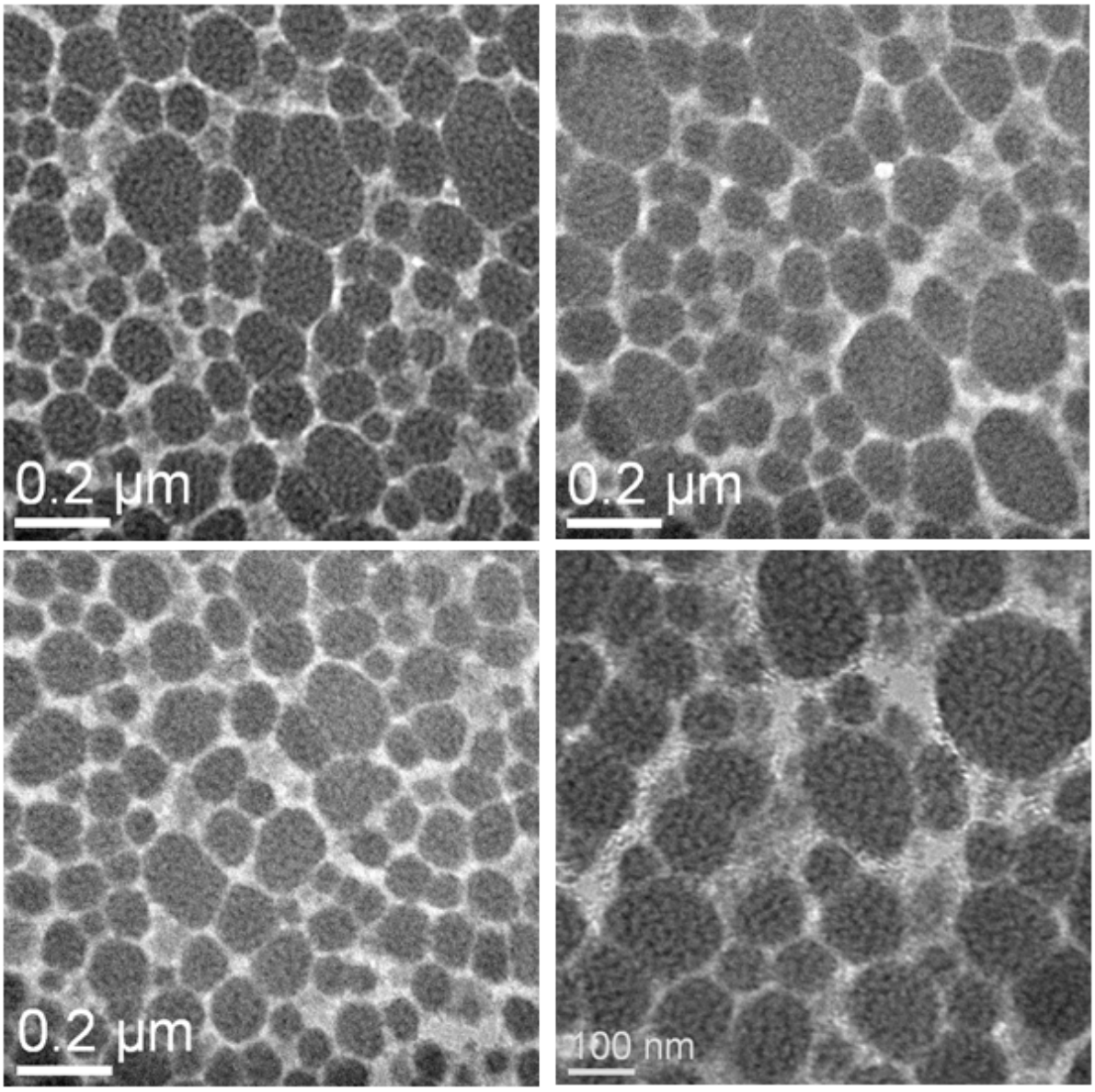

Figure 6.12 Additional cryo-TEM images of oxidized FTMA/phytantriol dispersions
Additional cryo-TEM images of dispersions containing 10% Oxidized FTMA, 2% DTAB, and 88% Phytantriol in aqueous 1 mM Li_2SO_4 with 10 mg Pluronic F-127 polymer as a stabilizer. These images of the system are consistent with the formation of cubosomes.

Figure 6.13 shows additional cryo-TEM images taken of aqueous dispersions containing 10% Reduced FTMA, 2% DTAB, and 88% Phytantriol in aqueous 1 mM Li_2SO_4 with 10 mg Pluronic F-127 polymer as a stabilizer. These images support the conclusions drawn from Fig. 6.6B that these dispersions form liposomes.

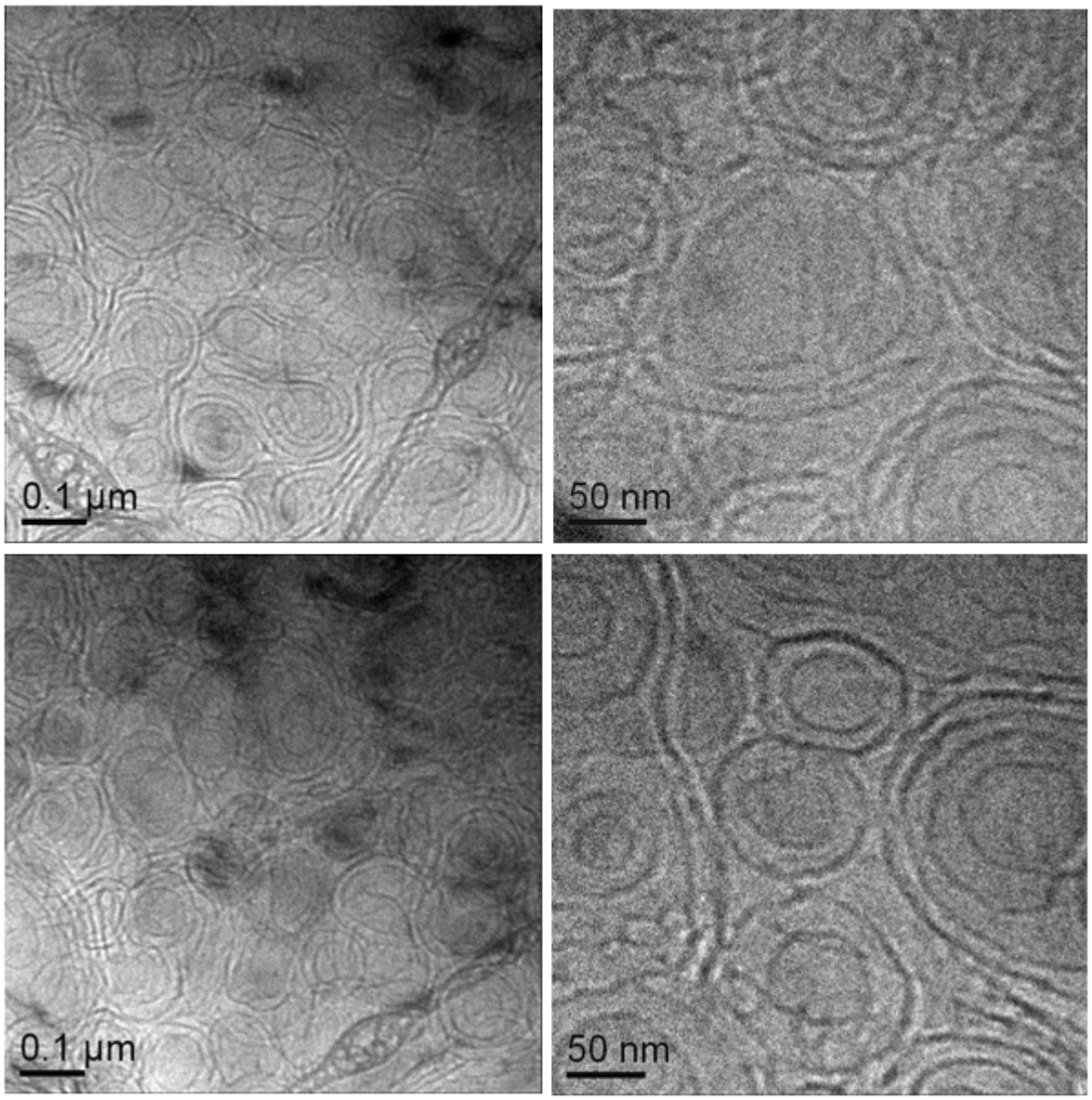

Figure 6.13 Additional cryo-TEM images of reduced FTMA/phytantriol dispersions
Additional cryo-TEM images of dispersions containing 10% Reduced FTMA, 2% DTAB, and 88% Phytantriol in aqueous 1 mM Li_2SO_4 with 10 mg Pluronic F-127 polymer as a stabilizer. These images of the system are consistent with the formation of liposomes.

Figure 6.14 shows cryo-TEM images taken of aqueous dispersions containing Phytantriol in aqueous 1 mM Li_2SO_4 with 10 mg Pluronic F-127 polymer as a stabilizer. These images suggest that phytantriol/water dispersions under the given conditions (25 °C, 10 wt% amphiphile) form cubosomes, in general agreement with past studies.[3]

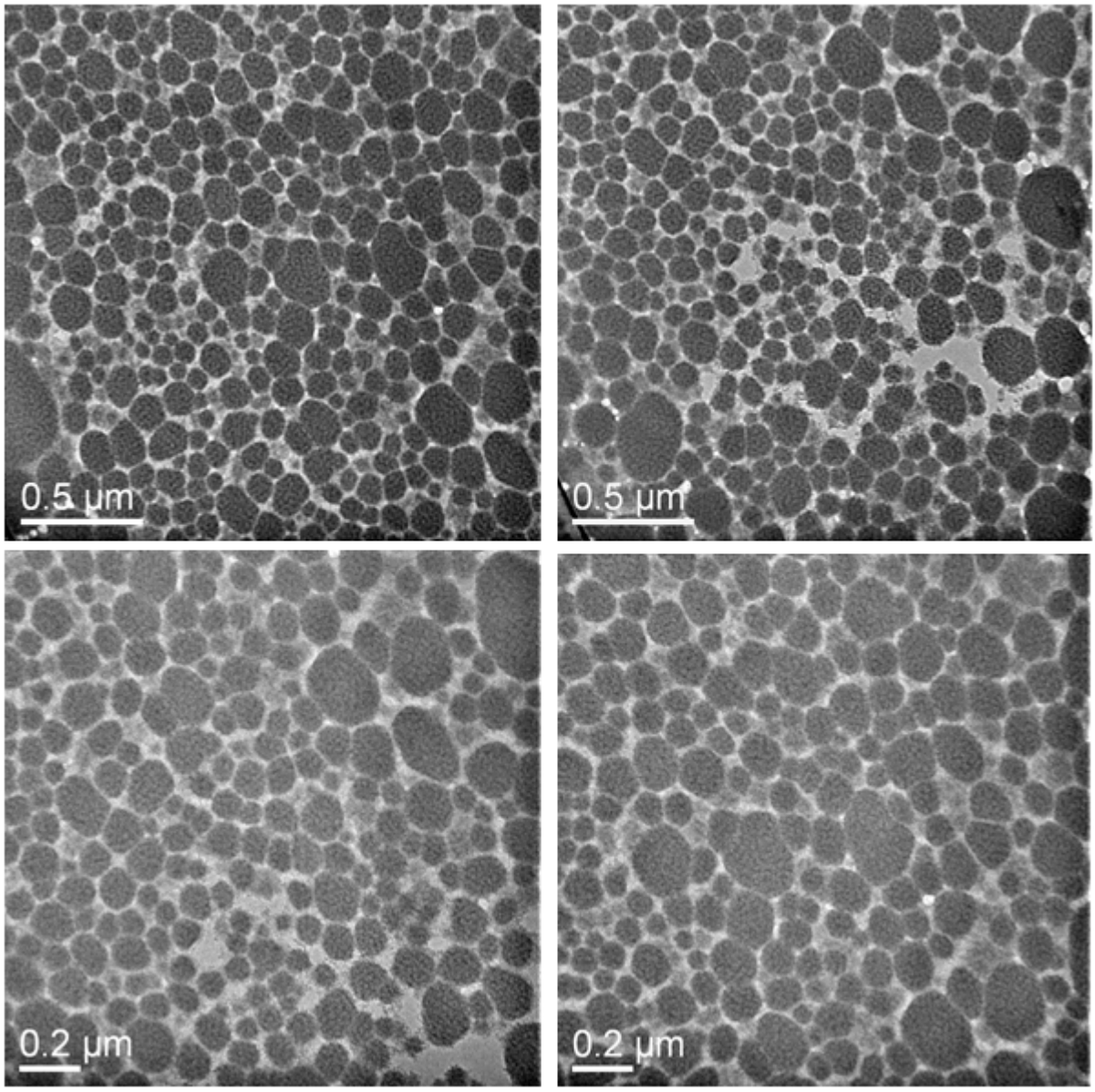

Figure 6.14 Additional cryo-TEM images of phytantriol dispersions without FTMA
Cryo-TEM images of dispersions containing Phytantriol in aqueous 1 mM Li_2SO_4 with 10 mg Pluronic F-127 polymer as a stabilizer. These images of the system are consistent with the formation of cubosomes.

Characterization of the samples used in controlled release experiments can be seen in Figures 6.15-6.16. Figure 6.15 shows an example of UV-visible spectra observed from the fractions of filtered solutions originally containing liposomes loaded with calcein blue (see main text for procedure details).

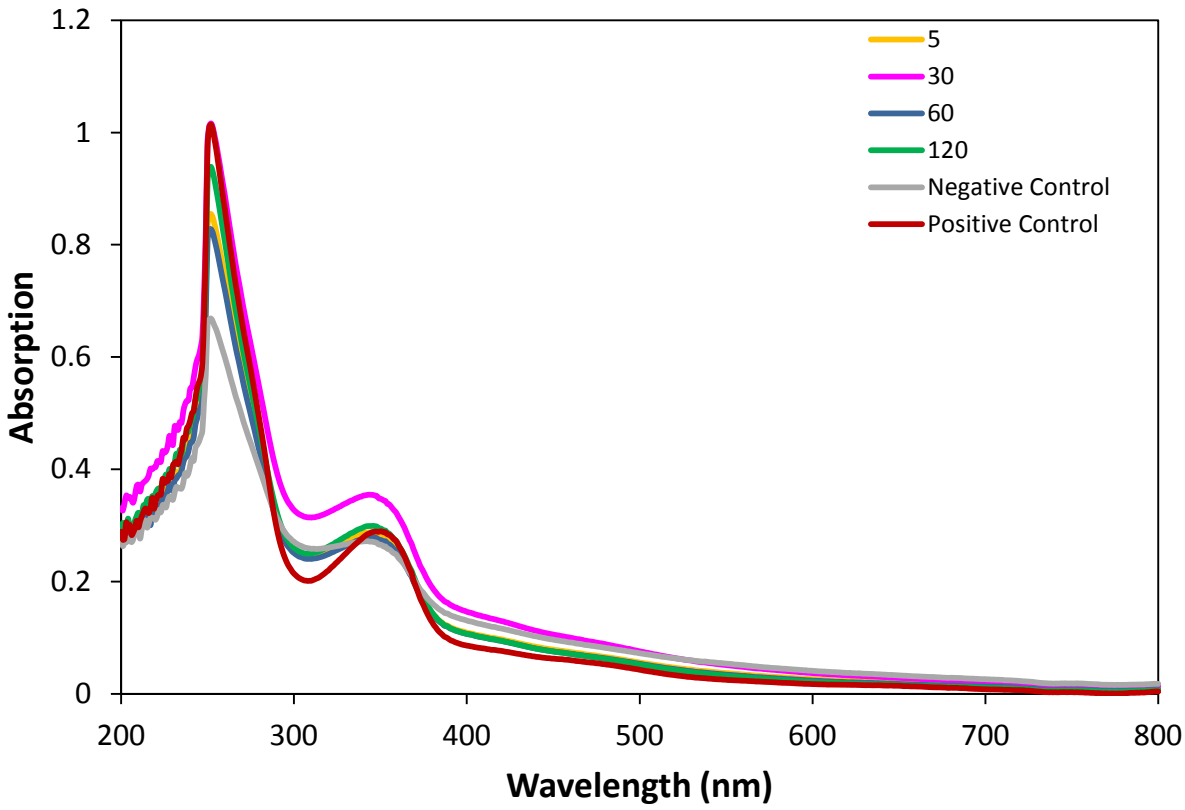

Figure 6.15 UV-vis spectra of solution fractions containing released calcein blue
UV-visible absorption spectra of fractions of filtered solutions originally containing liposomes loaded with calcein blue (see main text for procedure details). The peak around 340 nm corresponds to calcein blue content. These spectra were used to calculate the amount of calcein blue in these fractions by subtracting the absorbance baseline from the peak at 340 nm.

Figure 6.16 shows the arithmetic mean and standard deviation of the amount of calcein blue in each fraction of calcein blue loaded liposomes as determined via UV-visible spectrometry. The percentage released at each time point, P_t, shown in Figure 8 of the main text was calculated:

$$P_t = (C_t - C_{neg})/(C_{pos} - C_{neg}) \quad (6.3)$$

where C_t is the concentration of calcein blue at the same time point, C_{neg} is the concentration of calcein blue in the negative control, and C_{pos} is the concentration of calcein blue in the positive control.

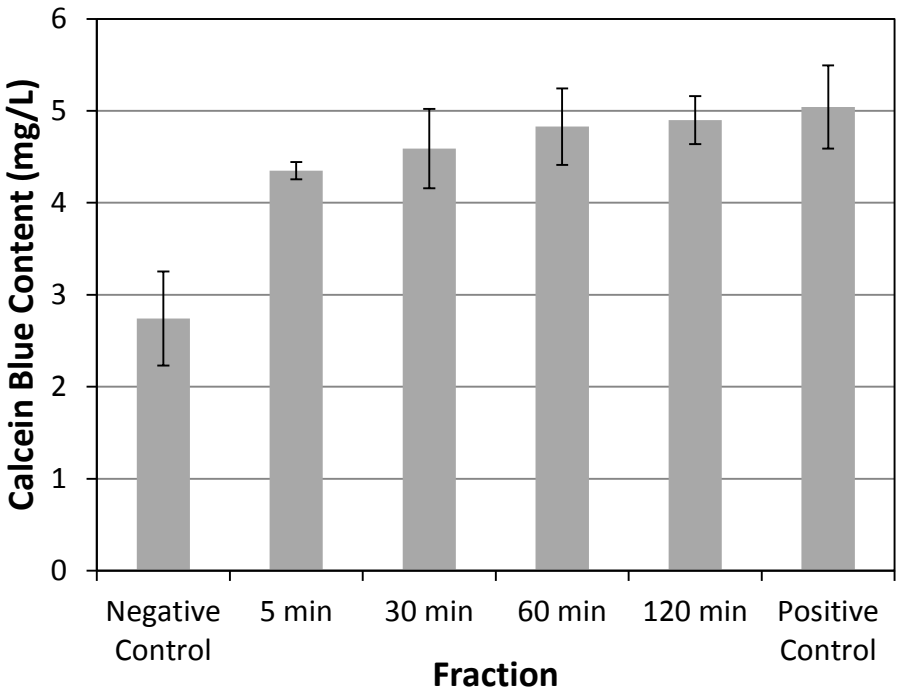

Figure 6.16 Quantification of released calcein blue in solution fractions
Arithmetic mean and standard deviation of the amount of calcein blue in each fraction of calcein blue loaded liposomes as determined via UV-visible spectrometry. The error bars represent the standard deviation of three independent experiments.

Chapter 7 : Summary and Future Directions

7.1 Summary

The research presented in this thesis focuses on redox-dependent changes in the molecular architecture of ferrocenyl surfactants and subsequent transformations in their self-assembly. Specifically, we utilize changes in the molecular architecture of 11-ferrocenyltrimethylammonium bromide (FTMA) to influence its self-assembly toward two objectives: (i) to control interfacial charge transfer between FTMA and a solid electrode and (ii) to trigger redox-dependent transformations in the phase state of lyotropic liquid crystalline dispersions through the incorporation of FTMA. Together these studies provide guidance for the design of systems that make use of responsive surfactants.

First, we sought to build a model system in which the reversible self-assembly of FTMA could be used to influence interfacial charge transfer. By performing cyclic voltammetry (CV) with alkanethiol-functionalized gold electrodes in contact with aqueous solutions containing FTMA, we observed a significantly greater anodic peak current than cathodic peak current (i.e. current rectification; I_a/I_c = 17). In contrast, in CVs performed using the non-self-assembling ferrocenyl mediator hydroxymethyl ferrocene (HMeFc), we observed only slight current rectification (I_a/I_c = 1.7). These results suggest that the self-assembly of FTMA is critical to the current rectification we observed in CVs performed on solutions containing it. We ascertained from the scan rate dependence of the CVs with FTMA that the anodic current primarily results from FTMA in bulk solution diffusing to the electrode while the cathodic current results only from oxidized FTMA adsorbed to the surface of the electrode. Notably, the reaction of oxidized FTMA in bulk solution is inhibited. With insights from quartz crystal microbalance and images

collected via atomic force microscopy, we concluded that the current rectification observed in CVs with FTMA is due to the formation of interfacial reduced FTMA hemimicelles on the surface of hydrophobized electrodes that prevent oxidized FTMA in bulk solution from accessing the electrode. This conclusion is further supported by CVs performed with solutions containing a mixture of FTMA and dodecyltrimethylammonium bromide (DTAB) that revealed interfacial assemblies of DTAB are able to block oxidized FTMA from adsorbing on the electrode, resulting in a greater degree of current rectification ($I_a/I_c > 80$) than was observed with FTMA in the absence of DTAB. These results demonstrate that the self-assembly of a redox mediators at a hydrophobized electrode can be used to influence charge transfer.

Second, we investigated the effect of redox-triggered transformations of the molecular architecture of surfactants on their mixing within assemblies. Specifically, we compared the redox-dependent behavior of FTMA with that of a ferrocenyl surfactant with the ferrocene group adjacent to the head group (N,N-dimethylferrocenylmethyldecyl ammonium bromide; DMFA). We found, by using surface tension and light scattering measurements, that reduced and oxidized FTMA do not form mixed aggregates but that reduced and oxidized DMFA do mix in assemblies formed in bulk solution or at the air/water interface. Whereas both redox states of DMFA have the molecular architecture of a conventional surfactant (in the case of oxidized DMFA, a conventional surfactant with a divalent headgroup) and reduced FTMA has a conventional architecture but oxidized FTMA has a bolaform architecture, these results support the conclusion that the change in molecular architecture of FTMA upon oxidation underlies the demixing of the two redox states within aggregates. Motivated by our findings that the current rectification observed with FTMA at a hydrophobized electrode can be enhanced by the addition of DTAB, we also investigated the mixing of FTMA (in either redox state) with DTAB within assemblies

formed in bulk solution or on hydrophobic solid surfaces. Through the use of quartz crystal microbalance and atomic force microscopy, we found that reduced FTMA forms mixed interfacial assemblies with DTAB (which has conventional surfactant architecture) but oxidized FTMA does not. We found that the rules governing mixing in micelles in bulk solution also apply to adsorbed micelles at hydrophobic solid surfaces but not to assemblies at the air/water interface. Overall, these results demonstrate conclusion that mixing/demixing between reduced and oxidized FTMA, or between FTMA in either redox state with DTAB, stems from the molecular architecture of the surfactants. These results support our conclusions above that demixing between reduced and oxidized FTMA in assemblies at hydrophobized electrodes contributes to current rectification.

Third, we investigated the role of the surface chemistry of electrodes used in conjunction with the elicitation of current rectification by a self-assembling redox mediator. Specifically, we compared the current rectification observed in CVs using 0.1 mM FTMA at gold electrodes that had been functionalized with 1-dodecanethiol (DT; hydrophobic; $I_a/I_c = 8 \pm 2$), N,N,N-trimethyl-(11-mercaptoundecyl)ammonium (TMUA; positively-charged; $I_a/I_c = 1.4 \pm 0.1$), and 11-mercaptoundecansulfonide (MUS; negatively-charged; $I_a/I_c = 3.4 \pm 1.2$). The scan rate dependence of our cyclic voltammograms shows that more adsorbed reduced FTMA is needed in order to form a layer that blocks oxidized FTMA from the electrode than can be generated from the reduction of adsorbed oxidized FTMA. Together with insights from QCM and AFM, we conclude that the increased adsorption of reduced FTMA necessary to form a layer that blocks oxidized FTMA from the electrode underlies the decreased degree of current rectification observed with FTMA in the absence of DTAB at negatively-charged electrodes compared to hydrophobized electrodes. We observed that the complete inhibition of measurable cathodic

faradaic current could be recovered by the addition of DTAB, which does not leave the electrode surface during a cyclic voltammogram, as a co-surfactant. At positively-charged electrodes, we observed little interfacial self-assembly of FTMA and no apparent effect of self-assembly on the observed charged transfer. Together these results suggest that either hydrophobic or negatively-charged electrodes should be used in the design of rectifying devices that use the self-assembly of FTMA to achieve current rectification, and if negatively-charge electrodes are used, DTAB is also needed as a co-surfactant.

Fourth, we demonstrated that a self-assembling redox mediator can be used to block recombination reactions while allowing for dye replenishment in a working dye-sensitized solar cell. Specifically, we compared and contrasted the power generation of dye-sensitized solar cells that used as a redox mediator either FTMA or the otherwise comparable non-self-assembling redox mediator (2-methyl-1-ferrocenylmethyl) trimethylammonium iodide (MFMT). These cells were fabricated using titania films, with an adsorbed photosensitizing dye and functionalized with a dodecylphosphonate monolayer, supported by a fluorine-doped tin oxide glass electrode. The cells made using FTMA generated 17.5 ± 0.2 μW of power, whereas cells using MFMT produced only 3 ± 2 μW, suggesting that self-assembly plays an important role in the rectifying ability of FTMA as a redox mediator within a dye-sensitized solar cell. We also prepared FTMA-based cells without a dodecylphosphonate film and found that hydrophobization of the electrode surface is necessary to generate significant power in FTMA-based solar cells. Together, the results reported in this paper demonstrate that self-assembly can be used in the design of cells capable of rectifying current and generating power and provide a framework for the design of future systems to improve upon the performance of the cells described here.

Fifth, we showed that redox-triggered changes can be made in lyotropic liquid crystalline dispersions via the incorporation of FTMA into phytantriol-based assemblies. Specifically, we demonstrated that assemblies formed from mixtures containing 10% reduced FTMA and 90% phytantriol (by surfactant wt%) adopted lamellar configurations while mixtures containing 10% oxidized FTMA and 90% phytantriol formed inverse bicontinuous cubic phases when dispersed. Subsequently, we demonstrated that lamellar aggregates (88% Phytantriol, 10% Reduced FTMA, and 2% DTAB) could be transformed into cubic-phase aggregates by the oxidation of FTMA through the addition of $Fe_2(SO_4)_3$ as a redox trigger. We found the kinetics of this transformation to be tunable by altering the amount of DTAB in these samples. Finally, we encapsulated a solute (calcein blue) within the assemblies in a lamellar-phase FTMA/DTAB/Phytantriol dispersion and released the solution upon the addition of $Fe_2(SO_4)_3$ as a redox trigger. The insights obtained from this chapter show that redox-triggered changes in the molecular architecture of FTMA can be utilized in the design of redox-triggered controlled release schemes.

Overall, the work presented in this thesis demonstrates that the redox-dependent self-assembly of FTMA can be exploited to both (i) influence interfacial charge transfer processes in potentially useful ways and (ii) trigger redox-dependent transformations in the phase state of lyotropic liquid crystalline dispersions. Together, the work described in this thesis assists with the understanding of phenomena related to redox-triggered changes in the molecular architecture of ferrocenyl surfactants and provides guidance into the design of systems using these phenomena.

7.2 Future Directions

7.2.1 Electrochemistry of Mixtures of Redox-Inactive Surfactant and Non-Self-Assembling Redox Mediators

The results described in this thesis show that current rectification can be achieved between a solid electrode and a self-assembling redox mediator in aqueous solution. This rectification was further enhanced by the addition of a redox-inactive co-surfactant that is miscible with one redox state of the mediator but not with the other redox state. These results raise the question of whether, when a redox-active co-surfactant is present, it is necessary that the redox mediator itself be able to self-assemble. In general, for current rectification to occur in the presence of an adsorbed layer of redox-inactive surfactant on the electrode surface, it is merely necessary that the redox mediator be able to enter the assembly in one redox state but not the other. As such, we propose the design of systems in which a redox-inactive co-surfactant, such as DTAB or SDS, forms a monolayer on an electrode and a non-self-assembling redox mediator enters the assembly in one redox state but not in the other. Some mediators that may be of potential use in such a system include hydroxymethylferrocene, MFMT, and methylviologen derivatives, which past studies[1-3] have found to associate with surfactant assemblies in their reduced but not their oxidized redox state. Systems that use non-self-assembling redox mediators used in conjunction with a redox-inactive surfactant may be advantageous compared to self-assembling mediators because non-self-assembling mediators likely exhibit faster diffusion due to lower molar masses and a lack of bulk self-assembly, which potentially allows for easier charge transfer for the replenishment of electrons to the oxidized dye. Allowing for faster replenishment of oxidized dye would permit considerable improvement to be made over the dye-sensitized solar cells we fabricated in Chapter 5.

7.2.2 Electrochemistry of Mixtures of FTMA and Redox-Inactive Bolaform Surfactants

The work discussed in this thesis focused on the use of the self-assembly of FTMA as a method of achieving current rectification through the inhibition of cathodic current, while allowing anodic current between solid electrodes and an aqueous redox solution. While the suppression of cathodic current is important in the design of dye-sensitized solar cells, other technologies, such as solar water splitters,[4-7] require aqueous systems that are also able to inhibit anodic currents while allowing cathodic current. Because the addition of conventional co-surfactant led to a further suppression of cathodic current by blocking the (bolaform) oxidized FTMA from the electrode, we propose to add bolaform surfactant as a co-surfactant in order to instead block reduced FTMA from the electrode surface, thereby suppressing anodic current. The selection of bolaform surfactant must be chosen carefully in order to ensure that it is able to competitively adsorb over reduced FTMA, reduced FTMA is unable to form mixed assemblies with it, and oxidized FTMA is able to form mixed assemblies with it. The experiments proposed here would provide additional possible utility for the principles governing the mixing of ferrocenyl surfactants within assemblies that were investigated in this thesis.

7.2.3 Effects of Variations in FTMA Molecular Architecture

The vast majority of the experiments performed in this thesis used the redox-dependent self-assembly of FTMA to either rectify current or alter the phase state of LLC dispersions. However, in general, the principles governing mixing of surfactants within micellar assemblies discussed in this thesis can be applied to surfactants of varying molecular. For example, in Chapter 3, while we found that the reversible changes in FTMA self-assembly responsible for the current rectification observed in this thesis stem from changes in the molecular architecture of FTMA with changes in redox state, we also found that the reduced and oxidized forms of

DMFA form mixed aggregates. Specifically, we propose investigating the applicability of the self-assembly of two classes of ferrocenyl surfactants toward the aims presented in this thesis.

First, we propose to vary the chain length of the hydrocarbon chain of the ferrocenyl surfactants used to elicit current rectification in future studies. In chapter 5, we found that the power generation by the FTMA-based solar cells we fabricated was limited by the ability of reduced FTMA to deliver electrons to the oxidized dye. However, at the increased concentrations of FTMA far above its critical micelle concentration needed to deliver electrons to the dye rapidly, we observed a loss in the current rectification due to changes in the demixing between reduced and oxidized FTMA. We hypothesized that these difficulties may be overcome by decreasing the length of the aliphatic chain of FTMA because the critical micelle concentration would also increase. Past studies[8,9] have shown that both the critical micelle concentration and the morphology of assemblies formed differ amongst linear ferrocenyl surfactants of differing aliphatic chain lengths. We propose investigating the relationship between the aliphatic chain length and the electrochemical behavior exhibited by ferrocenyl surfactants at hydrophobized electrodes with the aim of improving upon the current rectification observed here.

Second, we propose to investigate the use of double-tailed and gemini ferrocenyl surfactants in both electrochemical systems and in LLC dispersions. Because the morphology of assemblies formed by double-tailed and gemini surfactants is sensitive to small changes in molecular architecture,[10] we would expect that morphological changes may occur between assemblies containing the reduced states and those containing the oxidized states of these surfactants. Support for this hypothesis can be seen in past studies[9] that have shown that the critical aggregation concentration of gemini ferrocenyl surfactants to differ by oxidation state. Furthermore, we hypothesize that assemblies formed by double-tailed and gemini ferrocenyl

surfactants may also exhibit demixing between the reduced and oxidized redox states that allows for influence of charge transfer properties between ferrocenyl surfactant redox mediators and functionalized electrodes. These molecular architectures offer an additional range of co-surfactant materials that may selectively displace either redox state from the electrode surface and allow for further opportunity to control interfacial transfer. In addition to use for the influence of electrochemical effects, we would also expect double-tailed and gemini surfactants to influence the phase state of LLC dispersions in ways that were not achievable through the introduction of FTMA. For example, we may be able to achieve redox control over the phase state of inverse bicontinuous hexagonal and inverse discontinuous cubic phases in room-temperature dispersions with the introduction of gemini and double-tailed ferrocenyl surfactants.

7.2.4 Selection of Alternative Dyes for FTMA-Based Dye-Sensitized Solar Cells

In Chapter 5, we demonstrated that a self-assembling redox mediator could be used in dye-sensitized solar cells to allow desirable anodic current while blocking unwanted cathodic current. This allows for electrons to be replenished to the N3 dye, which is oxidized after excitation and the subsequent loss of an electron, while inhibiting the transmission of electrons from the electrode to the redox mediator. The system we designed was built as a proof-of-concept and was not optimized for the use of FTMA as a redox mediator, or even for the use of aqueous redox solutions. As a result, the cells we designed are less efficient than the traditional iodide/triiodide cells for which the selection of dye and semiconductors used in the cell were optimized. Past studies show that the ruthenium-based dyes typically used in iodide/triiodide dye-sensitized solar cells are non-optimal for aqueous cells.[11- 16] Specifically, one study found that carbazole-based dyes were more effective than ruthenium-based dyes in an aqueous cell using ferricyanide as a redox mediator.[16] The use of water as a solvent in dye-sensitized solar

cells leads to degradation of cell performance over time, such as that from the desorption of dye or loss of electrons through hydrolysis on the titania surface.[18] Future work toward the design of more effective dye-sensitized solar cells based on a self-assembling redox mediator should include studies comparing and contrasting alternative dye materials for use in contact with aqueous solutions containing ferrocenyl surfactants.

7.2.5 Incorporation of Nonionic Ferrocenyl Surfactant into LLC Dispersions

In the work presented in Chapter 6, we incorporated FTMA into phytantriol-based LLC dispersions as a method of achieving redox-control over the phase state of the aggregates in the dispersion. However, the phase state of LLC aggregates containing cationic surfactant is strongly dependent on the ionic strength of the aqueous solution in the continuous phase,[17] which limits their applicability in biological systems. In order to overcome ionic strength-dependent effects on the phase of the LLCs, we propose to investigate the incorporation of non-ionic redox surfactants, such as ethoxylated ferrocenyl surfactants, as a means to achieve phase transitions independent of electrolyte strength such as can be used in biological systems. We anticipate that redox-triggered changes in phase state will be achievable without the interactions between ionic headgroups in reduced FTMA. These studies will provide insight into the application of redox-triggered LLC phase changes in biologically relevant systems for drug delivery.

7.3 References

1. P. Brugger, M. Grätzel, *J. Am. Chem. Soc.* **1980**, *102*, 2461-2463.

2. M. Grätzel, *Farad. Discuss.* **1980**, *70*, 359-374.

3. K. Monserrat, M. Grätzel, *J. Chem. Soc., Chem. Commun.* **1981**, *4*, 183-187.

4. A. Kudo, T. Miseki, *Chem. Soc. Rev.* **2009**, *38*, 253–278.

5. F. E. Osterloh, *Chem. Mater.* **2008**, *20*, 35–54.

6. W. J. Youngblood, S.-Y. A. Lee, K. Maeda, T. E. Mallouk, *Acc. Chem. Res.* **2009**, *42* (12), 1966-1973.

7. L. J. Minggu, W. R. W. Daud, M. B. Kassim, *Int. J. Hydrogen Energy* **2010**, *35*, 5233–5244.

8. B. S. Gallardo, K. L. Metcalfe, N. L. Abbott, *Langmuir* **1996**, *12* (17), 4116–4124.

9. B. S. Gallardo, N. L. Abbott, *Langmuir* **1997**, *13* (2), 203–208.

10. S. Manne, T. E. Schaffer, Q. Huo, P. K. Hansma, D. E. Morse, G. D. Stucky, *Langmuir* **1997**, *13* (24), 6382–6387.

11. C. H. Law, S. C. Pathirana, X. Li, A. Y. Anderson , P. R. F. Barnes, A. Listorti, T. H. Ghaddar, B. C. O ′ Regan, *Adv. Mater.* **2010**, *22* (40), 4505–4509.

12. H.-L. Lu, T. F.-R. Shen, S.-T. Huang, Y.-L. Tung, T. C.-K. Yang, *Sol. Energy Mater Sol. Cells* **2011**, *95* (7), 1624–1629.

13. Y.-S. Jung, B. Yoo, M. K. Lim, S. Y. Lee, K.-J. Kim, *Electrochimica Acta* **2009**, *54* (26), 6286–6291.

14. C. H. Law, O. Moudam, S. Villarroya-Lidon, B. C. O'Regan, *J. Mater. Chem.* **2012**, *22* (44), 23387–23394.

15. H. Zhang, L. Qiu, D. Xu, W. Zhang, F. Yan, *J. Mater. Chem. A* **2014**, *2* (7), 2221–2226.

16. T. Daeneke, Y. Uemura, N. W. Duffy, A. J. Mozer, N. Koumura, U. Bach, L. Spiccia, *Adv. Mater.* **2012**, *24* (9), 1222–1225.

17. Q. Liu, Y.-D. Dong, T. L. Hanley, B. J. Boyd, *Langmuir* **2013**, *29*, 14265–14273.